



**AFRL-RX-WP-TR-2016-0149**

**COOPERATIVE MATERIALS RESEARCH PROJECTS-  
STUDENT RESEARCH PROGRAM III  
Student Research Program To AFRL/RX  
A Summary of Various Materials Research Projects**

Mark Groff – AFRL/RXOP

**Southwestern Ohio Council for Higher Education**

**27 MAY 2015  
Final Report**

**Distribution Statement A.  
Approved for public release: distribution unlimited.**

**(STINFO COPY)**

**AIR FORCE RESEARCH LABORATORY  
MATERIALS AND MANUFACTURING DIRECTORATE  
WRIGHT-PATTERSON AIR FORCE BASE, OH 45433-7750  
AIR FORCE MATERIEL COMMAND  
UNITED STATES AIR FORCE**

## NOTICE AND SIGNATURE PAGE

Using Government drawings, specifications, or other data included in this document for any purpose other than Government procurement does not in any way obligate the U.S. Government. The fact that the Government formulated or supplied the drawings, specifications, or other data does not license the holder or any other person or corporation; or convey any rights or permission to manufacture, use, or sell any patented invention that may relate to them.

This report was cleared for public release by the USAF 88th Air Base Wing (88 ABW) Public Affairs Office (PAO) and is available to the general public, including foreign nationals.

Copies may be obtained from the Defense Technical Information Center (DTIC)  
(<http://www.dtic.mil>).

AFRL-RX-WP-TR-2016-0149 HAS BEEN REVIEWED AND IS APPROVED FOR  
PUBLICATION IN ACCORDANCE WITH ASSIGNED DISTRIBUTION STATEMENT.

//SIGNATURE//  
\_\_\_\_\_  
MARK GROFF  
Plans and Programs Branch  
Integration and Operations Division  
Materials and Manufacturing Directorate

//SIGNATURE//  
\_\_\_\_\_  
ANDREW T. JEFFERS  
Plans and Programs Branch  
Integration and Operations Division  
Materials and Manufacturing Directorate

This report is published in the interest of scientific and technical information exchange, and its publication does not constitute the Government's approval or disapproval of its ideas or findings.

# REPORT DOCUMENTATION PAGE

*Form Approved*  
OMB No. 0704-0188

The public reporting burden for this collection of information is estimated to average 1 hour per response, including the time for reviewing instructions, searching existing data sources, gathering and maintaining the data needed, and completing and reviewing the collection of information. Send comments regarding this burden estimate or any other aspect of this collection of information, including suggestions for reducing this burden, to Department of Defense, Washington Headquarters Services, Directorate for Information Operations and Reports (0704-0188), 1215 Jefferson Davis Highway, Suite 1204, Arlington, VA 22202-4302. Respondents should be aware that notwithstanding any other provision of law, no person shall be subject to any penalty for failing to comply with a collection of information if it does not display a currently valid OMB control number. **PLEASE DO NOT RETURN YOUR FORM TO THE ABOVE ADDRESS.**

<b>1. REPORT DATE (DD-MM-YY)</b> 27 May 2015	<b>2. REPORT TYPE</b> Final	<b>3. DATES COVERED (From - To)</b> 27 January 2009 – 27 April 2015	
<b>4. TITLE AND SUBTITLE</b> COOPERATIVE MATERIALS RESEARCH PROJECTS- STUDENT RESEARCH PROGRAM III Student Research Program to AFRL/RX A Summary of Various Materials Research Projects		<b>5a. CONTRACT NUMBER</b> FA8650-09-2-5800	
		<b>5b. GRANT NUMBER</b>	
		<b>5c. PROGRAM ELEMENT NUMBER</b> 62102F	
<b>6. AUTHOR(S)</b> Mark Groff – AFRL/RXOP (Government Editor)		<b>5d. PROJECT NUMBER</b> 4348	
		<b>5e. TASK NUMBER</b>	
		<b>5f. WORK UNIT NUMBER</b> X023	
<b>7. PERFORMING ORGANIZATION NAME(S) AND ADDRESS(ES)</b> Southwestern Ohio Council for Higher Education 3155 Research Blvd. Suite 204 Dayton, OH 45420		<b>8. PERFORMING ORGANIZATION REPORT NUMBER</b>	
<b>9. SPONSORING/MONITORING AGENCY NAME(S) AND ADDRESS(ES)</b> Air Force Research Laboratory Materials and Manufacturing Directorate Wright-Patterson Air Force Base, OH 45433-7750 Air Force Materiel Command United States Air Force		<b>10. SPONSORING/MONITORING AGENCY ACRONYM(S)</b> AFRL/RXOP	
		<b>11. SPONSORING/MONITORING AGENCY REPORT NUMBER(S)</b> AFRL-RX-WP-TR-2016-0149	
<b>12. DISTRIBUTION/AVAILABILITY STATEMENT</b> Distribution Statement A. Approved for public release: distribution unlimited.			
<b>13. SUPPLEMENTARY NOTES</b> PA Case Number: 88ABW-2016-5818; Clearance Date: 23 Nov 2016. This document contains color.			
<b>14. ABSTRACT (Maximum 200 words)</b> This Technical Report gives a summary of the research projects of the Cooperative Agreement with AFRL/RX, completed during the period of time from 1 September 2013 to 30 September 2014. Research results are summarized and any related activities are also included. Projects include research in such areas as nonmetallic materials; metals and ceramics; electromagnetic materials; system support materials; integrity; materials engineering and computer activities.			
<b>15. SUBJECT TERMS</b> nonmetallic materials metals & ceramics electromagnetic materials, system support and manufacturing			
<b>16. SECURITY CLASSIFICATION OF:</b>			<b>17. LIMITATION OF ABSTRACT:</b> SAR
<b>a. REPORT</b> Unclassified	<b>b. ABSTRACT</b> Unclassified	<b>c. THIS PAGE</b> Unclassified	
<b>18. NUMBER OF PAGES</b> 379		<b>19a. NAME OF RESPONSIBLE PERSON (Monitor)</b> Mark Groff	
<b>19b. TELEPHONE NUMBER (Include Area Code)</b> (937) 656-9549			

## REPORT DOCUMENTATION PAGE Cont'd

### 6. AUTHOR(S)

#### University of Dayton:

Erica Gaussa Emily Stienecker Alexander E. Saurber Zack Driscoll Ashley White Daniel R. Esposito Andrew Aronow Sarah Hierath Henry Bourassa Ongela Helm Hadil Issa Brittanie Rooths Sarah Barnes Emily Erdman Matthew Shea Victoria Hutten Emily Fehrman-Cory Arthur Siwecki Aubrey Steele Rachel (Smith) Naguy Randall Stevenson Jessica Dagher Allison Ecker

#### Wright State University:

Rachel Swiger Mackenzie Kirby Jonathan H. Marshall Eugene Whatley Mallory Lyle Matthew Edge Jordan Speers Anna Porter Eric Michael Tipps Cody Weddell Ian Wolford Aaron Cherry Morgan Spicer Stephen Bricker Jessica Hendricks Madelyn Hill Michelle Harr Jason Anders Jason Beckman Daniel Reilly Alec Blankenship Michael Morris Michael A. Rybak Tyler Rammel Clint Hirtzinger Jason Anders Katherine Hitchcock Travis Tidball Tinnuade Daboiku Austin T. Christopher Jessica Hendricks Adam Donovan Nicholas Engel Tyler Weihing Daniel Rapping Garrett DeFazio

#### Cedarville University:

Stephanie Long, Krishawn Ward, Rachel Smith, Joshua Sommers

#### Alabama A&M University:

Dontrel Reynolds

#### Central State University:

Talion Grace

#### Michigan State University:

Heather M. Booth

#### Jackson State University:

Teresa Cemeritte

#### University of Cincinnati:

Eliot F. Gomez, Emory Beck-Millerton, Brad Cumby

#### University of Texas at El Paso:

Mark D. Flores

#### University of Texas at San Antonio:

Daniel M. Sparkman

#### Georgia Institute of Technology:

William D. Musinski

#### Clark Atlanta University:

Vernecia Person

#### Louisiana Tech University:

David Cossey

#### The Ohio State University:

Regina Gallagher

### GOV project leads:

<b>AFRL/RXCM</b>	S. Lee Semiatin; Jaimie Tiley; Jeff Simmons; Adam Pilchak; Patrick J. Golden; Reji John
<b>AFRL/RXCC</b>	Max Alexander; Lawrence Matson; Mike Cinibulk; David Mollenhauer; Eric Jones; Craig Przybyla; Timothy Breitzman
<b>AFRL/RXCA</b>	Eric Lindgren; James Blackshire
<b>AFRL/RXA</b>	Melvin D. Hoke
<b>AFRL/RXAN</b>	Kurt G Eyink; Gail Brown; Elizabeth Steenbergen; Andrey Voevodin; Michael Check; Donald Dorsey; Shanee Pacley; Charles E. Stutz; Shin Mou
<b>AFRL/RXAS</b>	James Grote; Rajesh Naik; Rajiv Berry
<b>AFRL/RXAP</b>	Joy Haley; Jonathan Vernon ; Urbas Augustine; Thomas Cooper; Christopher Tabor; Kent Averett; Neil Murphy
<b>AFRL/RXSA</b>	Steve Thompson; Brett Bolan; Alan Fletcher; Jeff Calcaterra
<b>AFRL/RXSC</b>	Dave Madden
<b>AFRL/RXLM</b>	Michael Groeber
<b>AFRL/RXOC</b>	Bryon Foster; Brian Stucke
<b>AFRL/RXOE</b>	Steve Reichard; Wade W. Brower
<b>AFRL/RXOP</b>	Robyn Mack
<b>AFRL/RXPS</b>	David Zelmon

# TABLE OF CONTENTS

Project #		Page #
0004.3	PROCESSING SCIENCE FOR METALLIC TPS MATERIALS .....	1
0007.1	HEAT TREATMENT OF POWDER METALLURGY SUPERALLOYS .....	5
0007.2	HEAT TREATMENT OF POWDER-METALLURGY SUPERALLOYS .....	11
0007.3	HEAT TREATMENT OF PM SUPERALLOY R&D.....	15
0034.2	ELECTROMAGNETIC PROTECTION – STRUCTURES/DETECTION.....	18
0035.1	MOLECULAR BEAM EPITAXY OF QUANTUM COUPLED STRUCTURES ...	23
0056	NUCLEOBASE IN ORGANIC LIGHT EMITTING DIODES .....	27
0059.1	PHOTOPHYSICAL PROPERTIES OF NONLINEAR CHROMOPHORES .....	37
0059.2	PHOTOPHYSICAL PROPERTIES OF NONLINEAR CHROMOPHORES .....	40
0066.1	CTE TAILORING IN HYBRID MATERIALS .....	44
0072.1	NONMETALLIC MATERIALS DIVISION TECHNICAL SUPPORT .....	51
0081	PREPARATION AND CHARACTERIZATION OF ULTRA HIGH TEMPERATURE CERAMIC MATERIALS.....	57
0090	TRANSMISSION ELECTRON MICROSCOPY OF NANOSTRUCTURED MATERIALS .....	62
0097	CHEMIST .....	67
0099.2	EXCHANGE-SPRING COMPOSITE MAGNETS WITH HIGH ENERGY PRODUCT .....	73
0101	MATERIALS INTEGRITY BRANCH SUPPORT.....	79
0105	EM MATERIALS ENGINEER .....	82
0109.1	SINGLE-CRYSTAL MICROSTRUCTURE CHARACTERIZATION .....	85
0110	MATERIALS AND MANUFACTURING DIRECTORATE NETWORK SUPPORT .....	89
0111.1	INFORMATION OPERATION BRANCH TECHNICAL SUPPORT .....	91
0119.1	CERAMICS GROUP LABORATORY TECHNICIAN #2 .....	94
0122	MODEL VALIDATION FOR IMPEDANCE SPECTROSCOPY .....	98
0124	ENVIRONMENTAL AND ENERGY ENGINEERING ANALYSIS.....	101
0129	TOOLS FOR TOMOGRAPHIC RECONSTRUCTION OF MICROSCOPE IMAGES.....	105

0132.1	SYNTHESIS AND CHARACTERIZATION OF DNA BIOPOLYMER/NONLINEAR OPTICAL (NLO) CHROMOPHORE THIN-FILMS DEPOSTIED BY MATRIX ASSISTED PULSED LASER EVAPORATION (MAPLE).....	110
0135	AFM CHARACTERIZATION OF OPTICAL AND ELECTRONIC STRUCTURES .....	115
0138.1	MODELING THE ROLE OF MICROTTEXTURE ON THE FATIGUE BEHAVIOR OF TITANIUM ALLOYS USING LINEAR ELASTIC FRACTURE MECHANICS .....	120
0142.1	OPTICAL CHARACTERIZATION OF SEMICONDUCTOR NANOSTRUCTURED MATERIALS .....	125
0142.2	OPTICAL CHARACTERIZATION OF SEMICONDUCTOR NANOSTRUCTURED MATERIALS .....	129
0146	LAYER BY LAYER ASSEMBLY OF GRAPHENE FOR WEARBALE ELACTRONICS .....	131
0147	THIN FILM DEVICES .....	137
0149.2	LABORATORY AUTOMATION AND DATA ANALYSIS .....	139
0152	ANGLE RESOLVED EMISSION/ABSORPTION TECHNIQUE FOR ANALYSIS OF A SERIES OF GOLD NANOPARTICLE DECORATED CARBON NANOTUBES.....	144
0153	COMPOSITE MATERIAL SENSING RESEARCH USING ULTRASOUND SENSING AND MODELING .....	151
0155	FABRICATION AND CHARACTERIZATION OF DNA BIOPOLYMER-NONLINEAR OPTICAL (NLO) CHROMOPHORE FILMS .....	156
0157	COMPOSITE DAMAGE TOLERANCE AND PERFORMANCE.....	163
0158	MODELLING THE EFFECTS OF SHOT-PEENED RESIDUAL STRESSES AND INCLUSIONS ON MICROSTRUCTURE-SENSITIVE FATIGUE OF NI-BASE SUPERALLOY COMPONENTS .....	175
0159	IMPROVE ENERGY TECHNOLOGIES .....	179
0160	EVALUATION OF ALTERNATE FIBER FORMS FOR A HOT TRAILING EDGE STRUCTURE .....	182
0161	HIGH TEMPERATURE SYNTHESIS OF LOW DIMENSION STRUCTURES .	188
0162	EFFECT OF MICROSTRUCTURE ON SMALL CRACK GROWTH IN Ti-6Al-4V	196
0163	LIQUID METAL FOR TUNABLE CONFORMAL ANTENNAS .....	203

0164	ELASTOMERS SUPPORT .....	213
0165	ELASTOMER SUPPORT .....	215
0166	LABORATORY FACILITY ENGINEERING SUPPORT PROJECT .....	217
0168	EVALUATION OF ALTERNATE FIBER FORMS FOR A HOT TRAILING EDGE STRUCTURE .....	220
0169	PULSED LASER DEPOSITION FOR GLASS DIELECTRICS.....	227
0170	ORIENTATION-PATTERNED GALLIUM NITRIDE FOR QUASI PAHSED- MATCHED NONLINEAR OPTICS .....	230
0171	HAIRY NANO-PARTICLES: GENERAL BRUSH ARCHITECTURE.....	235
0172	COMPOSITE MATERIALS SUPPORTABILITY .....	243
0173	CERAMICS GROUP LABORATORY TECHNICIAN .....	253
0174	PHASE EVOLUTION FOR STRUCTURAL MATERIALS .....	257
0175	EVALUATION OF ALTERNATE FIBER FORMS OF AFR-PE-4 FOR B-2 HOT TRAILING EDGE STRUCTURE .....	261
0176	FIBER VOLUME FRACTION ANALYSIS WITH CERAMIC MATRIX COMPOSITES .....	266
0177	METALLOGRAPHIC RESEARCH ON ADVANCED CERAMICS FOR ELECTRON CHARACTERIZATION.....	271
0178	EXPLORATORY STUDIES IN THIN FILM OPTICAL COATINGS.....	275
0179	PREDICTION OF MATERIAL PROPERTY DISTRIBUTIONS WITH SMALL PROBABILISTIC MICROSTRUCTURAL MODELS .....	279
0180	DEVELOPMENT OF HIGH TEMPERATURE FULL FIELD METHODS TO UNDERSTAND THE BEHAVIOR OF STRUCTURAL MATERIALS FOR AIR FORCE APPLICATIONS.....	285
0181	INVESTIGATION OF NONLINEAR OPTICAL MATERIALS .....	292
0181.1	INVESTIGATION OF NONLINEAR OPTICAL MATERIALS .....	295
0182	CHEMICAL/ENVIRONMETAL ENGINEERING SOCHE STUDENT .....	300
0183	MECHANICAL ENGINEERING SOCHE STUDENT.....	303
0184	BIOPOLYMER BASED MACH ZEHNDER ELECTRO-OPTIC MODULATORS .....	305
0185	ELECTRONIC CHARACTERIZATION FOR GLASS AND CERAMIC DIELECTRICS .....	311
0186	ELECTRICAL CHARACTERIZATION OF SEMICONDUCTOR MATERIALS .....	315

0187	INVESTIGATION OF LIQUID CRYSTAL DISPERSIONS AND PHOTOSENSITIVE SURFACES .....	318
0188	NANOSCALE SURFACE TOPOGRAPHY CHARACTERIZATION .....	325
0189	2D THIN FILM GROWTH AND CHARACTERIZATION .....	333
0190	2 D MATERIAL SENSORS AND DEVICES .....	339
0191	PROCESSING AND CHARACTERIZATION OF CERAMIC MATRIX COMPOSITES .....	344
0192	PROCESSING AND CHARACTERIZATION OF CERAMIC MATRIX COMPOSITES .....	348
0193	CHARACTERIZATION OF TITANIUM ALLOYS FOR USE IN PROCESS MODELING AND LIFE-PREDICTION .....	351
0194	COMPUTER SCIENCE 3D MODELING, GRAPHICS, ENGINEERING MODELING AND ANIMATION .....	355
0196	MULTISCALE MECHANICS OF BOND SCISSION OF POLYMER COMPOSITES .....	358
0198	COMPOSITE DAMAGE TOLERANCE ASSESSMENT METHODOLOGIES ..	364
0199	STRUCTURAL MATERIALS EVALUATION .....	368

PROCESSING SCIENCE FOR METALLIC TPS MATERIALS

Project No. 0004.3

Erica Gaussa  
University of Dayton

31 August 2014

Government Project Leader  
Dr. S. Lee Semiatin  
AFRL/RXCM

Southwestern Ohio Council for Higher Education  
Student Research Program  
Agreement Number: FA8650-09-2-5800

## **Acknowledgements**

I would to thank Dr. S. Lee Semiatin for the amazing opportunity to conduct cutting-edge materials research for the United States Air Force. He has been an excellent mentor and leader and a vital part in my success as a student and growing professional. I would also like to thank Jared Shank, without whom I would not have learned exceptional technical skills required to operate a scanning electron microscope (SEMs). I would like to thank Tinu Daboiku, Mackenzie Kirby (SOCHE), Bill Saurber, and especially Mike Velze and Bob Lewis (UES, Inc.) for technical support with both data and sample processing. Finally, I would like to thank Emily Stienecker, Zack Driscoll, and Alex Saurber (SOCHE) for their help and contributions to this project.

## **General Description of Project**

Nickel-base superalloys are used in the aerospace industry for high-temperature rotating components. Superalloy powders are consolidated by “hot isostatic pressing, blind-die compaction, hot extrusion, or a combination of such methods to produce a billet” [1]. The processing parameters are created to ensure a two-phase microstructure which contains fine gamma grains and precipitates. This microstructure leads to a superplastic behavior, low flow stress and high strain-rate sensitivity [1].

This project’s main goal was to provide insight into the effect of standard and non-standard forging parameters on grain structure development during the final supersolvus heat treatment (SSHT). Two powder metallurgy samples, IN-100 and LSHR, were exposed to isothermal hot compression testing over a wide range of strain rates and temperatures. The materials were then imaged using backscatter-electron (BSE) imaging. Electron-backscatter diffraction (EBSD) was used to establish the details of the gamma-grain and gamma-prime-precipitate evolution. Both the BSE images and the EBSD data provided a basis for interpreting the factors that could affect the grain-structure evolution when an alloy was SSHT’ed.

## **Description of Research**

The focus of the research was the processing of metallic materials for thermal protection systems (TPS) and aircraft engine disks. Research was conducted to establish the effects of process variables on the evolution of microstructure and defects during wrought processing. Two metallic alloys were examined, a gamma titanium aluminide (“TiAl”) and a nickel-base superalloy material. The various microstructures developed during processing were characterized using optical and scanning electron microscopes (SEMs). Specific features such as grain size, phase proportions, and remnant lamellae (in TiAl), and grain size and recrystallized volume fraction in Ni alloys were determined through quantitative analysis on electronic images. The presence of defects such as cracks, cavities, residual porosity, etc. was also documented. These results were used to define optimal processing windows for the aerospace alloys

## **Results**

An example EBSD image is shown in Figure 1. The figure on the left shows the sample prior to the de-twinning process while the right is the sample after it was detwinned.

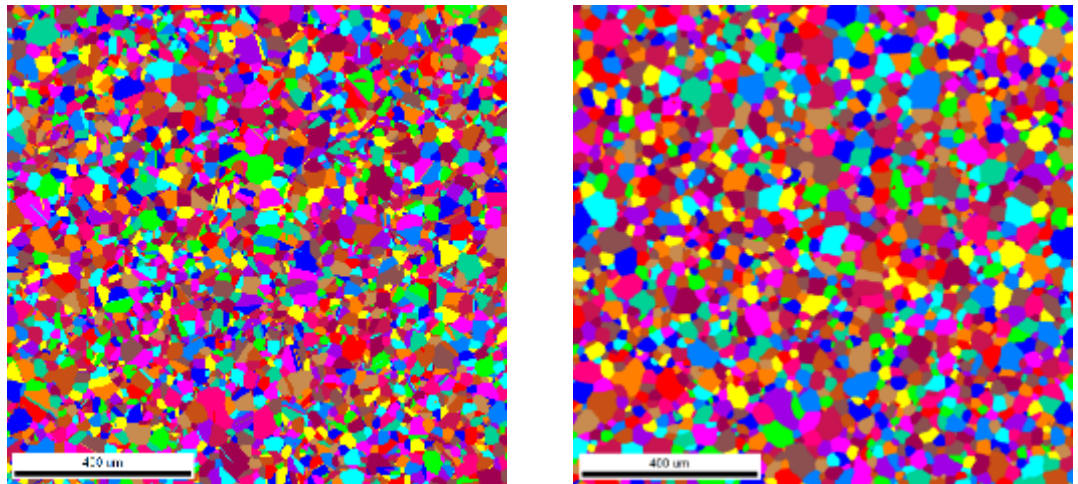


Figure 1. Example of EBSD images of nickel superalloy.

These images were used to determine the size of the gamma grains and precipitates.

BSE images were taken using a scanning electron microscope (SEM). The goal was to capture the precipitates inside the gamma grains. The other method used to calculate precipitate size utilized the FoveaPro add-on in Photoshop. The precipitates were “hand-painted” in Photoshop, and the data were collected using Fovea pro. Typical before-and-after BSE images can be seen in Figure 2. The percent of the particles inside of the grain and on the grain boundary were calculated from the pictures. The total area fraction and the equivalent diameter were also calculated.

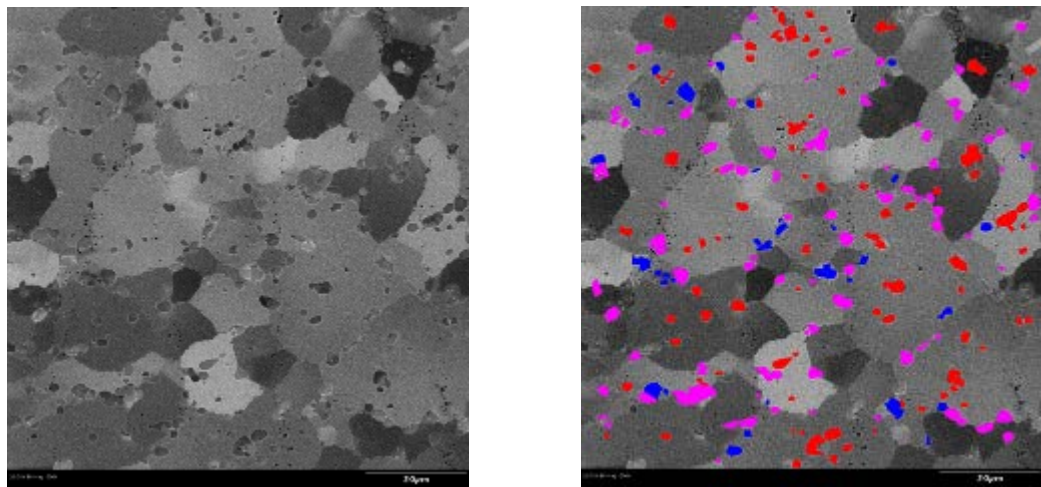


Figure 2. Left: Prior to hand painting. Right: After hand painting.

Point counting was used to double check the results from Fovea. The number of grid points was counted as were the number of particles fully on a grid intersection or partial on an intersection. The total area fraction was then calculated from those numbers.

It was found that for deformation temperatures of 1066°C and below, the sizes of both the gamma grains and gamma-prime precipitates were similar. This suggests that the precipitates were related to the gamma grain boundaries.

Finally, stress vs temperature curves were generated to analyze the plastic flow behavior of superalloy disk alloys which gives rise to residual stress following SSHT. An example of this is seen in Figure 3.

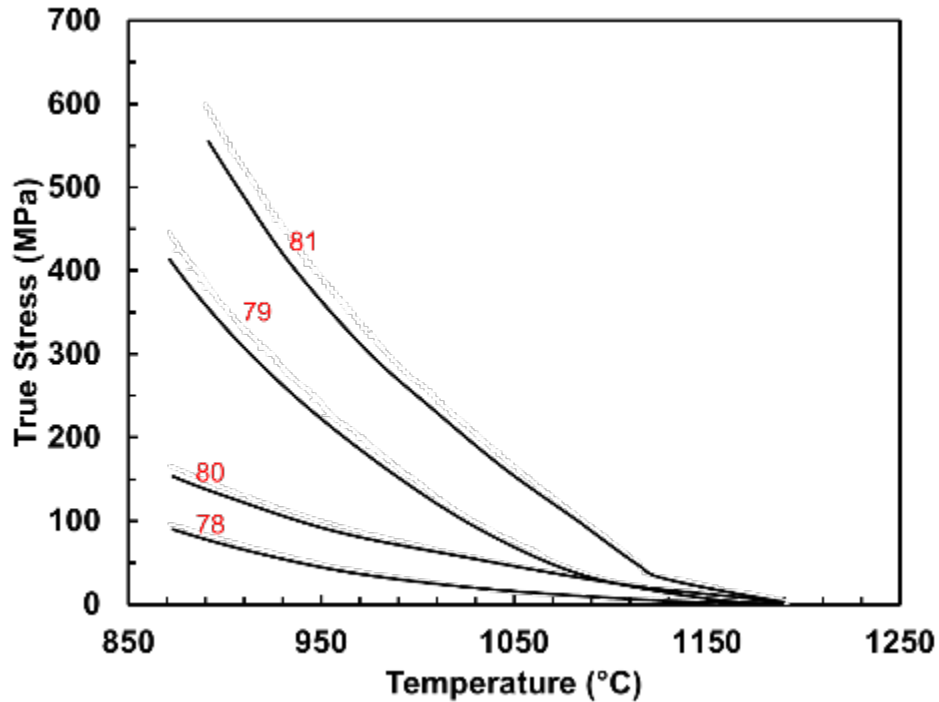


Figure 3. True Stress vs Temperature

## Conclusions

It was found that prior to SSHT the fraction of gamma-prime precipitates lying away from the boundaries depended on the processing conditions. Certain processing conditions may give rise to substantial coarsening of the gamma grain size during SSHT. The effect was attributed to the uniformity of the dissolution of gamma-prime precipitates.

## Works Cited

1. Semiatin, S.L., et. al. "The Effect of Forging Variables on the Supersolvus Heat-Treatment Response of Powder-Metallurgy Nickel-Base Superalloys", *Metallurgical and Materials Transactions A*, 2014, vol. 45A, in press.

HEAT TREATMENT OF POWDER METALLURGY SUPERALLOYS

Project No. 7.1

Emily Stienecker  
University of Dayton

26 September 2013

Government Project Leader  
Dr. Jaimie Tiley  
AFRL/RXCM

Southwestern Ohio Council for Higher Education  
Student Research Program  
Agreement Number: FA8650-09-2-5800

## **Acknowledgments**

There are so many great people and hard workers that I had the pleasure of working with on this project. Thanks to Dr. Lee Semiatin and Dr. Jaimie Tiley for direction on this project and for helping me learn the things that I needed to know about Materials Science. This is a field that I had never worked in before, so thank you for being patient with me and teaching me the basics. Thanks also to Sang-Lan Kim. She put so much time and effort into this project, making sure that we had good images to use, that I did not have to overwork myself to do tasks that were nearly impossible for me to do alone. Also thank you to Adam Shiveley, for writing programs to try to make my life easier, and to try to make the tedious steps of the process a little more efficient. And, thank you to Kevin Shiveley and Bob Lewis, who worked hard to help me make sure that the sample preparation was done correctly, and helped do a lot of troubleshooting when something went awry. I definitely could not have completed this task without the help of all of these people, so I am very grateful for all of their help.

## **General Description**

This project was conducted to examine the effects of heat treatment on two nickel superalloys, LSHR (Low-Solvus, High Refractory), and IN100 (a type of Inconel). These two superalloys have similar composition and chemical composition, but their lattice structures behave in different ways and their gamma prime precipitation concentrations differ, which makes them good to compare to each other. The goal of this project is to see what kind of heat treatment can be done on the material to make the microstructure the strongest for uses at high temperatures, specifically in the turbine of a jet engine.

This specific set of samples were precipitation samples, so the thing mainly being studied was the amount of gamma prime precipitation that came out at different temperatures during cooling, and the sizes and shapes of the precipitation particles. These superalloys have two main components to their microstructure, gamma matrix, and gamma prime precipitation. A majority of the metal is made up of this gamma matrix, which has a base element of Nickel, but also includes Chromium, Iron, Tungsten, Molybdenum, Titanium, and other nonmetal elements such as Carbon and Silicon. Gamma prime, although still mainly comprised of nickel, has slightly different concentrations of the different elements, making the composition of them different than that of the surrounding gamma matrix. The difference in composition makes the density of the gamma prime (as well as some other properties) different than that of the matrix around it, which makes the electrons bounce off of it differently, thus causing the visual contrast in the SEM.

It is known that secondary precipitations (gamma prime that was not present in the material above solvus temperature) are the most effective in the strengthening of the material, so that was the focus of the research. It was noted that at certain temperature, both primary (gamma prime that was there at solvus, and tertiary (gamma prime that precipitated out after the secondary gamma prime) were present, but those were left out in the analysis of the particle size and shape. By analyzing the secondary gamma prime precipitates formed at different times and temperatures in the heat treating process, a model can be made to be shared with other scientists and metals manufacturers telling them exactly what heat treatment they need to use to have the desired microstructure. This way, people in the future will not have to do these tests all over again to see what the results of this type of preparation would be, making the whole industry much more efficient.

## Description of Research

For this project there were two metals tested: LSHR and IN100. Because a direct comparison was being done between the two types of material, they were both subjected to similar types of heat treatments. Some of the cooling rates differed slightly though due to differing properties of the material. The samples were initially heated up to a temperature higher than their solvus temperatures and held there so that all of the gamma prime is able to dissolve into the gamma matrix. This made the metal supersaturated with gamma prime, so then when they were cooled down, the gamma prime would tend to precipitate back out of the matrix. Then, half of the samples were cooled at a fast cooling rate (250 or 300°F/min) and the other half were cooled at a slow cooling rate (20°F/min). Within each of the different cooling rates, the each of the samples were cooled down to a different temperature ranging from 1500°F to 2130°F. Once the metals were cooled down to the desired temperature, they were water quenched. In other words, they were dropped into very cold water in order to effectively freeze the microstructure. Freezing the microstructure creates the ability to see what the microstructure resembled at the moment it reached that quench temperature. Theoretically, water quenching is like cooling the samples infinitely quickly, and therefore there would be no time for the microstructure to change with temperature during that process. However, since it is impossible to cool something infinitely quickly, there was still some evidence of the particle shapes and sizes changing with respect to time and temperature during the quenching process. During this heat treatment process, the temperature of the metal was monitored by using a thermocouple inserted radially into the center of the metal billet in a hole drilled specifically for temperature measuring purposes.

After the metal samples were heat treated, they were cut with a diamond blade saw to down the center where the thermocouple well was located. Since that is the location where the temperature was monitored, it was the most accurate location in the sample from which the analysis could be done. The sample was then mounted in 1" diameter Polyfast mounting compound, and polished to a mirror finish using diamond suspension. For the last polishing step, there are several different solutions that can be used. The one most commonly used is a colloidal silica solution called Mastermet, but on these samples in particular the silica bonded very easily to the metal surface, making it impossible to clean off during the cleaning process, and covered up all the data that we might have been able to get in the SEM. So because of that dilemma, a focused ion beam (FIB) cleaning technique to remove all of the dirt and colloidal silica that was left on the surface after the polishing and cleaning steps.

After the whole preparation process was completed, then the samples were imaged using SEM techniques on an FEI Sirion microscope. The following imaging conditions were used: 3.0 kV Acceleration voltage; 3.0 mm working distance; spot size 4.0. Images were taken at several different magnifications for each sample.

After acquiring the images, they were then analyzed using a combination of Adobe Photoshop, the Fovea Pro Plug-in for Photoshop, Matlab, and Microsoft Excel. The gamma prime particles, which were very visible after the FIB cleaning, were highlighted and shaded in using Photoshop, and then Fovea Pro was used to calculate the area and equivalent diameter of each of the particles. Then, the total area fraction of gamma prime particles was calculated by summing up the areas of all of the particles and then dividing it by the total area of the sample imaged. There was a sample size of at least 200 particles (sometimes there were thousands of particles depending on the heat treatment) to make sure that there would not be any sample size

error. The data calculated from the images was: the average size of the particle as reported by the equivalent diameter (diameter of the particle assuming that its cross section is a circle); total area fraction of gamma prime particles; and the particle density, or the number of gamma prime particles per square meter. There was a derived theoretical maximum curve for the gamma prime area fraction as a function of temperature, which the collected data was compared to as well (see figure 1).

## Results

It was found that at higher temperatures, the experimental data followed the theoretical curve very closely, but then as the temperature decreased there was more and more deviation. There were also some instances where an experimental data point fell above the theoretical maximum area fraction curve (also see figure 1). This was explained by the fact that the cooling during the water quench at the end of the heat treatment process was not instantaneous cooling, and therefore there was time for the existing particles to grow, making the area fraction higher than expected.

When looking at particle sizes, histograms were made showing approximately how many particles there were in a given size range. These histograms were then directly compared to each other to see how the populations of particles changed geometrically with quench temperature (see figure 2).

It could be seen, though, not only were the samples with the same cooling rates compared to each other, but the average particle size with respect to the two different cooling rates was also compared (see figure 3). This showed that the size of the particles did not actually change all that much with respect to quench temperature in the fast cooled samples compared to the slow cooled samples. This makes sense though, because the gamma prime in the fast cooled samples did not have as much time to grow as the slow cooled ones, since they underwent the same temperature decrease in a shorter amount of time.

As figure 3 shows, there were still some points in the data that did not follow the anticipated trends. As for this point in the 20°F/min distribution at around 1750°F, it was believed that it was because there was another population of gamma prime that had been generated at that temperature. These are tertiary gamma prime particles, which are very small (since they had just been formed) and spherical in shape. Since the new gamma prime particles were so small, counting them brought down the entire average particle size, which skewed the data slightly.

When I left there, Dr. Tiley, Dr. Semiatin, and myself were still in the process of trying to explain the points that did not make sense, like the one I just described. We were also trying to figure out how to determine which particles were tertiary and how to take them out of our analytical data without having to do that data analysis all over again. Also it was nearly impossible to tell which particles were tertiary gamma prime at some temperatures because they grew to the size of some of the secondary gamma prime particles. Due to these obstacles, the project was not yet finished when I left, and therefore, final conclusions could not yet be made by the researchers.

Figures and Tables

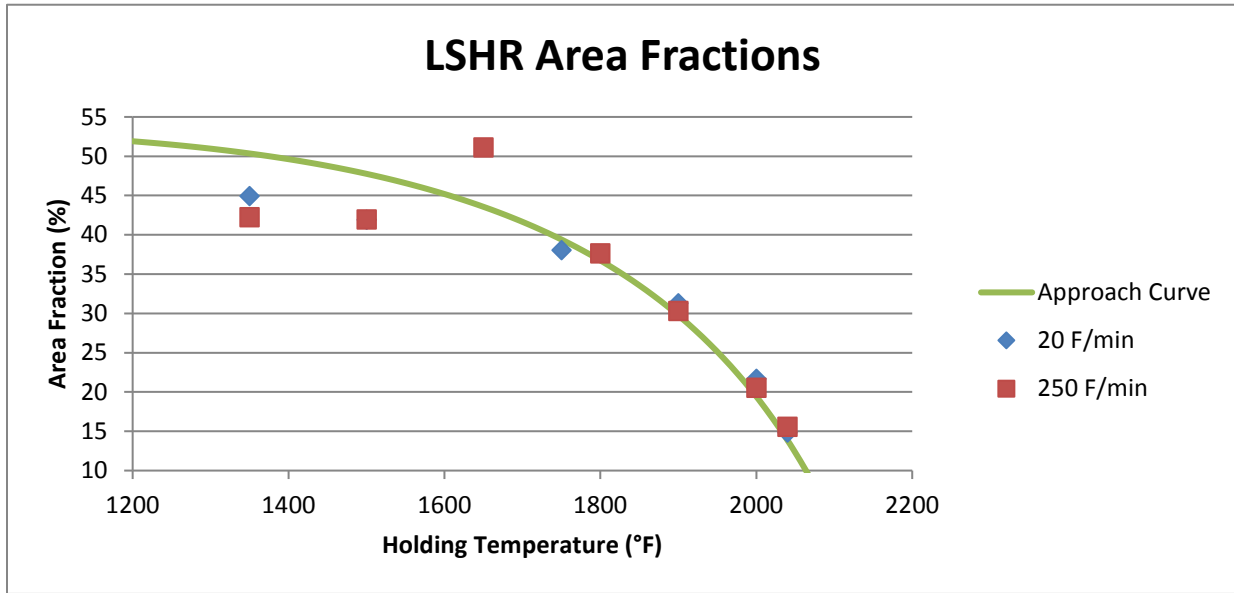


Figure 1 – Gamma prime area fraction in LSHR as a function of quench temperature

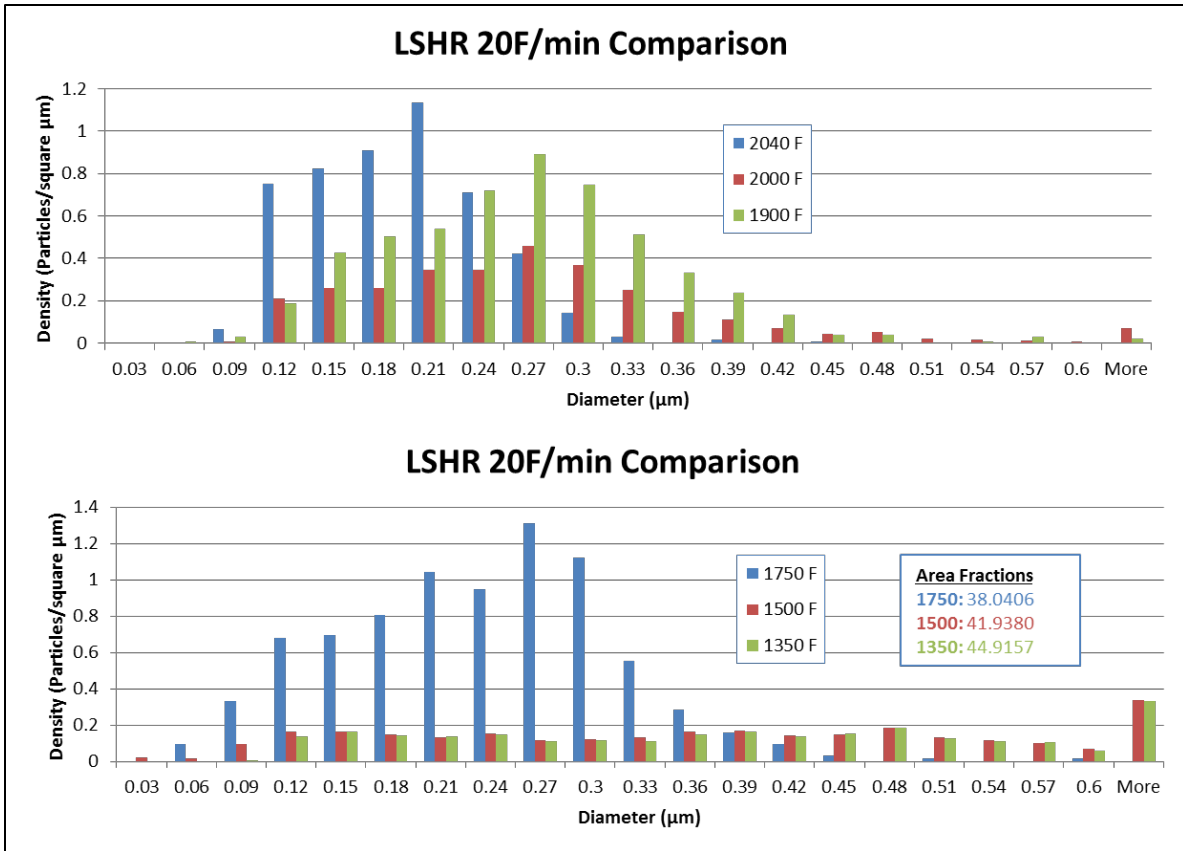


Figure 2 – Gamma prime particle size histogram comparisons

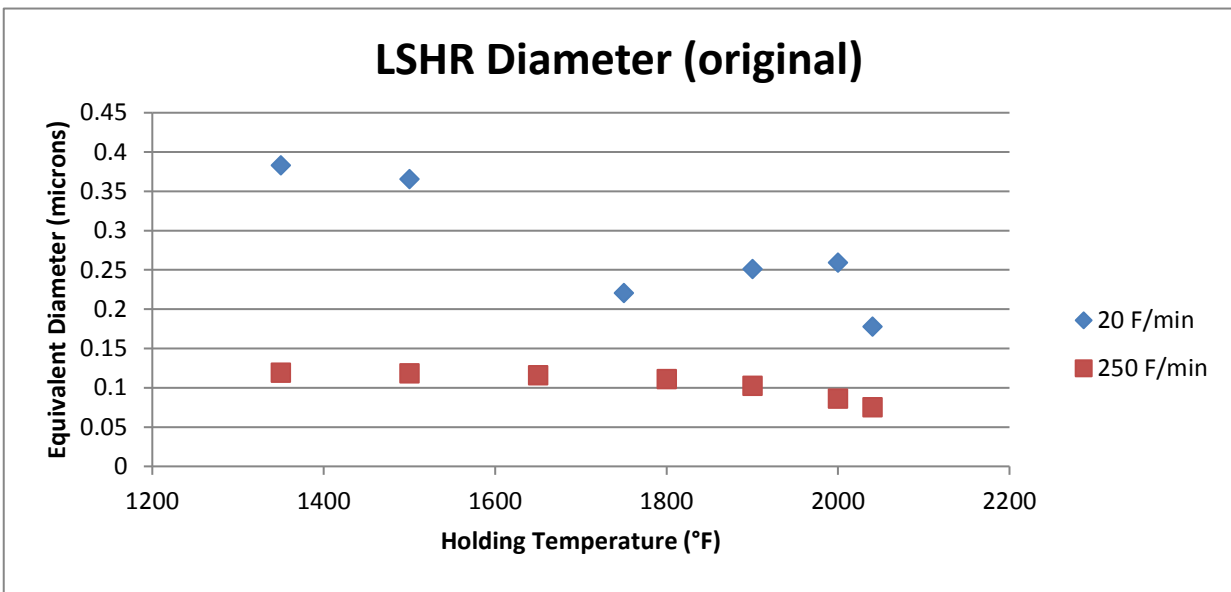


Figure 3 – Gamma prime average size comparison in LSHR

HEAT TREATMENT OF POWDER-METALLURGY SUPERALLOYS

Project No. 007.2

Alexander E. Saurber  
University of Dayton

31 August 2014

Government Project Leader  
Dr. S. Lee Semiatin  
AFRL/RXCM

Southwestern Ohio Council for Higher Education  
Student Research Program  
Agreement Number: FA8650-09-2-5800

## **Acknowledgements**

I would like to thank Dr. Semiatin for the opportunity to participate in materials research for the United States Air Force, as well as the opportunity to learn the scientific and engineering processes in a professional setting. I would also like to thank Marie Cox, who has been a great guide for the project, especially in introducing the properties of and specific processes used to create superalloys. I would like to thank Bill Saurber, Mike Velez, and Bob Lewis (UES, Inc.) for the training and support on the various pieces of lab equipment used to process specimens. I would like to thank Jared Shank (UES, Inc.) for the excellent training I received manipulating the scanning electron microscope (SEM) in order to view specimen surfaces. I would also like to thank Erica Gaussa (SOCHE), Marie Cox, and Bill Saurber for their contributions, including the demonstration of image processing techniques, and aid in preparing specimens for microscopy.

## **General Description of Project**

Nickel-based superalloys are commonly used in the aerospace industry due to their resistance to high temperatures. Two nickel-based superalloys, Waspaloy and “Low-Sovus, High Refractory” (LSHR), are widely used in jet engines as disks because of their excellent creep and crack-growth resistance (Pollock & Tin, 2006). Research was conducted to establish the effect of thermo-mechanical processing variables on the microstructure of Waspaloy in order to predict and control microstructural properties of the material in the future. Metallographic techniques were used to analyze and quantify gathered data to obtain the average grain size and gamma prime size distribution.

## **Description of Research**

Bars of Waspaloy were cogged and hot-rolled, then cut into smaller rods as needed. The rods were coated in glass to slow oxidation as the rods were treated to different temperatures for different amounts of time. After the heat treatment was completed, the rods were quenched in a container of water to freeze the state of the microstructure. A circular saw with a silicon carbide blade was then used to cut an axial cross section of each rod, which was then mounted, ground, and polished using traditional metallographic techniques. In the rough-grind phase, grit paper and silicon carbide paper were used, followed by a finer polish with a water-based diamond solution on low-nap pads. The polish was finalized by a colloidal silica and hydrogen peroxide solution on a soft, low-nap pad. The colloidal silica and hydrogen peroxide solution provided as an etchant on the surface to make gamma grains and gamma prime precipitates visible under an SEM. Finally, sample surfaces were imaged and analyzed using the backscatter electron feature on an FEI SIRION SEM.

## **Results**

Image analysis of the samples found that different heat treatment temperatures and times had an effect on the microstructure. The entire rod did not dissipate the heat evenly during the heat treatment, meaning recrystallization was still visible from the hot-rolling process used to form the bars. An average recrystallization zone was established to be about four millimeters in from the surface of the rod.

After analysis of each trial, it was observed that the grains grew in diameter and that the gamma prime tended to dissolve at the higher temperatures. The samples heat treated at a higher temperature for a set amount of time tended to have fewer gamma prime precipitates than samples heat treated at a lower temperature for the same amount of time.

Table 1. The differing microstructures of heat treated samples of Waspaloy

Time (days)	Temperature (°F)	Primary gamma prime diameter (µm)	Grain diameter (µm)
8	1697	0.47	19.6
8	1796	0.49	17.9

As seen in Table 1, the Waspaloy sample that was heat treated for 8 days at 1697 degrees Fahrenheit had a smaller grain diameter and a marginally smaller primary gamma prime diameter compared to the Waspaloy sample treated for 8 days at 1796 degrees Fahrenheit.

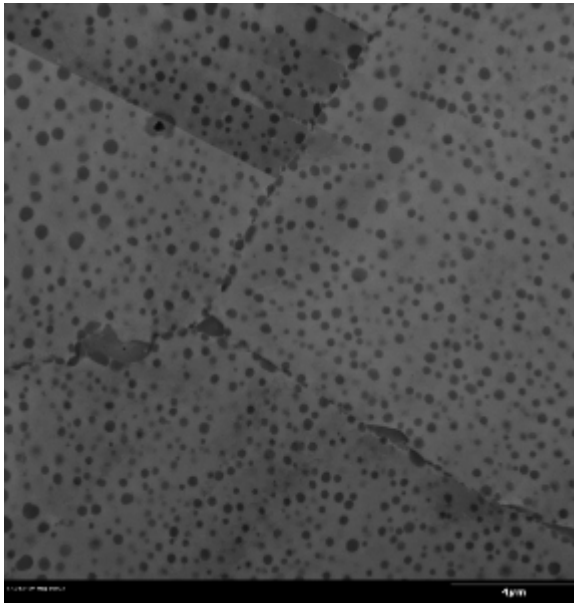


Figure 1. SEM Image at 5000x of Waspaloy gamma prime particles. The sample was heated for 8 days at 1697°F.

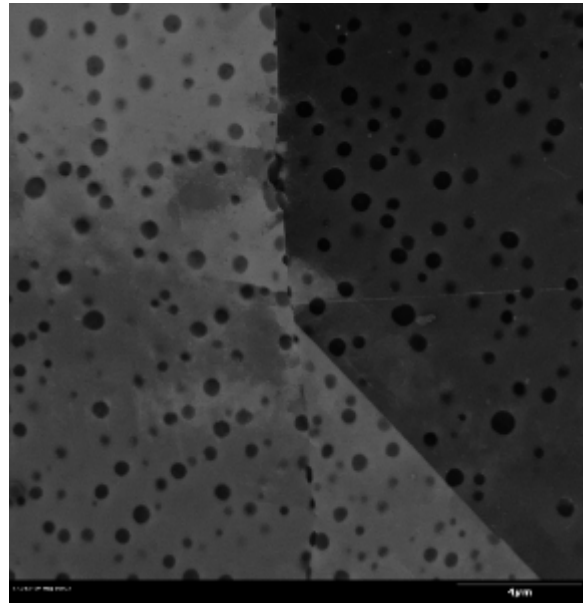


Figure 2. SEM Image at 5000x of Waspaloy gamma prime particles. The sample was heated for 8 days at 1796°F.

The results in Figures 1 and 2 showed that comparatively, the Waspaloy sample subjected to a lower temperature showed an overall higher area fraction of gamma prime than the Waspaloy sample subjected to a higher temperature. The tertiary gamma prime dissolved into the gamma

grains in the sample heated at a higher temperature, accounting for the marginally larger grain diameter. Heating the alloy at a lower temperature grows the grains to a smaller size and allows for smaller, more concentrated gamma prime particles, which strengthen the alloy, making it more useful for its applications.

### **Works Cited**

Pollock, Tresa M., & Tin, Sammy. "Nickel-Based Superalloys for Advanced Turbine Engines: Chemistry, Microstructure, and Properties." *Journal of Propulsion and Power* Vol. 22, No. 2, (March-April 2006): 361-374. PDF File.

HEAT TREATMENT OF PM SUPERALLOY R&D

Project No. 0007.3

Zack Driscoll  
University of Dayton

25 November 2013

Government Project Leader  
Dr. Lee Semiatin  
AFRL/RXCM

Southwestern Ohio Council for Higher Education  
Student Research Program  
FA8650-09-2-5800

## Acknowledgements

I would like to thank Dr. Lee Semiatin for the opportunity to work on this project and for the opportunity to work with the many different researchers and other professionals in the labs.

## General Description of Project

The goal of this project is to create a model that can help predict the behavior of certain metals during forging. The metals that the project is specifically working on are IN100 and LSHR. These metals are superalloys and have special properties compared to other types of metals. In order to create this model, different steps during the formation of the finished metal were applied to the metal such as heat treatment, compression, and cooling. After the metal went through one of these steps it was polished and imaged. The purpose of this was to take a snapshot of the metal at each step so it could be analyzed and different properties of the metal could be quantitatively and qualitatively measured. An example of the image and the typical microstructure are shown in Figure 1. After varying each step and analyzing the results it is possible to create a model of how the metal is behaving between each of these steps. If the processes of forging these metals can be better understood a more efficient forging technique could be developed and potentially more efficient metal to be used for engine parts. These engine parts could save on fuel costs for airplanes which in the long run could save a great deal of money for whoever uses these techniques. Specifically the project was focused on the metal used in creating an engine disk. These disks are subject to a wide range of temperatures and forces and therefore must be able to withstand extremes on both ends safely and reliably. Therefore the project is also attempting to figure out the most efficient way of making an engine disk that can withstand these conditions.

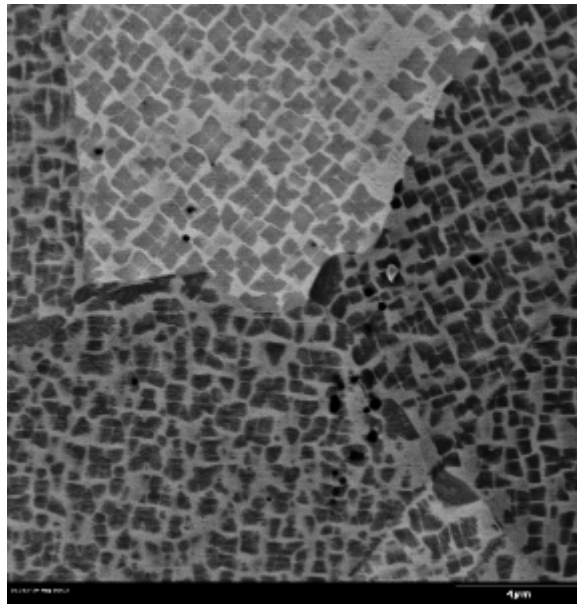


Figure 1. Scanning electron microscope image of the grain structure of an IN100 superalloy

## **Description of Research**

After each step of a given processing sequence, a metal sample was examined using several different methods in order to get an accurate description of all of the useful properties of the metal. The metals come out of the different processes in a rough condition and were cut, polished, and cleaned before they can be analyzed. They were cut into different sections and these sections were mounted and the flat surfaces were ground to 9 micron finish using sandpaper of different grit and then polished to .5 micron finish using diamond paste and eventually a polishing machine until they had virtually no scratches. The samples were then cleaned using different methods depending on the composition of the metal, different metals respond differently to different cleaning methods. Once the samples were cleaned they were imaged using a scanning electron microscope at a high magnification. The metals also were imaged by a back scatter detector to get the grain profile of the metal. These images were then used to determine different properties of the metals. The images showed grain size and particle distribution throughout the metal. Using a program on Photoshop it was possible to measure the size of each of the particles based on a scale that the microscope places on each image. Then using Excel the data were compiled and analyzed based on other data obtained from previous tests. After this analysis, models were created that accurately described the way the metal changed during processing.

## **Results**

The project is still in progress on and it will be continuing for several months. Each step of the forging process takes a long time and the analysis of the new material also takes a few weeks. However some trends have already began to become apparent. The grain size grew slowly while being heated. Once the metal reached the solvus temperature, the grains began to grow rapidly to a much larger size. Combining these properties with compressing the metals and cooling the metals creates a variety of microstructures. These different microstructures each which have different strengths and weakness need to be applied to different parts of the engine in different ways. An engine is subjected to a wide range of temperatures and forces and each part of an engine needs to be able to withstand these effects. Different microstructures are better suited for certain environments and a better understanding of how each of these microstructures are formed will lead to a more efficient engine because more efficient parts can be manufactured.

ELECTROMAGNETIC PROTECTION – STRUCTURES/DETECTION

Project No. 0034.2

Ashley White  
University of Dayton

31 August 2014

Government Project Leader  
Max Alexander  
AFRL/RXCC

Southwestern Ohio Council for Higher Education  
Student Research Program  
Agreement Number: FA8650-09-2-5800

## Acknowledgments

Thank you to Max Alexander, Ben Wilson, Brittany Campbell, Kevin Davis, and to Nick Conquest for the technical guidance and support.

## General Description of Project

Work involved the electronic/magnetic property measurements of materials used for radio frequency field detection and electromagnetic interference shielding efforts for the purposes of coaxial cables. The project has entailed the preparation of composite samples, containing various organic and inorganic nanoparticles. Samples are tested for shielding effectiveness as well as for mechanical fatigue and post fatigue shielding effectiveness.

## Description of Research

Work on this project has included an extensive review of the literature, reporting on the initial design of experiments as shown in Table 1, determining a baseline cable type (RG-316), designing a shielding test setup, fabricating and measuring the unfatigued baseline shielding effectiveness of metal and Nanocomp's carbon nanotube wrapped shields.

**Table 1 Design of Experiments**

<b>Material</b>	<b>Layers of Shielding</b>	<b>Received</b>
Aluminum	1	Yes
Silver coated copper	1	Yes
Silver coated copper	2	Yes
Nanocomp CNT	1	Yes
Nanocomp CNT	2	Yes
ASI CNT paper	1	No
ASI CNT paper	2	No

More recent efforts were focused primarily on manufacturing cables using the new carbon nanotube paper from Applied Sciences Inc., ASI, with help from Minnesota Wire. After collaborating and delegating the creation of these ASI shielded cables their reflection loss, insertion loss, and voltage standing waving ratio were measured, which can be seen in Figure 1.



**Figure 1: Air Force Research Labs testing to measure reflection loss, insertion loss, and voltage standing wave ratio**

In addition, a recently completed improved version of a previous cable set was examined, including a single and double layer carbon nanotube shielded cables. The goal was to improve the manufacturing capability, as well as the shielding effectiveness of this updated set over the originally investigated cables. This group of cables was also measured for reflection loss, insertions loss, and voltage standing wave ratio on the new network analyzer at the Air Force Research Labs (see Figure 1).

Following the manufacturing of the cable sets and in house testing, cables were examined to test their shielding capabilities. Research was conducted at the national institute for aviation research in Wichita, Kansas.

The cables underwent two series of tests. The first method uses an unshielded coaxial cable to determine the overall shielding effectiveness, the results of which can be seen in Figure 4. This is done by using an injection probe and measuring induced current on an unshielded cable in a reverberation chamber and subtracting the measurement taken on a shielded cable. This yields the power that the cable effectively shields. The purpose of this method is to more directly compare results with that of previously taken shielding data of prior materials, especially within any literature. The downside of this method is that it does not account for inherent different resonances within the test cables, compared to that of the control unshielded cable. In addition the injection probe has limited power strength. This set-up, method 1, can be seen in Figure 2.

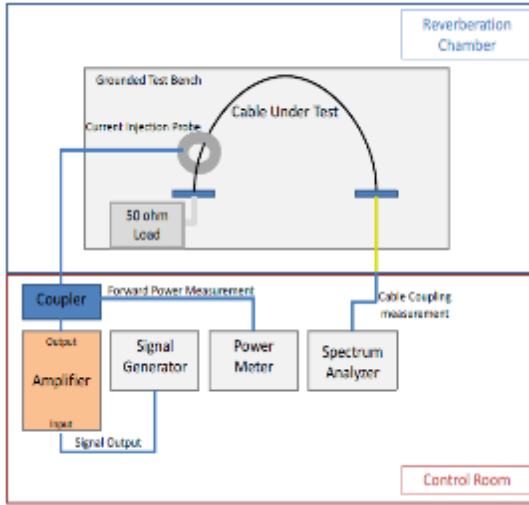


**Figure 2: Method 1 Setup**

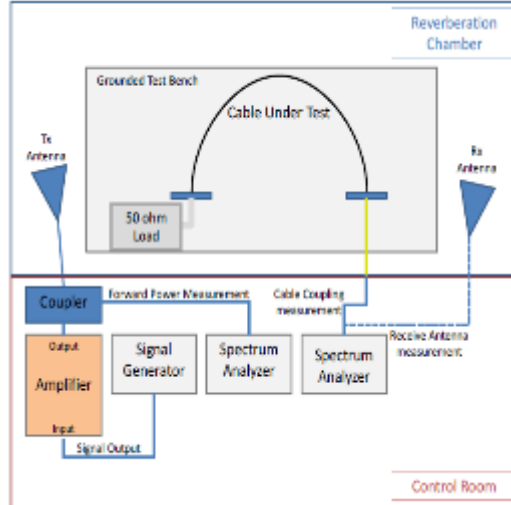


**Figure 3: Method 2 Setup**

The other method, method 2, used was adjusting the forward power received on the tested cable using a baseline antenna in the reverberation chamber. In addition a statistically uniform field was created by using a large spinning paddlewheel to regulate the higher frequency power output in the chamber. The shielding effectiveness was determined by taking the power measured on the shielded cable and deducting the uniform power measured from the antenna in the chamber. This method gives the benefits of eliminating resonance data while creating a strong, randomly polarized, isotropic and uniform electromagnetic field within the chamber. This allowed the peak power of which test cables were subjected to, to easily be measured. The results of this method can be seen in Figure 5.

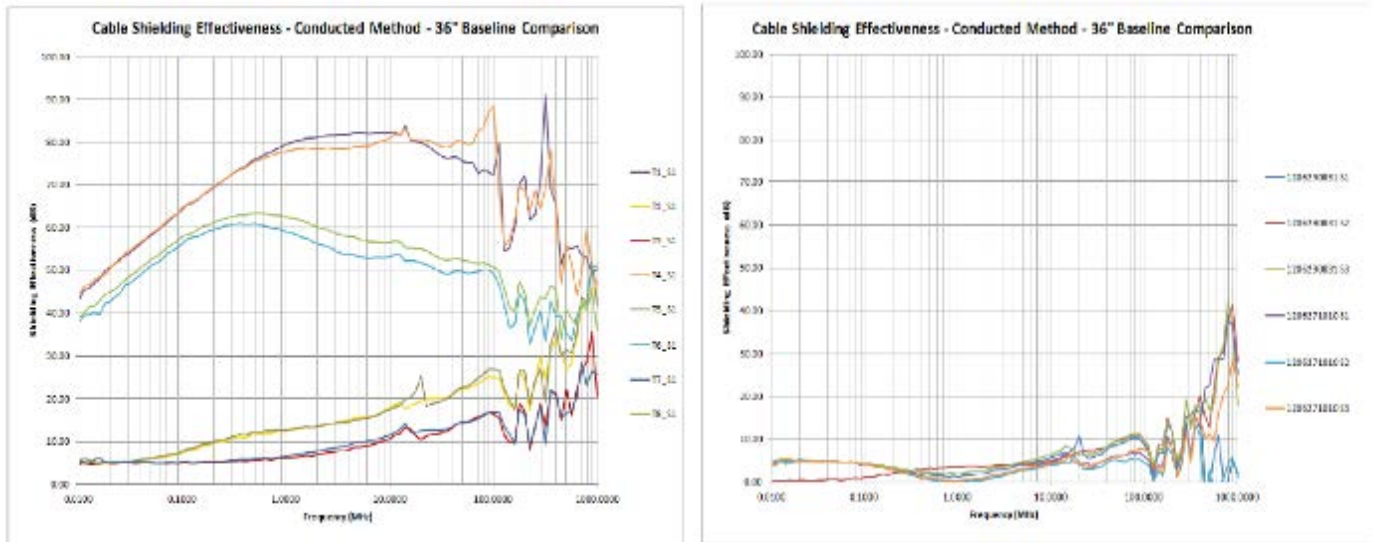


**Figure 4: Lower Frequency, method 1, Shielding Effectiveness for second generation cables (left) and ASI shielded cables (right)**

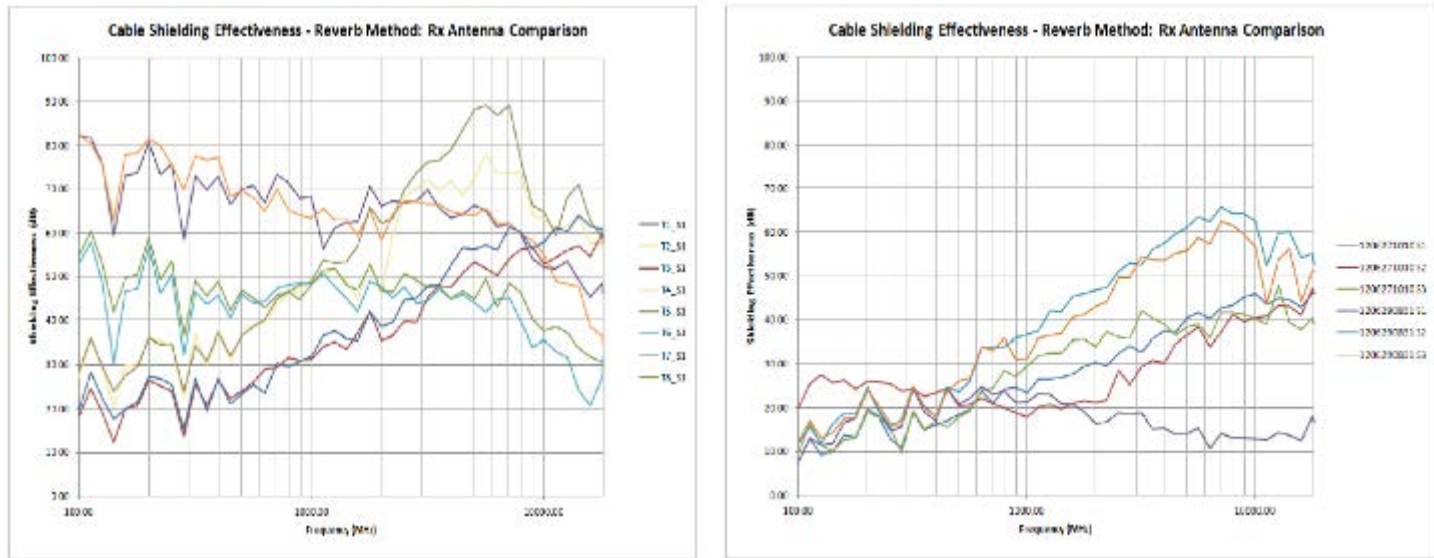


**Figure 5: Higher frequency, method 2, Shielding Effectiveness for second generation cables (left) and ASI shielded cables (right)**

## Results

Carbon nanotube based shields show marketed improvement over traditional cable shielding above the Gigahertz frequency range. The shielding supplied by Nanocomp Inc. outperformed the Applied Science Inc. shield at a wider band of frequencies. This research will continue to investigate shielding capabilities of nano-enabled materials. The next stage includes investigating the effects of fatigue on cable conduction and cable shielding effectiveness.

MOLECULAR BEAM EPITAXY OF QUANTUM COUPLED STRUCTURES

Project No. 0035.1

Daniel R. Esposito  
University of Dayton

13 June 2014

Government Project Leader  
Dr. Kurt G. Eyink  
AFRL/RXAN

Southwestern Ohio Council for Higher Education  
Student Research Program  
Agreement Number: FA8650-09-2-5800

## **Acknowledgements**

I would first like to thank my employer SOCHE for providing me the opportunity to work in AFRL over the past three years. I would also like to thank the research team of which I was fortunate to be a member during my time here, including, but not exhaustively, Mr. Steven Fenstermaker, Mr. Larry Grazulis, Dr. Krishnamurthy Mahalingam, and several fellow interns. Above all, I am grateful for the guidance and mentorship of my project leader Dr. Kurt Eyink, who has taught me a great deal and helped me develop as a student and aspiring scientist.

## **General Description of Project**

The overarching project corresponding to the title of this report consists of developing a technique to fabricate quantum dots (QDs) of precise sizes at specified locations for quantum memory applications. In an attempt to bypass the random self-assembly process normally used to grow QDs, a process is being tested which involves nano-patterning samples (planar InAs grown on GaAs substrates) to adjust the surface tension followed by annealing them under high arsenic overpressure with the goal of QDs pulling up in specified locations. In order to nano-pattern a sample, it must be removed from the ultra-high vacuum (UHV) molecular beam epitaxy (MBE) system; when it is reintroduced to the MBE system, the oxides which formed from exposure to air must be removed in order to view the sample morphology—in other words, it must be cleaned. At this point, the dominant cleaning procedure involves heating the sample to nearly 400 degrees Celsius under arsenic overpressure while using hydrogen radicals to remove the oxides. The hydrogen radicals are only effective when the sample is hot, yet this procedure also simultaneously anneals the sample. Sample cleaning under this procedure takes about an hour, so the first hour of annealing—which could include evaporation and morphology changes—takes place without monitoring. Thus, it became desirable to develop a technique to clean the samples without raising the temperature in order to better control and understand the subsequent annealing process. This project attempts to do so by cleaning samples with hydrogen plasmas assisted by ultra-violet light. The hope is that the ultra-violet light will excite the oxides enough in order for the high-energy hydrogen plasmas to react with them, forming water molecules which will then evaporate from the sample surface.

## **Description of Research**

The MBE system in this lab had an unused chamber built off to the side; in this project, this chamber was repurposed for the new cleaning technique. First, a high-intensity, long-wave ultra-violet lamp with a funnel was purchased. A metal shell was drawn up and machined to attach the funnel of the UV lamp to the shield surrounding a bombco window (Figure 1).



Figure 1. Ultra-Violet Light Setup

Next, a system needed to be constructed to allow hydrogen to enter the chamber. A lecture bottle of hydrogen was attached first to a regulator, then to a shut-off gas valve, and finally to a mass flow controller. From there, the pipe continued to the chamber. The flow of the hydrogen was controlled via a power supply/readout device. In order to light the plasma, power had to be channeled to the flow via an external source. After discovering the hydrogen would not light on its own, an argon bottle was substituted in place of hydrogen; the argon lit without trouble, but without a separate pipeline, there was no way to introduce the hydrogen in order to light it as well. Therefore, a second system identical to the first was constructed to allow two gases to enter the chamber simultaneously. The decision was made to make helium the ignition gas. Thus, the plan was for helium to enter the system, be ignited to form a plasma, and then introduce hydrogen which would become a plasma before finally shutting off the helium. The system is shown in Figure 2 below.



Figure 2. Hydrogen (Top) and Helium (Bottom) Gas Control Systems

## Results

As of now, the system has been fully constructed—the ultra-violet light source is in place, and the two gas-flow systems are operational. During the first test run, the helium plasma lit, but in an unfortunate coincidence, the water pump to the cooling system broke. Since replacing the pump, attempts to light the helium plasma have been unsuccessful. As of the writing of this report, the system is being investigated to examine the cause behind the sudden inability to light the helium plasma. Once the helium plasma is lit, it will be possible to run experiments testing the cleaning abilities of hydrogen plasma on ultra-violet light-excited oxides. The chamber still has room to add a heating cell should we need to warm the sample, although the temperature would be kept far below the annealing temperature of 400 degrees Celsius.

NUCLEOBASE IN ORGANIC LIGHT EMITTING DIODES

Project No. 0056

Eliot F. Gomez  
University of Cincinnati

30 September 2014

Government Project Leader  
Dr. James Grote  
AFRL/RXAS

Southwestern Ohio Council for Higher Education  
Student Research Program  
Agreement Number: FA8650-09-2-5800

## Acknowledgments

Thank you to my academic advisor Dr. Andrew Steckl for allowing me to be a part of the high quality research at the UC Nanolab and providing excellent guidance. Gratitude is also extended to my co-advisor Dr. Jim Grote for generous financial support during my graduate studies. Thank you to all my colleagues, past and present, especially Dr. Hans Spaeth for training me during my early years as a graduate.

## General Description of Project

Natural electronics is the area of research that investigates how natural occurring biological materials (biomaterials) can be implemented in conventional organic devices, such as the organic light emitting diodes (OLED) for display and lighting technologies, organic field-effect transistors (OFET) for memory and computer logic, and organic photovoltaic (OPV) for energy harvesting. Organic semiconducting molecules are typically synthesized molecules, leading to expensive and often potentially toxic materials. Natural electronics, however, finds materials in nature with excellent electronic properties. Many biomaterials, such as silk, proteins, comestibles, vitamins, and DNA, have already been integrated into organic devices.

The primary advantages of biomaterials in electronic devices are renewability, biodegradability, and low toxicity. Renewability will curb environmental by-products as consumer electronics proliferate and material demand increases. Biodegradability will abate environmental concerns of increasing landfills, much of it contributed by expired electronic products. Natural electronics uses the same ingredients found in plants and animals that typically have little to no toxicity. Furthermore, natural based materials are often less expensive due to their abundance.

In addition to the minimal environmental impact, natural materials can often enhance device performance. Nature has already finely-tuned many molecules for high performance. DNA, for example, was integrated into OLEDs to increase the brightness (luminance) and the efficiency nearly 300%. The astounding increase in performance was attributed to intrinsic properties of the DNA that enhance the emission output. The remarkable properties of DNA were also implemented in other devices, such as OFETs and OPVs. The advantages of DNA in electronics sparked rapid interest. However, the disadvantages of DNA were also clear. DNA required extensive processing, such as additional surfactants and purification, before it was usable in thin film electronics. Furthermore, DNA has a limited range of electronic properties for OLED. OLEDs are comprised of multiple layers of organic materials with various electronic properties that serve different roles. Substituting the various components of the OLED with natural materials will require a vast set of properties. There are many opportunities, especially for OLEDs, to explore with other natural biomaterials.

Nucleic acid bases (nucleobases) are small constituent of the DNA polymer chain as shown in Figure 1. There are five nucleobases: guanine, adenine, cytosine, thymine (found in DNA) and uracil (only found in RNA). Nucleobases are smaller in molecular size than DNA and easily thermal evaporate to form purified thin films (10 – 100 nm) in vacuum systems, which is essential for OLED fabrication. Thermal evaporation is advantageous over DNA solution spin coating because no additional purification or surfactants are necessary.

In this work, the optoelectronic properties of nucleobases were investigated and integrated into a conventional OLED. It was found that nucleobases have a wide range of

electronic properties that increase the freedom of OLED device design that also have implications in other organic devices. In this work, nucleobases replaced two organic (non-natural) layers in OLED. In addition, the efficiency of the OLED was increased a factor of 2 over the conventional device without nucleobases.

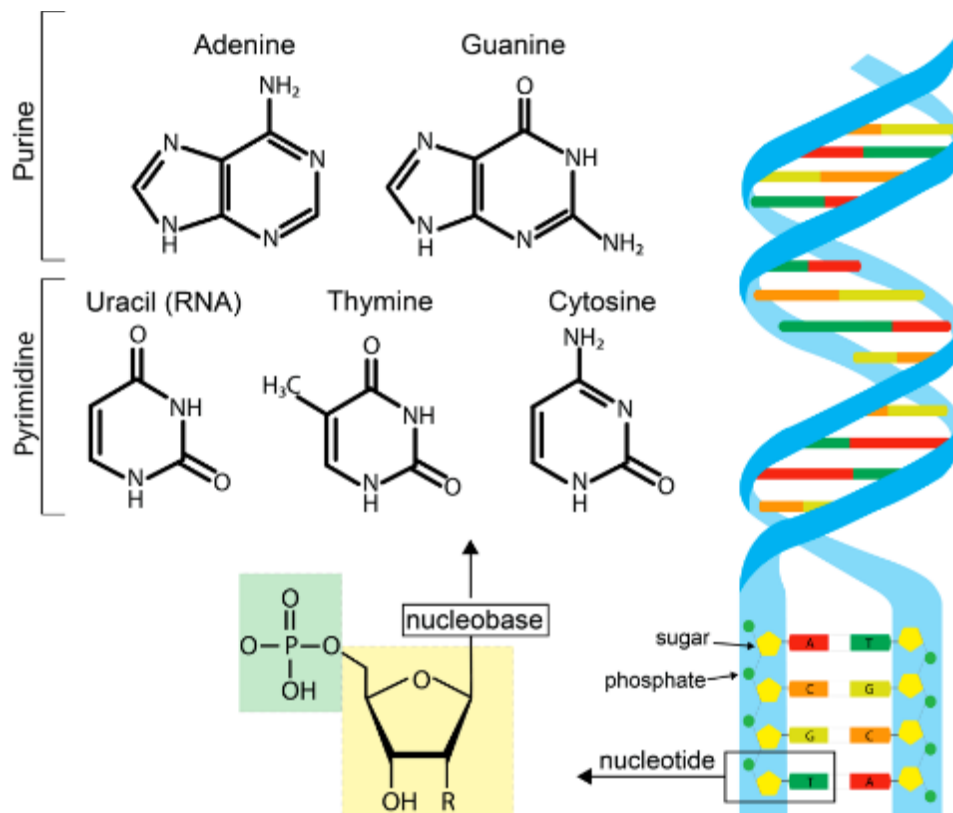


Figure 1. Nucleobases are part of the DNA nucleotide chains. Nucleotides comprise of a sugar/phosphate backbone with a nucleobase attached. Adenine and guanine are part of the purine family, while thymine, cytosine, and uracil (found in RNA) are pyrimidines.

## Description of Research

OLEDs were fabricated by thermally evaporating organics, nucleobases, and electrodes in a molecular beam deposition (MBD system, SVT Associates) onto a glass substrate. The parameters of the OLED were deposited according to similar devices previously characterized with each layer ranging in thickness from 10-40 nm. The OLED (consisting of 5 organic layers ~100 nm combined total thickness) was deposited on a glass substrate and had an active light emitting area of 4 mm<sup>2</sup>. Glass substrates were received with pre-patterned commercially available ITO, a transparent electrode for light emission out of the glass side of the device.

The substrates were cleaned with oxygen plasma for 10 minutes at 500 W (Plasma-Preen, Terra Universal Inc.). A conductive polymer (PEDOT:PSS) was then spin-coated on top of the glass/ITO at 2000 rpm for 20 s to produce a 40 nm layer. The PEDOT:PSS was baked at 120 °C for 15 min to remove any solvent and leave behind the conductive PEDOT:PSS thin film. The

device was then transferred to the MBD system for thermal evaporation of the remaining organics.

The reference OLED (Device I) was created with the following materials and parameters: ITO [90nm] / PEDOT:PSS[40nm] / NPB[17nm] / CBP:Ir(ppy)<sub>3</sub> (10wt%)[30nm] / BCP[12nm] / Alq<sub>3</sub>[25nm] / LiF[<1nm] / Al[40nm]. As a voltage is applied to the ITO and Al electrodes, electrons are injected from the Al into the organic layers, and holes (an electron void) are injected from the ITO. Electrons and holes travel through the device to meet and recombine in the emitting layer of the OLED shown in Figure 2a. The device emits green light as shown in Figure 2b. If recombination occurs elsewhere, light emission does not occur, which reduces the efficiency. Therefore, electron blocking layers (EBL) and hole blocking layers (HBL) are placed between the emitters.

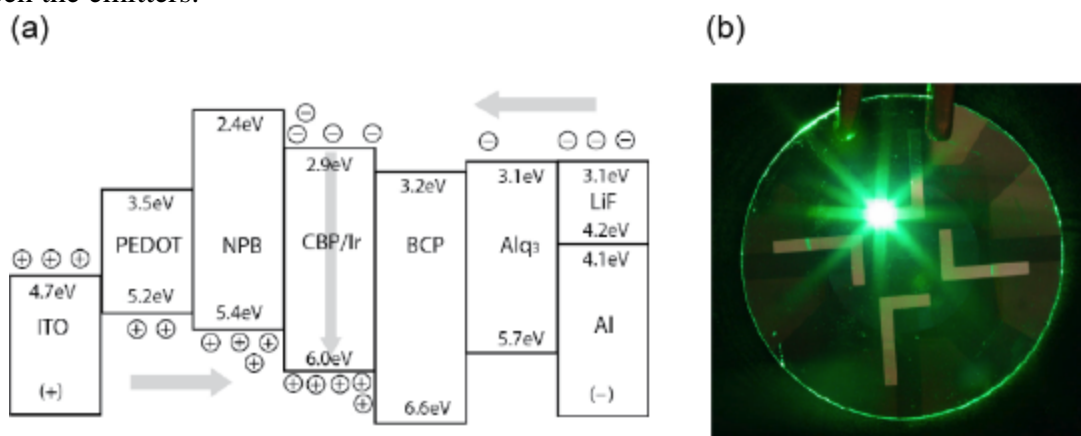


Figure 2. (a) The energy levels of the reference device (Device I) showing the electron and holes recombining in the emitting layer CBP:Ir to emit light. (b) A working green phosphorescent OLED device.

The energy level values (molecular orbital levels), intrinsic to every molecule, determines how electrons and holes traverse from layer to layer. The two energy levels of concern in OLEDs are ionization potential that affects hole transport, and electron affinity that affects electron transport. For example in Figure 2a, the ionization potential of NPB is 5.4 eV (low enough to permit hole transport) and its electron affinity is 2.4 eV (low enough to prohibit electron transport). EBL are materials that have a low ionization potential that permit holes to pass, but they have a low electron affinity that prevents electrons from entering the material. Contrarily, HBL have a high electron affinity that allows electrons to pass through to the emitting layer, but they have a high ionization potential and prohibit holes to enter. If an emitting layer is placed between a HBL and EBL, holes and electrons are confined and encouraged to recombine in the emitting layer, thus producing more light.

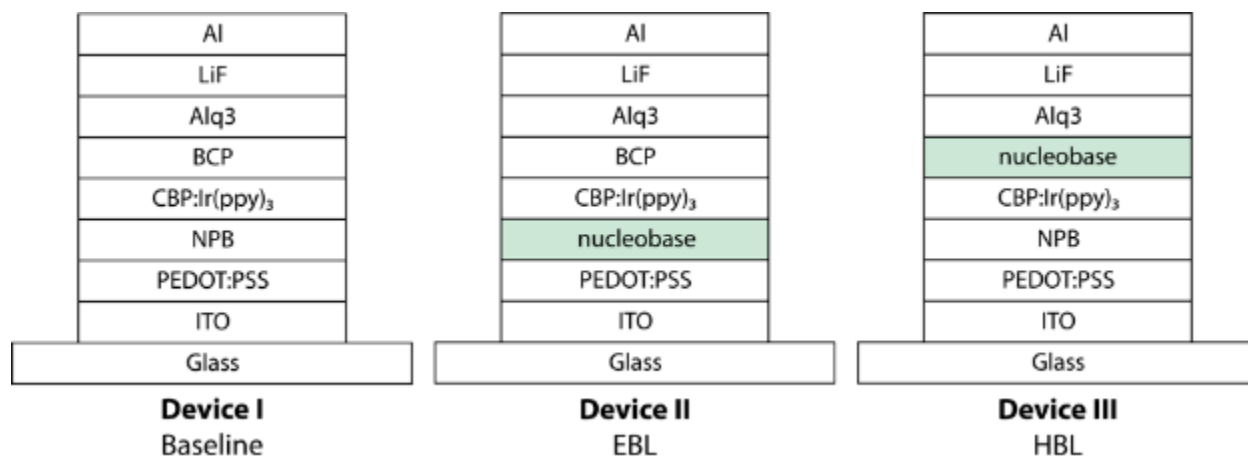


Figure 3. The three types of devices to show the nucleobase properties for OLED. The reference without nucleobases (Device I), the nucleobases in the EBL configuration (Device II) and in the HBL configuration (Device III).

The two layers that were substituted were NPB and BCP, the EBL and HBL, respectively. In Device II, NPB was replaced with the nucleobases at 17 nm (the thickness of the NPB in the reference device). Likewise, for Device III, BCP was removed and replaced with each nucleobase at 10 nm.

In each run a reference (Device I) was grown with a nucleobase OLED (either Device II or Device III). The completed OLED was then transferred to a nitrogen box for testing. Characterization of the OLED was done with a power supply to record voltage and current, and a CS-200 Minolta meter measured luminance. The voltage was increased from 0 to 20 V at 0.25 V intervals and the luminance was recorded at each step. Current efficiency was calculated by dividing luminance by current.

## Results

The results of the EBL device (Device II) are given in Figures 4. The voltage and current (I-V) plots are presented in Figure 4a and the luminance vs efficiency in Figure 4b. The I-V plot shows an interesting trend for the bases. The bases decrease in current in the order of  $G < A < C < T < U$ , with G just slightly lower than the reference device (Device I). The efficiency plot also reveals a similar (but not identical) trend, such that A has the highest maximum luminance ( $\sim 80,000$  cd/m<sup>2</sup>) and exceed the baseline maximum efficiency (58 cd/A). It was closely followed by G, while C, T, and U display the lowest luminance and efficiency. Device II for U was barely visible in light emission at peak luminance of  $\sim 10$  cd/m<sup>2</sup>.

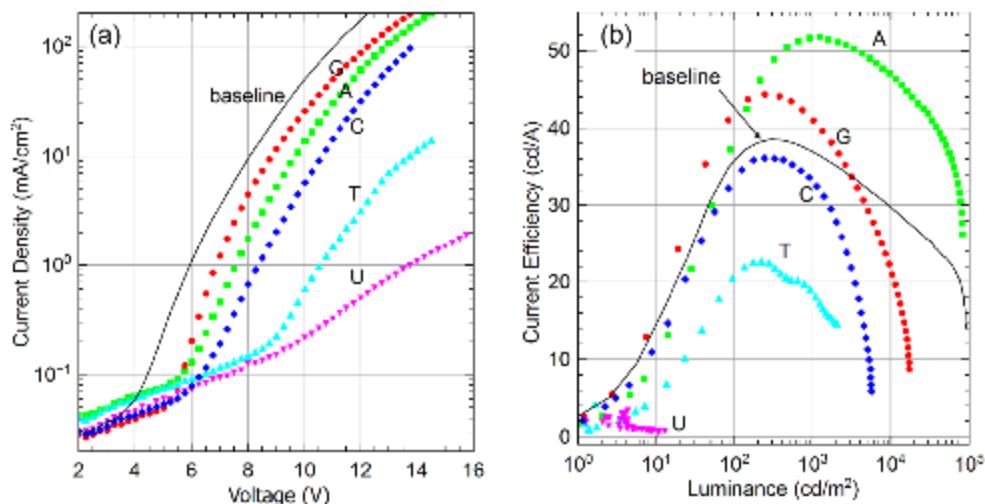


Figure 4. (a) Current density vs voltage for Device II of the nucleobases. (b) Luminance vs current efficiency for Device II.

The results of the HBL device (Device III) are given in Figure 5. The trend in efficiency and luminance in the EBL case (Device II) was reverse for the HBL case (Device III). U had the highest maximum luminance ( $\sim 14,000$  cd/m<sup>2</sup>) and efficiency (16 cd/A), while G was the lowest in performance (maximum luminance and efficiency of 10 cd/m<sup>2</sup> and 1 cd/A, respectively).

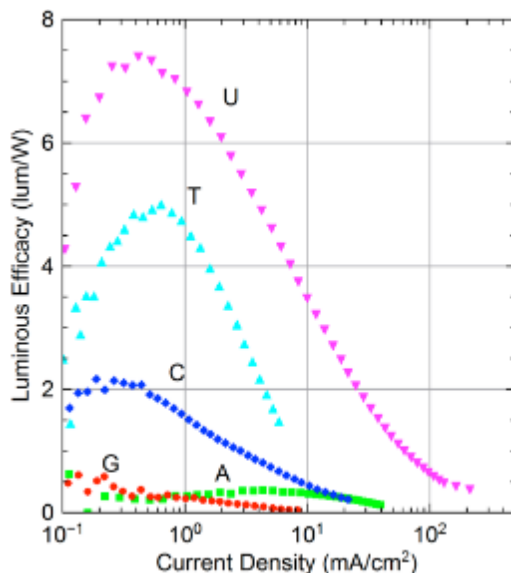


Figure 5. Luminance vs current efficiency plots for Device II.

The ionization potential and electron affinity values provide insight into the results of the nucleobase OLED experiments. Faber et al. have the energy levels of the nucleobases and these values are shown in Figure 6. The nucleobases have stepwise energy levels ranging from

EBL to HBL materials. G and A has the lowest ionization potential and electron affinity of all the nucleobases, thus would allow holes to transport while blocking electrons and serve as a good EBL. Conversely, C, T, and U have very high ionization potentials and electron affinities and serve well as HBL. The results of the OLED experiments confirm this finding. Adenine is the best performing EBL because the ionization potential matches well with the emitting layer (6.0 eV) and good hole injection was facilitated, while still confining electrons. Uracil was a poor EBL because it has a high ionization potential and prevents holes from entering the emitting layer. Likewise, U has very similar electron affinities to its adjacent layers and serves as a good electron injector while confining holes. But G is a very poor HBL because it has such a low electron affinity and prevents holes from injecting from the adjacent layer. The findings of the energy levels show that the nucleobases have stepwise energy levels that can serve as EBL or HBL.

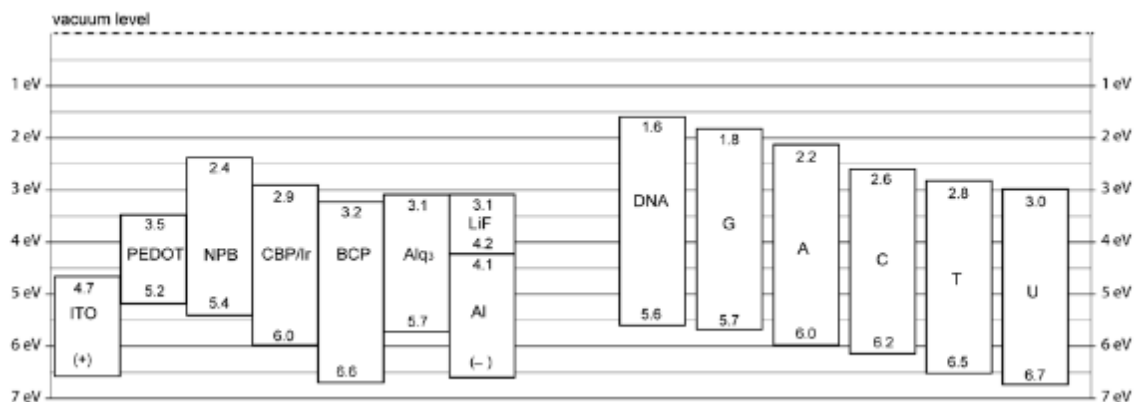


Figure 6. Energy level diagrams for the reference device (left) and all the individual energy levels for the nucleobases and DNA.

The final experiment shows how the EBL OLED can be optimized to achieve very high efficiency. The OLED stack Device II (EBL) was used except that the thickness of the EBL was decreased to 10 nm. It was found that using thymine as an EBL at 10nm significantly increased the device efficiency and luminance over the baseline. The results are shown in Figure 7. Thymine as an EBL obtained a maximum efficiency of 79 cd/A (nearly twice of that of the baseline at 40 cd/A) and nearly 135,000 cd/m<sup>2</sup>, which was higher than the 112,000 cd/m<sup>2</sup> of the baseline. Adenine, DNA, and NPB (reference) devices were also fabricated with the same parameters to compare with the thymine. Adenine and DNA at 10 nm were slightly above the baseline (~40-50 cd/A) with adenine slightly ahead of the DNA in efficiency. However, it is apparent that the high efficiency is unique to the thymine.

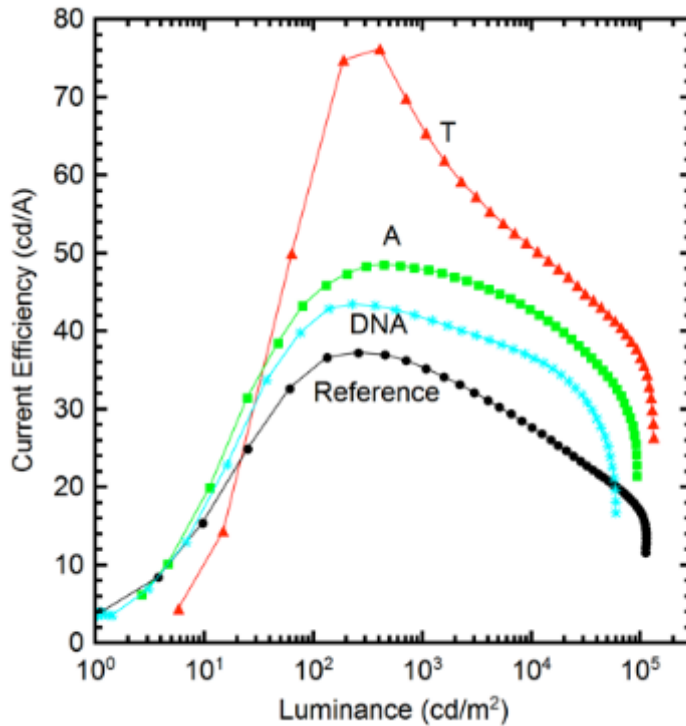


Figure 7. The results of the thymine in the Device II configuration at 10 nm. The results are also compared with similar device for adenine, DNA, and NPB (reference) at 10 nm showing a large improvement in efficiency for thymine.

The thymine results of high efficiency were surprising since previous experiments at 17 nm showed thymine to be an HBL and not an EBL. The cause of the high efficiency was investigated by atomic force microscopy (AFM) to observe the thin film formation of the emitting layer deposited on thymine. Thymine and NPB were deposited separately on a clean Si wafer to a thickness of 10 nm and AFM was performed on these thin films. Afterwards, CBP was deposited at 35 nm on top of the thymine and NPB, and the AFM was done. Figure 8 shows the results of the AFM. It was shown that the thymine caused the CBP thin film to create deep and wide craters in the film. These craters were not present in the reference NPB/CBP film. It is believed that the craters are causing enhanced injection of holes from the thymine to the CBP, which caused the increase in efficiency.

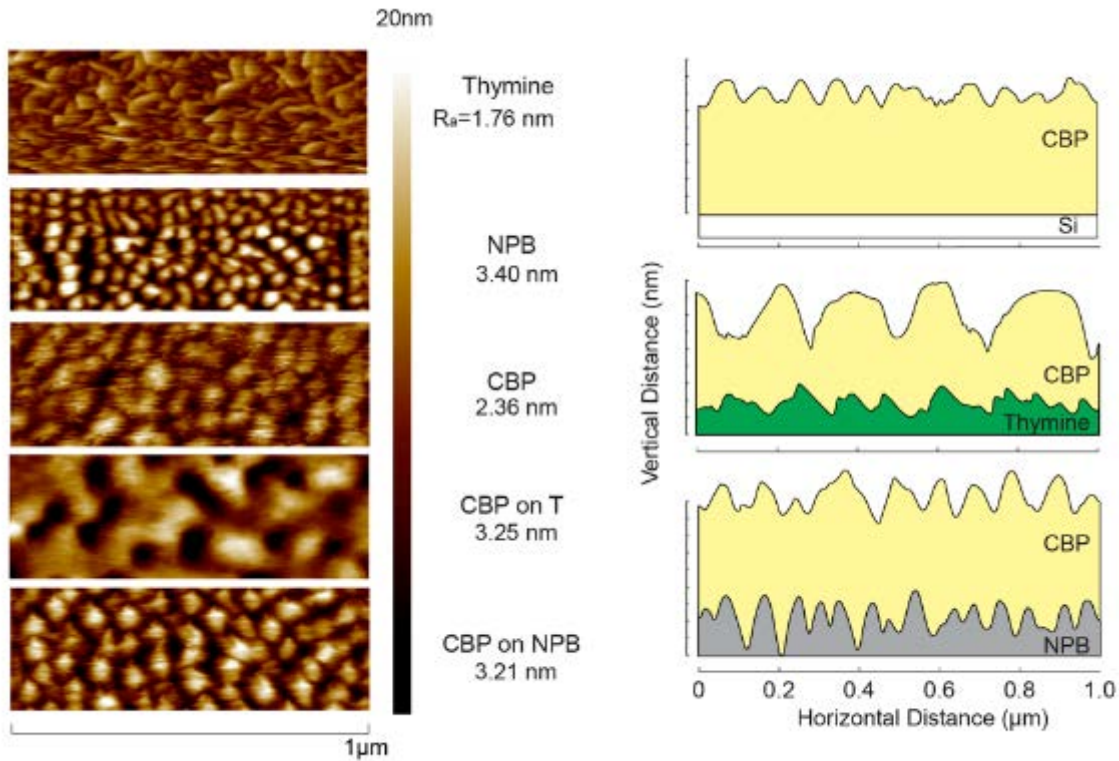


Figure 2. AFM results (left) show the different thin layer formations for thymine, NPB, and CBP on silicon, and also CBP on thymine and CBP on NPB.

In conclusion, nucleobases show great potential as a biomaterial for OLEDs and other future natural electronics devices. Nucleobases are renewable materials that are inexpensive and replace more difficult fabrication procedures of DNA. In addition, their diverse electronic properties have the potential to advance other natural electronic devices. The nucleobases have energy level properties ranging from an EBL to HBL, which increases the freedom of device design for other OLED, OPV, or OFET devices. Additionally, it was shown thymine as an EBL at 10 nm doubled the efficiency of OLEDs due to its unique thin film morphology with the emitting layer CBP. Nucleobases contribute to the growing list of materials available for natural electronics and will be an important contribution to future electronic devices.

## Work Cited

- Baldo, MA, et al. "Very High-Efficiency Green Organic Light-Emitting Devices Based on Electrophosphorescence." *Applied Physics Letters* 75 (1999): 4.
- Faber, Carina, et al. "First-Principles Gw Calculations for DNA and Rna Nucleobases." *Physical Review B* 83.11 (2011): 115123.
- Hagen, J. A., et al. "Enhanced Emission Efficiency in Organic Light-Emitting Diodes Using Deoxyribonucleic Acid Complex as an Electron Blocking Layer." *Applied Physics Letters* 88.17 (2006): 171109.
- Hirata, Kunio, et al. "Electroluminescence as a Probe for Elucidating Electrical Conductivity in a Deoxyribonucleic Acid-Cetyltrimethylammonium Lipid Complex Layer." *Applied Physics Letters* 85.9 (2004): 1627.
- Irimia-Vladu, Mihai. "'Green' Electronics: Biodegradable and Biocompatible Materials and Devices for Sustainable Future." *Chemical Society Reviews* (2014).
- Irimia-Vladu, Mihai, Niyazi Serdar Sariciftci, and Siegfried Bauer. "Exotic Materials for Bio-Organic Electronics." *Journal of Materials Chemistry* 21.5 (2011): 1350-61..
- Lagoja, Irene M. "Pyrimidine as Constituent of Natural Biologically Active Compounds." *Chemistry and Biodiversity* 2.1 (2005): 1-50.
- Rosemeyer, Helmut. "The Chemodiversity of Purine as a Constituent of Natural Products." *Chemistry & Biodiversity* 1.3 (2004): 361-401.
- Watson, J. D., and F. H. C. Crick. "Molecular Structure of Nucleic Acids: A Structure for Deoxyribose Nucleic Acid." *Nature* 171.4356 (1953): 737-38.

PHOTOPHYSICAL PROPERTIES OF NONLINEAR CHROMOPHORES

Project No. 0059.1

Rachel Swiger  
Wright State University

12 December 2013

Government Project Leader  
Dr. Joy Haley  
AFRL/RX

Southwestern Ohio Council for Higher Education  
Student Research Program  
Agreement Number: FA8650-09-2-5800

## **Acknowledgements**

Acknowledgments go to the Southwestern Ohio Council for Higher Education (SOCHE) and my colleagues at Wright-Patterson Air Force Base. My colleagues include Dr. Joy Haley, Dr. Thomas Cooper, Dr. David Stewart, Mr. Jonathan Slagle, Mr. Douglas Krein, Dr. Daniel Mclean, Dr. Mark Walker, and Mr. Matthew Dalton. Each one has challenged me in a way that has broadened my scholastic abilities and professional experience. I am extremely grateful that such an amazing opportunity was presented to me and for the support and opportunities my colleagues have given me.

## **General Description of Project**

Optical properties of nonlinear chromophores were analyzed using various steady-state and time-resolved spectroscopic techniques. Standard analytical solutions of these chromophores were prepared and used to determine their photophysical properties with proper instrumentation, including UV-Vis and fluorescence spectrophotometers, time-correlated single photon counting (TCSPC), and laser flash photolysis (LFP). Molar absorptivities, singlet and triplet-state lifetimes, and absorption and fluorescence spectra were obtained, and were important for determining the photophysical properties of the different chromophores. These properties were used to determine whether chromophores are suitable for different applications, depending on their absorption and kinetic capabilities.

## **Description of Research**

Standard analytical solutions were prepared by dissolving weighed amounts of solid chromophores into various solvents. Data extrapolated from the UV-Vis spectrophotometer was used to analyze the linear correlation between the concentration of the chromophore in solution and its absorbance. This correlation is known as the extinction coefficient or molar absorptivity. Spectra from the fluorescence spectrophotometer were used in conjunction with TCSPC. Fluorescence spectra were used to determine the maximum wavelength of emission for each chromophore, which was then used in TCSPC to determine the singlet-state lifetime. LFP was used to analyze the triplet-state lifetime and gather triplet-state absorption spectra.

## **Results**

An understanding of the basic principles of quantum mechanics was gained during the project, which helped greatly in an academic setting. Professional experience and laboratory experience outside of academia was gained as well, which will help to broaden upcoming career opportunities. Many chromophores proved to be excellent candidates for nonlinear applications while others did not.

## **Related Activities**

In April 2013, I was invited to attend the 245th American Chemical Society National Meeting and Exposition in New Orleans, LA. It was an unforgettable experience and one that most SOCHE students do not get to encounter. I presented in the physical science poster session

with research entitled “Photophysical Properties of Porphyrins and Phthalocyanines in Solution and Solid Matrices,” where I studied the effect of the host matrix on photophysical properties. I attended several other events for students, such as career and graduate school fairs, that have helped me considered my options for the future.

PHOTOPHYSICAL PROPERTIES OF NONLINEAR CHROMOPHORES

Project No. 0059.2

Stephanie Long  
Cedarville University

31 August 2014

Government Project Leader  
Dr. Joy Haley  
AFRL/RXAP

Southwestern Ohio Council for Higher Education  
Student Research Program  
Agreement Number: FA8650-09-2-5800

## Acknowledgments

The research presented in this report could not have been accomplished without the support and technical expertise of Dr. David J. Stewart, Dr. Tom Cooper, and Dr. Doug Krein.

## General Description of Project

Project Objective: Explore the optical properties of a variety of nonlinear organic and organometallic chromophores and develop structure property relationships within synthetic families. This objective is part of the overall goal of RXA as it allows materials developed here to be characterized for their optical properties. Materials with desirable properties are then examined in various morphologies to determine if they will be useful for potential applications within the Air Force.

## Description of Research

The research required characterization of the photophysical properties of several absorbing dyes. This characterization was completed mainly using an ultraviolet-visible spectrometer (UV-vis) to measure absorbance, a fluorometer to measure emission and excitation, and a time-correlated single photon counting (TCSPC) to measure lifetimes and determine the rate of decay. The dyes were also characterized using laser flash photolysis (LFP).

The UV-vis was used to measure the absorption spectra for each dye in a variety of solvents. Extinction coefficients were determined using Origin software by calculating the slopes of lines fit to plots of absorbance as a function of concentration at a particular wavelength.

The fluorometer gives the steady-state emission spectra of the dyes, which can be used to determine the energy of the emitting excited state and also the relative amount of charge-transfer in this state. Purity can be confirmed by measuring excitation spectra and ensuring they match the absorbance. The TCSPC measures the emission decay as a function of time at a specific wavelength. The instrument software can be used to fit the resulting curve either alone or by reconvolution with instrument response function to determine the lifetime of the emitting species. All data obtained can be inserted into Origin to graph and convey it in an organized manner.

## Results

There were two different focuses of the research. One of the focuses was a molecule containing a fluorene with a thiol group on one side and a nitrogen with two phenyl groups (Compound A, Figure 1). The other focus was a symmetrical, bidentate ligand where the nitrogens can chelate to a metal (Compound B, Figure 1). The primary focus of Compound A was the characterization of the dye and eight derivatives.

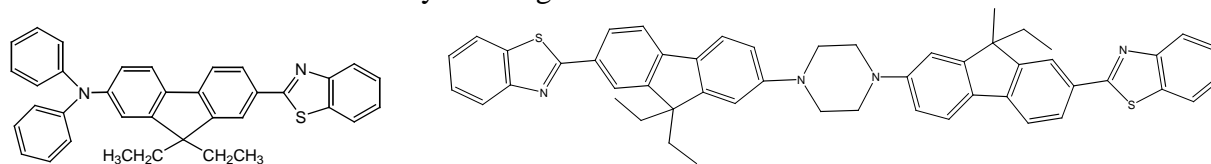


Figure 1. Compound A is pictured on the left and Compound B is pictured on the left.

The same data was collected for each dye: absorbance, emission, excitation, and lifetime in five different solvents ranging from nonpolar to polar. Each of the derivative dyes had a slight modification to the structure to allow for examination of the steric dependence on the photophysical properties. Four of the derivatives added bulky groups to the diphenylamino side in order to create steric hindrance with the fluorene backbone in order to see if that would prevent rotation and cause a certain conformation to be locked. The variations in the derivatives allowed observations to be made concerning the amount of charge-transfer character, donating abilities of the groups, and the resulting relations in the radiative rate constant. Figure 2 shows absorption spectra of both Compound A and one of its derivatives. Both show broadening with increasing solvent polarity, indicating some ground-state charge-transfer character.

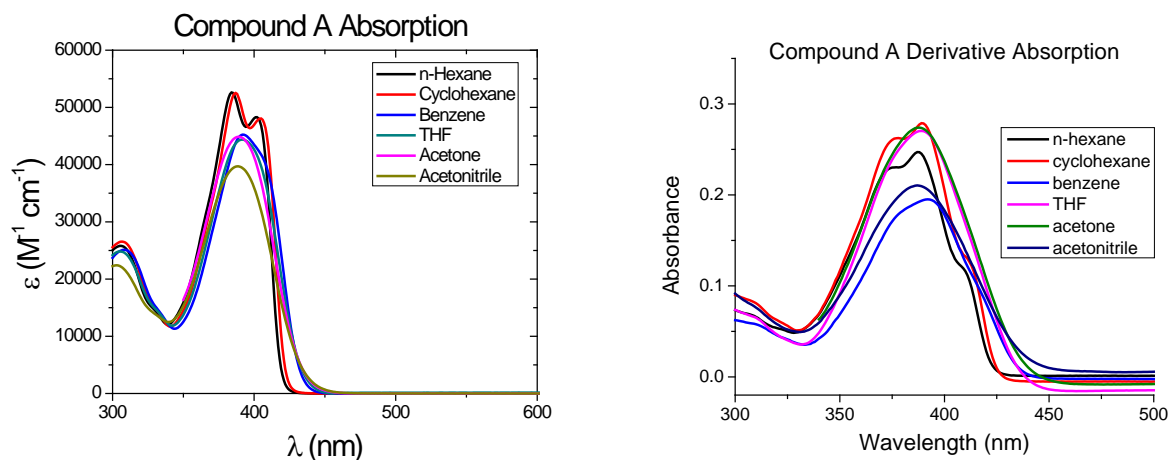


Figure 2. Compound A Derivative absorption has broader absorption than Compound A.

The results obtained from the study of these sterically hindered derivatives of Compound A support a twisted-intramolecular-charge-transfer (TICT) state being present in Compound A. Other derivatives were also synthesized that linked the present phenyl groups. Variations in the lifetimes and quantum yields indicate that there are changing vibrational modes due to the linkage of the phenyl groups.

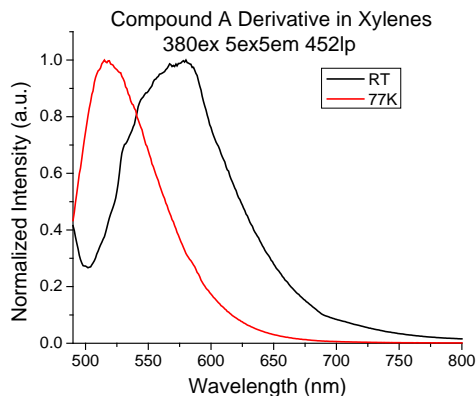


Figure 3. Emission spectra is measured for the dye in both room temperature and at 77K.

When the emission is more localized, the compound may decay faster due to more deactivating pathways because of the linked phenyl groups. There was also a temperature dependent study done on the dyes in nonpolar and polar solutions, as illustrated in Figure 3. The results from the graph allude to the conformation of the dye being locked once frozen.

Compound B is being analyzed to determine if a metal will bind to the nitrogens present and quench the emission of the dye. So far CuI, CuPF<sub>6</sub>, and Zn(OTf)<sub>2</sub> have been used to accomplish this goal. The CuI had solubility issues with the dye and the solvents it was soluble in, so research with that was ceased. CuPF<sub>6</sub> and Zn(OTf)<sub>2</sub> both showed results that were not expected where the emission of the dye actually became more exaggerated with the more metal present (Figure 4). This is due to the formation of a complex with the metal and dye which has its own distinct emission.

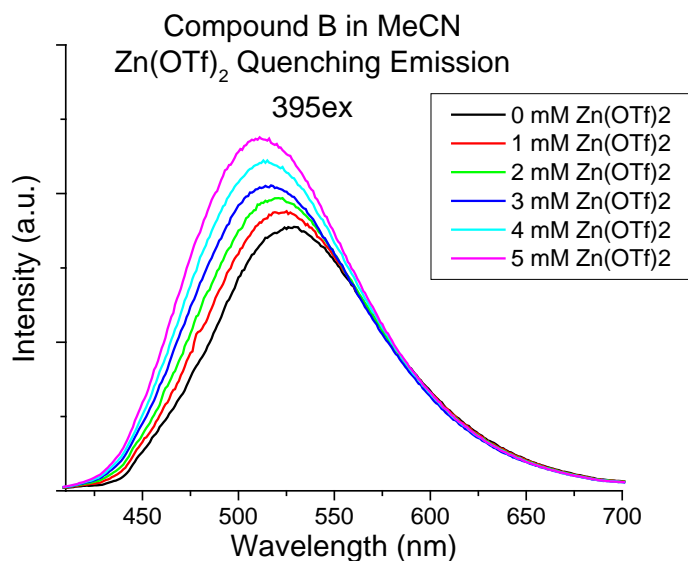


Figure 4. Emission of Compound B increasing with increasing Zn(OTf)<sub>2</sub>.

Data for Compound A and its derivatives with Laser Flash Photolysis still needs to be obtained, and further studies on metal quenching of Compound B will be conducted. On top of these two main projects, some research was done for other groups in the same organization where absorption and emission data was collected for both dye-modified polymer gold nanorods in water and liquid crystal monomers in THF and n-hexane. Any follow up studies will be pursued by the respective groups.

CTE TAILORING IN HYBRID MATERIALS

Project No. 0066.1

Mackenzie Kirby  
Wright State University

25 April 2014

Government Project Leader  
Dr. Jaimie Tiley  
AFRL/RXCM

Southwestern Ohio Council for Higher Education  
Student Research Program  
Agreement Number: FA8650-09-2-5800

## Acknowledgments

I would like to express my appreciation for Jaimie Tiley who served as a helpful, personable project leader, Sang Lan Kim who always did her absolute best to answer my questions, and Tinuade Daboiku who worked with me throughout the project.

## General Description of Project

Many high temperature material characteristics in nickel superalloys are influenced by the morphology, size, and distribution of precipitate particles in the matrix of the material. These precipitates are named  $\gamma'$ . The characteristics of these precipitates change with different cooling rates and quench temperatures. Therefore, when modeling material behavior, it is often important to accurately measure volume fractions, sizes, and morphologies of  $\gamma'$  at different conditions. The research presented here focused on two different methods of characterizing nickel superalloys: etching and focused ion beam (FIB) milling. The benefits and drawbacks of each method were analyzed in order to determine the most appropriate method to use when characterizing nickel superalloys for various other uses such as creep modeling.

## Description of Research

Samples from two nickel superalloys (IN100 and LSHR) were removed from the billet by wire electrical discharge machining (EDM). They formed 0.4 in diameter by 3.5 in long radial bars. The bars were then solutionized in an induction furnace at 2175°F in order to dissolve the remaining  $\gamma'$ . The bars were then cooled at either 20 or 250°F/min with a type K thermocouple after which they were water quenched. Samples were cut from the bar center near the thermocouple, mounted, and polished with standard metallographic techniques. They were finished with 0.05  $\mu\text{m}$  colloidal silica. The samples were cleaned in an ultrasonic bath with 1% Microclean solution, rinsed with ethanol, and dried with nitrogen gas.

After polishing, one of two possible methods was used to finish the sample and prepare it for imaging. The first and most commonly used method was to etch the sample, or preferentially dissolve away either the precipitates or the matrix. For this research, an etchant solution of 80 ml HCl, 80 ml HNO<sub>3</sub>, 80 ml H<sub>2</sub>O, and 2.4 grams of molybdic acid was used for 10 seconds after which the sample was immediately removed and submerged in a sodium bicarbonate solution in order to neutralize the acid. Images were taken in the area near the thermocouple, as seen in Figure 1. The samples were imaged using a FEI Sirion scanning electron microscope (SEM) in ultra-high resolution (UHR) mode with the through-the-lens (SEI) detector at a working distance of 5mm. The beam operated at 12kV and a spot size 4.0. Calibration standards were also imaged at each magnification. A sample images is shown in Figure 2.

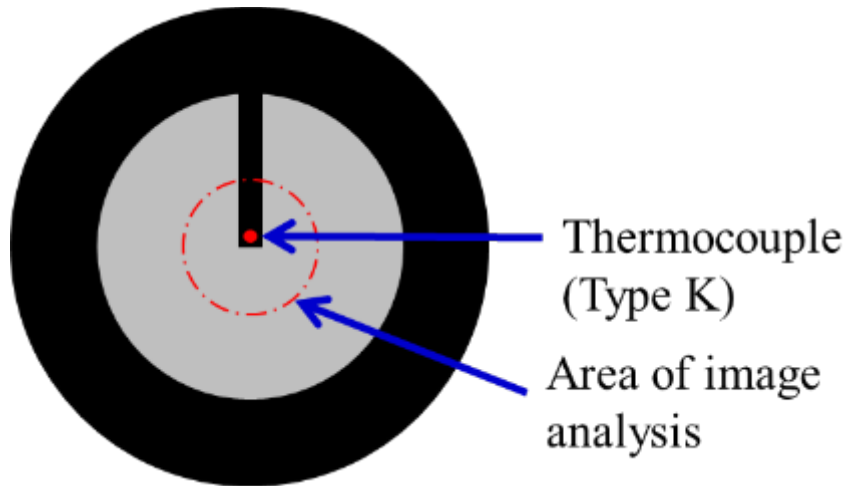


Figure 1: Illustration of sample highlighting the area of image analysis.

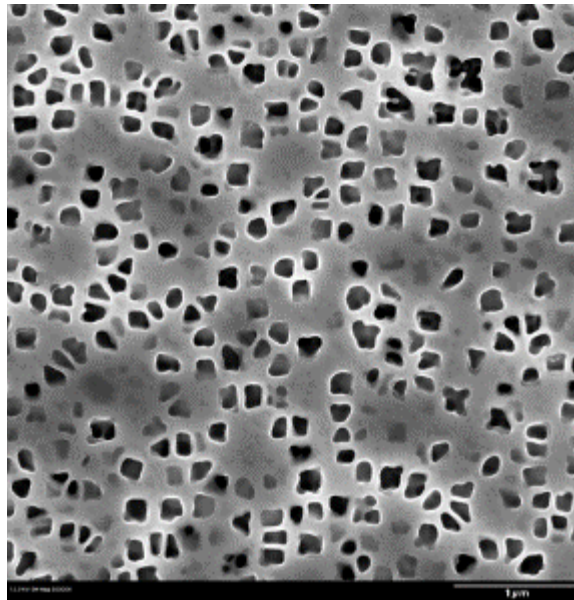


Figure 2: LSHR sample, taken on an FEI Sirion SEM at 20KX, Secondary Electron Image, 12kV, working distance 5 mm, etched.

The second method used is to FIB mill the sample. As shown in Figure 3, the sample was first cut in half to create a new surface perpendicular to the original. This surface was also polished using standard metallographic techniques and was finished at 1 μm with diamond slurry. The sample was then positioned in the FEI DB235 focused ion beam (FIB) microscope at a working distance of 5mm. The ion current started at 5nA and progressed to 500pA. With this technique, the beam cleaned parallel to the original polished surface and therefore created a minimum of damage to the sample. Progress between each run of cleaning was checked using a FEI Sirion SEM in UHR mode with the SEI detector at 2-5 kV with spot size 6.0. After cleaning, images were taken using the same SEM at a working distance of 2mm. A sample image is shown in Figure 4.

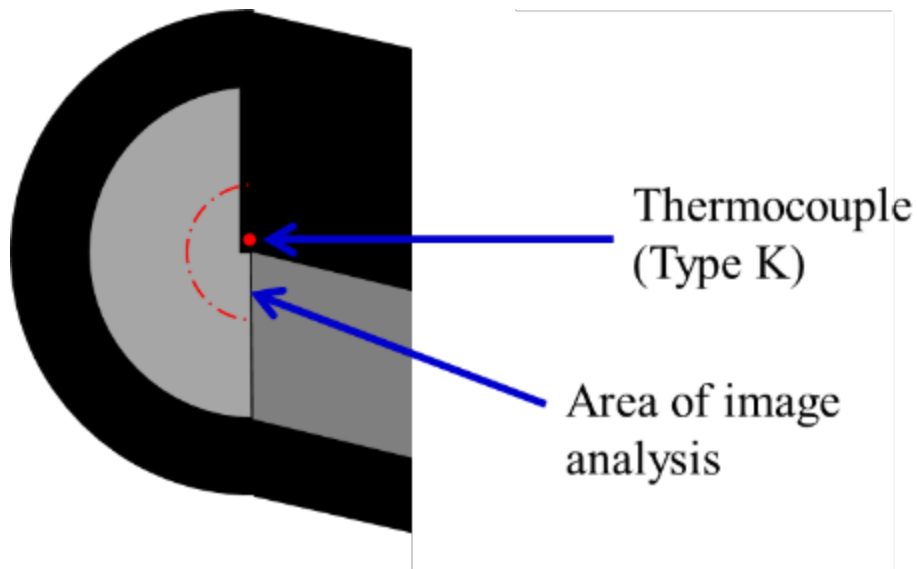


Figure 3: Illustration of sample prepared for FIB milling which highlights the area of analysis.

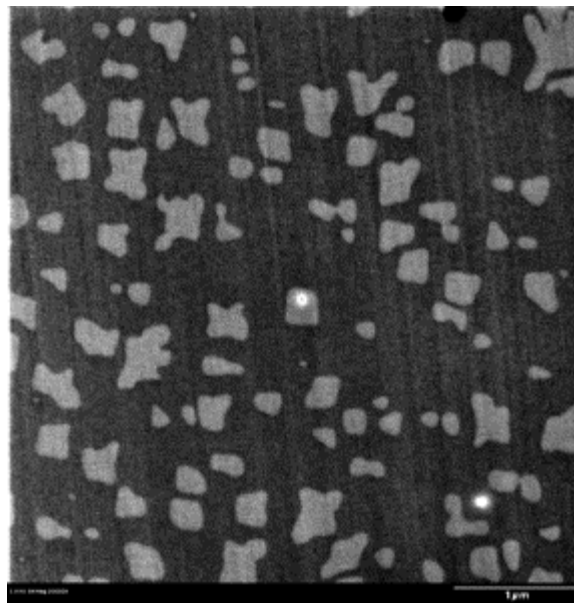


Figure 4: LSHR sample, taken on an FEI Sirion SEM at 20KX, Secondary Electron Image, 5kV, working distance 5 mm, FIB Milled.

Segmentation techniques were then performed for both methods. Precipitates were sectioned using the lasso tool in Photoshop v 11.0.2 and highlighted by color according to their morphology (primary, secondary, tertiary). A sample image is shown in Figure 5. Filters provided by Fovea Pro then segmented each type of precipitate and output a text file with size and shape information. These files were opened in Microsoft Office Excel and used to calculate area fraction and histograms for equivalent diameter.

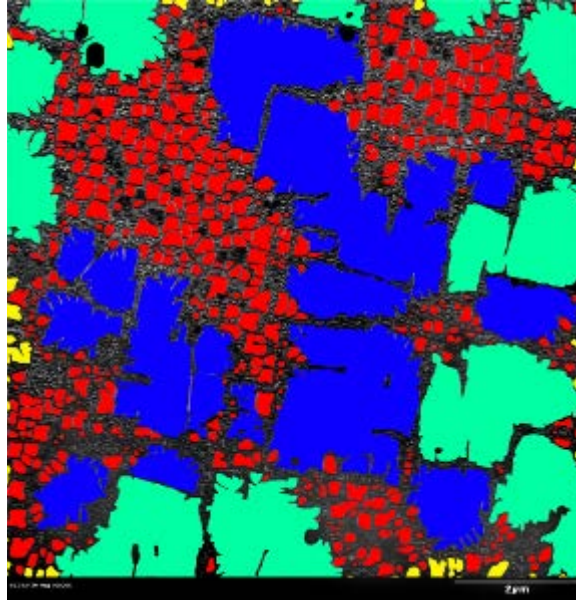


Figure 5: IN100 sample, taken on an FEI Sirion SEM at 10KX, Secondary Electron Image, 10 kV, working distance 5 mm, FIB Milled.

## Results

For each sample, the equivalent diameter and area fraction were determined using both methods for the fast cooled and slow cooled samples. The graphs for area fraction are shown below in Figure 6. The graphs for equivalent diameter are shown below in Figure 7.

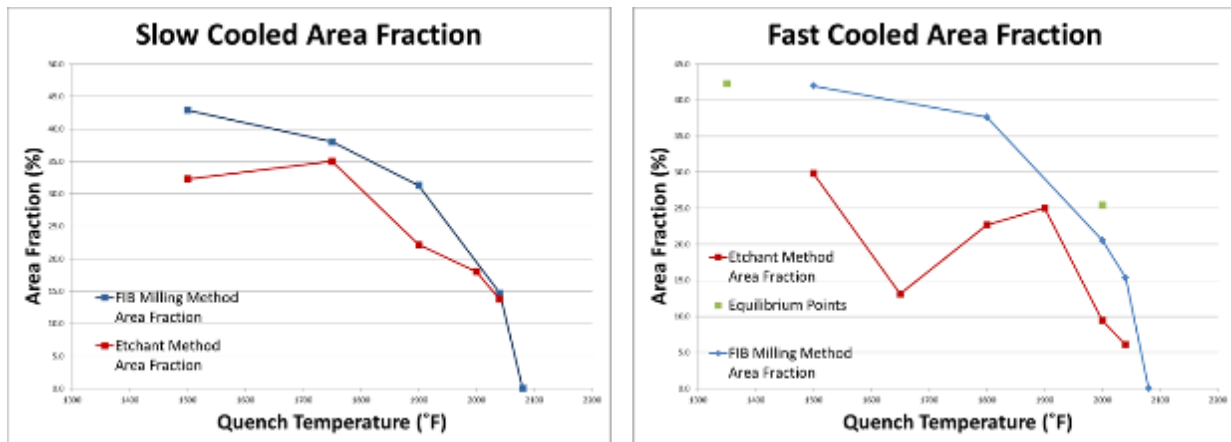


Figure 6: Comparison of area fraction found using etching versus FIB milling for both slow cooled and fast cooled samples.

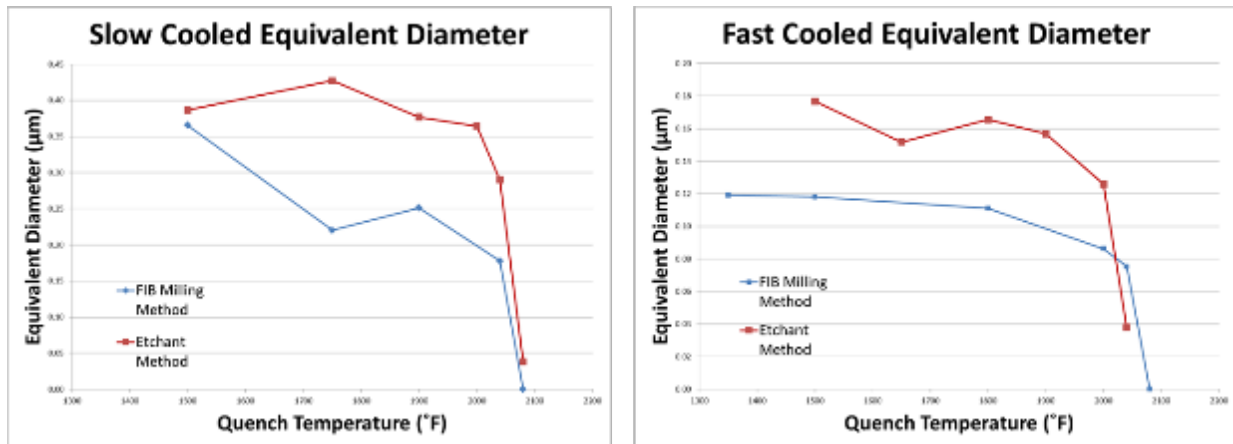


Figure 7: Comparison of equivalent diameter found using etching versus FIB milling for both slow cooled and fast cooled samples.

As seen in Figure 6, the etchant method found a consistently lower area fraction when compared to the FIB milling method. The curve for the FIB milling method is also far smoother and tracks closer to the equilibrium points found for the fast cooled samples. The opposite true is found for equivalent diameter with etching giving consistently higher values for both the slow cooled and the fast cooled samples. When observing the comparison of images for the two different methods shown in Figure 8, these values make sense. It appears that the etchant method preserves a far fewer number of small diameter precipitates which would simultaneously lower the area fraction and drive the statistics for equivalent diameter higher.

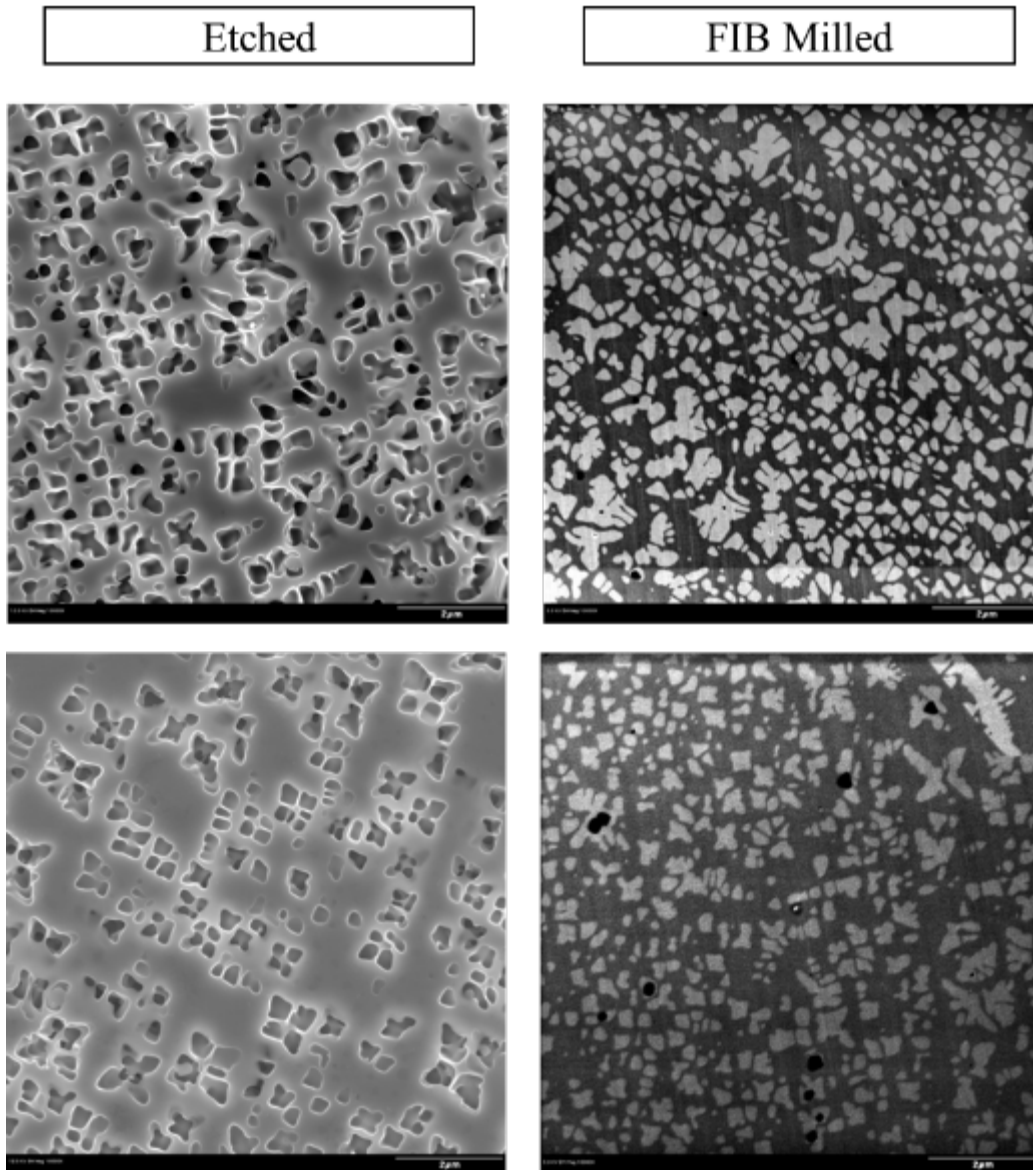


Figure 8: Comparison of images for two samples which were both etched and FIB milled.

### Conclusions

Although the etchant method is far cheaper and easier than the FIB milling method, accuracy is compromised in the form of a larger equivalent diameter and a smaller area fraction than in reality.

NONMETALLIC MATERIALS DIVISION TECHNICAL SUPPORT

Project No. 0072.1

Jonathan H. Marshall  
Wright State University

8 November 2013

Government Project Leader  
Melvin D. Hoke  
AFRL/RXA

Southwestern Ohio Council for Higher Education  
Student Research Program  
Agreement Number: FA8650-09-2-5800

## **Acknowledgments**

I would like thank Karen Olsen and Melvin Hoke for the providing me with an opportunity to succeed at AFRL.

## **General Description of Project**

The project was to provide direct support to the Nonmetallic Materials Division senior leadership. Tasks involved data entry, compilation and graphing of ongoing research and development efforts within the Division in order to develop a comprehensive and focused assessment of those programs to the leadership. Another aspect of the project was to monitor supplies and equipment purchases as well as assist in laboratory management processes, i.e. Logistics.

A significant duty completed during the project was the implementation of a visual basic enhanced Access database to contain, manage, and analyze all Government Purchase Card (GPC) transactions within RXA. This database replaced manual paper process for over 500 personnel and is used to capture over 5000 annual transactions. Responsibilities included: Use Case and Test Case development, User Acceptance testing, requirements gathering, wireframe development, graphic design, and GPC compliance testing.

## **Description of Research**

The Access database created was named Order Management and Efficient GPC Accounting (OMEGA). There was a need to improve upon the old method of tracking GPC purchases. This process starting by filling out an Excel order form; then emailing the order form to a project leader who would then email the order form to an Approving Official (AO) and finally emailing the order form to a GPC Card Holder. Once received by the Card Holder, the order would be completed and the form would be printed out and handed to another employee to input into a larger Excel tracking database. The new process would have a user input the information onto a form in Access which would populate the database and allow the project leader, AO, and Card Holder the ability to view and approve the order without email correspondence. This new process also reduces the number of times the information is input into a table or form.

The first step to implementing the Access database was to meet with the User base and gather requirements. Through several meetings the business rules were detailed and the entire process was outlined. This enabled the creation of Use Cases which are a tedium step-by-step break down of a current process which allows a smoother transition into a development scheme. After many several Use Cases were written, a new set of Use Cases were developed which translated the current process into a formulaic process which would be used within the focus of the development team. Wire frames were also completed to give the developers a better understanding of the visual expectations.

Once the Use Cases were completed, the development began. Throughout the development process there was constant communication between the developers, the requirements liaison, and the end users. This ensured an end product that would meet the expectations and requirements.

Upon completion of the database Test Cases were completed to determine the thoroughness of the database as well as check for any bugs or defects. As the database was launched and became the official tool to request a purchase, several training meetings were conducted to ensure end users were fluent in the new process.

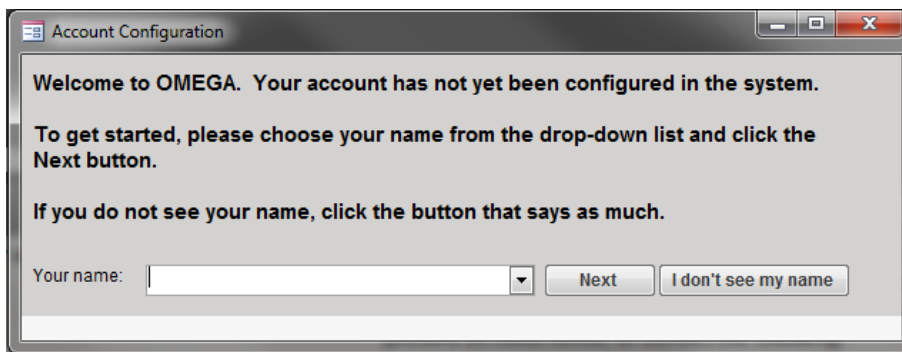
## Results

Once production began on the database and a name was chosen, a design scheme was established and a logo was created, Figure 9.



**Figure 9: OMEGA Logo**

Form construction and design was paramount to ensure a smooth flow and transitions throughout the database. Several examples of form design include **Figure 9: OMEGA Logo**, **Figure 11: OMEGA Main Page**, **Figure 12: New Order Form**, and **Figure 13: Order Status**.

A screenshot of a software window titled "Account Configuration". The window has a standard Windows-style title bar with minimize, maximize, and close buttons. The main content area is light grey and contains the following text: "Welcome to OMEGA. Your account has not yet been configured in the system." followed by "To get started, please choose your name from the drop-down list and click the Next button." and "If you do not see your name, click the button that says as much." Below the text is a form with a label "Your name:" followed by a white text box with a downward-pointing arrow on the right side. To the right of the text box are two buttons: "Next" and "I don't see my name".

**Figure 10: Account Configuration**



**Figure 11: OMEGA Main Page**

A core structure of OMEGA is the use of Role Based Access (RBAC). RBAC accompanied with the accounts allows for different permissions levels in OMEGA, e.g. Research Area Managers, Approving Officials, Card Holders, and Super Admins. OMEGA is tailored to each permission level and will display menu options accordingly.

The New Order form, **Figure 12**, features auto populated fields dependent upon selections made on the form. It also features a comments section which is a complete dialog between a basic user and approvers.

The screenshot shows the 'New Order Form' in the OMEGA system. The interface is organized into four main sections:

- Step 1: Fill out all required fields**: This section contains several input fields:
  - Tracking Number: 74
  - Requestor: [Empty]
  - Requester Date: 11/21/2011 2:11:46 PM
  - Delivery Location: [Empty]
  - VendorID: [Empty]
  - Vendor Phone: [Empty]
  - Vendor Website: [Empty]
  - Research Area: [Dropdown menu]
  - Card Holder: [Empty]
  - Research Area Manager: [Empty]
  - Approving Official: [Empty]
  - Alternate Approving Official(s): [Empty]
- Optional: Enter comments about the order.**: A large text area for 'Comments'.
- Step 2: Upload attachments if needed**: A table with columns for 'Attachment Name' and a paperclip icon for uploading. One attachment is listed with the name '0(1)'.
 

Attachment Name	Upload Icon
0(1)	[Paperclip]
- Step 3: Enter line items and shipping/handling**: A table for entering items.
 

Item Description*	Item Number*	Item Type*	Approval Type*	Approval #*	Unit Price*	Quantity*	Extended Pr*
[Empty]	[Empty]	[Empty]	[Empty]	[Empty]	[Empty]	[Empty]	[Empty]
- Summary**: Fields for 'Subtotal:', 'Shipping/Handling:', and 'Total:'.
- Step 4: Submit the completed form**: 'Submit' and 'Cancel' buttons.

**Figure 12: New Order Form**

Another great feature of OMEGA is that a user can view real time statuses of the orders requested. In **Figure 13**, the goal was to provide the user with a simple graphical interface that clearly displays the status of an order.



Figure 13: Order Status

PREPARATION AND CHARACTERIZATION OF ULTRA HIGH TEMPERATURE  
CERAMIC MATERIALS

Project No. 0081

Eugene Whatley  
Wright State University

31 August 2014

Government Project Leader  
Dr. Lawrence Matson  
AFRL/RXCC

Southwestern Ohio Council for Higher Education  
Student Research Program  
Agreement Number: FA8650-09-2-5800

## **Acknowledgements**

I would like to thank Dr. Lawrence Matson, Dr. Heedong Lee, Dr. Il-seok Park, Brian, Melvin Petry, Kristin Keller, Michael Kinsella, Dr. Michael Cinibulk, and the rest of the Ceramics Research Team for their continued contribution to my research.

## **General Description of Project**

Research is being done on Ultra High Temperature Ceramics (UHTC) to be used for hypersonic leading edges and other UHTC applications. In conducting research, there are several different processing techniques used in creating the UHTC materials. Alloyed powders are made by Arc Melting (AM) commercial grade powder mixtures in order to get the alloy chemistry uniform throughout the powders. The powder is then cold compacted in to pellets using Cool Isostatic Press (CIP) and then the compacted powers are consolidated using Spark Plasma Sintering (SPS). The consolidated material is then cut, grounded, mounted, and polished for microstructural analysis and mechanical property testing. Characterization of these UHTC samples included light microscopy, Scanning Electron Microscopy, and X-Ray analysis.

## **Description of Research**

In this project, research was being done on UHTC alloys based on Tantalum Carbide (TaC) system, which is one of the highest melting point materials known to man but they are usually not thermal shock resistant due to their high CTEs and have low thermal conductivities. Since it is very difficult to change the thermal properties of a material to a high value, the approach taken here was to use processing and chemistry to conduct microstructural control and improve the strength and toughness of the materials so that it could withstand higher thermal stress loading without cracking. In depth research is being done on the different ceramic alloy system, to see how different chemistries, processing techniques, consolidation techniques, affect thermal-mechanical properties and oxidation behavior. Based on how the samples are affected, the “best” alloys are being screened for uses as leading edges for hypersonic vehicles or other UHTC applications.

## **Processing of Alloyed Powders**

In order to make alloyed carbide material between pure Ta<sub>2</sub>C to pure TaC (see Figure 1) we mixed different percentages of commercial grade tantalum metal powders with TaC powders in an ethanol carrier fluid and then blended them together using a Thinky Mixer that operated between 1000-2000 rpm. Once these powders are uniformly blended, we then dry the resultant slurry using a vacuum oven. This produced a dried powder cake, which we then brock up and sieved back into a powder form, which contained a uniform mixture of the Ta and TaC powders. These mixed powders were then placed into a molding bag and Cool Isostatic Pressed (CIP) into a semi solid form that could either be placed into an arc melt machine (AM) for alloying via solidification or into the spark plasma sintering machine SPS for alloying by solid state diffusion. In this study we use the arc melting (melt-rapid solidification approach) to make the alloyed powders with the desired chemistry and contained a very fine microstructures. The arc melting process uses an argon plasma torch (that similar to an electric welder set-up), which

produces a high energy arc from a tungsten stinger to the grounded sample container. The molten pool produced by the arc allows for complete mixing of the chemistry on an atomic level. Then as the arc is moved away from the molten pool, the melt solidifies rapidly producing an alloy that is a cigar shaped bulk material, which contains a very fine nano-scaled microstructure.

Unfortunately, it is very hard to produce a part shape using arc melting so usually these alloyed pucks are then broken up into alloyed powder form using a shatter box and sieving to the desired mesh size. The alloyed powders still contain the nano sized microstructure and then are re-consolidated into a shape part by another process such as SPS, extrusion, hot pressing, Hipping or pressure less sintering (note these are diffusion controlled processes). The size of the resulting microstructure of the consolidated part and its mechanical properties are then controlled by grain growth caused by the amount of heating times and temperature required to get full density for the chosen process. These diffusion controlled consolidation processes are list in the order of shortest heating time required for full density verses the longest heating time (i.e. finer microstructure to largest microstructure).

In this research we used Spark Plasma Sintering (SPS) to consolidate the alloyed powders, keeping the microstructure fine. SPS is like hot pressing but where DC current is ran through the graphite die (Joule Heating) that holds the sample instead of heating by an external heating source like induction or resistance heaters. This process allow the sample to be heated and consolidated very fast before much grain growth occurs. This allows the material to retain its very fine microstructure and hence it usually shows very good mechanical properties compared to the other consolidation methods, which take longer times at temperature to consolidate a materials.

### **Characterization of the powders and bulk alloyed materials**

As previous mention in this work we made alloyed powders by arc melting pucks and then pulverizing them in a Shatter box back to alloyed powders. A small portion of the sieved powders was used for X-Ray analysis using a Bruker D2 Phaser X-Ray Diffractometer to get an idea of if the phases content. SEM was used to get an idea of the phase sizes, microstructure features and distributions. The rest of the alloyed powder was SPSed in a graphite dies at various temperatures to identify the condition where 100% dense material could be formed. The SPS creates a 1 inch puck that is covered with graphite, which is then ground off using a diamond wheel (74-45 $\mu$ m), polished down to 1 $\mu$ m using a Gold Label cloth, and fine polished to 0.05 $\mu$ m using a Chemomet cloth. Microstructural characterization is then done on this polished sample by light microscopy and SEM to study the microstructural features and distributions, SEM/EDX to identify the elemental analysis chemistries of the phases present and then X-Ray analysis to identify the phases present. The data from each of these characterization methods is essential in showing how the microstructure is affected when heated up to different temperatures and pressures in the consolidation study of Ta-Carbide alloys.

The polished 1 inch puck is then cut into rectangular shaped bars of the same size. These bars are then polished to eliminate any crack or scratches on the sample. Once polished, the bars are placed in the Synergie 400, a machine that applies a bending force to the bar at a certain rate until the bar is broken. The room temperature load-deflection data collected is used to calculate the bend strength Ta-Carbide samples. Some of the bars are notched with a diamond saw and bend tested to determine the toughness of the material. This test shows how the phase type size and distribution in the sample correlates to the strength and toughness of the alloys. Some tests

are performed at elevated temperature to see how the bend strength and toughness behave as a function of test temperature.

Oxidation testing is performed using numerous methods including static furnaces, torch testing and the exhaust port of a scramjet engine; however these tests are conducted by a different group of scientist. The data from these tests, along with the information from the thermal mechanical property evaluation is used to down select the Ta-Carbide alloy for the desired application, such as is hypersonic leading edge.

## Results

This research shows that there are different phases in the Tantalum Carbide system [ $Ta_2C$ ,  $Ta_4C_3$  and  $TaC$ ] (Figure 1) and alloys which contain different amounts of these phases affect the thermal mechanical properties of the material.

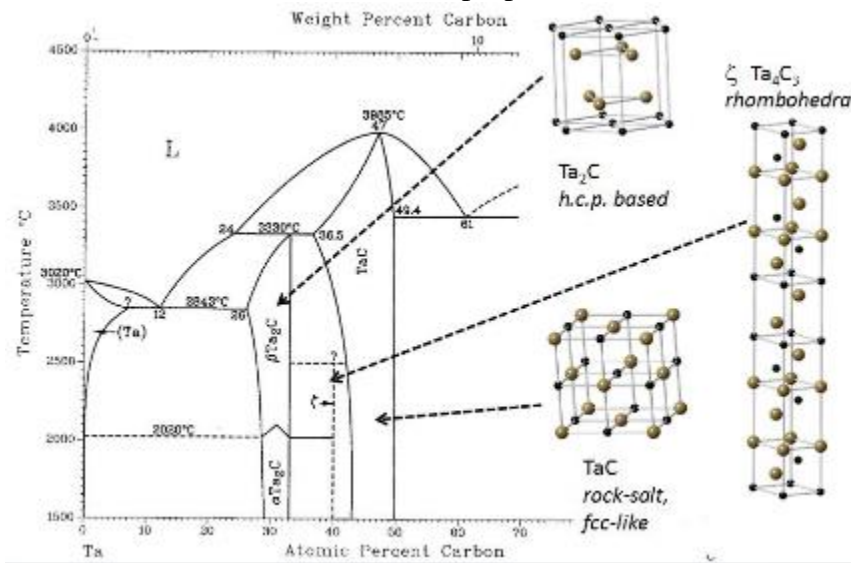


Figure 1. Phase Diagram

The peaks that are obtained from the X-Ray analysis of the different chemistries studied in this research are shown in (Figure 2). Note: composition C0 formed single phase  $Ta_2C$  while C6 formed single phased  $TaC$ . The composition inbetween C0 and C6 form multi phased alloys.

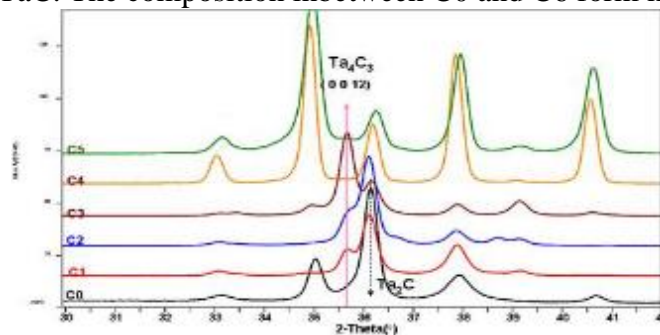


Figure 2. X-Ray Diffraction peaks for Tantalum Carbide

According to the mechanical testing done in this study both the processing and chemistry affects the microstructures of the material, as well as the strength and toughness (Figure 3 and Figure 4).

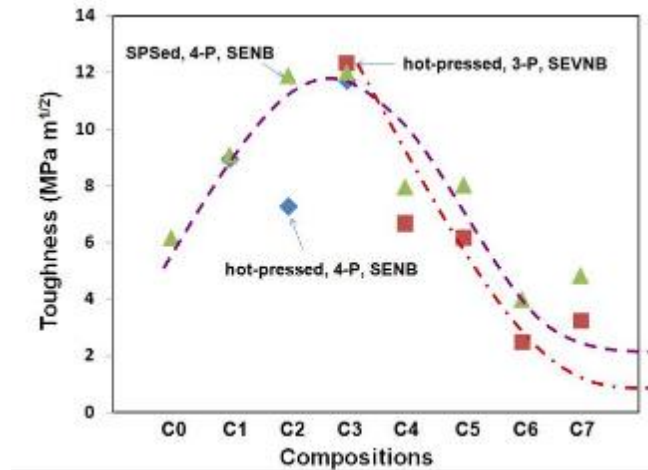


Figure 3. Bending Strengths of Tantalum Carbide by Composition

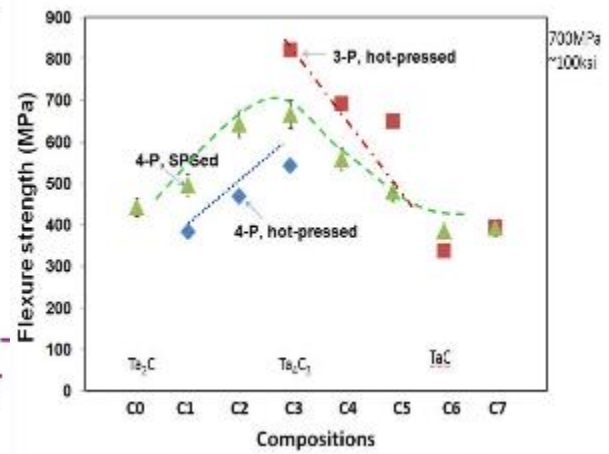


Figure 4. Fracture Toughness (KIC) of Tantalum Carbide by Composition

From Figure 3 and 4, one can see that composition C3, which contain high aspect ratio grains of  $Ta_2C$  and  $Ta_4C_3$  phases has the best strength and toughness of the alloys studied in this work. It is important to note that the toughness is one of the highest ever seen in a ceramic material.

## Conclusions

The results of this work showed that Ta-C based alloys could be made very strong and tough by alloying powders on the atomic level through a rapid solidification process called arc melting and rapid consolidation of the alloyed powders by the process called Spark Plasma Sintering. The composition with the highest strength and toughness was the C3 composition which contained acicular, high aspect ratio grains of  $Ta_2C$  and  $Ta_4C_3$  phases.

The equipment used in the study was: Arc Melter, shatter box, sieves, light microscopy, Scanning Electron Microscopy/EDS, X-Ray Diffractometer, Cool Isostatic Press (CIP), Spark Plasma Sintering (SPS) and a mechanical testing machine.

TRANSMISSION ELECTRON MICROSCOPY OF NANOSTRUCTURED MATERIALS

Project No. 0090

Andrew Aronow  
University of Dayton

22 August 2014

Government Project Leader  
Dr. Gail Brown  
AFRL/RXAN

Southwestern Ohio Council for Higher Education  
Student Research Program  
Agreement Number: FA8650-09-2-5800

## **Acknowledgements**

I'd like to give a sincere and very special thanks to the following for their help and support and for giving me such an incredible opportunity: Krishnamurthy Mahalingam, Dr. Gail Brown and Kurt Eyink

## **General Description of Project**

Transmission Electron Microscopy (TEM) is a microscopic process which utilizes the wave property of diffraction in order to view the diffraction pattern produced when a beam of electrons passes through a material. This diffraction pattern allows for visualization of the objects in question on an atomic scale, thus illuminating the crystalline structure of these materials, and providing information on their physical and electrical properties and allowing feedback on growth methods' effects.

## **Description of Research**

The purpose of the project at Wright-Patterson Air Force Base is to determine the best procedures of sample preparation for Transmission Electron Microscopy (TEM) in order to discover the structural properties of grown materials including Erbium Arsenide (ErAs) metal nano-particles and Indium Arsenide (InAs) Quantum Dot structures, and InAs/InGaAsSb superlattice structures. Viewing a material's crystalline structure with TEM requires a very thin (~100nm) film of the sample and obtaining this can be a highly complex task. Different materials/analyses require different procedures. This project has led to effective processes for the materials listed above. Ion beam milling was used to prepare both the cross-sectional and plane-view ErAs metal nano-particles and InAs Quantum Dot material, and Focused Ion Beam (FIB) Milling was used to prepare both superlattice and oxide materials. Reiteration has proved these methods to be highly effective at producing excellent TEM films.

Transmission Electron Microscopy (TEM) is a microscopic process which utilizes the wave property of diffraction in order to view the diffraction pattern produced. This diffraction pattern allows for visualization of the objects, which in this case are Erbium Arsenide metal nano-particles, Indium Arsenide quantum dot structures, InAs/InGaAsSb superlattices, and Iron oxides. TEM lets the operator view the crystalline structure of these materials, giving information on their physical and electrical properties and allowing feedback on growth methods' effects.



Figure 1: Titan Transmission Electron Microscope

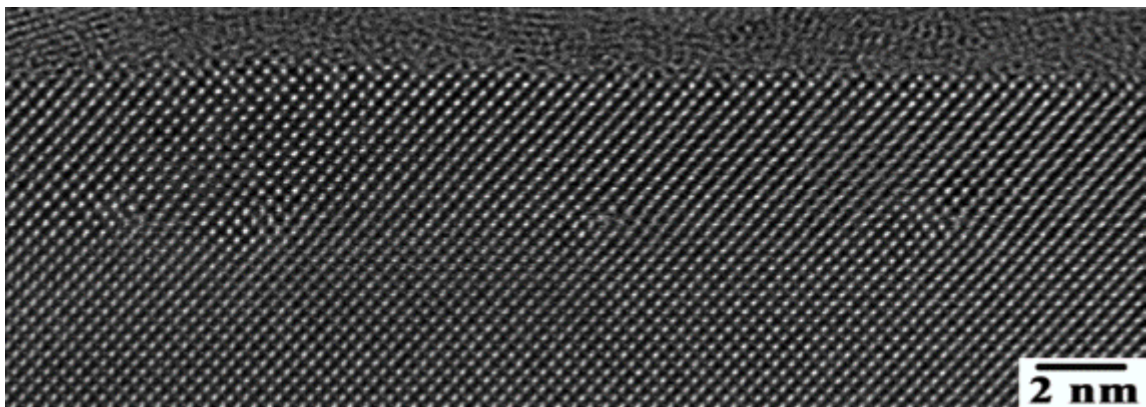


Figure 2: HRTEM image of an InAs epitaxial layer grown on GaAs showing formation of Lomer dislocations

Metal nanoparticles demonstrate the property of optical field enhancement. That is, when light shines upon a surface with metal nanoparticles, the light is enhanced near the metal nanoparticle. When a quantum dot is located within this field enhancement, increased absorption, emission, and optical non-linearities may be expected.

When InAs is grown in a metal rich environment, it grows in a planar configuration. In typical self-assembled quantum dot formation, as the layer thickens, the strain becomes too high and a quantum dot nucleates, relieving the strain and lowering the energy. But here, as the layer becomes thicker, dislocations are formed which prevent 3D growth. By nano-patterning this film, small regions of InAs are formed which have more material than needed to form a critical nuclei formed during self-assembly. Then by annealing with As, Quantum Dots develop from the nano-patterned regions.

A superlattice is a material made by the stacking layers of varying materials, and this project worked with primarily InAs/InGaAsSb. When the materials used are semiconductors, as these are, new unique semiconductor properties are exhibited by the superlattice.

## Results

Ion beam milling is the method most commonly employed for TEM sample preparation. It involves shooting ionized argon at a prepared sample, until enough of the sample is milled to be electron-transparent. The preparation is a labor intensive process, turning a sample into a 50 $\mu$ m thick slice made of four bars, similar to fingers of a flat palm, glued to a molybdenum grid.

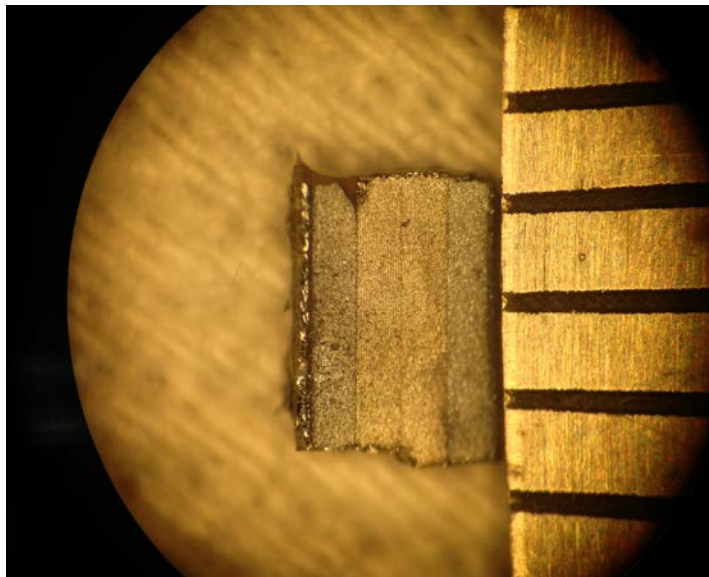
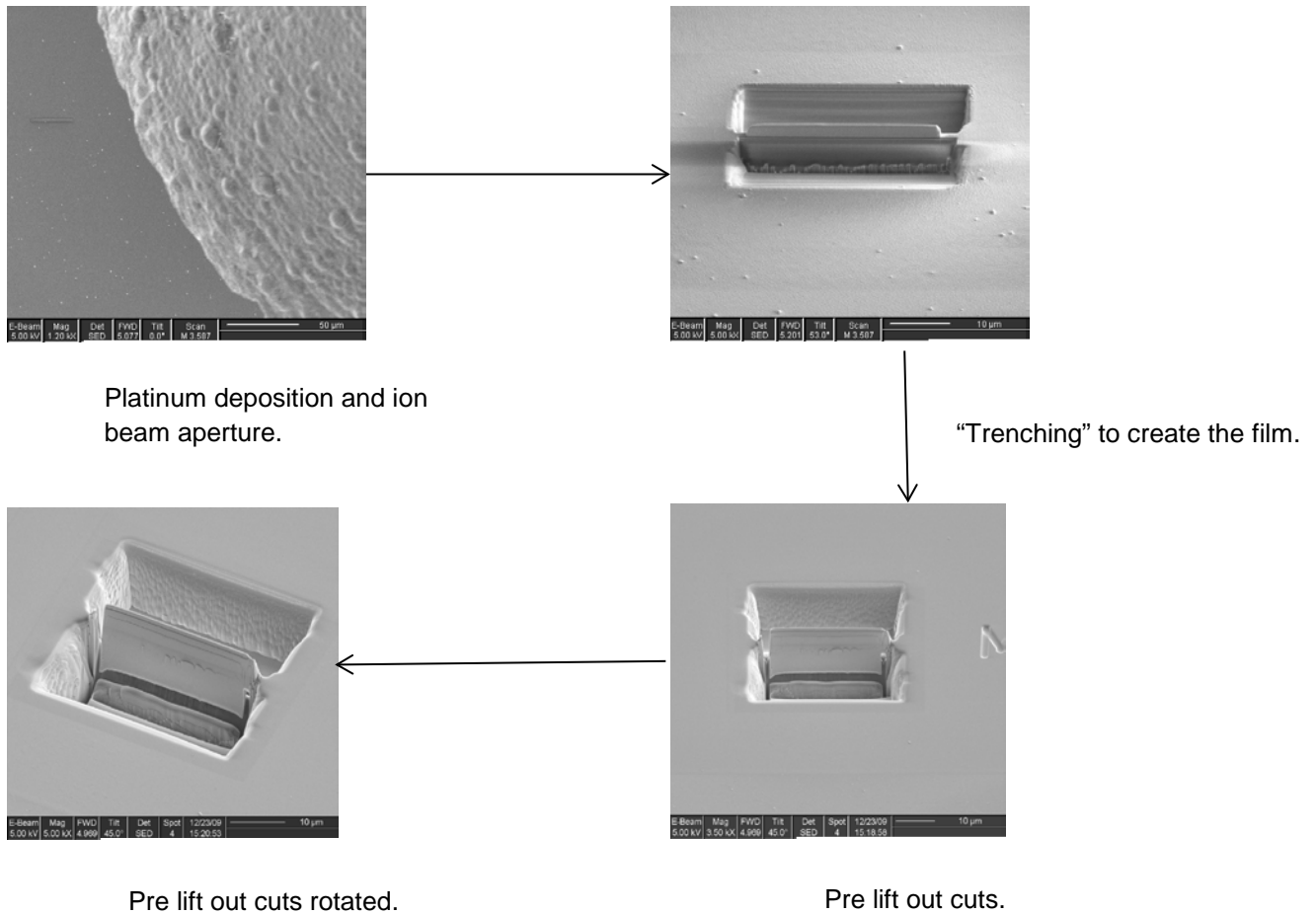


Figure 3: A slice of a cross-sectional stack next to a millimeter ruler.

Focused Ion Beam Milling (FIB), unlike ion beam milling, is a much less labor intensive process, but rather completely computer operated. The special thing about FIB is that it allows for highly selective positioning of the TEM foil, as its motors and ion guns are much finer than the hand. In the FIB, there are three major components: an ion gun, an electron gun, and a probe. Each of the guns has two purposes, milling/depositing and viewing, that is, each can fire at the sample and each can give sight as to what is happening with the sample. FIB's technique is as

such: The operator starts by putting in the sample, just as received, with the film side up. The operator then selects the region from which the film is desired and deposits platinum on top to protect the film. Material is then trenced out on both sides of the platinum cap, creating a wall that will become the foil. The operator then mills away the base and a side of the film, and attaches the probe to the sample by depositing platinum on both, positioned next to each other. The last remaining side of the film still attached to the sample is then cut, and the probe is lifted out, with the sample bonded. The sample is then attached to a holder, all still within the FIB, and final thinning is done, until the thickness measures to around 100 nm.

Figure 4: Focused Ion Beam (FIB) Milling's sequence



The project has demonstrated and expounded upon the effective methods for preparing samples for Transmission Electron Microscopy, allowing a more complete understanding of the physical and electrical properties of the materials other researchers are growing.

CHEMIST

Project No. 0097

Mallory Lyle  
Wright State University

31 August 2014

Government Project Leader  
Mr. Max Alexander  
AFRL/RXCC

Southwestern Ohio Council for Higher Education  
Student Research Program  
Agreement Number: FA8650-09-2-5800

## **Acknowledgements**

I would like to thank Wright-Patterson Air Force Base and the Southwestern Ohio Council for Higher Education (SOCHE) for collaborating together and allowing me the opportunity for this experience. More specifically, I would like to thank Brittany Edwards for facilitating my SOCHE employment, as well as Max Alexander for acting as my government POC and guiding me through my research. I would also like to thank the professional guidance of Dr. Tom Ekiert, Dr. Garth Wilks, Dr. Klint Simon, and Dr. Matt O'Malley. Lastly, I would also like to acknowledge my past and present co-workers for their continued support: Angela Griner, Cory Flynn, Brandon Yocum, Jennifer Lippold, Ashley White, Anna Porter, Benjamin Wilson, and Brittany Campbell.

## **General Description of Project**

*From Project Description*

*AFRL/RXCC requires an undergraduate/graduate chemist or materials engineer to support developing technologies to produce smaller, lighter and more sensitive antennas. To meet these goals nanocomposite materials with low electrical losses & independently tailoring permeability & permittivity are desired. Obtaining such systems is key to enhancing conformal antenna gain, reducing antenna aperture size & improving bandwidth control. In this effort the student will produce high aspect ratio magnetic oxide nanoparticles which will be subsequently aligned. These materials will be produced using microwave synthesis techniques.*

Magnetic oxide nanoparticles were synthesized using solvothermal decomposition via microwave techniques. Once the particles were synthesized, they were characterized using a variety of techniques, included X-ray diffraction, transmission electron microscopy, scanning electron microscopy, and superconducting quantum interference device. The particles were then utilized in a composite for further testing.

## **Description of Research**

It has recently been found that the magnetic properties, crystallinity and chemical behavior of magnetic iron oxide nanoparticles can be very useful in a variety of fields, including some medical applications, frequency-focused devices and antenna substrates. Currently, there are a variety of different methods through which these particles can be synthesized, the newest and most uninvestigated being microwave synthesis. This study aims to discover a potential trend between microwave synthesis time and particle size and crystallinity of both iron ferrite and cobalt ferrite magnetic nanoparticles, with initial thoughts being that increased microwave time would increase both particle size and crystallinity. Results of the study show that while both types of particles do increase in size over time, the maximum size is seen for iron ferrite nanoparticles at 10 and 30 minutes and 120 minutes for cobalt ferrite nanoparticles. These results correspond with the crystallography data, namely that the most ideal crystallinity is achieved at these times.

In recent years, magnetic iron oxide nanoparticles have shown to be of interest in a variety of fields due to their unique behavior, crystallinity and magnetic properties. Currently,

these nanoparticles have shown to be useful in electronics, namely frequency-focused devices, biosensors, medical diagnostics and drug delivery, as well as antenna substrates. The specific application of the nanoparticles depends on the type of metal incorporated in the crystal structure of  $MFe_2O_4$ , as the “M” metal affects the magnetic properties of the particles, namely permeability, permittivity and resistivity [2,273]. Magnetic nanoparticles are also of interest because of their low cost of production as well as their relatively simple synthetic means in some cases [1,1].

At present, there are several different methods through which magnetic nanoparticles can be synthesized. The first is through co-precipitation methods [1,1], typically involving aqueous metal salt solutions followed by the addition of a base [3, 1228]. The second is through solvothermal decomposition, usually involving an organometallic compound or compounds dissolved in a high boiling point organic solvent and reacted at high temperature and pressure for a given time [3, 1228].

Solvothermal decomposition is unique in that there are many different vessels that can be used in order to generate the high temperature and pressure needed to create nanoparticles. A Parr reactor is the most common vessel for synthesis, and while the particles are well-behaved, the reaction time needed is much too long. The use of microwave techniques in order to create the necessary thermal conditions is currently being investigated, as it serves as a quicker and simpler way to synthesize nanoparticles. This paper focuses on the synthesis of ferrite and cobalt ferrite nanoparticles using fixed precursor properties and microwave methods over varying times.

$Fe_3O_4/\gamma-Fe_2O_3$  and  $CoFe_2O_4$  nanoparticles were synthesized by microwave assisted solvothermal decomposition of iron (III) acetylacetonate ( $Fe(acac)_3$ , Sigma Aldrich, 97%) and cobalt (II) acetylacetonate ( $Co(acac)_2$ , Sigma Aldrich) in benzyl alcohol (Sigma Aldrich,  $\geq 99.0$ ). All chemicals were used as received without additional purification.  $Fe_3O_4/\gamma-Fe_2O_3$  ( $CoFe_2O_4$ ) nanoparticles were produced by placing 1.00 gram of  $Fe(acac)_3$  (0.2667g  $Co(acac)_2$  and 0.7332g  $Fe(acac)_3$ ) to 20mL of benzyl alcohol under mild stirring and allowed to stir continuously for four hours. Aliquots of 5mL were removed from each solution and placed in 10mL glass microwave vials with a magnetic stir bars. The resulting solutions were microwave heated at 175 °C for varying times with max power and pressures of 300 Watts and 250 psi, respectively. The resulting nanoparticles were washed three times with ethanol via centrifugation at 8,000 RPM, then allowed to dry under ambient conditions.

The crystal structure and Scherrer size were determined by powder X-ray diffraction (XRD) using Rigaku D/Max 2500 (50 kV, 300 mA) equipped with a graphite monochromator, selecting  $Cu K\alpha_{1,2}$  radiation ( $\lambda = 1.54178 \text{ \AA}$ ) with a step size of  $0.05^\circ$  and a scan rate of  $2^\circ/\text{min}$ . Particle size and morphology were analyzed by transmission electron microscopy (TEM) performed with a Philips CM200 equipped with a  $LaB_6$  cathode operated at 200 kV. TEM samples were prepared by adding a small amount of material to heptanes with a small addition of decanoic acid then sonicated for 5 min. A few drops of the resulting suspension were then placed on an ultrathin carbon film on holey carbon support film copper TEM grids. Magnetic measurements were performed via a Quantum Design MPMS-XL7 Superconducting Quantum Interference Device (SQUID).

## Results

As one can see in Figure 14, the crystal structure for the  $\text{Fe}_3\text{O}_4$  and  $\text{CoFe}_2\text{O}_4$  crystallites is Spinel for nearly all reaction times. However, Figure 14a shows that while a five minute reaction time does yield  $\text{Fe}_3\text{O}_4$ , the product has not yet reached a Spinel crystallinity structure. Comparing the five-minute reaction in Figure 14a to that in 14b, it is noticed that  $\text{CoFe}_2\text{O}_4$  reaches a completely Spinel structure even after such a short reaction time, while  $\text{Fe}_3\text{O}_4$  crystallites need a minimum of ten-minutes of heating in order to form Spinel crystallinity. In Figure 14a, the sharpest and thinnest peak is at both the 10 minute and 30 minute reaction mark, indicating that crystallites at this time will be the largest. After this time, the peaks in Figure 14a begin to broaden again, indicating that the crystallites are becoming smaller while still maintaining the same crystal structure. In Figure 14b, the patterns indicate that the largest crystallites for  $\text{CoFe}_2\text{O}_4$  system will be seen at the 120 minute mark, as referenced by the peak sharpness. Figure 14b also indicates that the crystallites are steadily growing larger as reaction time increases, as seen by the subtle change in peak breadth from sample to sample.

The XRD data in Figure 14 can be well-tied into the TEM images seen in Figure 15. The particles in Figure 15a are that of a five minute reaction yielding  $\text{Fe}_3\text{O}_4$ . The relatively uncontrolled size and shape of these particles is reflected in the corresponding XRD pattern in Figure 14a. More specifically, the particles have not yet reached a consistent crystal structure, resulting in very small (see Figure 14) particles with some agglomerations. The five-minute reaction yielding  $\text{CoFe}_2\text{O}_4$ , as seen in Figure 15d, results in rounder and more well-defined particles as referenced by the respective XRD pattern in Figure 14b. The remaining pictures in Figure 15 are consistent with their corresponding XRD patterns, namely that the two systems have formed Spinel crystalline particles. Also, the particles in Figure 15b are smaller than those in 2c, as the XRD beak breadth supports. The same relationship holds for the Figures 15e and 15f, with the particles in image 15f being slightly larger than those in Figure 15e, as illustrated by the major XRD peak size and shape in Figure 14b.

Table 1 summarizes the relationship between TEM and XRD characterization through the use of X-fit analysis and particle sizing. The XRD patterns of  $\text{Fe}_3\text{O}_4$  and  $\text{CoFe}_2\text{O}_4$  in Figure 14 show that the largest particles should be seen at the 10/30minutes and 120 minute reaction marks respectively. X-fit analyses of these patterns indicate that the largest particles are seen at these times, as referenced in Table 1. This idea is supported by TEM image particle sizing, as the largest particle sizes are recorded at the above mentioned times, also referenced by Table 1. Lastly, the size trend of  $\text{Fe}_3\text{O}_4$  and  $\text{CoFe}_2\text{O}_4$  nanoparticles as reaction time increases is also supported by the data in Table 1. More specifically, as time increases,  $\text{Fe}_3\text{O}_4$  nanoparticles start at their smallest size at 5 minutes, increase to the largest size at 10 and 30 minutes, and then decrease in size at later times. For the  $\text{CoFe}_2\text{O}_4$  system, particles gradually increase in size as time increases, with the largest particles being seen at 120 minutes. Though the relative size measurements of the particles for XRD and TEM analysis do appear to vary from one another, the nature of the two respective sizing processes allow for this variance and deviation.

Figures and Tables

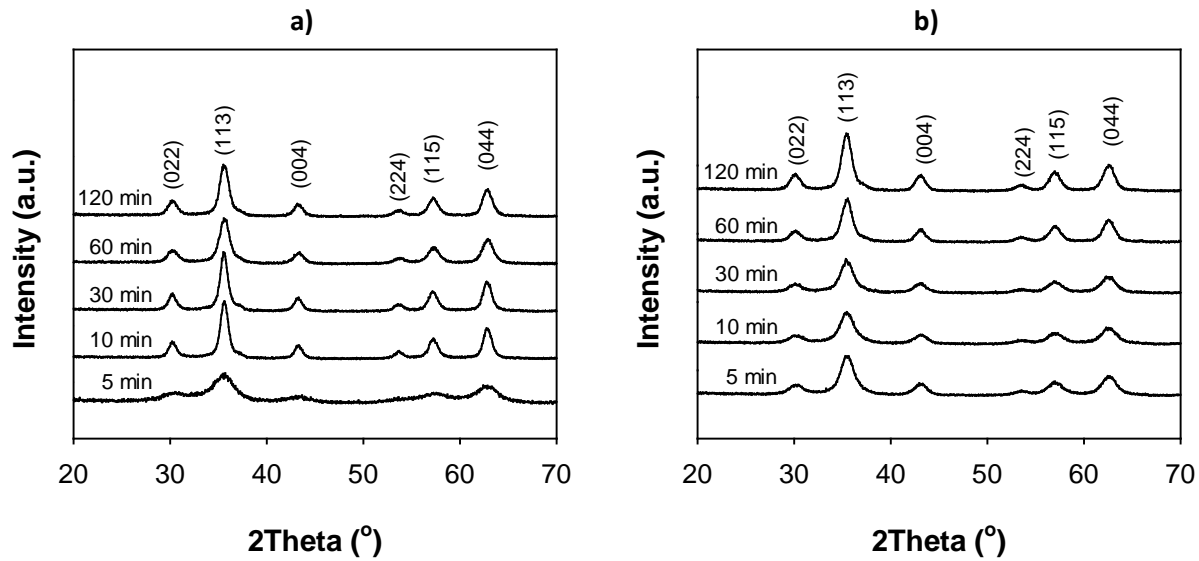


Fig. 14: XRD results for  $\text{Fe}_3\text{O}_4$  (a) and  $\text{CoFe}_2\text{O}_4$  (b)

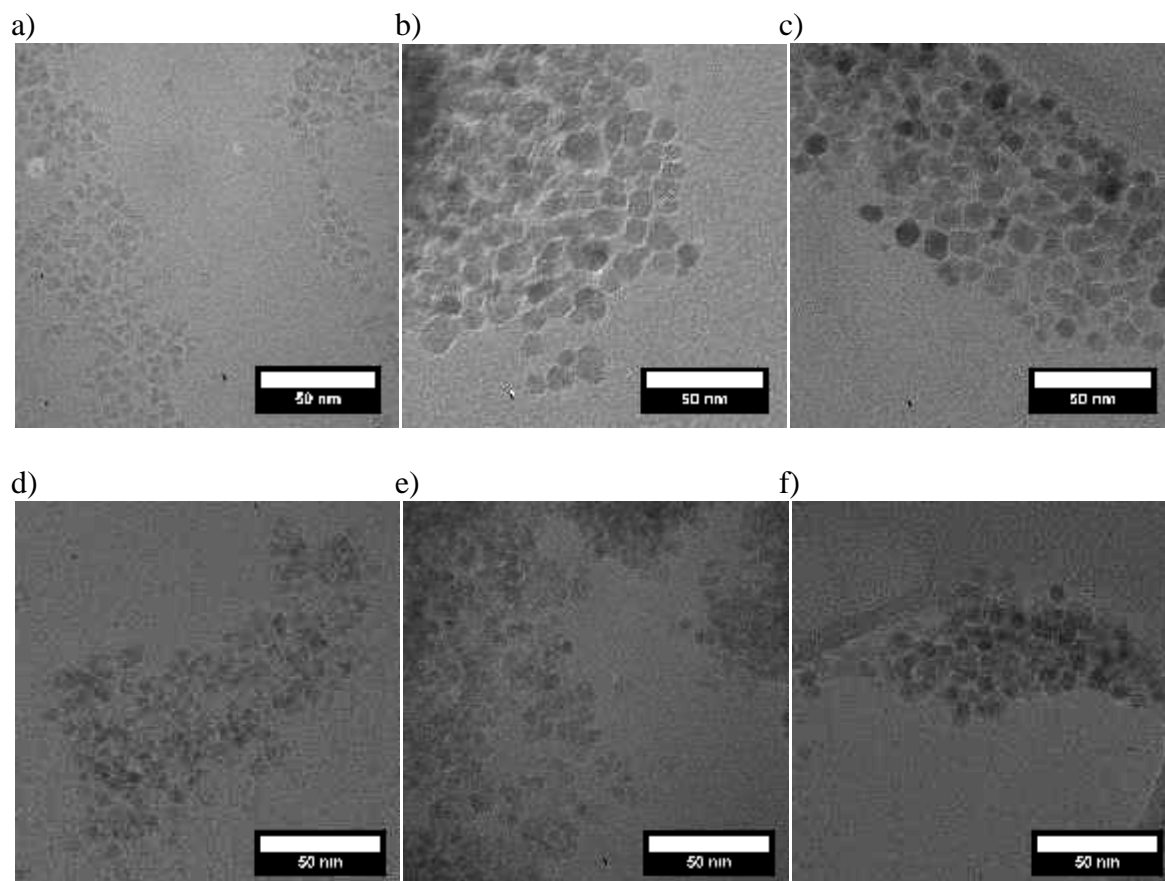


Fig. 15: TEM images for  $\text{Fe}_3\text{O}_4$  (a, b, c) and  $\text{CoFe}_2\text{O}_4$  (d, e, f) at 5 minutes (a,d), 30 minutes (b,e) and 120 minutes (c,f)

**Table 1:** Yield, XRD, TEM and Magnetic Analysis Values for for Fe<sub>3</sub>O<sub>4</sub> and CoFe<sub>2</sub>O<sub>4</sub>

Time	Fe <sub>3</sub> O <sub>4</sub>						CoFe <sub>2</sub> O <sub>4</sub>					
	Yield (g/vial)	XRD		TEM	M <sub>s</sub>	H <sub>c</sub>	Yield (g/vial)	XRD		TEM	M <sub>s</sub>	H <sub>c</sub>
	a(Å)	∅ (nm)	∅ (nm)	emu/g (300K)	Oe		a(Å)	∅ (nm)	∅ (nm)	emu/g (300K)	Oe	
5min	0.0462	8.34 (6)	2.9(7)	5(1)	21.7(5)	0.2(5)	0.0267	8.3(1)	2.4(6)	5.7 (7)	54(1)	0.8(5)
10min	0.0410	8.359(5)	9.8(4)	12 (3)	57.1(6)	0.4(5)	0.0435	8.39(1)	5.6(3)	5.3 (9)	48.5(9)	0.8(5)
30min	0.0287	8.366(3)	9.7(4)	11 (3)	57.4(7)	0.5(5)	0.0173	8.395(6)	5.9(2)	5.7 (7)	51(2)	0.9(5)
60min	0.0402	8.355(5)	7.4(3)	8 (2)	50.9(9)	0.4(5)	0.0097	8.393(5)	7.4(3)	7.0 (9)	62(1)	2.8(5)
120min	0.0494	8.360(5)	8.5(3)	9 (2)	54.2(5)	0.5(5)	0.0186	8.396(4)	7.5(2)	6.5 (9)	67(1)	4.1(5)

### Works Cited

1. Ajroudi, L., S. Villain, V. Madigou, N. Mliki, and Ch. Leroux. "Synthesis and microstructure of cobalt ferrite nanoparticles." *Journal of Crystal Growth* 312: 2465-2471. Web. 29 July 2014.
2. Schüth, Ferdi, An-Hui Lu, and EL Salabas. "Magnetic Nanoparticles: Synthesis, Protection, Functionalization, And Application." *Angewandte Chemie International Edition* 46: 1222-1244. Web. 29 July 2014.
3. Sun, Shouheng, Hao Zeng, David Robinson, and Simone Raoux. "Monodisperse MFe<sub>2</sub>O<sub>4</sub> (M = Fe, Co, Mn) Nanoparticles." *Journal of the American Chemical Society* 126: 273-273. Web. 29 July 2014.

EXCHANGE-SPRING COMPOSITE MAGNETS WITH HIGH ENERGY PRODUCT

Project No. 0099.2

Matthew Edge  
Wright State University

31 August 2014

Government Project Leader  
Dr. Lee Semiatin  
AFRL/RXCM

Southwestern Ohio Council for Higher Education  
Student Research Program  
Agreement Number: FA8650-09-2-5800

## **Acknowledgments**

I would like to thank several different people who have been extremely helpful during my work here at WPAFB. The project I have been working on has been a cross directorate program with both RX and RQ, and I have received help from individuals in both directorates. I would like to thank my mentor Dr. Horwath of RQ for helping me to settle in and teaching me many invaluable aspects of research work as well as daily government works tasks. I would also like to thanks Dr. Semiatin of RX for helping me to process in with RX and helping to obtain me lab access. I would also like to thank all the contractors and government personnel in RQ who have assisted me in this project, including Alex Sheets, Serhiy Leontsev, Zafer Turgut, and Helen Shen.

## **General Description of Project**

During this project the main object was to research and find new combinations of materials that can be used to produce magnets that will have characteristics comparable to that of current rare earth magnets. This is an important goal because of the wide use of these types of magnets in most all power systems and electronics in use today. The current supply of rare earth magnets comes almost exclusively from China and is subject to unexpected changes in price and supply numbers. To combat this, it is essential to find a way to get away from this dependence on rare earth magnets by developing suitable replacement materials, something that is being researched at WPAFB.

## **Description of Research**

To complete this research several different subset projects were worked on. One of these projects was the analysis of treating iron oxide powders to try to produce a fairly strong magnetic material. The main goal of this project was to infuse the iron powder with nitrogen, which is believed to improve the magnetic properties. This was done by taking ordinary iron oxide powder and treating it in a several step process to see what different properties would result. The powder was first heated in a tube furnace while running hydrogen over it for a set length of time and then further treating this powder in the tube furnace while running ammonia, which contains nitrogen, over it. After this the material was then milled in a mixer/mill for a total of 2 hours in order to see how this would affect the grain size. All of this was done in an environment that was free of oxygen, in order to prevent oxidation of the iron. To complete this project, a tube furnace was needed for the heat treatment, a glove box to prepare samples after treatment, a mixer/mill to mill the samples, and an x-ray diffraction machine (XRD) and scanning electron microscope (SEM) to analyze the results. After preparing the samples in the tube furnace and mill they were analyzed using XRD to see the elements present and the SEM to see the structure of the powder.

Another project worked on during this summer was preparing a pulse magnetizer system to magnetize any powders that needed their magnetic domains aligned. The pulse magnetizer was created from an already existing bank of high voltage capacitors that were capable of delivering high voltage and current pulses that are in the micro second range. To modify the system to magnetize materials, calculations first had to be done to see what type of solenoid and level of current would be necessary to create the correct magnetic field needed of approximately

5-10 Teslas. After the calculations were finished and the solenoid made, the current bank was fired to assure that it was in working order. Then a sample coil was used with two rare earth magnets placed inside and a pulse was sent through it to see if it would realign the magnets as it was supposed to. The pulse itself was monitored using fiber optics and an oscilloscope.

The last project worked on over the summer was the preparation of more powders to develop magnetic materials. This project consisted of combining iron and nickel powders and then combining that mixture with a samarium and cobalt mixture. To combine the iron and nickel, they were first measured out to the correct atomic ration and then placed in an arc melter, an instrument that melts materials together using high currents. This formed a button of metal which was then placed in a rolling mill and flattened. Then the flat ribbon was cut into small pieces and run in a mixer/miller machine. To mill this material it was mixed with liquid chemicals, to aid in the milling process, and a ratio of small milling balls, this was then put into the mixer/miller which vibrates the sample for a set amount of time. Samples of the material were taken out for analysis at set intervals of 4, 8, 12, and 16 hours. After the material was milled each of the samples taken out at different times was then prepared for analysis by both the SEM and XRD. The material was then analyzed using these two methods. The mixture of this material with the samarium cobalt is ongoing currently.

## **Results**

From the first project worked it was found that the treatment did not result in a significant change in the elements of the iron oxide. The flakes that were seen under SEM were not the size and shape that was desired, and from the XRD results shown in figures 1, 2, and 3 it can be seen that there are no additional peaks showing any presence of nitrogen. All three of the figures have peaks at the same places, while if there was nitrogen present then in figure 3 there would be additional peaks. The conclusions from this are that the method of preparing the samples resulted in no detectable nitrogen, and therefore a different treatment method will have to be tried. A different treatment method of heat treating at different temperatures and replacing the milling with sonication to break up the samples is currently being tried, but no results are yet available.

For the pulse magnetizer the test results showed that the solenoid made would align the magnetic poles of some samples magnets. The solenoid made was not insulated well enough though and there was dielectric breakdown of the insulation between the windings. This solenoid was rewrapped with two layers of insulation and is currently being tested. Whether or not it will work for some of the powders needed to be aligned remains to be seen, as the project is still being completed.

For the last project with the iron nickel and samarium cobalt, figures 4 and 5 showed what ball milling time was optimum for the production of the correct flake sizes, and the XRD showed what ball milling time produced the correct sized flakes for the application they would be used for. It was found that the ball milling time of 8 hours, the results of which are seen in figures 4 and 5, produced the most optimum flake size and structure, and is being used to combine with the samarium cobalt powders. This powder is smooth and small enough so it will bond well with the samarium cobalt. The project is still ongoing at the present time.

**Figures & Tables**

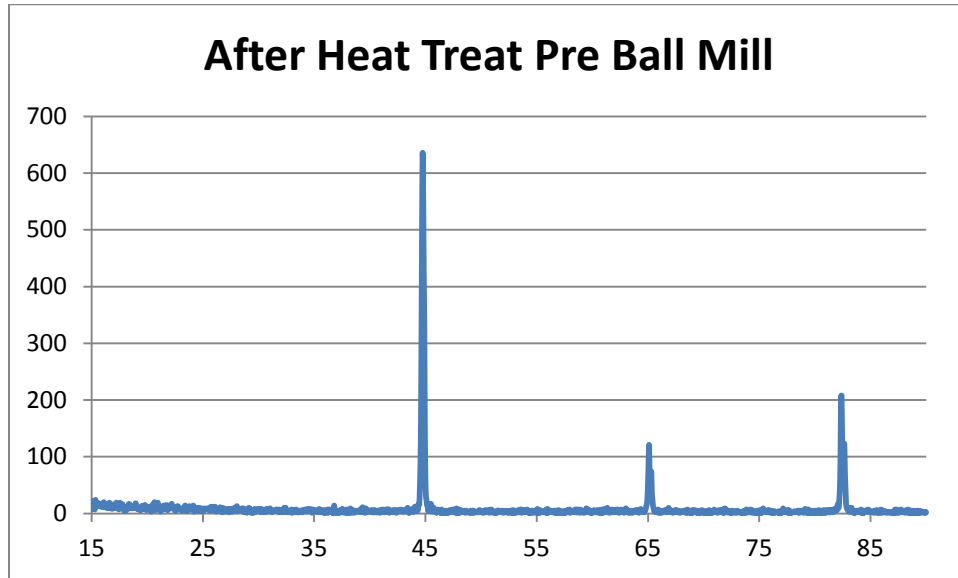


Figure 1. XRD results of iron oxide powder after first heat treatment with hydrogen.

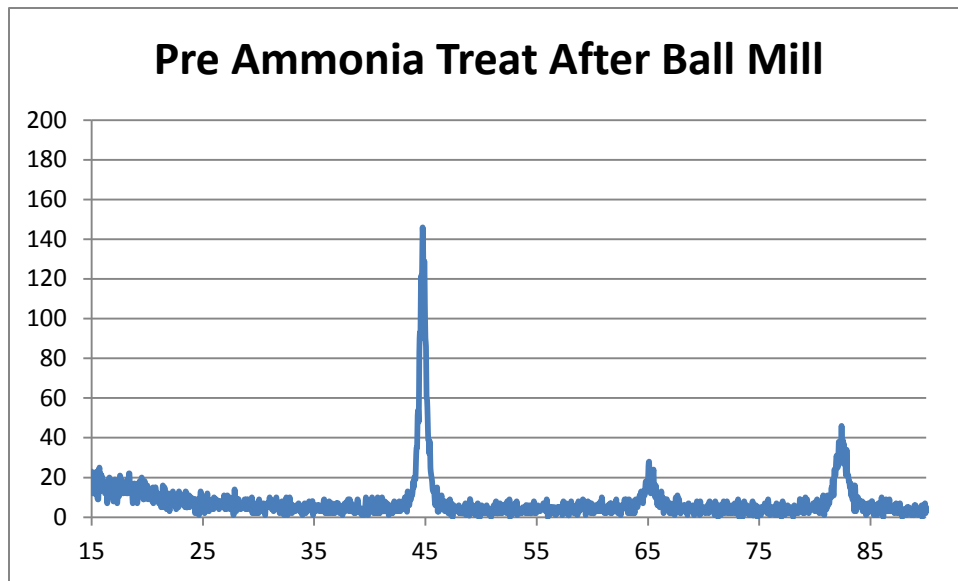


Figure 2. XRD results of iron oxide powder after first heat treatment and milling for 2 hours.

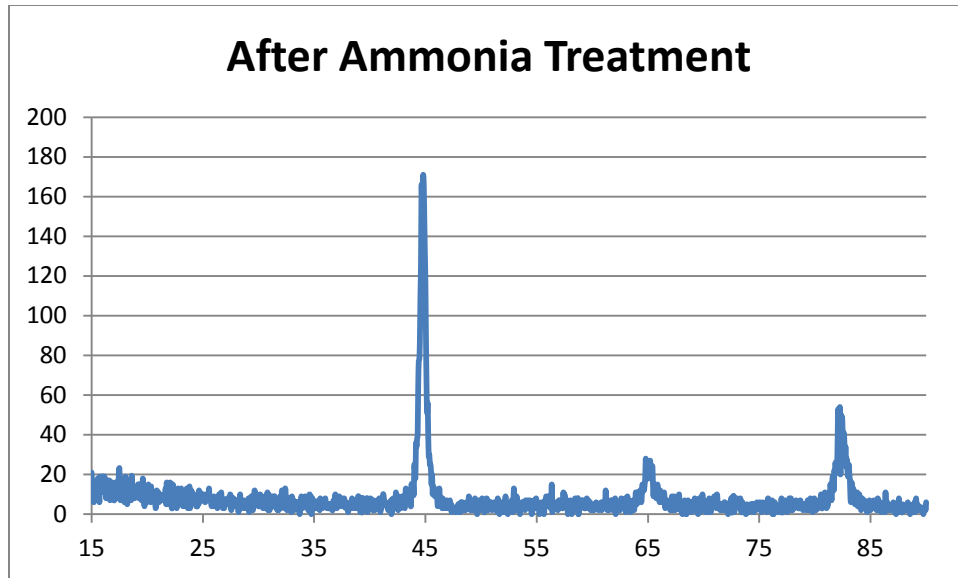


Figure 3. XRD results of iron oxide powder after second heat treatment with ammonia.

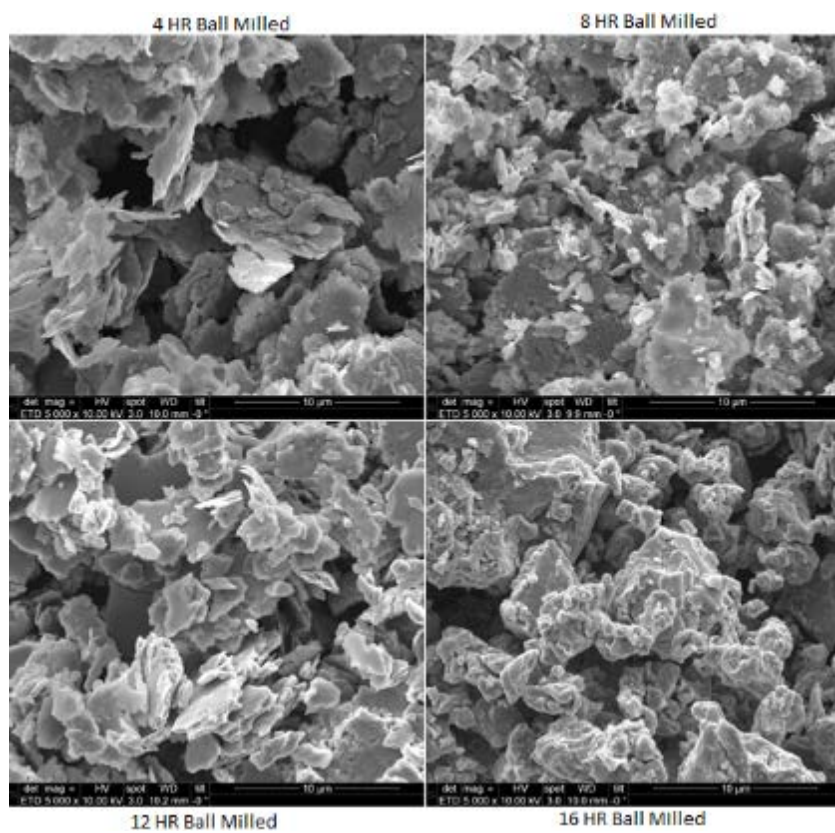


Figure 4. SEM results of iron nickel powder after ball milling treatments.

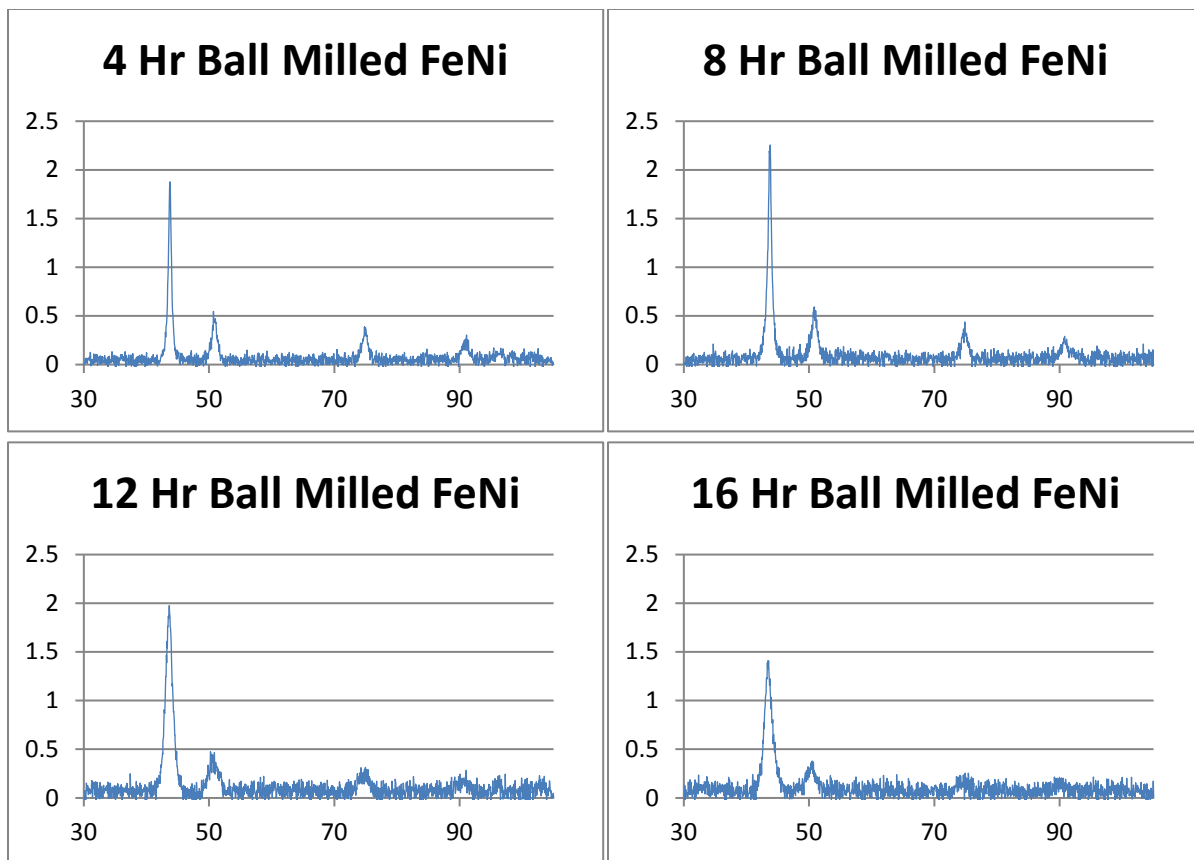


Figure 5. XRD results of iron nickel powders at different ball milling times.

MATERIALS INTEGRITY BRANCH SUPPORT

Project No. 0101

Jordan Speers  
Wright State University

31 August 2014

Government Project Leader  
Mr. Steve Thompson  
AFRL/RXSA

Southwestern Ohio Council for Higher Education  
Student Research Program  
Agreement Number: FA8650-09-2-5800

## **Acknowledgements**

I would like to thank Chuck Wagner who initially hired me and has since retired living the good life. He stuck his neck out for me and opened the door for this great opportunity. I am thankful for Mary Ann Phillips who is now my current branch chief and has continued to fight and secure funds for my position so that I was able to continue my education in the lab. Next on my list of thanks is Steve Thompson who pleaded my case with management and fought to allow my contract extensions which also allowed my continued presence in the lab. Nick Jacobs is the lab engineer who patiently answered all my questions and guided me throughout my lab time. He was the engineer who helped me dive deeper into an understanding of the lab and what it is we do. Ken Combs is the lead lab technician who took baby steps with me as I began understanding the lab needs and he was also patient with me as I developed the testing skills needed to become a good engineer. I must also thank Brittany Edwards for all her hard work and dedication as she has painstakingly monitored all my times and paperwork needed to keep this a seemingly easy job to have. In many ways thank you seems to be an easy way out as I believe I owe all these individuals much more than a thank you.

## **General Description of Project**

Lab equipment was moved, rebuild, and reorganized to better assist materials testing. Test machines were serviced and positioned in a way that help the lab's technician's complete day to day activities in a timely and organized manner.

## **Description of Research**

Once the lab was rearranged and set up was complete testing of various materials was performed using screw driven mechanical test machines as well as servo hydraulic machines. Materials were tested in a number of ways according to ASTM test standards. Each and every material tested, in one way or another, directly impacted the safety and sustainability of the Air Force and its airmen. Each test had its own set of required data and outcomes to complete the testing. The data from the test was compiled and analyzed with the help of Microsoft Excel. Some test and programs required additional analysis and graphs which were used to better understand the physical properties of the material. A standalone software program entitled Grapher was used for graphing needs. Mechanical screw driven machines were used in testing the tensile strength of the materials. The tensile test is normally the first test run on a material. It helps determine the static strength which is used in calculating the stresses needed in component design. Servo hydraulic test machines were utilized in fatigue testing due to their ability to run at high cyclic frequencies. Fatigue testing is used to determine the length of time a certain material can withstand a certain load prior to failure. It helps in making calculated decisions on how long an aircraft can be used before maintenance and repairs will need to be made.

## Results

Due to the nature of the contract one specific project wasn't seen from start to finish. A number of different materials were tested and observed for a number of different applications. One such material tested was a two ply composite. The composite was blasted with Wheat Starch to remove paint. There were different pressures used to determine the optimal pressure that had the most effect while causing the least amount of damage. This was proven by putting new composite material through a tensile test and then placing composite that had been blasted through the same process of testing. The results showed very similar ultimate strengths with minimal variance. Figure 1 shows the results of the tensile test of three un-blasted test specimens and three blasted specimens with Wheat Starch. The first three (1-3) specimens are the un-blasted and the last three (4-6) are blasted. The lines are very hard to tell apart proving a very similar strength. Stress is on the Y-axis and the strain is on the X-axis.

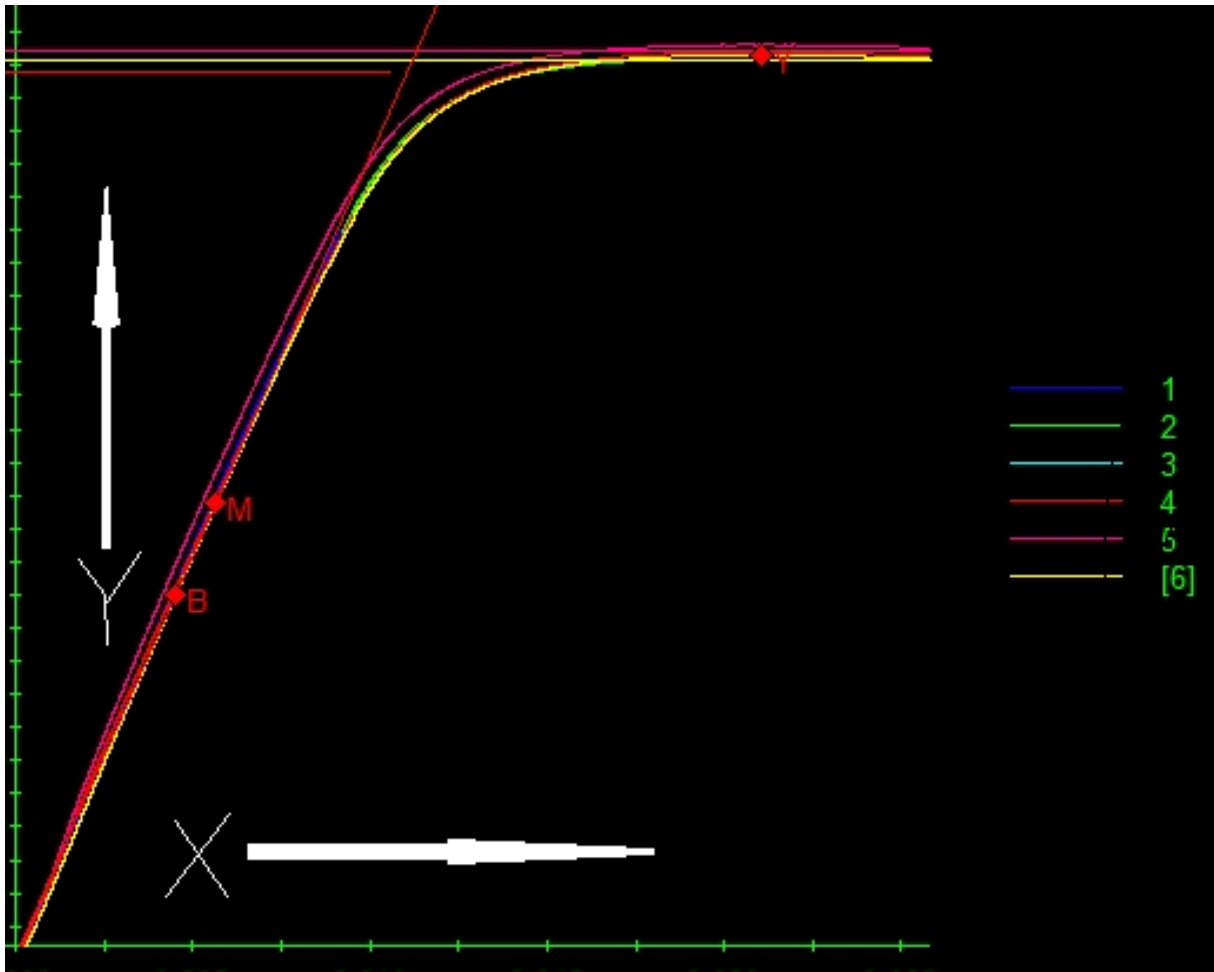


Figure 1: results of the tensile test

EM MATERIALS ENGINEER

Project No. 0105

Anna Porter  
Wright State University

13 August 2014

Government Project Leader  
Mr. Max Alexander  
AFRL/RXCC

Southwestern Ohio Council for Higher Education  
Student Research Program  
Agreement Number: FA8650-09-2-5800

## **Acknowledgments**

I would like to thank the members of my research group whom I collaborated with including Dr. Thomas Ekiert, Brandon Yocum, Brittany Campbell, Benjamin Wilson, Cory Flynn, Angie Griner, Jennifer Lippold, Ashley White, Mallory Lyle, Capt. Theodore Shillig, Dr. Garth Wilks, and Dr. Gerard Simon. I would like to extend a special thanks to Max Alexander for giving me the opportunity of working with this research group. I appreciate the training I received on various instrumentation from Dr. Thomas Ekiert, Scott Apt, Laraba Kendig, Bob Wheeler, and Benjamin Wilson. I would also like to extend great thanks to SOCHE for providing this student research program, and the guidance and leadership Marcia Hutcheson and Brittany Edwards provided.

## **General Description of Project**

The ultimate goal of this project was to produce flexible composite materials that had both high and tailorable permittivities and permeabilities based on sample thickness, particle loading fraction, and particle size. These composite materials hold many possible applications, including the miniaturization of antennas, and incorporation into other microwave devices. By modifying the permittivities and permeabilities of a composite, it is possible to improve the signal gain, reduce reflective losses, decrease antenna size, and increase the bandwidth. Composite samples were first manufactured by loading Polydimethylsiloxane (PDMS) with iron oxide ( $\text{Fe}_3\text{O}_4$ ) from Sigma Aldrich, and once the technique was perfected, composites were manufactured using cobalt iron oxide ( $\text{CoFe}_2\text{O}_4$ ) particles synthesized in house. These particles had been produced via solvothermal decomposition techniques by another group member.

## **Description of Research**

The production of PDMS composites loaded with  $\text{Fe}_3\text{O}_4$  were carried out using a Thinky centrifugal mixer. The PDMS contained two parts, a base and a curing agent. To prevent early curing (due to the heat produced while mixing in the Thinky), the  $\text{Fe}_3\text{O}_4$  powder was added and mixed into the base prior to adding the curing agent. The base and  $\text{Fe}_3\text{O}_4$  particles were mixed in the Thinky for five minutes at 1500 rpm, then defoamed for five minutes at 1500 rpm. Curing agent was added to the base and  $\text{Fe}_3\text{O}_4$  mixture, and mixed in the Thinky for five minutes at 1500 rpm, then defoamed for another five minutes at 1500rpm. This procedure was carried out with  $\text{Fe}_3\text{O}_4$  particles that were  $<5\mu\text{m}$  and  $<50\text{nm}$  in size. The amount of  $\text{Fe}_3\text{O}_4$  added to each composite was calculated by volume percent loading fraction. The composites loaded with in house particles were prepared with a different method. Upon production of the  $\text{CoFe}_2\text{O}_4$ , the particles were coated in decanoic acid, and volumetrically separated into heptanes. This mixture was then added to the PDMS base, mixed and defoamed in the Thinky for five minutes each, at 1500 rpm. This mixture was then left in an oven at  $50^\circ\text{C}$  to cure.

## **Results**

Upon curing of the composites loaded with  $\text{Fe}_3\text{O}_4$ , it was determined that the method of production best fits composites with an  $\text{Fe}_3\text{O}_4$  volume loading fraction of 10 percent or less, due to the amount of bubbles produced with loading fractions above this. These composites were produced at thicknesses of 3mm and 8mm, and their permittivity and permeability were measured in a Network Analyzer. Pictures were also taken with an optical microscope. It was found that diluting the PDMS with heptane resulted in a composite with no bubbles, if not over diluted (PDMS does not cure if diluted too much), but presented a problem with particles gravitationally separating to the bottom. Dry particles were attempted to be coated with decanoic acid in order to better suspend the particles, but was relatively unsuccessful. The in house  $\text{CoFe}_2\text{O}_4$  particles were coated in decanoic acid immediately after production, in the yielding solution. This method was very successful in providing particles that were coated in decanoic acid, most likely due to the fact that the particles were not dried. The composites produced with these decanoic acid coated  $\text{CoFe}_2\text{O}_4$  particles were of fairly decent quality, and the particles were fairly evenly dispersed. Again, it was important to not use excessive amounts of heptane in the mixture, since this produces composites that don't cure, and were most likely to have settled particles. Excess heptane containing the  $\text{CoFe}_2\text{O}_4$  was allowed to evaporate off so the PDMS was not excessively diluted. The composites produced with the in house particles were free of bubbles, and the particles were mostly evenly dispersed. These samples have the potential to be tested for permattivity and permeability measurements in the future.

SINGLE-CRYSTAL MICROSTRUCTURE CHARACTERIZATION

Project No. 0109.1

Eric Michael Tipps  
Wright State University

31 August 2014

Government Project Leader  
Dr. Michael Groeber  
AFRL/RXLMN

Southwestern Ohio Council for Higher Education  
Student Research Program  
Agreement Number: FA8650-09-2-5800

## **Acknowledgments**

The author would like to thank Dr. Michael Uchic and Dr. Michael Groeber for the opportunity to work on this project and for aiding in the research. In addition the author would like to thank the technicians that provided their knowledge and experiences to this project; Bob Lewis and Mike Vasquez.

## **General Description of Project**

The purpose of the project was to construct 2D and 3D representations of single-crystal microstructures from turbine blade specimens and perform statistical analysis on their attributes. The surfaces of multiple single crystal nickel alloy turbine blades were examined in order to create the 2D representations. These representations were then used to identify micro-crack data. Particular focus was on the largest of the cracks found as well as the area fraction of the micro cracks compared to the total surface area of the sample. In order to obtain the 3D representations an automated system was used to collect layers of 2D representations that could then be stacked together to create the 3D model.

## **Description of Research**

In order to achieve the desired representations, the blade samples were first cut into twelve one centimeter slices and mounted using an epoxy resin. Once mounted the samples were polished using a method developed over the course of the project with help from Bob Lewis. This method of polishing began with 600 grit paper on a polishing wheel at 400 rpm followed by 1200 grit paper at the same speed. These steps were followed by using 3 micron diamond suspension polish on a texmet pad at 200 rpm, and finally a 1 micron diamond suspension was used on a texmet pad. In between each of these steps the samples were cleaned using distilled water and soap to ensure the finer polishes were not contaminated with leftover material from previous polishing steps. After the hand polishing had been completed the sample was placed in a vibratory polisher with 1 micron diamond solution for approximately 24 hours. Once polished the samples were cleaned with micro soap followed by ethanol in an ultrasonic machine. After cleaning the sample was imaged using an optical microscope at 160. The process of imaging involved using a program called Axiovision. This program allowed for the large samples to be imaged swiftly and accurately. The program collects images across the entire sample using pre-set dimensions and auto focus. Upon completion the program produces between 50 and 1000 individual images of the sample. The grayscale of these images often varies between images so to correct for this the images are leveled using a program developed in Matlab. Once all the images are uniform they are stitched together into 1 large image using the Fiji software. Once the large image has been created it is possible to isolate the micro-cracks. This is done in Matlab using both a high and low threshold value selected upon inspection of the image. The low value ensures that only micro-cracks are segmented while the high value ensures the entire crack is segmented. Using this method it is possible to accurately identify both the total area and area fraction of the micro-cracks. In addition to this it is possible to find the largest crack and the average distance between cracks.

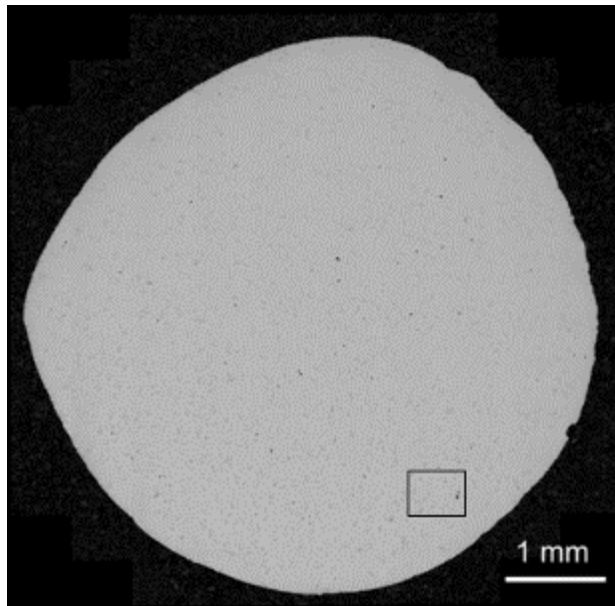


Figure 16: Stitched image of slice number 2 of blade 42C.

Section	Total Area (mm <sup>2</sup> )	A <sub>v</sub> Pore	# Pores	Max ESD (μm)	μ/σ ESD (μm)	Mean ESD (μm)
2	35.9	0.128%	1031	72.8	1.50/0.68	5.65
3	113.7	0.084%	793	54.0	2.20/0.62	10.93
4	219.6	0.033%	1266	43.4	1.53/0.80	6.36
5	81.6	0.021%	651	37.9	1.18/0.72	4.22
6	139.2	0.046%	1922	42.0	1.21/0.78	4.54
7	139.8	0.073%	7180	40.3	1.05/0.60	3.42
8	150.9	0.027%	914	59.1	1.36/0.79	5.32
9	168.8	0.020%	837	53.0	1.29/0.77	4.88
10	208.3	0.026%	1637	58.2	1.16/0.78	4.32
11	450.4	0.038%	7018	56.8	1.12/0.70	3.94
12	511.8	0.036%	2741	46.9	1.76/0.71	7.66
13	233.6	0.088%	1794	56.4	2.08/0.68	10.09

Figure 17: Data set collected from blade 42C images as well as miniaturized 42C stitched images.

## Results

The table below shows the data set for one of the blades collected during the project. There are a few trends that can be seen in this data as well as a few outliers. The outliers in the chart are shown by the gray numbers, as opposed to the standard black. The outliers are all have much higher values when compared to the rest of the samples. This suggests that the sample was not polished and or cleaned well enough before imaging, therefore these samples were taking back through the polishing and cleaning process referenced above. In addition to the data collected the table also include miniaturized version of the stitched and segmented samples. By observing these smaller images it is possible to get a view of what the full blade looks like.

MATERIALS AND MANUFACTURING DIRECTORATE NETWORK SUPPORT

Project No. 0110

Cody Weddell  
Wright State University

25 April 2014

Government Project Leader  
Mr. Bryon Foster  
AFRL/RXOC

Southwestern Ohio Council for Higher Education  
Student Research Program  
Agreement Number: FA8650-09-2-5800

## **Acknowledgements**

I would like to thank Kevin Hutten for sharing his experience and professionalism with me. I would also like to recognize the members of the Help Desk, Windows Admins and Unix Admins, who helped to teach me troubleshooting techniques and for their general courtesy. And lastly I would like to express my sincere appreciation to Mr. Brian Stucke and Mr. Bryon Foster, who have helped me to be able to stick around for so long and also for the excellent example they have set for me.

## **General Description of the Project**

Work is being done in direct support of the Materials and Manufacturing Directorate Researchers. Tasks involved include assisting with the design of new networks to meet requirements for research projects and assistance in the installation of network switches, fiber, cabling and network cards. Installation, repair and removal of Cat5e copper, VF45 and also LC network drops takes up a very large portion of work time. Tasks also involve troubleshooting network issues relating to research and performing the repairs. A large portion of work being done includes consultation with researchers. There is also monitoring of network supplies and network equipment to ensure availability to guarantee support of the Directorate research projects.

## **Description of Research**

Research being done includes the design and implementation of research network demands. Function involves working directly with researchers as well as with construction crews to determine networking needs and possible options available to the researcher. Direct consultation with researchers about their networking needs translates to the direct installation and application of network equipment which can be in the form of Cat5e copper, VF45 or LC fiber network drops. Equipment used includes network analyzers, network technologies (switches and other nodes) and also construction tools for installation.

## **Results**

The Materials and Manufacturing Directorate produces world class research in a large variety of materials science. In the growing technological world top tier research demands top tier technology. Network implementations must continue to evolve and progress with the level of higher research being conducted in order to continue to facilitate AFRL's ongoing goal of remaining a leader in materials design and research.

INFORMATION OPERATION BRANCH TECHNICAL SUPPORT

Project No: 0111.1

Heather M. Booth  
Michigan State University

31 August 2014

Government Projects Leader  
Mr. Brian Stucke  
AFRL/RXOC

Southwestern Ohio Council for Higher Education  
Student Research Program  
Agreement No: FA8650-09-2-5800

## **Acknowledgments**

I have had the pleasure of working in the Materials & Manufacturing Directorate for almost two and a half years and I must say that it has been a very fortunate opportunity through SOCHE. Everyone has been great to work with and I am grateful for the work opportunities I have had. I want to thank all my supervisors (Brian Stucke and SOCHE), and formal/informal mentors (Brittany Edwards, Brian Kesson, Steve Mahurin, and Josh Morrow), for seeing opportunities they thought I was suitable for and encouraging me to go for them. I am thoroughly impressed by my tenure here as I am always supported in any venture I wanted to take. It was my support system here at RX that gave me the tools to be able to do it ALL in work and school. I want to thank SOCHE for giving me this opportunity and experience. I'd especially like to thank the RXOC Family for your time, support, and the opportunity to learn and succeed.

## **General Description of Project**

Direct support is being provided to the Information Operation Branch Technical, in support of a broad array of tasks to support research and development efforts of the Materials & Manufacturing Directorate. Work provides support to a broad array of tasks and projects needed to accommodate the vast amounts of Directorate-wide research occurring in the RX complex. Tasks and projects primarily provided support for the RX Software Assurance Custodian and the RX Cybersecurity Office, together with the RX Computer Support Helpdesk team. These include 1) records and database management, 2) processing, distribution, and filing of scientific software, 3) patching of Malware scanning stations, 4) execute remanence security procedures of unclassified media, and 5) preparation cybersecurity training and presentation material. Through the management of these tasks and completion of projects, appropriate procedures and applied skills are learned to succeed in a government research-oriented directorate.

## **Description of Research**

Work provided is in direct support of the Information Operations Branch Technical supporting Directorate-wide research in the Materials & Manufacturing Directorate. Tasks and continuous projects are provided by the RX Software Assurance Custodian, the RX Computer Support Helpdesk team, and the RX Cybersecurity Office.

Assistants is provided to the RX Software Assurance Custodian through continuous support in records and database management, in conjunction with processing, distributing, and filing of scientific software for insulation on research and development computers for to the RX Computer Support Helpdesk team. In the RX Cybersecurity Office, projects provide support to network vulnerabilities through the patching of Malware scanning stations and analyzing of related processes to achieve optimum efficiency. Projects similarly include the proper inventory and execution of remanence security procedures in the disposal of unclassified media (i.e. hard drives, tapes, CDs, etc.). Under leadership review, cyber security training and presentation material are also developed for presenting cyber security highlights, safe computer use tips, information technology current events, and guidance for the directorate researchers to facilitate a secure computing environment for Directorate-wide research systems.

Tasks and continuous projects provide direct support in records and database management, software distribution, network vulnerabilities, and remanence media inventory and

destruction. Enhancements and alterations are applied to current processes and procedures based on team discussions and feedback, in addition to re-organization and filing maintenance. Through the completion of projects and the management of tasks, practical application of learned skills and procedures are demonstrated, to support of the Information Operations Technical Support Branch.

## **Results**

Procedures and skills learned are applied in a government office and technical research directorate settings. Based on team discussions and feedback, enhancements and modifications are implemented in current processes and procedures to achieve optimum productivity.

Projects and tasks provide a variety support to the RX Cyber Security Office including file maintenance, updating, and re-organization. Government records and data management procedures are well-educated and performed, along with an introduction to professional and research software, including processing, distributing, and filing of these computer software programs. Continuous projects assisted in an understanding for the need of weekly patching of network vulnerabilities through antivirus updates of Malware stations, regular inventory and execution of remanence security procedures of unclassified media of media (i.e. hard drives, tapes, CDs, etc.), and the monthly updating of the Cybersecurity Office computer tips, regulations, and current events board. Projects also include the completion of the Computer Incident Reporting Procedures; a quick reference documentation cards that was updated for the organization and distributed to all RX office computers across the directorate.

While providing the necessary skills and proper procedures to succeed in a government technical research-oriented work environment, these tasks and projects help to demonstrate an applied understanding of the necessity of this work, which assists the RX Software Assurance Custodian, the RX Help Desk team, and the RX Cybersecurity Office.

CERAMICS GROUP LABORATORY TECHNICIAN #2

Project No. 0119.1

Ian Wolford  
Wright State University

31 August 2014

Government Project Leader  
Dr. Mike Cinibulk  
AFRL/RXCCM

Southwestern Ohio Council for Higher Education  
Student Research Program  
Agreement Number: FA8650-09-2-5800

## **Acknowledgments**

Working at AFRL has been tremendous. I could not have picked a better training environment for a materials science student. I never could have imagined how much I would learn. I would like to thank all of the researchers who I've had the pleasure to serve during my time with SOCHE; Mike Kinsella, Geoff Fair, Mike Cinibulk, Matt O'Malley, Kristi Keller, Carmen Carney, Thomas Key, Pavel Mogilevsky, and Sheena Winder.

## **General Description of Project**

Assigned tasks included sample preparation of ceramic and composite samples, electron microscopy, characterization of high strength ceramic fibers and matrices, particle size analysis, X-ray diffractometry, as well as data and image analysis.

The primary goal of the project was to assist in basic scientific research on composite fibers and matrices in support of structural material advancement and is presented as two major research efforts. The first effort was a proof of concept exploration of amorphous content quantification by X-ray Diffraction (XRD) using the spike-in method. The second experiment was a demonstration of the spike-in method quantifying the effect of loading a preceramic polymer with seed powder. The results of this research may lead to improved processing and performance of ceramic matrix composites.

## **Description of Research**

The goal of the first effort was to prove that by mixing a known crystalline standard powder, the spike-in agent, with another experimental powder the crystalline content and amorphous content of the experimental powder could be determined by phase fraction analysis via Rietveld refinement. A test matrix was developed to compare a series of powder mixtures containing three components; the experimental powder silicon carbide (SiC), the spike-in agent (National Institute of Standards and Technology 676a Alumina or aluminum oxide  $Al_2O_3$ ), and amorphous glass powder. Two experiment types were outlined in the test matrix. In the first experiment the amount of glass was held fixed while the relative amounts of Alumina and SiC were varied. Four different ratios were tested. The 50/50 SiC/Alumina ratio proved the most promising candidate, so during the second experiment the ratio of SiC to alumina was fixed at 50/50 and the amount of glass was varied.

The individual powder ratios were mixed with an alumina mortar and pestle. Once fully mixed, the powder mixtures were scanned on the Bruker D2 Phaser X-ray Diffractometer. The resulting X ray diffraction (XRD) patterns are presented below in Figure 1. Topas, a Rietveld refinement software package, was used to analyze the set of experimental scans. By mathematically approximating the effect of the crystalline structure the software generates a simulated XRD pattern. The Rietveld refinement process uses a series of numerical approximations, based on the predicted crystal structure and composition, to converge on the most probable ratio of crystalline content within sample. The crystalline information input into Topas was based on crystal structure (lattice parameters, atomic positions, thermal parameters, etc.) for the compositions being studied, specifically silicon carbide and the known crystalline standard alumina. Once Topas has refined the crystalline values it outputs the quantified fractions of crystalline and amorphous components.

The goal of the second research effort was to measure the change in crystal growth of SiC seeded SMP-10 (a preceramic polymer which decomposes to crystalline SiC at high temperature) as a function of time, temperature, and solids loading. Beta-SiC (<1 $\mu$ m) was used as a seed powder. A test matrix was designed using five different solids loadings, 5%, 15%, 25%, 35% and 50%, the time at pyrolysis temperature was fixed at one hour, and the pyrolysis temperatures were varied in increments of 100°C from 1100°C to 1800°C. This effort also used the Rietveld spike-in method with alumina as a spike-in agent

After mixing SMP-10 with beta-SiC, and curing at 250°C overnight, the resulting mixtures were ground with alumina powder using a Boron Carbide mortar and pestle. The powders were then scanned on the Rigaku Ultima IV X-ray Diffractometer. MAUD, a Rietveld refinement software was used to analyze the resulting diffraction patterns. The first round of analysis required a secondary XRD scan of SMP-10 pyrolyzed without seeding. This was compared to the scan of the SiC-seeded SMP-10 to quantify how much SiC crystallized due to the presence of the seed powder versus how much SiC grew natively from SMP-10 as it solidified. At higher temperatures SiC begins to form two polymorphs, alpha and beta SiC. So the second round of MAUD analysis required two SiC models to find the total sample crystallinity.

## Results

Effort 1: The crystalline values found during the spike-in validation were compared to the known mass values. Error values were then calculated, using primarily Microsoft Excel. The measurement error was found to be comparatively low, on the order of 1%. This result shows that the spike-in method for Rietveld refinement could be used to find small amounts of amorphous content in a crystalline Silicon Carbide based material.

Effort 2: The effect of solids loading and pyrolysis temperature on SMP-10 varied both with solids loading and temperature within the 1-hour test group. Beginning at 1100°C the solids loading is the driving force for nucleated growth, but this effect peaks at 25%. As shown in Figure 2 the effect of solids loading on seeded crystal nucleation for 25%, 35% and 50% is effectively identical until 1400°C. All solids loadings peaked at around 50% nucleated growth, regardless of temperature. These quantified trends can be used to maximize reduction of porosity

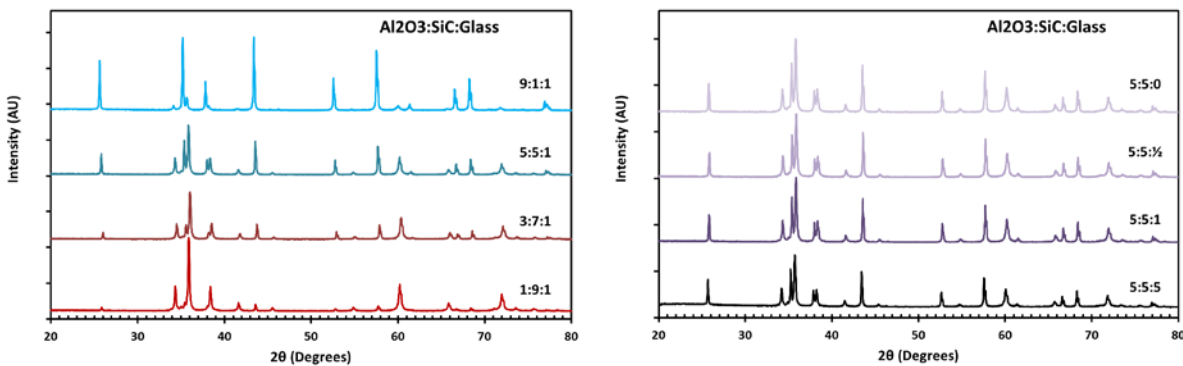


Figure 1, X-ray diffractions patterns for Amorphous Content Analysis Experimental when infiltrating ceramic matrix composites with SiC seeded SMP-10. Quantification of nucleated SiC yielded similar total crystallinity to commercially available fibers.

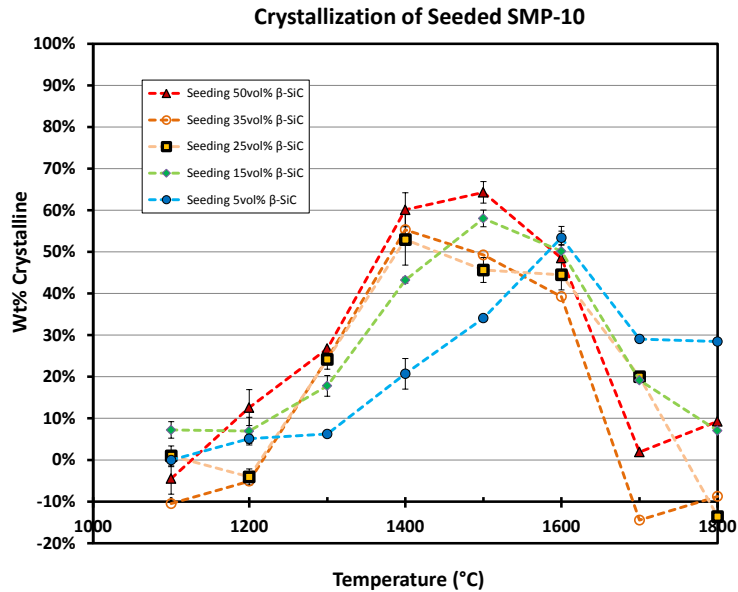


Figure 2, Effect of 5%, 15%, 25%, 35% and 50% Solids Loading on Seeded Crystal Nucleation

### Related Activities

I am scheduled to present at MS&T 2014 on the Experiment 2 listed above. The title of the talk is “Quantifying Amorphous Content of SiC Loaded Pre-ceramic Polymers”.

A large portion of my time in RXCC has been devoted to sample preparation for scientists in the research group who needed my assistance. I also worked with Major Sheena Winder of AFIT in a training/consulting capacity regarding her PhD work specifically with regard to sample preparation. She has since moved to RXAN and I continue to work with her on XRD setup and calibration. I have also provided XRD support for Matt Edge, a fellow student in RXCM.

MODEL VALIDATION FOR IMPEDANCE SPECTROSCOPY

Project No. 0122

Aaron Cherry  
Wright State University

1 August 2014

Government Project Leader  
Dr. Eric Lindgren  
AFRL/RXCA

Southwestern Ohio Council for Higher Education  
Student Research Program  
Agreement Number: FA8650-09-2-5800

## Acknowledgments

I would first like to acknowledge Dr. Steve Russ for considering me as a student intern in the RXCA branch and for giving me this wonderful opportunity. I would also like to thank Dr. Jeremy Knopp for introducing me to the project I have been working on for three years as well as Dr. John Aldrin from Computational Tools that proposed my research problem and has given me guidance on experimental procedures even all the way from Illinois. I would also like to thank Dr. Eric Lindgren for giving me guidance on the direction of experimentation as well as teaching me engineering and networking concepts. My close mentors include Matthew Cherry, Dr. Amanda Criner, Ryan Mooers, and Dr. Shamachary Sathish. I would also like to acknowledge their contributions to my work and my development as a researcher.

## General Description of Project

Model Validation for Impedance Spectroscopy

## Description of Research

Nondestructive evaluation (NDE) and inspection (NDI) are the processes of inspecting materials without the need for disassembling aircraft and evaluating the structural integrity of the material and the lifespan of the part. However, the wings and fuselage incorporate complex geometries such as multiple layers of metals linked together with bolts. To effectively test for defects in such complicated conditions, the effects of added geometric complexities must be characterized in terms of their effects on eddy current (EC) testing. In this study, numerical models such as COMSOL and VIC-3D were used to predict the effects of the interface conditions between layers of metals much like the wings and hull of aircraft.

## Results

VIC-3D was used to model the differences in EC signal due to a notch between a case with a floating notch inside a solid aluminum block and a notch in the surface of the bottom layer in a layered aluminum specimen (Figure 1). The model predicted approximately a 50 percent change in signal between the two cases and was validated by the experimental data taken from the first study. Furthermore the model predicted a slight linear change in impedance signal due to changing the gap with “g”. This relationship was evident in the reactance data taken experimentally; however, there was too much variability in the resistance data to make a clear comparison.

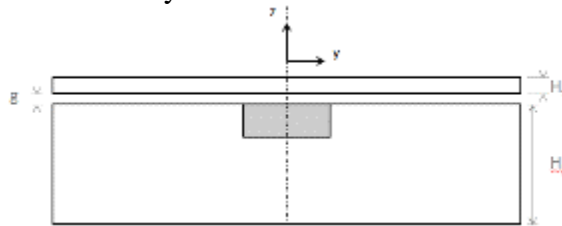


Figure 1. Diagram of the geometry of this study (grey area is an EDM notch).

By polishing the plates and applying pressure to push them together, electrical contact was achieved between the plates. Despite the extra precautions, the experimental data seemed to compare well with the simulation incorporating a 0.06mm gap. It can be concluded that because of practical reasons such as the oxide layers surrounding the metals as well as yet more surface roughness even at a mirror polish, the contact between the two plates is still not ideal enough to behave as one plate in terms of ECT. Furthermore, it can be said that a gap or interface condition should be incorporated or kept in mind when taking EC scans of or modeling layered media.

### **Works Cited**

**A.J. Cherry**, J. Knopp, J. C. Aldrin, H. A. Sabbagh, T. Boehnlein, and R. Mooers, "Role of Varying Interface Conditions on the Eddy Current Response From Cracks in Multilayer Structures," *Review of Progress in Quantification of Nondestructive Evaluation*,32, pp. 456-463, (2012)

**Aaron J. Cherry**, Matthew R. Cherry, John C. Aldrin, Eric Lindgren, Harold A. Sabbagh, Thomas Boehnlein, Ryan Mooers, Jeremy Knopp, "Role of Interface Conditions in Low Frequency Electromagnetic Testing of Multilayer Structures," *Review of Progress in Quantification of Nondestructive Evaluation*, **in progress (2015)**.

### **Related Activities**

For the first summer of my internship in RXCA, I made a poster for the AFRL Summer Symposium and presented in front of our division figure heads. Also in the time I worked at RXCA, I had the pleasure of attending two international conferences: Review of Progress in Quantitative Nondestructive Evaluation 2012/2014. The manuscripts can be found in the work cited section. In the first conference that I attended in 2012, I had made and presented a poster in the student poster competition. I had the pleasure of making a power point and presented it in the 2014 conference that I attended.

ENVIRONMENTAL AND ENERGY ENGINEERING ANALYSIS

Project No. 0124

Morgan Spicer  
Wright State University

31 August 2014

Government Project Leader  
Mr. Dave Madden  
AFRL/RXSC

Southwestern Ohio Council for Higher Education  
Student Research Program  
Agreement Number: FA8650-09-2-5800

## Acknowledgments

I take this opportunity to express my gratitude to my supervisor, Mr. Dave Madden, for his guidance and mentoring throughout my research. I am obliged to team members of the Advanced Power Technology Office (APTO) for the valuable information provided by them in their respective fields. I would also like to thank University of Dayton Research Institute (UDRI) for the laboratory facilities, sharing literature and invaluable assistance. I am grateful for the collaboration during the period of my research project; it would not have been possible with the support of many people.

## General Description of Project

The algae program at UDRI was initiated with support from APTO to harness the high photosynthetic efficiency of algae as a way to capture CO<sub>2</sub>, reducing emissions, as well as generate an energy feedstock suitable for green diesel generation or as a biomass source. During the start of the program, two horizontal photobioreactor systems were provided to UDRI's Kettering Laboratory for testing and evaluation. UDRI quickly observed the horizontal systems limitations. UDRI designed a new algae system utilizing vertical photobioreactors that were implemented at the UDRI River Campus.

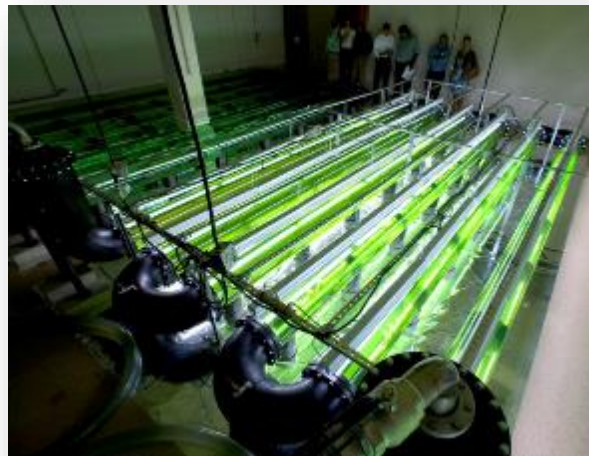


Figure 1. UDRI Kettering Laboratory Horizontal Algae System.

## Description of Research

Algae are among Earth's oldest living organisms, they are diverse photosynthetic organisms that are readily available in most environments. Algae vary in size and shape and can be classified as single-celled or complex multicellular forms. Algae shows rapid growth and can store energy in forms of oils and carbohydrates, making it among the most promising long-term sustainable sources of biomass and oils for fuel. Variables affecting the growth of the system are gas/liquid exchange between CO<sub>2</sub> consumed and O<sub>2</sub> released, light intensity, water pH, temperature, and algae species. UDRI defined three algae strains that survive the Ohio climate along with an optimized system that is functional 24/7, 365 days a year. The closed system feeds

all the essential nutrients and CO<sub>2</sub> into the tubes for the algae to grow. The new algae system developed operates at 4 tons/year of biomass with 80 reactor tubes.



Figure 2. UDRI River Campus New Vertical Algae System.

The algae is harvested and the extracted product is biocrude. The biocrude is then refined to be converted into a green diesel. The lipid extraction method developed allows for high value compounds such as fats, oils, sugars and functional bioactive compounds to be separated from the algae extract to make algae green diesel cost competitive with commercial fuels, and allows recycling of nutrients from the lipid extracted algae. Algae-based green diesel decreases fuel costs approximately 60% per gallon used, and decreases the carbon footprint 22.3 lb of CO<sub>2</sub> per gallon of diesel used.

If utilized, the algae biomass technology will enable the United States Air Force (USAF) to meet the USAF Energy Strategic Plan 2013, Priority Three, Goal 2 to increase facility use of alternative and renewable energy and Goal 3 to increase the use of alternative fuels in ground vehicles and equipment. Specifically, it is anticipated that use of the algae based carbon capture technology will enable an increase in facility consumption of renewable/alternative energy to 25% of total electricity use well ahead of schedule (by 2025). It will allow on-site generated renewable energy, and will make alternative fuels readily available at a cost competitive price. Also, algae biomass could potentially be an energy source suitable for expeditionary use (Priority Three, Goal 4) if combined with other technology such as onsite mobile liquid fuel generation/gasification by providing a safer alternative to transporting liquid fuel.

## Results

Therefore the vertical photobioreactors proved overall to be a more successful system. The new system was not space limited (10 times higher volume), lower-energy (75 times lower operating cost), and had a 20 times higher areal productivity (biomass yield / m<sup>2</sup> of land area,

and hence higher CO<sub>2</sub> capturing efficiency). UDRI also designed an energy efficient harvesting system and an energy efficient lipid extraction process yet to be tested.

In order to determine if this leading edge technology can support an Air Force Base, the path forward is to produce a large scale algae system that will be installed by a heat plant located on Wright-Patterson Air Force Base (WPAFB) to capture CO<sub>2</sub> and other Green House Gases (GHG) emitted from natural gas (NG) boilers. This algae system will produce 165 tons/ year of biomass and consist of 3,000 reactor tubes. This system will grow the amount of algae required to create enough biocrude that will then be refined into a green diesel. Pre-qualification testing of the green diesel will be done to determine characteristics of the fuel as an ideal drop-in biofuel for ground vehicles. If pre-qualification tests results are promising, more fuel qualification test will be performed to evaluate other aspects of the green diesel.

### **Works Cited**

Juniewicz, Debbie. "Agile Algae." University of Dayton Magazine Summer 2014: 37-41. Print.

TOOLS FOR TOMOGRAPHIC RECONSTRUCTION OF MICROSCOPE IMAGES

Project No. 0129

Stephen Bricker  
Wright State University

13 January 2014

Government Project Leader  
Dr. Jeff Simmons  
AFRL/RXCM

Southwestern Ohio Council for Higher Education  
Student Research Program  
FA8650-09-2-5800

## **Acknowledgements**

This student research project through SOCHE has been a huge learning experience. The opportunity to be a part of real research as an undergraduate student has been helpful both in learning what research is like, and in supplementing classroom learning. Thanks to Dr. Craig Przybyla and Dr. Jeff Simmons for their involvement and guidance on the project. Thanks to Dr. Lawrence Drummy for his help in learning AVIZO software for data visualization.

## **Project Description**

Advanced ceramic composites are currently being studied as alternatives to metal alloys for hot components in turbine engines. Current limitations are due to low strengths of ceramics compared with alloys. This has led to the development of ceramic matrix composite materials (CMC). CMCs are composed of a ceramic or carbon fiber surrounded by a ceramic matrix. Analyzing and understanding the microstructure is key in finding weak points in the material. This project primarily focuses on the processing and analysis of images taken on several CMCs. The goal is to use this information to create models of crack formation and propagation.

## **Research Description**

Images analyzed in this project were acquired primarily using a UES RoboMet.3D. RoboMet automatically completes serial sections by grinding off the top layer of the sample by a depth of approximately 1 micron. Each layer is then imaged with a Zeiss Observer.Z1M optical microscope. This produces a mosaic of images as shown in figure 1. The images that make up the mosaic have an overlap region with the images around them. These regions are compared and aligned using the weighted sum of square intensities. The vector shifts calculated for each image are used to produce a single large image. Each large image is aligned with the image below it in the stack using the same method. After aligning the images, the different classes are segmented using the expectation maximization and maximization of posterior marginals algorithm. Segmentation is necessary to be able to tell different parts of the image like fibers and matrix apart before extracting specific features.

Feature extraction is an important step in analysis. The composites analyzed in this project are composed of three to four features: Fibers, fiber coatings, matrix phases, and pores. Fibers were chosen for study because they are perhaps the simplest to model. Fibers are ellipsoidal when imaged, move semi-linearly through the sample, and are very important to the structure of the composite. Fibers are identified in Matlab using a Hough transform, and their centers and axes recorded. Using the found fiber positions and the shifts calculated for each image and layer, a 3D model of the fibers is constructed. Each layer of known fiber positions is compared with the next, searching for the fiber in the next layer that most closely matches its known position. When a match is found it is added as a continuation of the fiber. When a match is not found, the algorithm searches through a specified number of layers for a match and, upon finding one, interpolates the fiber positions between the found position and the last known position. After all the layers have been searched each fiber is fitted to a third order curve using a least squares approach. A 3D visual plot is shown from two perspectives in figure 2. Viewing from above makes the fiber paths apparent, while viewing from the side shows that they are moving in opposite directions.

Visualization of the fiber behavior is accomplished by adding a false color-scheme to the segmented images. Fibers are colored based on direction of movement and assigned color saturation based on magnitude of movement. Figure 2 shows two groups of fibers moving in opposite directions. Figure 3 shows how group boundaries are immediately apparent when fibers are colored by velocity. Coloring is done by the HSV color-model shown in figure 4. Separating the different groups or tows of fibers mathematically is done using the following equation.

$$\begin{bmatrix} V_{x,j} - V_{x,i} & V_{x,k} - V_{x,i} \\ V_{y,j} - V_{y,i} & V_{y,k} - V_{y,i} \end{bmatrix} \approx \begin{bmatrix} a & b \\ c & d \end{bmatrix} * \begin{bmatrix} X_j - X_i & X_k - X_i \\ Y_j - Y_i & Y_k - Y_i \end{bmatrix}$$

V represents the fiber ‘velocity’ for each fiber found by subtracting fiber positions in one layer from the next. Velocity here refers with movement in the x-y plane with respect to depth in the sample (z). X and Y are the fiber positions, and the unknown matrix represents some velocity gradient. The velocity gradient is computed for each set of three neighboring fibers and the eigenvectors and values are calculated for the matrix. These values represent the expansion, shear, or rotation present between neighboring fibers. For fibers moving together the magnitude is small, but at boundaries between fiber groups moving in opposite directions shear becomes apparent.

## Results

Fiber tracking techniques were developed and improved through the course of this project as well as visualization techniques for serial section CMCs. While the research is not yet to the stage where fiber group behavior can be used to model weak points in the material, the development of fiber velocity gradient and fiber coloring make identification of anomalies simple. Collecting data on these anomalies and how they affect the material is an important next step in creating more effective materials.

## Figures

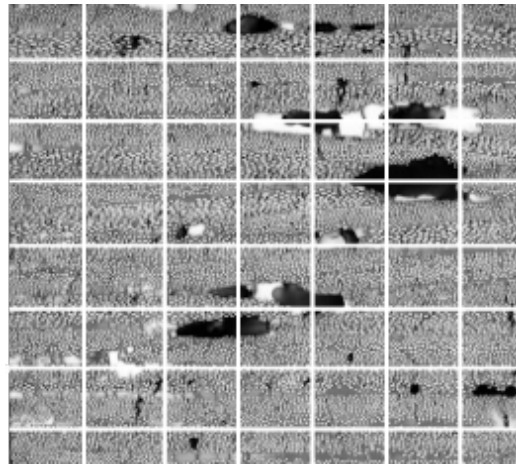


Figure 1: Each tile represents one image taken on the Zeiss optical microscope

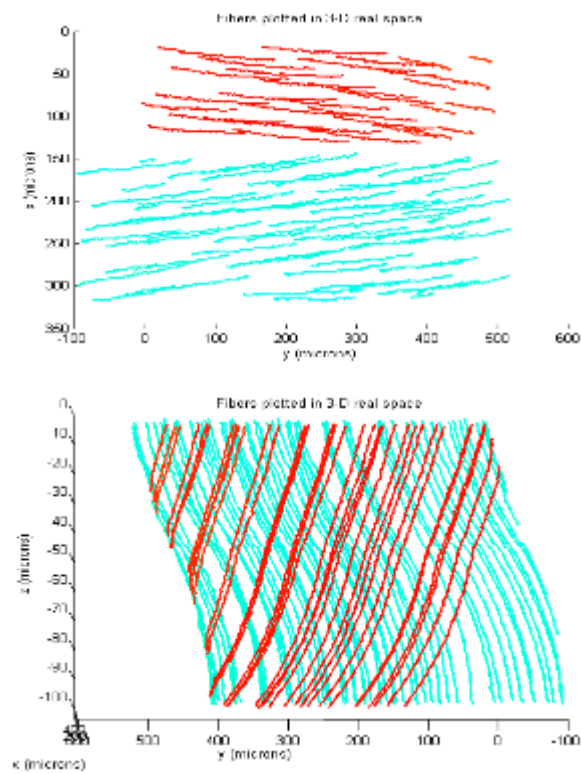


Figure 2: Fiber tracking as seen from the top and side. Color is determined by fiber direction

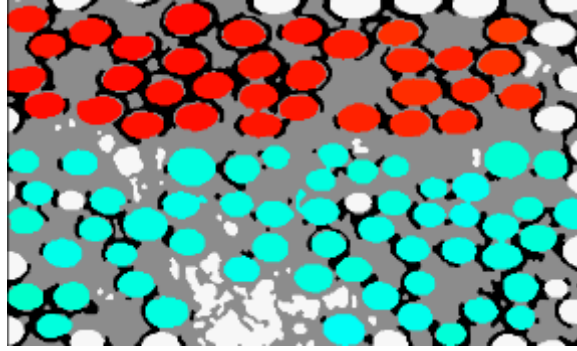


Figure 3: Fibers in this image belong to separate tows. Red moving right and blue moving left

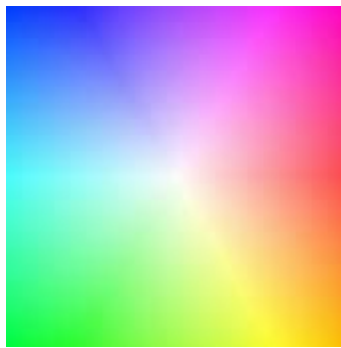


Figure 4: The white center represents no shift. Color represents direction and magnitude of fiber shift

SYNTHESIS AND CHARACTERIZATION OF DNA BIOPOLYMER/NONLINEAR  
OPTICAL (NLO) CHROMOPHORE THIN-FILMS DEPOSITED BY MATRIX ASSISTED  
PULSED LASER EVAPORATION (MAPLE)

Project 0132.1

Jessica Hendricks  
Wright State University

31 January 2014

Government Project Leader  
Dr. Tom Cooper  
AFRL/RXAP

Southwestern Ohio Council for Higher Education  
Student Research Program  
Agreement Number: FA8650-09-2-5800

## Acknowledgements

I want to thank Dr. Angela Campbell for giving me this opportunity. Dr. Tom Cooper took over the lead on the project which allowed me to continue and finish my thesis. Dr. David Stewart sat on my committee and offered invaluable advice. Dr. Doug Krein, Dr. Joy Haley, Ms. Hadil Issa, Dr. David Mast, and Dr. Richard Kleismit assisted in accomplishing the research. And a final thanks to Dr. Gregory Kozlowski for introducing me to Dr. Campbell and his work as my advisor.

## General Description of Research

The objective of this work is to investigate the photophysical properties of the two photon dye (TPA) AF455. AF455 is a chromophore that can absorb two photons instead of a single photon when excited. There are several areas of application: Bio-LEDs, Field Effect Transistors, and nonlinear optical coatings are three examples. Previous research has discovered increased absorption when AF455 is bound to DNA-CTMA (deoxyribonucleic acid- cetyltrimethyl ammonium). The work described here will focus on the binding studies between DNA-CTMA and AF455. Additional work was conducted under this project, the details can be found the thesis in the Related Activities section.

## Description of Research

The materials used in this study are AF455, the TPA chromophore, DNA-CTMA, toluene, and dimethylsulfoxide (DMSO). DNA must be electrostatically bound to CTMA in order to get it to dissolve in some organic solvents. The AF455 dye will dissolve easily in toluene, but not DMSO and the DNA-CTMA dissolves in DMSO, but not toluene. Both of these solvents must be used for that reason and ratios of them are studied to see which ratio has the best results.

The binding study samples were prepared in the following manner. A stock of AF455 with a concentration of 0.1264 mg/mL was prepared. A mass of 3.16 mg of AF455 was weighed on a sensitive balance on a weigh paper. This mass was then transferred into a volumetric flask of 25 mL volume. The weigh paper was held over the flask and toluene was poured over the paper into the flask. The flask was filled until the bottom of the meniscus was at the line. Then 0.3 mL of the AF455 stock was pipetted into cleaned 15 mL vials. Toluene and DMSO were added to the vials to get the appropriate ratio of toluene to DMSO creating the "ratio" stocks, see Table 1.

**Table 2: Binding Studies Stock Solutions Volumes**

Toluene %	DMSO %	Total Volume (mL)	AF455 Stock Volume (mL)	Toluene Volume (mL)	DMSO Volume (mL)
70	30	15.0	0.3	10.2	4.5
60	40	15.0	0.3	8.7	6.0
50	50	15.0	0.3	7.2	7.5
40	60	15.0	0.3	5.7	9.0
30	70	15.0	0.3	4.2	10.5

The concentration of the "ratio" stocks is 0.002 mg/mL. A new set of vials was cleaned to create the DNA stocks. The DNA-CTMA was weighed using the same balance as the AF455 and put directly into the vials. (The balance has a max mass of 22 g, the volumetric flask exceeds this, and the vials do not.) After the DNA-CTMA was added, the "ratio" stocks were pipetted into the vials, see Table 2.

**Table 3. DNA-CTMA Stock Mass**

Toluene %	Mass of DNA-CTMA (mg)	Total Volume (mL)
70	55.23	1.0
60	152.45	1.5
50	143.33	1.5
40	154.88	1.5
30	164.89	1.5

After the stocks were prepared, the "ratio" stock was pipetted into a cuvette at a volume of 2.5 mL. The absorbance of each of the "ratio" stocks was measured using the Cary 5000. After the initial measurement, a 100  $\mu$ L aliquot was added from the DNA-CTMA stock and a stir bar was inserted into the cuvette. This was then stirred for 10 minutes to allow for binding before being run in the Cary 5000. This process repeated until the 1.5 mL DNA-CTMA stock was completely used. Additional DNA-CTMA stocks were prepared in the same method described to continue the testing. When the testing was completed the data was processed using Microsoft Excel.

## Results

The complete results for the binding studies were only obtained for the 70% toluene sample. Figure 1 displays the results of absorbance vs. concentration.

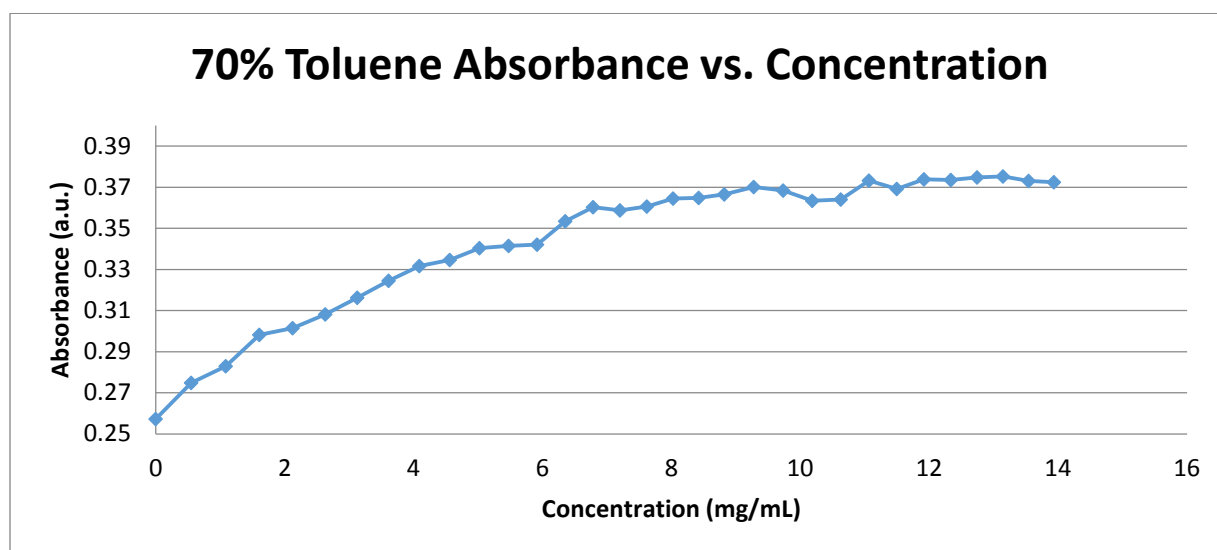


**Figure 18. 70% Toluene Absorbance v. Concentration Results**

Evidence of complete binding is seen. The curve does not increase in absorbance with increasing concentration after about 10 mg/mL. The results for the final testing of both 50% and 30% toluene are displayed in Figures 2 and 3.

In Figures 2-3, there is evidence of binding, but the point of being completely bound has yet to be reached. There is much higher absorbance for the 30% toluene sample compared to the two other samples. The testing must be altered to reach the point of complete binding for these two samples. Instead of starting the concentration at 0 mg/mL, the initial concentration should be increased to 60 mg/mL. The same process described in the Description of Research section should be continued with only the change in initial concentration.

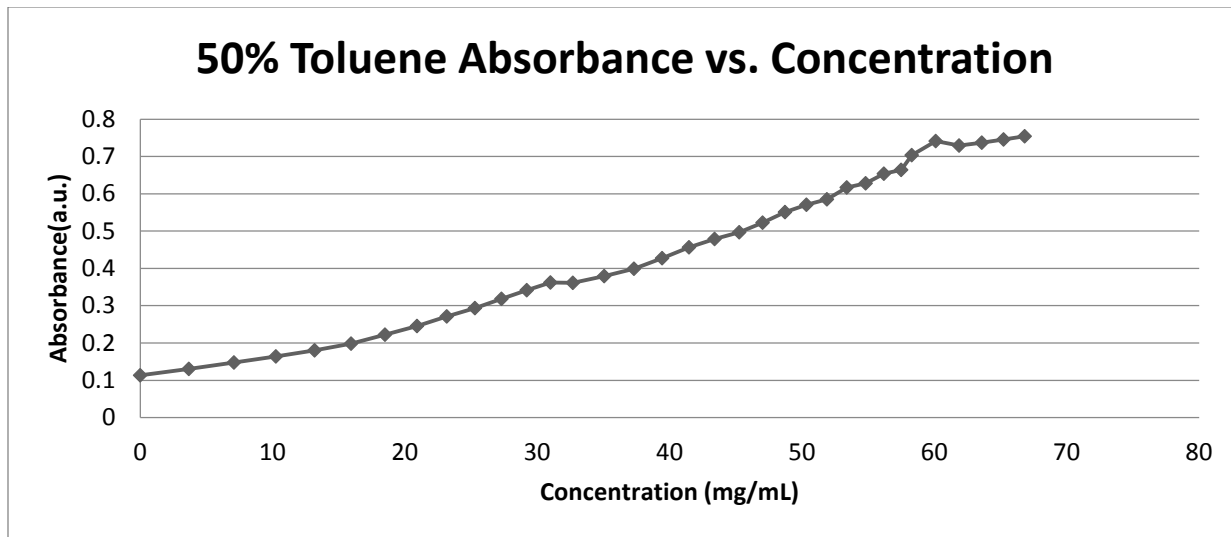


**Figure 19. 50% Toluene Absorbance v. Concentration Results**

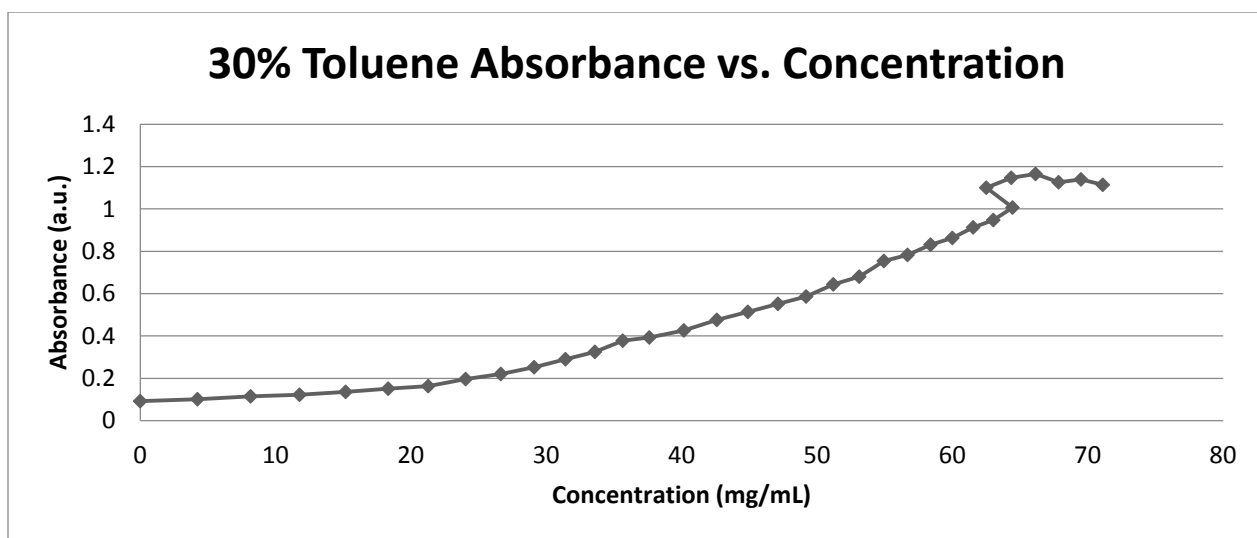


**Figure 20. 30% Toluene Absorbance v. Concentration Results**

## Related Activities

Additional work was conducted under this project that lead to a Master's Thesis in physics. The details of this work can be found in the author's Master's Thesis at Wright State University. The abstract follows:

This work studies the electromagnetic properties of AF455, a two photon dye, DNA bound with cetyltrimethyl ammonium (CTMA), in liquid solvent blends for use in thin film optical filters. The liquid properties of the materials are believed to be transferred to the films. The solvent blends used are ratios of toluene (T) and dimethyl sulfoxide (DMSO). The complex permittivity and permeability of the samples are measured using the short open coaxial line technique in the frequency range of  $1.0 \times 10^7$  Hz to  $2.0 \times 10^9$  Hz. In this frequency range, AF455 does not act as a two photon absorber. The results show there is an interaction between AF455 and DNA-CTMA that increases the real permittivity for two solvent blends (50-50, and 60-40, T-DMSO). There is also a clear conformation change in the samples with the solvents and DNA-CTMA only that is observed in the real permittivity. In the 70-30 blend, the conformation of the DNA-CTMA is a clear helix. In the samples with less toluene the conformation of the DNA-CTMA is a coil structure. The imaginary permittivity increases with the addition DNA-CTMA. The real and imaginary permeability are constant across all samples.

AFM CHARACTERIZATION OF OPTICAL AND ELECTRONIC STRUCTURES

Project No. 0135

Madelyn Hill  
Wright State University

1 May 2014

Government Project Leader  
Dr. Kurt Eyink  
AFRL/RXPS

Southwestern Ohio Council for Higher Education  
Student Research Program  
Agreement Number: FA8650-09-2-5800

## **Acknowledgements**

I would like to first thank the Air Force Research Laboratory for allowing me the opportunity to gain research experience. I would like to thank Larry Grazulis for mentoring me on atomic force microscopy (AFM) and for always answering my questions to further my knowledge of AFM. Next, I would like to thank Dr. Kurt Eyink for his guidance and knowledge about the science involved in my work. I would also like to thank Dr. David Zelmon, Dr. Brandon Howe and countless other researchers who allowed me to analyze their samples and for their help in better understanding how my work affected their research.

## **General Description of Project**

An Atomic Force Microscopy (AFM) was used to characterize the general morphology, electrical properties, and material properties for a variety of samples and growths. Materials analyzed included MBE grown Quantum Dots (QDs), Planer InAs used for nano-scribing and formation of QDs, graphene grown with MBE, CVD and Oxigon, 2D materials ( $\text{MoS}_2$ ) and Piezoelectric materials. Superlattice (SL) structures comprised of GaSb, InAsSb, InAs/GaSb, InAsSb/GaSb, and InAs/InGaSb . All of these samples were analyzed for general morphology but many also were analyzed using one or more of Electric Field Microscopy (EFM), Conductive AFM (C-AFM), Kelvin Force Microscopy (KFM) and Piezoresponse Force Microscopy (PFM).

The AFM consists of a cantilever with a sharp tip or probe attached to the end which is used to scan the surface of the sample. When the tip is brought into proximity of a sample surface, forces, such as Van Der Waals and static electrical charges, between the tip and the sample begin to interact, either pulling the tip into the sample or repelling it away. The AFM electronics are set to maintain the force on the tip at a constant value and to keep the tip a fixed height above the sample surface to prevent damage. As the tip moves across the surface, either in contact with the surface or oscillating above the surface, the force between the tip and surface may be adjusted to keep a constant distance between tip and surface. When the tip moves across the surface it generates information about the sample such as, topography, electrical properties or mechanical properties about the material. This data can then be processed and provide information about growth conditions or sample processing and guide changes in future growth or processing procedures. Figure 1 shows the basic components of an AFM.

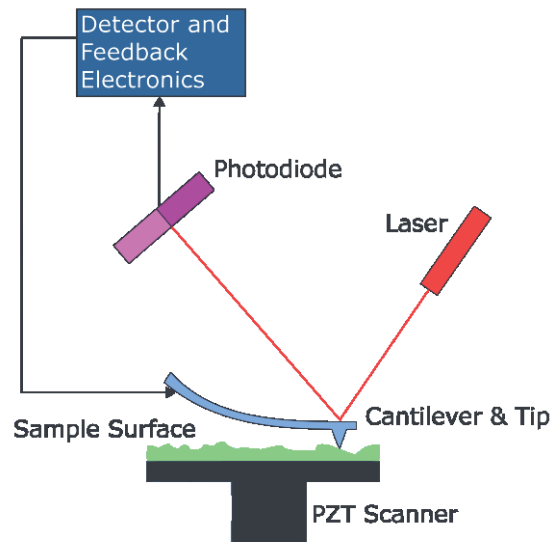


**Figure 21 Block Diagram of the Components Comprising an AFM**

### **General Description of Research**

The physical characterization of nanoscale structures used in quantum confined structures, such as quantum dots, carbon based materials, and other two-dimensional structures and nanostructures (e.g., nanodiamonds) are highly dependent on growth conditions, such as sample temperatures, growth rate, flux ratios, doping, and physical dimensions (e.g., size of the structure and material thickness). The growth conditions, sample preparation/handling before or after growth, and theoretical design of the structure directly affects the surface morphology, interface abruptness, and layer thickness, thereby influencing the electrical (electron and hole mobility), optical (photoresponse, photoluminescence line width and amplitude) characteristics, material properties such as, hardness/flexibility and magnetic properties. For understanding these properties, theoretical models are necessary to interpret the results of characterization techniques and sample processing procedures and to guide the growth of these materials. Theoretical models can be usefully employed to study how changes in processing and growth conditions affect electrical, magnetic, mechanical and optical characteristics. As a specific example, QD structures are typically formed via self-assembly; however, patterning the surface before growth at the sub-micron scale has been shown to influence the morphology and size distribution of the QD arrays. Device characteristics are directly related to the distribution, size, and shape of the QDs, as well as the surface morphology obtained for other epitaxially-grown structures. One of the many instruments used for characterizing various properties of electronic and optical materials is the Atomic Force Microscope (AFM).

Understanding the cause and effect of the many growth parameters consumes many sample growths and much time. One set of experiments focused on adjusting the cracking temperature of the Sb source during growth and finding if there is a correlation between the morphology and photo response. In general, as the cracking temperature was increased the

quality of the surface morphology decreased and the photo response decreased. As the cracking temperature increased pits formed and the RMS surface roughness increased. Figure 2 are 50 $\mu\text{m}$  images of samples grown at different cracking temperatures and the associated RMS roughness values. The images indicate as the temperature increases more pits form and the RMS roughness increases. The photo response also tended to decrease as the cracking temperature increased. The RMS roughness increased dramatically from a low of .15nm at the lowest temperature to a high of 8.29nm for the highest cracker temperature. Although this experiment was adjusting only the Sb cracker temperature and in this case the outcome was evident, many times there is interplay between the system parameters and the particular SL design.

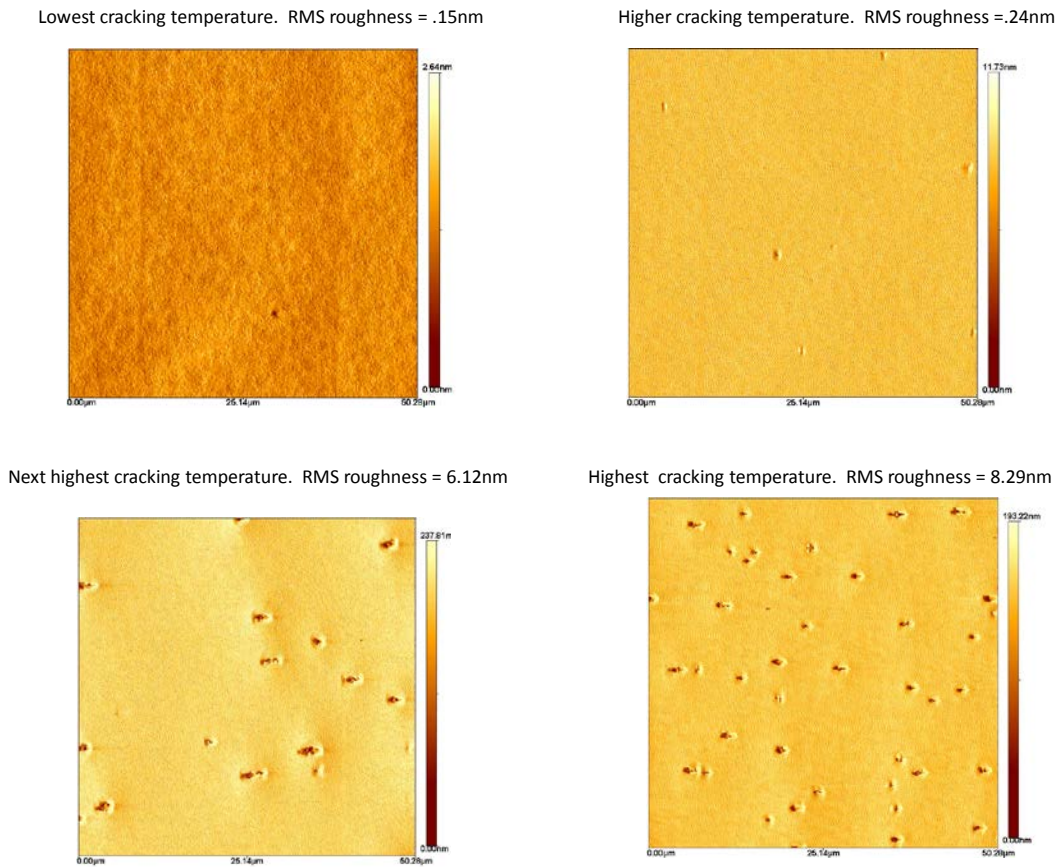


**Figure 2. Comparison of Superlattice Grown with Different Sb Cracker Temperatures**

Many semiconductor materials are grown with atomic layers in a process known as step flow growth. These surfaces will have the appearance of a set of stairs. The structure of these surfaces can provide useful information about the quality of the growth process and provide information on how to adjust the growth parameters to achieve a more uniform growth. Some examples of different types of step flow growth are shown in Figure 3.

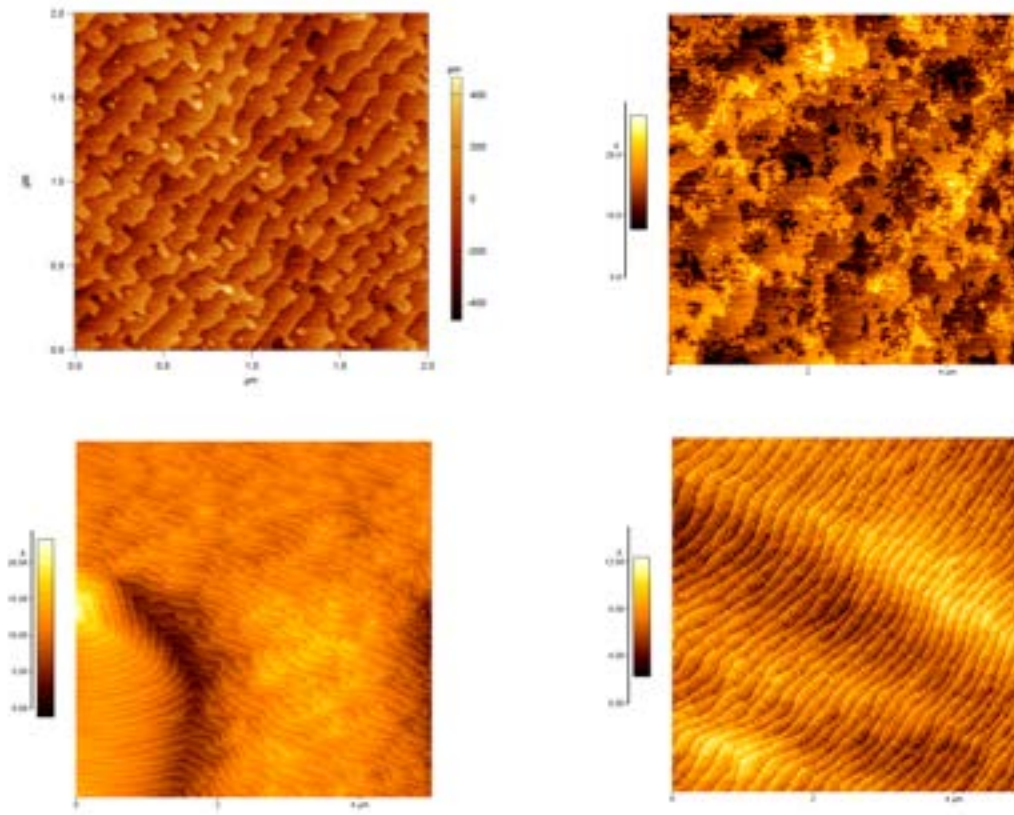


**Figure 3 Different Types of Step Flow Growth**

## Results

AFM images can give a researcher a better understanding how of their semiconductor materials interacted when variables were adjusted. Depending on the materials, atomic layers and flat samples are ideal, while others grow large features or holes in the sample. These growths and samples are used by researchers to develop semiconductor materials for their projects. Atomic force microscopy is one of many useful analyses for semiconductor materials.

MODELING THE ROLE OF MICROT texture ON THE FATIGUE BEHAVIOR OF  
TITANIUM ALLOYS USING LINEAR ELASTIC FRACTURE MECHANICS

Project No. 0138.1

Michelle Harr  
Wright State University

30 April 2015

Government Project Leader  
Dr. Adam Pilchak  
AFRL/RXCM

Southwestern Ohio Council for Higher Education  
Student Research Program  
Agreement Number: FA8650-09-2-5800

## Acknowledgments

I would like to thank my government point of contact and boss, Dr. Adam Pilchak, for hiring me and teaching me all the necessary material and skills necessary to work on this project. He has been an invaluable resource in my materials science education, especially in the field of fracture mechanics. I am very thankful for all the time, advice, and training with which he has mentored me.

## General Description of Project

The single most common cause for failure in metals is via the failure mechanism of fatigue. Fatigue is the weakening of materials that occurs in structures that undergo repeated cyclic stresses. Fatigue failure typically happens suddenly and at stresses much lower than the yield strength of the material. Due to the abrupt and widespread nature of fatigue failure, it is necessary to develop and refine a methodology to predict fatigue behavior as a function of material microstructure and texture. More recently, however, it has become evident that clusters of similarly oriented grains can lead to early fatigue failure. This occurs by long-range faceted fatigue crack growth, which is more rapid than the more classic mechanism of fatigue crack growth, viz. striation growth. In this study, these groups of similarly hard-oriented have been termed microtextured regions (MTRs).

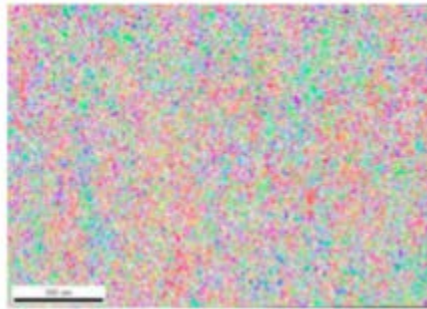


Figure 22: Electron Back Scatter Diffraction (EBSD) map of sample with Low Microtexture

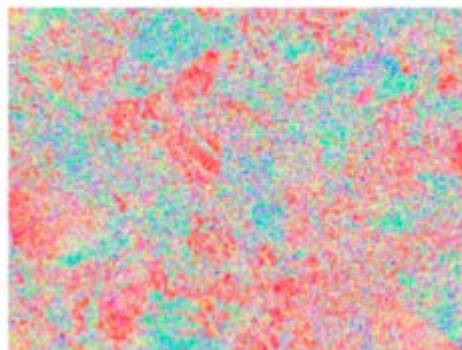


Figure 23: Electron Back Scatter Diffraction (EBSD) map of sample with High Microtexture

MTRs are a life affecting feature that is neither tracked nor accounted for in current design practices. By accounting for MTRs in fatigue lifetime predictions, an improved estimate of the number of cycles in post-initiation lifetimes can be found and the maximum allowable stress limitations on particular materials can be raised. Up to this point, no reliable model has existed for MTRs in cyclic or dwell fatigue. This research has sought to develop and validate a model to accurately predict fatigue lifetimes while maintaining continuity with existing design schema.

## Description of Research

Dr. Pat Golden, an AFRL researcher, wrote a MATLAB code to solve the relevant linear elastic fracture mechanics equations in ~2004 . This code enabled deterministic prediction of fatigue lifetimes resulting from a starter flaw of a given, known, geometry and long crack growth data. In the spring of 2013 this project was picked back up and the existing fatigue prediction code modified to account for sensitivity to MTRs. The code was also extended to introduce the effects of small cracks and dwell cycles on fatigue life. The original code relied on standard linear elastic fracture mechanics, but the changes made the crack growth rates dependent upon whether the crack occurred within a microtextured region. A variety of different parameters and inputs were used in the predictive model including grain size, grain morphology, MTR sizes, crack growth rates, initial crack size, initial crack location, materials constants, and stress intensity solution using semi-elliptical flaws. All of these inputs were then run through an iterative lifetime equation to determine the number of cycles to failure for a sample under fatigue loading.(Equation 1) The model is of an infinitesimally small slice through the gauge section of an axially loaded fatigue specimen that is subjected to either cyclic or dwell fatigue loading. For example, a cyclic loading cycle may oscillate in a triangle wave form between a minimum and maximum load of 700 MPa at a frequency of 0.5 Hz while in dwell loading holds a constant stress at the peak load of each interval for a 120 seconds. The number of cycles to failure is calculated as:

$$N_f = \int_{a_i}^{a_f} \frac{1}{\frac{da}{dN}} da \quad (1)$$

Where  $da/dN$  is the crack growth rate and  $a_i$  and  $a_f$  are initiation and final crack sizes respectively. An elliptic crack was then initiated on the thin slice of material with a variable size and location and an elliptical MTR was defined around the crack. Within this MTR the crack propagated with small crack rates consistent with faceted growth and propagated as a long crack outside of the defined elliptical MTR. The location of each crack trip was tracked along its expansion and as each tip breached the MTR the growth rate of that tip changed. The driving forces of the crack growth and lifetime prediction followed traditional continuum mechanics. (Equation 2, 3, 4)

$$K = F\sigma\sqrt{\pi a} \quad (2)$$

$$\Delta K = K_{max} - K_{min} \quad (3)$$

$$\frac{da}{dN} = C\Delta K^m \quad (4)$$

Where  $K$  is the stress intensity factor,  $\sigma$  is the remote stress,  $a$  is the crack length,  $F$  is the shape factor,  $da/dN$  is the crack growth rate, and where  $C$  and  $m$  are constants dependent upon

the microstructure. The crack growth rate was pulled from experimental data borrowed from accepted literature. Different crack rates for dwell and cyclic fatigue loading were used as displayed in past research. Small dwell cracks were shown to consume the entire MTR incredibly quickly before propagating outside of the MTR. On the other hand, small cyclic cracks were shown to only accelerate moderately within the MTR. Different initiation locations were also used for cyclic and dwell cracks. Experimental results show that dwell cracks typically initiate below the surface while cyclic cracks typically begin on the surface of the component. The stress intensity factor was then calculated at each tip of crack to determine whether it had exceeded the fracture toughness, and Equation 1 integrated to determine the lifetime of the crack. (Equation 2, 3, 4) The stress intensity solution changed dependent on whether the crack was surface initiated, subsurface, or corner connected. The mathematical formulas for these solutions were pulled from literature from Newman, Raju, and Forman.<sup>1, 2</sup>

After the model was developed, the sensitivity of crack lifetimes to various parameters was determined. By automating a variety of values for the initial crack size, initiation location, and micro textured region size and aspect ratio, the sensitivity of fatigue crack growth was inspected at each possible combination of inputs. These lifetime results were then plotted using Origin and analyzed.

## Results

The two plots in Figure 3 show that the lifetime of a cyclically loaded component decreased as the initial flaw size increases, but the impact the original flaw size decreased as the applied load decreased. By contrast, the initial crack size had a minimal effect of the dwell fatigue lifetime at all stress levels. This was because the accelerated crack growth rate in the MTR for cyclic cracks overshadowed the small increase in stress intensity and the slightly faster initial crack growth rate. At lower applied stresses, the lifetime was more dependent upon the size of the MTR than on the size of the initial crack size. Finally, these two plots show the relative importance of initial flaw size increased as applied stress increases while the dependence on the MTR size decreased slightly.

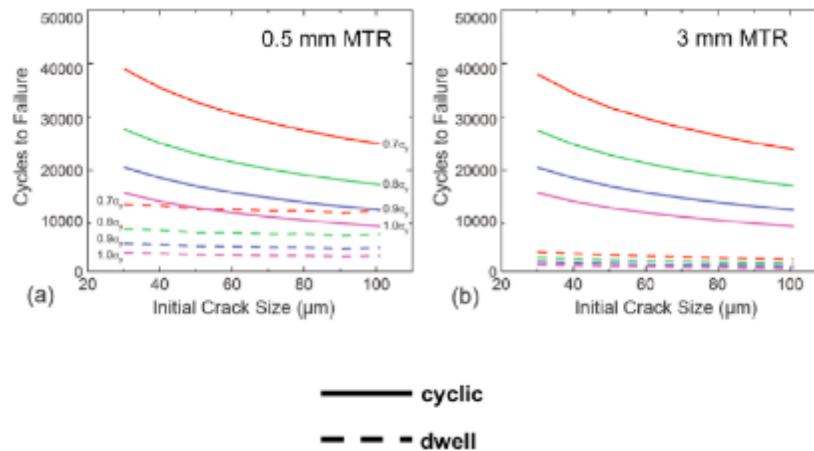


Figure 24: Plots of Lifetimes vs. Initial Crack Size

The following figure shows the correlation between the crack initiation site and the lifetime of the component. (Figure 4) There was up to a 33% difference in the lifetime of the sample depending on the location of the initiation site. The lowest lifetimes occurred when the

cracks initiate on the edges of the sample and the center initiated cracks have the displayed the longest lifetimes.

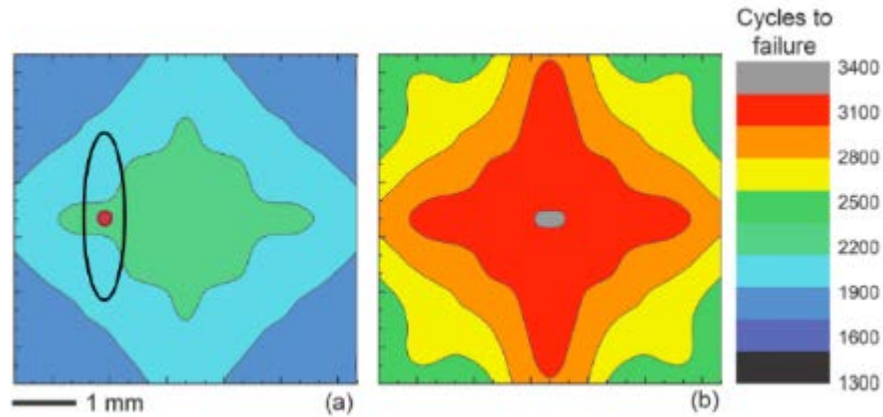


Figure 25: Contour Plot of Lifetime at Various crack initiation points

This project is still in progress and more results are forth coming. The model is currently under the process of being validated by comparing the predicted lifetimes to experimental results. It is also being expanded to predict lifetimes beyond the inclusion of MTRs and to continue to improve upon current fatigue models and simulations.

### Works Cited

1. J.C. Newman, I.S. Raju, NASA Tech. Memo. 85793, NASA Langley Research Center, Hampton, VA, 1984.
2. R.G. Forman, V. Shivakumar, in; Fracture Mechanics, vol. 17, ASTM STP 905, 1986, pp. 59-74.

OPTICAL CHARACTERIZATION OF SEMICONDUCTOR NANOSTRUCTURED  
MATERIALS

Project No. 0142.1

Sarah Hierath  
University of Dayton

9 May 2014

Government Project Leader  
Dr. Elizabeth Steenbergen  
AFRL/RXAN

Southwestern Ohio Council for Higher Education  
Student Research Program  
Agreement Number: FA8650-09-2-5800

## Acknowledgements

I would like to express my sincere gratitude to Dr. Elizabeth Steenbergen and Dr. Gail Brown for allowing me the opportunity to perform research for this project. I would also like to thank Dr. Steenbergen for her encouragement, support, and guidance throughout my time at the Air Force Research Laboratories. In addition to Dr. Steenbergen and Dr. Brown, I would also like to extend my appreciation to Dr. Kurt Eyink, Dr. David Zelmon, Dr. Kent Averett, and Dr. Said Elhamri for their assistance and kind instruction throughout my research experience.

## General Description of Project

Optical characterization of semiconductor nanostructured materials was conducted utilizing the non-destructive spectroscopic technique of Photoluminescence (PL). The nanostructured materials that were studied included InAs/InAsSb superlattices (SL) and ErAs/InAs quantum dot structures. This research was performed in order to determine the energy, the full width at half maximum (FWHM), and the integrated intensity of the peak emission from the sample over a varying range of intensities and temperatures. The goal of the research involving the InAs/InAsSb SLs was to determine the impact of varying beryllium doping levels and also the effect of annealing on the optical properties of the samples. The goal in studying the ErAs/InAs quantum dots was to determine the result of varying InAs spacing and ErAs deposition time within the structure.

## Description of Research

PL is a spectroscopic technique in which a sample is illuminated with light causing excitation of electrons in the valence band to the conduction band. The research conducted utilized a laser with excitation wavelength of 532nm. When the electrons of the sample are excited into the conduction band, they leave behind a pseudo particle called a hole. As the electrons come down from the conduction band and reenter the valence band they can recombine with the hole in a process known as radiative recombination. Radiative recombination leads to the emission of a photon. The light of the photons emitted from the sample are then sent through Fourier Transform Infrared (FTIR) spectrometer (an interferometer which consists of a series of mirrors and apertures). A Fourier Transform is then performed and the final product is an emission spectrum which can be analyzed in order to determine the emission intensity, the energy, the FWHM, and the integrated intensity of the peak. The research conducted varied either the input power of the laser (intensity dependence) or the temperature of the sample (temperature dependence).

Following the Fourier Transform the data can be viewed using a program called GRAMS which plots the emission intensity (a.u.) as a function of wavenumber ( $\text{cm}^{-1}$ ) and allows for visual comparison of multiple PL spectra. Intensity dependence data consists of increasing the input power of the laser from 10 mW to 1990 mW in varying increments at a constant temperature (between 4-10 K) while temperature dependence data consists of increasing the temperature of the cryostat from ~10 K to ~300 K in varying increments at a constant input power. A PL spectrum is generated for each intensity or temperature point.

The PL spectra were analyzed utilizing a computing program called OriginPro. The PL measurements were imported into an Origin file and the emission intensity as a function of

energy (eV) was plotted with both axes on linear scales and also with the emission intensity on a logarithmic scale as a function of energy on a linear scale. Each PL spectrum was fit with a Gaussian curve fit to determine the peak energy location, the integrated intensity and the FWHM of the PL peak. Lorentzian curve fits were also conducted on each PL spectrum; however Gaussian fits gave more consistent results. After curve fitting was completed, the peak position, FWHM, and integrated intensity were tabulated and used to conduct a series of plots. These plots included integrated intensity as a function of input intensity (of the laser, in  $\text{W}/\text{cm}^2$ ), the input power (of the laser, mW) as a function of integrated intensity, the FWHM as a function of input intensity, and the peak location as a function of input intensity.

The PL system consisted of a BOMEM FTIR, a closed-cycle cryostat with CsI window, a laser with excitation wavelength of 532 nm, and a lock-in amplifier.

## Results

The Be-doping study of the InAs/InAsSb SLs involved six samples; sample A was undoped, and samples B-F that were doped with beryllium concentrations of 0.5, 1, 3, 5, and 7 ( $\times 10^{16} \text{ cm}^{-3}$ ) respectively. The results of the effect of beryllium doping levels on the InAs/InAsSb SLs showed that the Be-doped SLs had lower energy PL peaks than the undoped SL. For the doped SLs, with an excitation intensity of  $1.3 \text{ W}/\text{cm}^2$  and a temperature of 4 K, as the Be-doping concentration increased, the PL peak energy increased. The PL peak intensity increased until the Be-doping concentration was  $3 \times 10^{16} \text{ cm}^{-3}$  after which the PL peak intensity decreased. These PL spectra are shown in Figure 1.

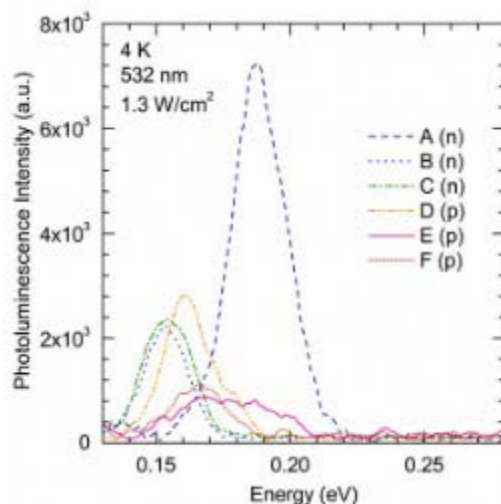


Figure 1. PL spectra for Be-doping samples taken at 4 K with excitation intensity of  $1.3 \text{ W}/\text{cm}^2$  (Steenbergen, 2013).

The initial results of the ErAs/InAs quantum dot study were evaluated and it was found that there was a need to refit the PL spectra utilizing a multi-peak Gaussian curve fit in order to obtain more accurate results. Final conclusions were not yet made, as the multi-peak fit had not been conducted.

## Works Cited

Steenbergen, Elizabeth, Elhamri, Said, Asel, Thaddeus, Mitchel, William, Hierath, Sarah, and Gail Brown. "Impact of Be-doping on the material properties of InAs/InAsSb type-II superlattices for infrared detection." SPIE Proceedings 8993 (2013).

## Related Activities

In addition to conducting optical characterization of nanostructured semiconductor materials, I also completed a number of tasks involving lab organization. I updated a standard operating procedure (SOP) for the use of the lasers in the laboratory and proofread a paper to be published by Dr. Steenbergen. I updated the list of equipment assigned to the laboratory and placed rubber lining throughout the shelving and cabinets of the laboratory, underneath electrical devices. I also assembled a storage cabinet and labeled various storage units throughout the laboratory.

In conjunction with a course at the University of Dayton, I presented a portion of my research in poster format at the Ohio Regional American Physical Society meeting at Youngstown State University and also at the Stander Symposium at the University of Dayton. The research presented was on the effect of annealing on the optical, structural, and electrical properties of InAs/InAsSb SL. One sample, of Be-doping concentration of  $5 \times 10^{16} \text{ cm}^{-3}$  was successfully annealed at 460°C for 1 minute utilizing Rapid Thermal Annealing. PL, X-Ray diffraction (XRD), and Hall-effect measurements were taken on the sample prior to annealing and XRD was taken on the sample after the annealing was completed. X-Ray diffraction is a technique in which incident x-rays hit a sample and are diffracted into a detector. The angle at which the x-rays are diffracted depends on the structure of the sample and allows for structural characterization. Hall-effect measurements included determination of the Van der Pauw voltages, sheet resistivity, carrier concentration and mobility, and sample type (n or p).

OPTICAL CHARACTERIZATION OF SEMICONDUCTOR NANOSTRUCTURED  
MATERIALS

Project No. 0142.2

Henry Bourassa  
University of Dayton

31 August 2014

Government Project Leader  
Dr. Elizabeth Steenbergen  
AFRL/RXAN

Southwestern Ohio Council for Higher Education  
Student Research Program  
Agreement Number: FA8650-09-2-5800

## **Acknowledgements**

I would like to thank Dr. Said Elhamri for his help in providing the opportunity to interview with Dr. Steenbergen for the position. I would also like to thank Dr. Elizabeth Steenbergen for providing me with this amazing research opportunity here at Wright-Patterson Air Force Base. I would like to thank Dr. Kurt Eyink and Dr. Gail Brown for allowing me to work with them when Dr. Steenbergen was gone earlier as well as now while she is on maternity leave.

## **General Description of Project**

This project uses photoluminescence measurements in the characterization of semiconductor nanostructured materials at varying excitation intensities as well as temperatures. These measurements are closely related to research done on life time of semiconductor materials. This is important in order to know how these materials can be used in devices as well as which ones can be used for specific devices.

Due to lab renovations the experimental set up had to be taken down and stored for safe keeping. The process of getting the lab ready for renovations was long and arduous. Due to the current state of the lab data acquisition has been postponed until the renovations are completed.

## **Description of Research**

The process for each sample was as follows, samples were mounted on the cold finger of the closed system cryostat. Then the alignment of the laser was checked to ensure that the laser was on the sample. The cryostat then had a vacuum pulled on it. Once the cryostat was under sufficient vacuum the compressor was turned on and the cooling process began. Once the cryostat was cooled to four degrees Kelvin or eight degrees Kelvin (depending on the cryostat in use) intensity dependent data was taken. Data was obtained using a Fourier transform infrared spectrometer (FTIR). The intensity dependent data ranged from 10 milliwatt (mW) excitation intensity to 1990 mW. After intensity dependent data was taken it was used to determine a suitable intensity for temperature dependent data. Once the temperature dependent data has been taken all data taken on the sample is placed on a CD in order to transfer the files from the stand alone computers that run the FTIR's and take the data, to the secure view computer in order to perform data analysis. Each sample takes a minimum of one day for data collection. This summer there was data taken for approximately 30 samples. Data analysis is done using software called Origin. Origin was used for plotting graphs, curve fitting, as well as table making, calculations, and organization of data.

## **Results**

The results of the data taken this summer have yet to be determined. The meaning of the results will be discussed when Dr. Steenbergen returns from maternity leave. Till then data analysis in Origin will be performed on data already taken.

LAYER BY LAYER ASSEMBLY OF GRAPHENE FOR WEARABLE ELECTRONICS

Project No. 0146

Krishawn Ward  
Central State University

31 August 2014

Government Project Leader  
Dr. Urbas Augustine  
AFRL/RXAP

Southwestern Ohio Council for Higher Education  
Student Research Program  
Agreement Number:

## **Acknowledgements**

I would like to thank Dr. Urbas Augustine for taking the time out his busy schedule to sit with me and guide me through this whole project from the start. Another person who I would like to thank is Doug Krien. He was very patient with me throughout the whole project and was always there when I had a question or needed any materials, he did not hesitate to help me. Giorgio Bazzan and Mike Dillion also played a huge role in this project. They trained me everyday on the necessary machines and instruments until I was familiar and comfortable with using them on my own. These people taught me a lot throughout the course of this project and would like to thank them all.

## **General Description of Project**

The objective of this project was to combine fabrics and electronics as a whole by making a radio conductive fabric by getting nanometer sized graphene sheets small enough to settle inside fabric. This objective would be carried out by using the layer by layer process or layer by layer assembly. Layer by layer assembly is when a substrate is soaked in oppositely charged polymers to create bilayers onto the substrate. The reason for using graphene to make this radio conductive fabric is because of the good characteristics graphene has to carry out this objective. Graphene is a good RF conductor (radio frequency). The flexibility of graphene is a good characteristic because this way the graphene will be flexible enough to settle inside fabric with it being stiff. Also it can withstand a high amount of temperature, which is beneficial so when the graphene is settled in the fabric it will not heat up quick.

## **Description of Research**

The graphene was prepared out of the substance graphite. To prepare the graphene 22mg of CTAB the approach that was taken was peeling the graphite sheets using an ultrasound. The ultrasound uses high frequency sounds that vibrate the graphene and peel them into single sheets. The sheets were then separated using a machine called a centrifuge. Vials are placed inside of the centrifuge and spun at high speeds for whatever the set time is and separates the layers from the excess clumps of graphene. The graphene was then dialyzed for 1 hour. After the graphene was dialyzed a negatively charged polymer called polyethylenimine (PEI) was used to bind to the proteins in the positively charged graphene. There was no measured amount of PEI to inside the graphene. The goal at this stage was to add drops of PEI inside of the graphene until the pH was stable at 9. When the pH stabilized the graphene was then dialyzed for a final time for 24 hours.

After the graphene was made the layer by layer assembly was then performed. PAA (poly acrylic acid) being the negatively charged polymer and graphene being positively charged layers can be built. Instead of wasting fabric to run test, glass slides were cleaned and used to soak inside of the polymers. There were six vials. One vial was filled with graphene and the other vial was filled with PAA. The other four vials were filled with water to rinse off the glass slides.

The glass slides in the layer by layer process started off being soaked in each polymer for 5 min. The glass slide is negatively charged, so it was first soaked in the graphene which is positively charged. Then it is soaked in the water for five minutes to wash off the excess graphene to make one thin layer on the glass slide. After being soaked in the first vial of water

the glass slide was dried with nitrogen and put inside the spectrometer. The spectrometer was set to measure absorbance. Light is sent from one side of the sample and comes out the other side and the amount of light that is absorbed is recorded and put in a graph. The more light that is absorbed shows that there is more and more polymer on the glass slide. After measuring the graphene then the glass slide is then soaked inside the negatively charged PAA for five minutes and this process is repeated back and forth until a decent amount of layers is formed. After successfully creating bilayers of graphene oxide onto the glass slides, fabrics were then used to begin to create the Radio conductive fabric.

The same procedure that was used with the glass slides are used with the fabric. The fabric that was used was a pure white cotton fabric. The fabric was cut into 8 strips. These 8 strips are to monitor the build graphene oxide build up on the fabrics. To further clean the fabric they are soaked in bleach for five minutes and dried.

The all the strips of fabric was soaked in the PAA for 5 minutes, then soaked inside 4 beakers of water sitting inside a sonication bath for 5min each.

The first strip will be run with nothing deposited onto it to view the fabric as a clean white strip. The second strip will show one layer of PAA. The second strip will show one layer of PAA and one layer of graphene oxide. The third strip will have one layer of PAA, 1 layer of graphene oxide, and one layer of PAA and etc.

## Results

After running numerous trials there were no layers of graphene. So the soak time in the polymer was changed. In figure one it shows the results given from the spectrum after the first few trials. Instead of soaking the glass slides in the polymer for five minutes each, the slides were soaked for an hour each. The soak time was increased because the polymer probably wasn't soaking long enough for it to adhere to the slide.

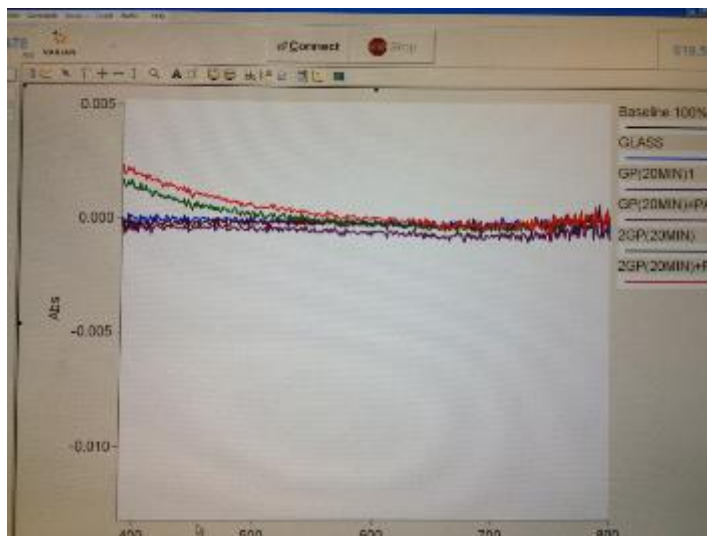
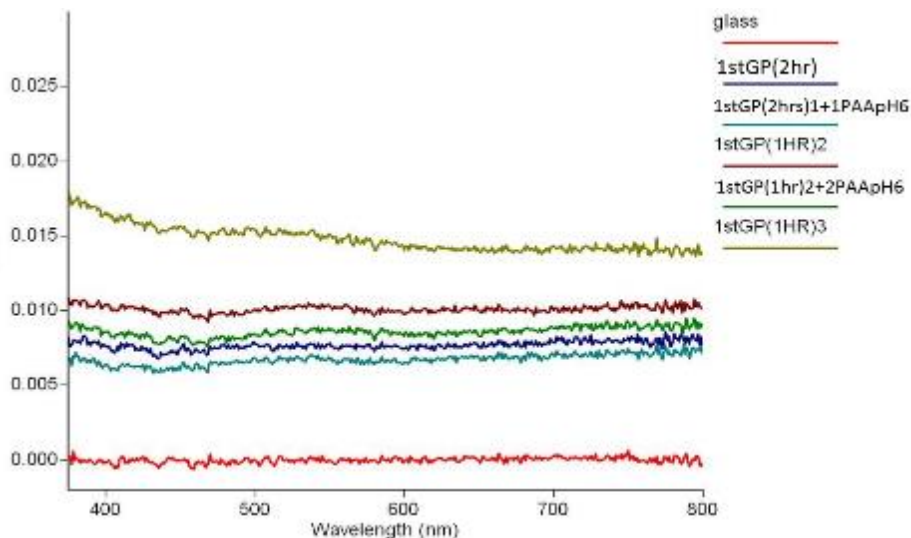


*Fig.1*

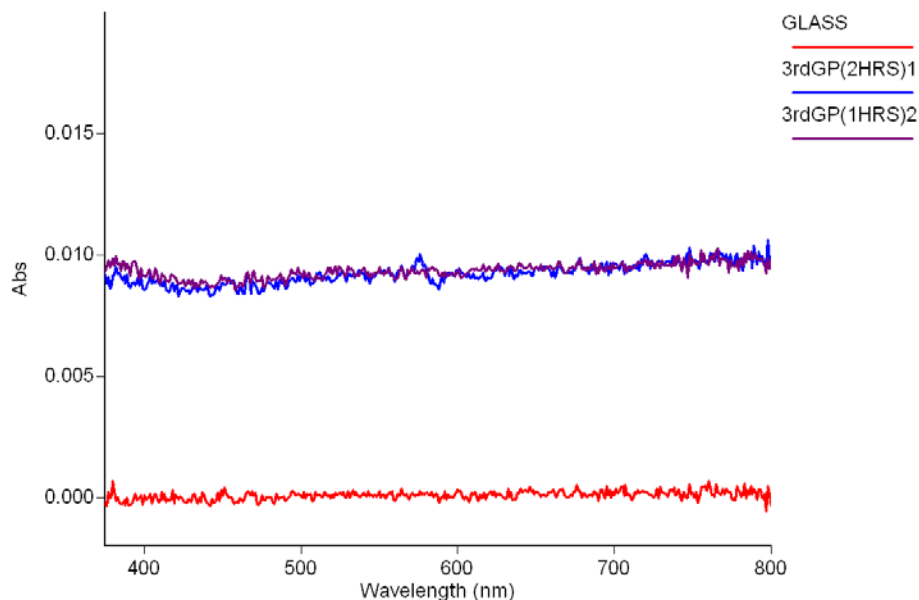
Increasing the soak time shows that the time had little effect on the slide. There were no uniform layers that showed on the graph. The factors that could be giving these uniformed

layers could be the graphene could be breaking down too fast. An observation was made when the graphene is sitting for a couple days it begins to aggregate.

A commercial graphene oxide was purchased and used instead of the regular graphene. Graphene oxide is not as good as regular graphene because of the oxygen that's inside the graphene will make the fabric heat up faster but, it still can be used for this experiment. After replacing the regular graphene with the commercial graphene oxide, multiple bilayers were able to be seen building up on the glass slide when read through the spectrometer.

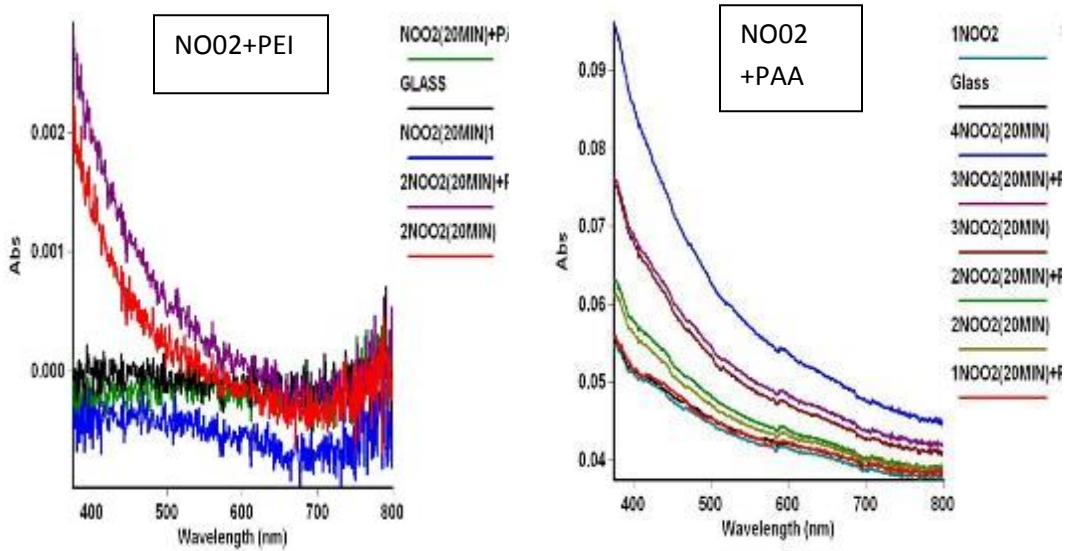


After repeating these bilayers, to show that the graphene indeed needed the PAA to Build these layers and that the PEI would not be suitable to create these graphene bilayers.

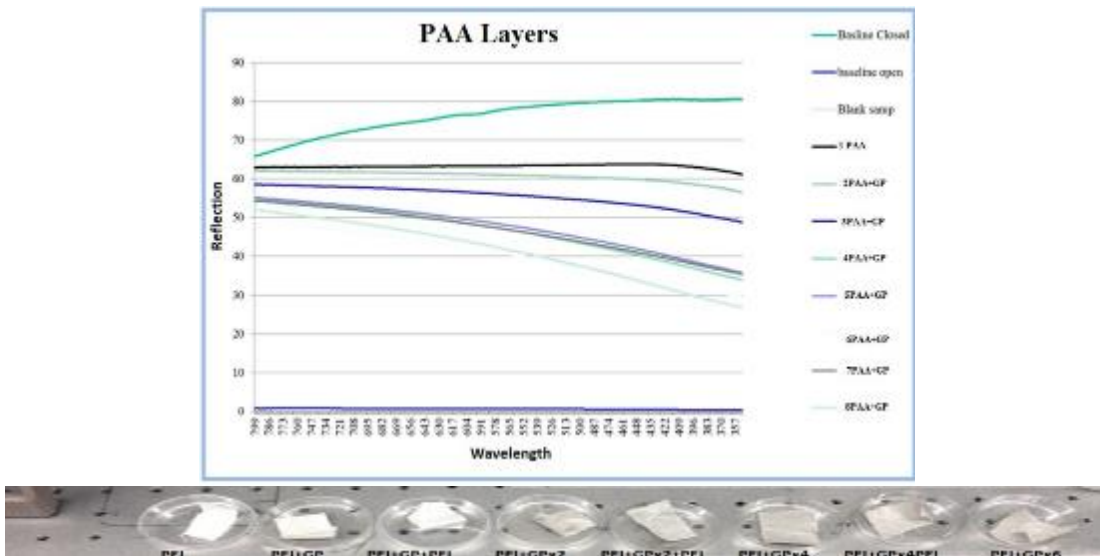


*Graphene on Graphene spectrum. No build up.*

To show that the Graphene oxide will not be able to build multiple bilayers when soaked with PEI, test was run with both the PAA and the PEI.



When the graphene oxide is deposited on the fabric and read through the spectrometer, bilayers were seen on the built up on the fabric. Currently the experiment is in the event of taking these fabrics and measuring the conductivity for future results.



### Work Cited

Guoxiu Wang, Juan Yang, Jinsoo Park, Xinglong Gou, Bei Wang, Hao Liu, and Jane Yao. "Facile Synthesis and Characterization of Graphene Nanosheets" *J. Phys. Chem. C* 2008, 112, 8192-8195

Sile S Ugur, Merih SaruSik, and A Hakan Aktas. "The Fabrication of nanocomposite thin films with TiO<sub>2</sub> Nanoparticles by the Layer-by-layer deposition method for multifunctional cotton fabrics." *Nanotechnology* 21 (2010) 325603.

THIN FILM DEVICES

Project No. 0147

Jason Anders  
Wright State University

31 August 2014

Government Project Leader  
Dr. Andrey Voevodin / Dr. Michael Check  
AFRL/RXAN

Southwestern Ohio Council for Higher Education  
Student Research Program  
Agreement Number: FA8650-14-2-5800

## **Acknowledgements**

I would like to thank Dr. Andrey Voevodin for bringing me into his group. I would like to thank my advisor, Dr. Gregory Kozlowski for helping my transition into this new project, as well as continuing support toward my PhD. I would like to thank the help and support that I have received from Dr. Michael Check. I also would like to thank my employer, Brittany Edwards from SOCHE for allowing me to be on base.

## **General Description of Project**

Transition metal dichalcogenides (TMCs) are important in scalability for electronic devices. They are scalable down to the atomic level, creating essentially two dimensional structures. These structures can be used in transparent, flexible, In house equipment used in growing the thin films include: pulsed laser deposition (PLD), magnetron sputtering, chemical vapor deposition (CVD), and molecular beam epitaxy (MBE).

## **Description of Research**

The first approach toward building thin film devices involved the creation of shadow masks in coordination with magnetron sputtering of material. Shadow masks allow deposition of material in a specific region on the substrate. Once the mask is removed, coverage is restricted to the area of the mask, acting as a stencil. Additional material, with masks of various design, were used to build up the layers in a vertical stack.

## **Results**

The technical details of developing the mask in terms of high resolution laser etching were worked out with the laser engineer. Devices made from masks are currently being tested for Field Effect Transistor properties.

LABORATORY AUTOMATION AND DATA ANALYSIS

Project No. 0149.2

Jason Beckman  
Wright State University

31 August 2014

Government Project Leader  
Dr. Donald Dorsey  
AFRL/RXAN

Southwestern Ohio Council for Higher Education  
Student research Program  
Agreement Number: FA8650-09-2-5800

## **Acknowledgments**

I would like to thank everyone at AFRL that has helped me during my internship, but most importantly, I would like to express appreciation to the people who helped me with this project. Brittany Edwards, my SOCHE advisor, ultimately made this opportunity possible. Dr. Don Dorsey, Dr. Eric Heller and Dr. Elizabeth Moore provided me with the theoretical guidance necessary to interpret the data that was collected. John Hoelscher and Jeff Brown acted as my mentors, giving me hands on guidance and constant feedback, ultimately leading to the success of this project.

## **General Description of Project**

The degradation of commercially processed Gallium Nitride (GaN) High Electron Mobility Transistors (HEMTs) was studied during constant voltage, long duration electrical stress tests. Previous literature has suggested that the reliability of GaN HEMTs is questionable due to degradation during hot electron stress, among other factors. This project sought to study the effects of hot electron conditions on these devices. From current-voltage (IV) measurements made before, during, and after stress, changes in drain current ( $I_d$ ) and gate leakage current ( $I_g$ ) could be seen immediately following stress. With rest and exposure to light, however, recovery is observed with no permanent degradation on the device, even after undergoing stress testing with drain voltages up to 200V. It is deduced that there is little permanent degradation due to hot electron stressing and limited reliability concerns in the GaN HEMTs that were tested at typical operating conditions.

## **Description of Research**

The devices tested were commercially made GaN HEMT structures. Figure 1 shows a basic form of HEMT structure. Two lots of transistors were tested, one with, and one without a source connected field plate. All transistors tested were cut from the same wafer. The devices were grown on a Silicon Carbide (SiC) substrate with an Aluminum Gallium Nitride (AlGaN) barrier, and a GaN buffer. Each device was mounted in the standard method, in an LPA package, using silver bearing epoxy, and wire bonded with 0.0007" gold wire.

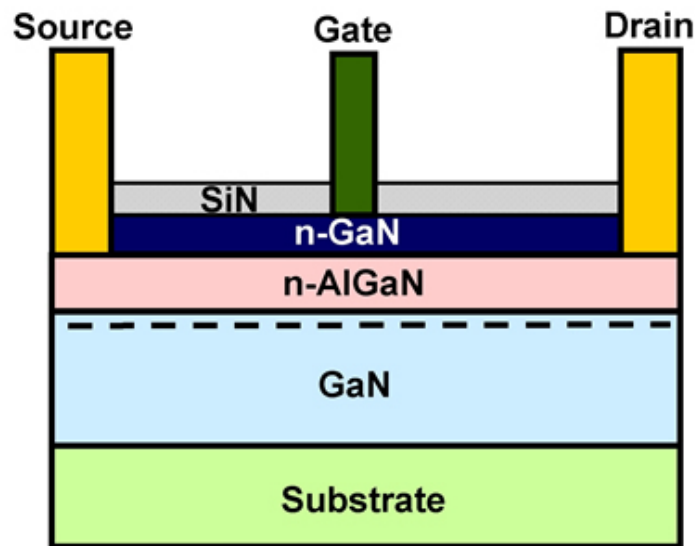


Figure 26 A Generic GaN HEMT structure

Samples were tested utilizing a Keithley 2612A Source Measurement Unit (SMU). Shielded coaxial cables were used to connect the SMU to the custom copper test block, where the devices were operated. Light exposure was done with an AmScope HL-250-A white light source and measurements were recorded using custom test code written in the Keithley TSP software. The code was adjustable and automated to allow long duration stressing at any gate and drain voltages. Characterization could be programmed at set intervals, and could be adjusted to collect several families of measurements.

The hot electron stress testing was conducted at drain biases ( $V_d$ ) ranging from 30V to 200V. Gate bias ( $V_g$ ) was selected to be the voltage that induces hot electron effects, and varied based on the specific device. The samples were electrically characterized pre and post stress by a IV family of curves. Each stress step consisted of a set number of hours at a hot electron condition, followed by an electrical characterization.

## Results

The samples were stressed with the main purpose of inducing degradation in GaN HEMTs at an accelerated rate. Care was taken to minimize degradation due to thermal effects, in order to better study the hot electron degradation mechanisms. Approaches to inducing device degradation through hot electron stress have been reported in the literature. After failing to observe significant permanent degradation after stressing the device at a drain voltage of 30V and a gate voltage of -2V, the drain voltage was increased to 200V. The devices were stressed at drain voltages of 200V and a gate voltage of -2.5V for a duration of 150 hours. Baseline measurements were taken pre and post stress and can be seen in figures 2 and 3. It can be seen that the post-stress IV and  $G_m$  curves (dotted lines) show minimal change compared to the pre-stress curves.

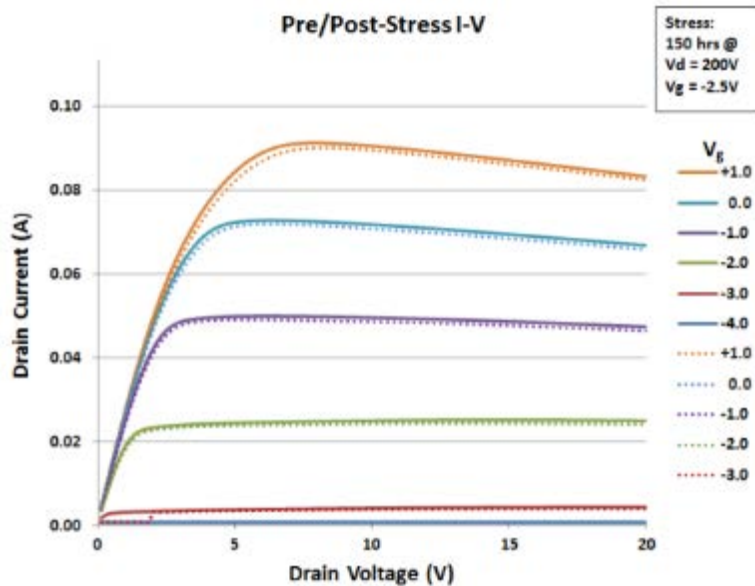


**Figure 2:** Pre vs. Post Stress IV-Family

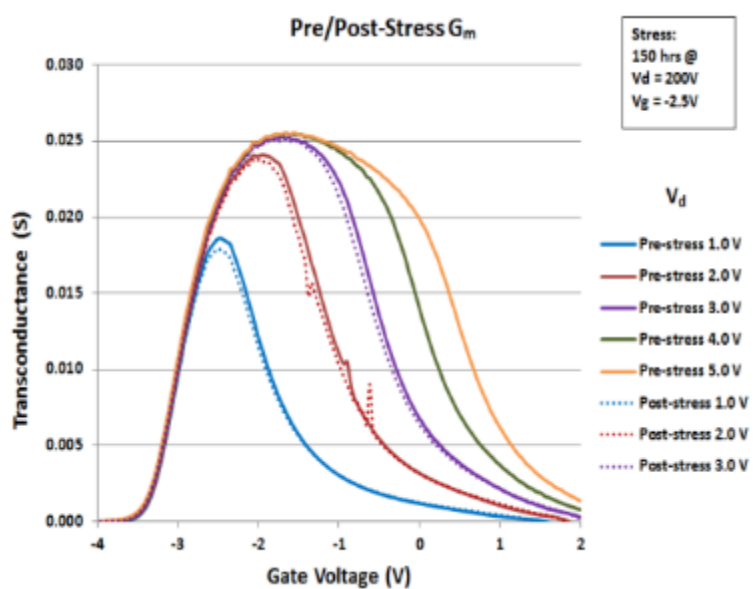


**Figure 3:** Pre vs. Post Stress Transconductance

Hot electron stressing using known and reported stress conditions was conducted on a commercially processed sample lot of devices to evaluate the extent of hot electron degradation. At a drain voltage of 200V, minimal change is seen in the drain current and transconductance, indicating that either hot electron degradation has not occurred or that the devices were not experiencing hot electron stress. At nominal operating conditions and elevated drain voltages, temporary degradation from fast-resetting traps was observed, but no permanent degradation from hot electron stress was observed. It can be concluded that previous doubts about the reliability of GaN HEMTs may no longer be founded, and tests among a larger lot of commercial devices should be performed.

## Works Cited

- B. Poling, J. Brown, E. Heller, B. Stumpff, J. Beckman, A. Hilton, "Hot Electron Stressing,"
- B.D. Christiansen, R.A. Coutu Jr., R. Vetury, J.B. Shealy, E.R. Heller, B. Poling, G.D. Via, "Reliability Testing of AlGaIn/GaN HEMTs under Multiple Stressors," IEEE IRPS Conf., 2011, pp. CD.2.1-CD.2.5

ANGLE RESOLVED EMISSION/ABSORPTION TECHNIQUE FOR ANALYSIS OF A  
SERIES OF GOLD NANOPARTICLE DECORATED CARBON NANOTUBES

Project No. 0152

Teresa Demeritte  
Jackson State University

29 July 2014

Government Project Leader  
Dr. Rajesh Naik  
AFRL/RXAS

Southwestern Ohio Council for Higher Education  
Student Research Program  
Agreement Number: FA8650-09-2-5800

## **Acknowledgments**

My deepest appreciation goes to Dr. Angela Campbell and Dr. Augustine Urbas for the opportunity of starting this project with them during the summer of 2012 and 2013 and Dr. John T. Grant for training on the XPS and data processing. I would also like to thank Dr. Rajesh Naik for being a great mentor and allowing me to join his group the summer of 2014 and his postdoc Dr. Abrin Schmucker for his dedication and guidance. Thank you to Asheley Blackford/The Research Collaboration Program for your mentorship and to SOCHE for financial support. Last but not least I would like to thank Dr. Benji Maruyama, his group and Dr. Weijie Lu for their assistance in growing the carbon nanotubes used in this project.

## **General Description of Project**

This project focused on the synthesis of vertically aligned carbon nanotubes on various substrates and modifying them with gold nanoparticles for use as potential blackbodies absorbers, purification systems, and biosensors. Carbon graphitic materials are good absorber because of their  $\pi$ -band optical transitions. Vertically aligned carbon nanotubes (VACNT) in particular appear extremely dark. We intend to develop plasmonic blackbody absorbers by adding gold (Au) coated nanostructure to vertically aligned carbon nanotube (GNP/VACNT) films to produce materials with optical absorbing properties superior to VACNT films or metal nanostructures alone

A blackbody absorber could be produced using a thin film composed of anisotropic gold nanoparticles and carbon nanotubes in its active layer. This device architecture would combine the plasmonic wavelength tenability of gold nanoparticles in the infrared with the visible light absorbing ability of carbon nanotubes to offers an ultra-wide spectral range that can be used in various applications.

## **Description of Research**

Vertically aligned carbon nanotubes were grown using a catalyst-gas mixture at very high temperatures by chemical vapor deposition (CVD). In order to control the diameter, length, and density of VACNTs, the identity of the catalyst and substrate were manipulated or the ratio varied, while the pressure, temperature, the flow rate and residence time was kept constant to obtain optimal results.

### *Vertically Aligned Carbon Nanotube Growth Using Chemical Vapor Deposition:*

The VACNTs were prepared by using a CVD technique on sapphire, quartz, and carbon substrates using previously published protocols. Briefly, a 10 nm aluminum layer and a 1.5 nm iron catalyst layer were deposited on each substrate in advance using an atomic layer deposition technique. Substrates were added to a quartz tube before being placed in a furnace. The VACNTs were grown at 750 ° C in a Ar/H<sub>2</sub> buffer gas (15 vol% H<sub>2</sub>) by injecting a mixture of xylene and ferrocene as the carbon source. Nanotube growths were characterized using scanning electron microscopy (SEM) (Figure 1) and Raman spectroscopy.

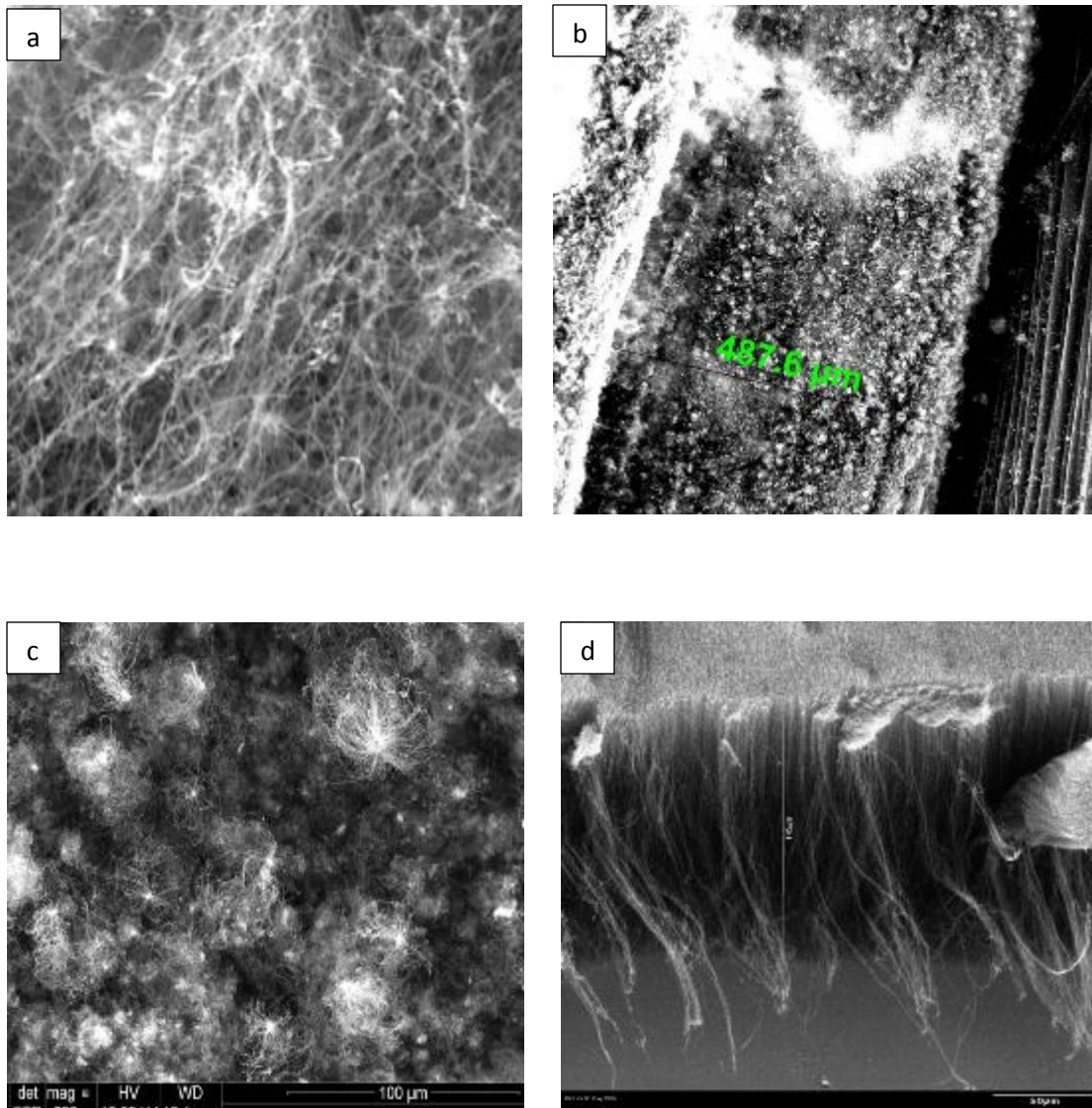


Figure 1. SEM images of carbon nanotubes grown with CVD on different substrates with constant growth condition. a) CNT grown on SiO<sub>2</sub> substrate. b) Side view CNT grown on carbon foil substrate and c) top view of carbon foil substrate. d) Side view of CNT grown on sapphire substrate.

#### *Vertically Aligned Carbon Nanotube Growth using Ultra High Vacuum*

To remove some of the challenges of growing carbon nanotube (CNT) using chemical vapor deposition, an ultra high vacuum (UHV) chamber was used for diffusion controlled metal catalytic growth of carbon nanotube. Silica substrates were etched with HF and allowed to dry. The substrate was oxidized at 1000 ° C for four hours to form SiO<sub>2</sub>. Using a DC magnetron sputter, 50 nm of amorphous carbon and 5 nm of Ni were deposited onto the SiO<sub>2</sub> substrates. Vertical structures were formed by annealing the substrates under UHV at 600 ° C for 20 minutes in oxygen at a partial pressure of 10<sup>-8</sup> Torr. CNTs were characterized using x-ray photoelectron spectroscopy (XPS), atomic force microscopy, and SEM (Figure 2).

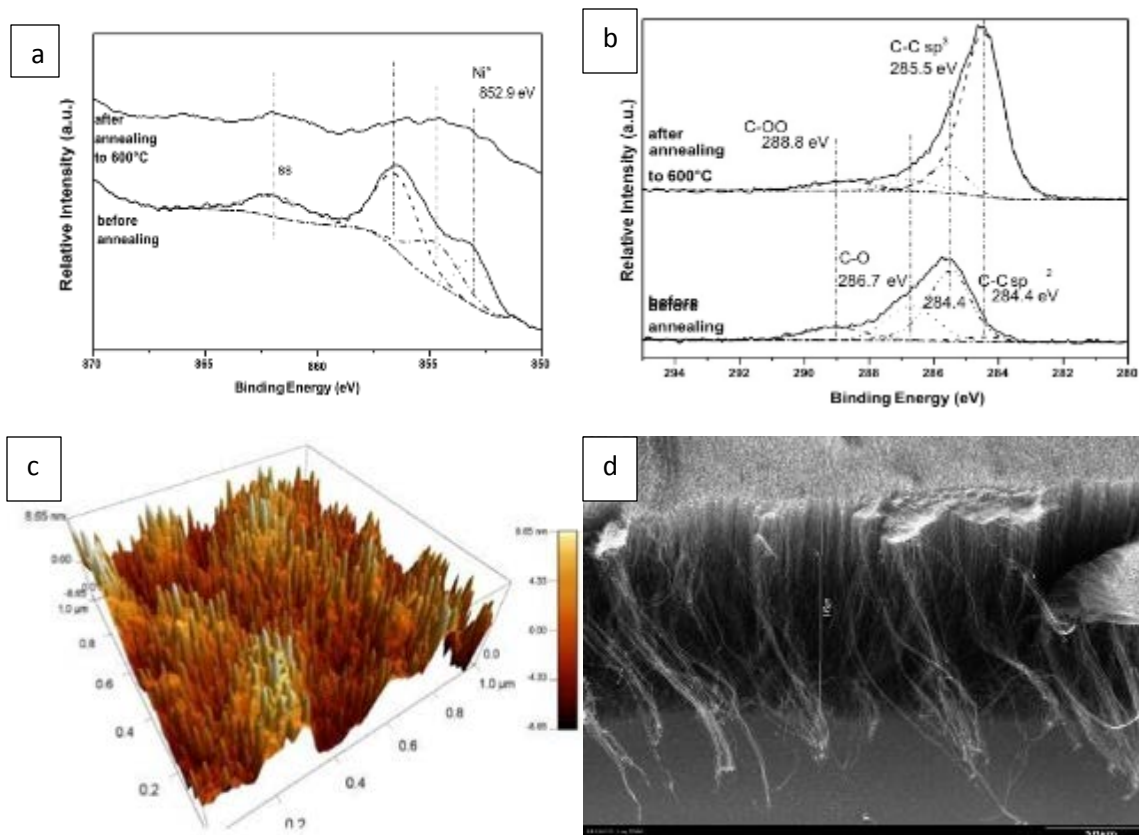


Figure 2. Characterization of CNT grown using ultra high vacuum in the presence of oxygen. a) XPS of Ni before and after annealing b) XPS of C<sub>2</sub> before and after annealing c) AFM of CNT growth showing formation of vertical structures. d) SEM of CNT growth using UHV.

#### *Gold Nanoparticles Formation on VACNTs with annealing:*

We initially planned to decorate VACNTs with 50 nm gold (Au) nanoparticles. The Au nanoparticles would have formed by a high-temperature annealing process. A 50 nm Au layer would have been deposited using a sputter coater. The Au/vertically aligned CNTs were to be placed into quartz tube and evacuated. A high-purity Ar gas would have been introduced and heated at 1000 °C for 5 min. After careful consideration we found that this process would be too costly and are looking into alternative methods to decorate VACNTs.

#### *Synthesis of anisotropic gold nanoparticles:*

##### Gold nano-popcorns

The gold nano-popcorn will be prepared using a two-step process. First spherical gold seeds will be synthesized by mixing aqueous solutions of  $2.5 \times 10^{-4}$  M hydrogen tetrachloroaurate(III) hydrate (HAuCl<sub>4</sub>) with  $10^{-4}$  M trisodium citrate (TSC) in 20 mL of double- distilled deionized water (18 MΩ). 60 μL ice-cold, of 0.1 M freshly prepared aqueous solution of sodium borohydride, (NaBH<sub>4</sub>) will then be added under vigorous stirring. The final solution should be a bright red and kept in the dark for at least 2 hours before use. The nano-popcorn will then be

grown using the seed-mediated growth procedure in the presence of Cetyl trimethylammonium bromide (CTAB). For this preparation, we will dissolve 0.05 g of CTAB in 46.88 mL of H<sub>2</sub>O by sonication in a small vial, followed by the addition 2 mL of 0.01 M HAuCl<sub>4</sub> · 3H<sub>2</sub>O under constant stirring. Next, 0.3 mL of 0.01 M Silver nitrate (AgNO<sub>3</sub>) and 0.32 mL of 0.1 M ascorbic acid (AA) drop wise will be added to the solution to mixed properly. The solution should turn from yellow to colorless and 0.5 mL of gold nano-popcorn seed will be added and allowed to stir for 2 min.

#### Gold nanorods (Park's method)

The Au NRs will be synthesized by a seed-mediated growth process in presence CTAB growth solutions and AgNO<sub>3</sub>. The seed solution will be prepared by dissolving 0.025 mL of 0.1 M HAuCl<sub>4</sub> in a 10 mL aqueous 0.1 M solution of CTAB. 0.6 mL of freshly prepared, ice-cold 0.01 M NaBH<sub>4</sub> solution will then added into the mixture under vigorous stirring for approximately 1 minute. The seed solution should be allowed to rest for 10 mins before being added into the growth solution. The growth solution was prepared by mixing 0.5 mL of 0.1 M HAuCl<sub>4</sub>, 0.08 mL of 0.1 M AgNO<sub>3</sub>, and 100 mL of 0.1 M CTAB followed by the addition of the 0.55 mL of 0.1 M ascorbic acid solution as a mild reducing agent. The prepared solution will then be divided into five vials, each containing 20 mL of growth solution. Varying the volume of seed solution (8, 16, 32, 80, and 160 µL) will be added into each vial, and the solution will gently be shaken for 30 s. The as-made Au NR solution should be kept at 25 °C for 24 h to ensure the complete growth.

#### Concave cubes (O'Brien's method)

Briefly, as-synthesized nanorods will first be centrifuged two times for 15 minutes at 8,000 rpm to remove excess reagents, each time resuspending the nanorods in 50 mM CTAB. An extinction spectrum should be collected to determine nanorod concentration, and using 50 mM CTAB the nanorod solution will be brought to 2 OD. Then this solution will be brought to a final HAuCl<sub>4</sub> concentration of 90 µM and allowed to gently stir for 4 hours at 40°C. Centrifuged the solutions two times for 30 min at 11,000 rpm, resuspending the nanoparticles each time in 100 mM cetylpyridinium chloride (CPC) to terminate the reaction. It should be noted that batch-to-batch variations in the nanorod synthesis could affect the optimal concentration of HAuCl<sub>4</sub> required for dissolution. To account for this, small 0.5 mL test batches should be etched over a range of HAuCl<sub>4</sub> concentrations (60-100 µM in 10 µM increments) and the resultant solutions can be analyzed by UV-Vis spectroscopy and as the gold concentration is increased in this process, the aspect ratio of the nanorods decreases until a sphere- like geometry is observed. To synthesize concave rhombic dodecahedra (CRD), 20 mL of 10 mM CPC, 350 µL of 10 mM HAuCl<sub>4</sub>, 4.5 mL of 100 mM ascorbic acid, and 6 mL of seeds (at 1 OD concentration) will be mixed in succession and allowed to grow for ~15 minutes. Next, the CRD solution will be centrifuged two times for 10 minutes at 10,000 rpm and the CRD resuspended in 50 mM CTAB each time. CRD dissolution was performed at 40°C, in 50 mM CTAB, with a CRD concentration of 1 OD, and a typical final HAuCl<sub>4</sub> concentration of 60 µM, with gentle stirring for 4 hours. As described above, small 0.5 mL test batches should be used to ensure appropriate dissolution conditions. It should be noted that decreasing the volume of seeds added to the CRD synthesis can increase CRD size, and these CRD can be used to produce larger nanoparticle seeds with no loss in

quality up to 100 nm. Concave cubes will be prepared with a protocol modified from Lu, et al. Briefly, 5 mL of 100 mM CPC, 250  $\mu$ L of 1 M HCl, 250  $\mu$ L of 10 mM HAuCl<sub>4</sub>, 62.5  $\mu$ L of 10 mM AgNO<sub>3</sub>, and 47.5  $\mu$ L of 100 mM ascorbic acid will be mixed with varying seed volumes and allowed to react for 2 hours.

#### Concave cubes (Zhang method)

Au seeds can be prepared by quickly injecting 0.60 mL of ice-cold, freshly prepared 10 mM NaBH<sub>4</sub> into a rapidly stirring solution containing 0.25 mL of 10 mM HAuCl<sub>4</sub> and 10.00 mL of 100 mM cetyltrimethylammonium chloride (CTAC). The seed solution is allowed to stir for 1 minute and then left undisturbed for 2 hours. A growth solution is prepared by consecutively adding 0.50 mL of 10 mM HAuCl<sub>4</sub>, 0.10 mL of 10 mM AgNO<sub>3</sub>, 0.20 mL of 1.0 M HCl, and 0.10 mL of 100 mM ascorbic acid is added to 10.00 mL of 100 mM CTAC. The seed particles are serially diluted in 0.1 M CTAC to generate solutions ranging from 1/10 to 1/104 the concentration of the original seed solution. A typical synthesis of concave cubes is initiated by the addition of 0.1 mL of the diluted seeds to the growth solution. The reaction is swirled immediately after the addition of the seeds and then left undisturbed for 24 hrs.

## Results

Carbon nanotubes were grown using several different growth conditions. Growth could not be controlled using CVD; different CNT carpets were produced using identical growth conditions. The use of ultra high vacuum seems to be a promising alternative to CVD growth. Vertically aligned carbon nanotubes were grown by diffusion of nickel in an amorphous carbon source using oxygen at 10<sup>-8</sup> Torr. The nickel is believed to catalytically promote the growth of CNTs by converting the sp<sup>3</sup> carbon to sp<sup>2</sup> carbon as confirmed by x-ray photoelectron spectroscopy. Atomic Force Microscope images confirmed the growth of vertical structural features and Raman scattering data indicated the formation of SWCNT bundles. Gold nanoparticles were synthesized and characterized for use with CNTs. This project is still on going, and the decoration of VACNTs with GNP is the next step in this project.

## Works Cited

- Kumar, Suresh, Inderpreet Kaur, Keya Dharamvir, and Lalit M. Bharadwaj. "Controlling the Density and Site of Attachment of Gold Nanoparticles onto the Surface of Carbon Nanotubes." *Journal of Colloid and Interface Science* 369.1 (2012): 23-27.
- Mizuno, K., J. Ishii, H. Kishida, Y. Hayamizu, S. Yasuda, D. N. Futaba, M. Yumura, and K. Hata. "A Black Body Absorber from Vertically Aligned Single-walled Carbon Nanotubes." *Proceedings of the National Academy of Sciences* 106.15 (2009): 6044-047.
- Muratore, C., A.n. Reed, J.e. Bultman, S. Ganguli, B.a. Cola, and A.a. Voevodin. "Nanoparticle Decoration of Carbon Nanotubes by Sputtering." *Carbon* 57 (2013): 274-81.
- Nessim, Gilbert D., Donatello Acquaviva, Matteo Seita, Kevin P. O'brien, and Carl V. Thompson. "The Critical Role of the Underlayer Material and Thickness in Growing Vertically Aligned Carbon Nanotubes and Nanofibers on Metallic Substrates by Chemical Vapor Deposition." *Advanced Functional Materials* 20.8 (2010): 1306-312.
- O'Brien, Matthew N., Matthew R. Jones, Keith A. Brown, and Chad A. Mirkin. "Universal Noble Metal Nanoparticle Seeds Realized through Iterative Reductive Growth and Oxidative Dissolution Reactions." *Journal of The American Chemical Society* 136.21 (2014): 7603-606.
- Park, Kyoungweon, Hilmar Koerner, and Richard A. Vaia. "Depletion-Induced Shape and Size Selection of Gold Nanoparticles." *Nano Letters* 10.4 (2010): 1433-439.
- Tan, Lling-Ling, Wee-Jun Ong, Siang-Piao Chai, and Abdul Rahman Mohamed. "Growth of Carbon Nanotubes over Non-metallic Based Catalysts: A Review on the Recent Developments." *Catalysis Today* 217 (2013): 1-12.
- Velamakanni, Aruna, Carl W. Magnuson, K. J. Ganesh, Yanwu Zhu, Jinho An, Paulo J. Ferreira, and Rodney S. Ruoff. "Site-Specific Deposition of Au Nanoparticles in CNT Films by Chemical Bonding." *ACS Nano* 4.1 (2010): 540-46.
- Villoria, Roberto Guzmán De, A. John Hart, and Brian L. Wardle. "Continuous High-Yield Production of Vertically Aligned Carbon Nanotubes on 2D and 3D Substrates." *ACS Nano* 5.6 (2011): 4850-857.
- Zhang, Jian, Mark R. Langille, Michelle L. Personick, Ke Zhang, Shuyou Li, and Chad A. Mirkin. "Concave Cubic Gold Nanocrystals with High-Index Facets." *Journal of the American Chemical Society* 132.40 (2010): 14012-4014.

COMPOSITE MATERIAL SENSING RESEARCH USING ULTRASOUND SENSING AND  
MODELING

Project No. 0153

Ongela Helm  
University of Dayton

25 August 2014

Government Project Leader  
Dr. James Blackshire  
AFRL/RXCA

Southwestern Ohio Council for Higher Education  
Student Research Program  
Agreement Number: FA8650-09-2-5800

## Acknowledgments

I would like to thank my AFRL mentor, Dr. James Blackshire for his guidance and support. I would also like to thank Darius Johnson, Mike Gillespie, and Aaron Modic, and Celeste Cooper who have also worked on this project and have provided some of the preliminary results for my current research. I am also particularly thankful to Dr. Stephan Russ, Asheley Blackford, and the SOCHE program for giving me the opportunity to work with Air Force Research Laboratory and the Material State Awareness and Supportability Branch.

## General Description of Project

A method for determining the three-dimensional depth profile of a surface-breaking crack-like feature is presented based on near-field surface acoustic wave (SAW) signal responses. Three-dimensional finite element models were used to study the forward problem, where the characteristic near-field scattering of a surface acoustic wave incident on a simulated crack was investigated. Experimental validation of the modeling predictions was accomplished using a wedge transducer for surface wave generation and a scanning laser vibrometry system for surface wave detection. The characteristic near-field amplitude response in reflection and in transmission was measured and modeled for flat-bottom, angled, and curved-bottom localized notch features, where a simple linear inversion method was developed, which provided an effective means for characterizing and mapping the three-dimensional depth profile of surface-breaking crack-like features with depths in the micron to millimeter range.

## Description of Research

Measurement points immediately in front of and behind a surface breaking, crack-like feature are of interest (Figure 1). In particular, the out-of-plane displacement levels at those two locations vary in a systematic manner with the surface-breaking feature depth. As depths increase, scattering from the front root ( $S_1$ ) will combine with the incident Rayleigh wave ( $R_i$ ), with reflected energy from the front face ( $R_R$ ), and with transmitted energy along the front face ( $R_{T1}$ ) to create an enhanced displacement field immediately in front of the surface-breaking feature. Enhancements of the energy in front of the surface-breaking feature will continue to increase as depths increase until the penetration depth of the SAW begins to approach the feature depth ( $d$ ). Beyond  $d/\lambda \gg 1$ , reflected and transmitted energy levels are expected to level-out, as incident ( $R_i$ ), reflected ( $R_R$ ), transmitted ( $R_{T1}$ ), and front root scatter ( $S_1$ ) waves stabilize and combine to produce the enhanced displacement levels immediately in front of the feature, while the transmitted ( $R_{T2}$  and  $R_{T3}$ ) Rayleigh waves and scattered back root ( $S_4$ ) energies will stabilize and combine to give minimal displacements immediately behind the feature.

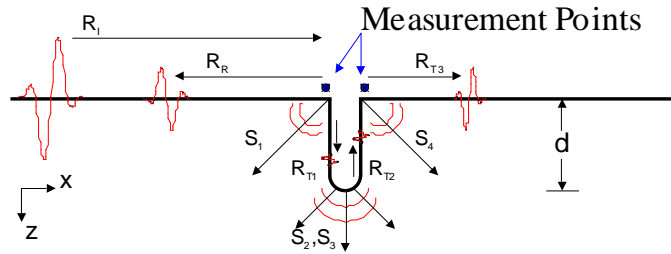


Figure 27. Schematic diagram of Rayleigh wave ( $R_i$ ) incident on surface-breaking, crack-like feature with reflected wave ( $R_R$ ) from front face, scattering from front root ( $S_1$ ), scattered wave from tip ( $S_2$ ), scattered wave from back root ( $S_4$ ), and transmitted Rayleigh waves ( $R_{T1}$ ,  $R_{T2}$ ,  $R_{T3}$ ).

A series of 3D-finite element models were used to study the behavior of the Rayleigh wave interactions with surface-breaking, crack-like feature as depicted in Figure 2. The model was developed in a commercially available finite element package PZFlex, which is designed and optimized for elastic wave propagation analysis. The model geometry depicted in Figure 2 was chosen to approximate a 1/2-penny surface-breaking crack. The overall dimensions of the model included a 10 mm x 10mm cross-section and 20mm length, with the rounded bottom, 1/2-penny feature located along the top surface at the mid-line along the geometry length. The feature was oriented normal to the top surface and had a width of 25  $\mu\text{m}$ , with depths varying from 0 microns on the left and right sides to a maximum depth of 500 microns at the midpoint in the transverse direction.

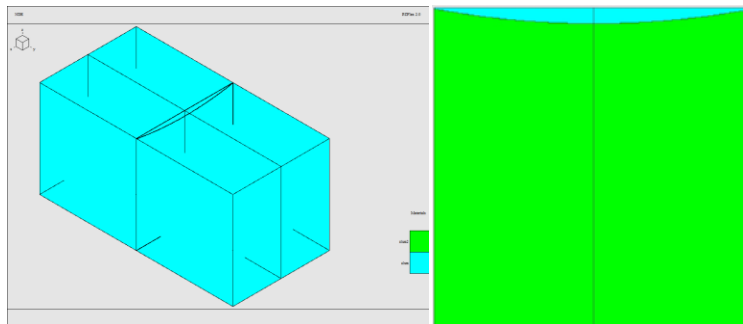


Figure 28 . Schematic of 3D finite element model geometry (left), and cross-section of surface-breaking, crack-like feature (right).

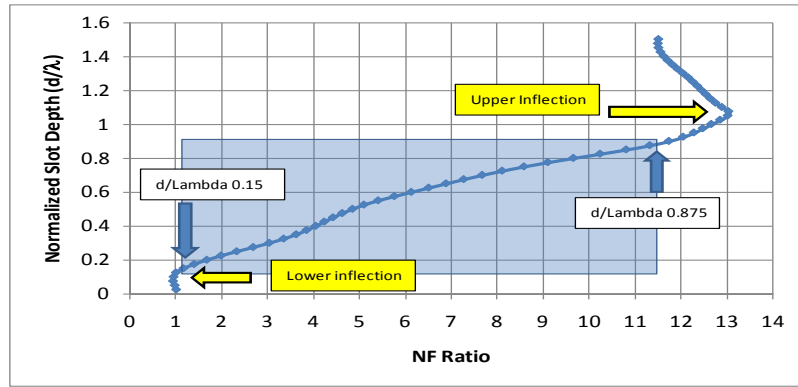
The material properties of aluminum were used for the study with a density of 2700  $\text{kg/m}^3$ , longitudinal velocity of 6419.88 m/s, shear velocity of 3039.86 m/s, and Rayleigh velocity of 2996 m/s. A shear-dipole excitation source was applied along the top left surface to generate and propagate a Rayleigh wave along the material surface towards the 1/2 penny feature. The separation distance between the source and the 1/2-penny feature (10 mm) was chosen to provide adequate separation of the surface skimming longitudinal wave, bulk waves, and Rayleigh wave, which are all generated using the shear dipole source excitation. Absorbing boundary conditions were applied to the all of the exterior surfaces except for the top surface, which was set to be a free boundary.

Figure 3 (bottom) provides the characteristic curves for the near-field signal ratio –vs normalized slot depth. By taking the ratio of the normalized peak-to-peak signals immediately in front of and behind the crack-like feature, the curve in Figure 3 is produced. A linear trend is

observed for this ratio plot between the  $d/\lambda_R \in 0.15-0.875$  range, which can be used to estimate the local crack depth using the equation:

$$d = \left( \lambda_R \left( A + B_1 NF_{ratio} \right) \right) \quad , \quad (1)$$

where  $\lambda_R$  is the SAW wavelength, and  $NF_{ratio} = NF_T / NF_R$  is the ratio of the measured peak-to-peak amplitude levels immediately in front of and behind the notch, respectively.



**Figure 29** Characteristic curve of near-field signal ratio –vs normalized slot depth.

In addition to a linear trend, a polynomial regression fit was analyzed to the characteristic curve to obtain a sixth order inversion formula:

$$d = \lambda_R \left( A + B_1 NF_{ratio} + B_2 NF_{ratio}^2 + B_3 NF_{ratio}^3 + B_4 NF_{ratio}^4 + B_5 NF_{ratio}^5 + B_6 NF_{ratio}^6 \right) \quad , \quad (2)$$

These inversion formulas for crack depth estimation were then applied to forward 3D models to quantify depth prediction accuracy.

## Results

The proposed methodology for estimating the local depth of a crack-like feature uses the simple linear transform equation (Equation 1) and the polynomial equation (Equation 2), where  $A_1$  and  $B_1 - B_6$  are proportionality constants dependent on the specific crack geometry,  $\lambda_R$  is the Rayleigh wavelength, and  $NF_{ratio} = NF_R/NF_T$  is the ratio of the measured displacement amplitudes immediately in front of ( $NF_R$ ) and behind ( $NF_T$ ) the feature. Because Rayleigh waves are inherently 2-dimensional in nature, the local depth in the transverse direction can be mapped if spatially resolved displacement measurements in the transverse direction are made. Figure 4 provides an example of the predicted depth profile vs actual depth profile for an rounded slot in aluminum, and a model-based ½-penny crack-like feature where good agreement is observed for the actual depths versus predicted depths for the 6<sup>th</sup> order inversion prediction.

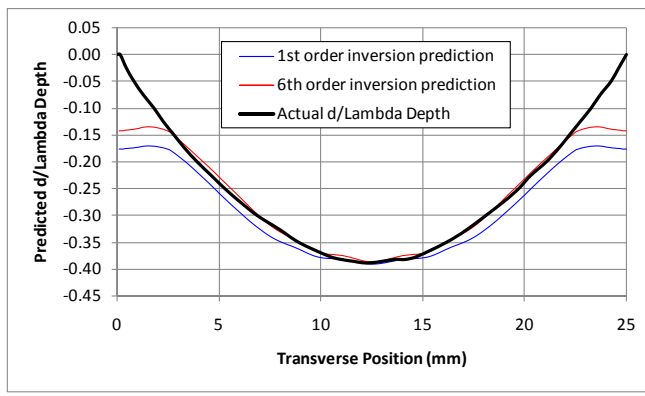


**Figure 30** Near-field reflect and transmit peak signals vs. position (top), and predicted local depth for rounded slot (bottom).

FABRICATION AND CHARACTERIZATION OF DNA BIOPOLYMER-NONLINEAR  
OPTICAL (NLO) CHROMOPHORE FILMS

Project No. 0155

Hadil Issa  
University of Dayton

31 August 2014

Government Project Leader  
Dr. Thomas Cooper  
AFRL/RXAP

Southwestern Ohio Council for Higher Education  
Student Research Program  
Agreement Number: FA8650-09-2-5800

## **Acknowledgments**

This opportunity of collaboration between the University of Dayton, Air Force Research Laboratories (AFRL/RXAP), and Southwestern Ohio Council for Higher Education (SOCHE) has been enlightening and rewarding. These endless collaboration efforts open doors and opportunities for students to explore the many research fields that are yet to be explored and understood. Of course, these endless efforts bring along those who deserve the highest of appreciation for their advice, consultation, time and endless efforts to help make sense of what at first seems like chaos. I am extending my appreciation to Dr. Charles Browning, Dr. Angela Campbell, Dr. Thomas Cooper, Dr. Jim Grote, Dr. Fahima Ouchen, Dr. Perry Yani, Doug Krein, David Stewart, Jonathan Slagle, Dr. Hilmar Koerner, Megan Pike, Gerald Landis, Kristi Singh, Larry Brott, Joe Slocik and Kurt Eyink for their technical/research expertise. I would also like to extend my appreciation to Dr. Ruth Pachter, Brittany Edwards, Asheley Blackford, Chris Muratore, Dr. Rajesh Naik, Dr. Dean Evans, Brian Anderson, Deyanira Reid and Dan Brewer for their support, guidance and time.

## **General Description of Project**

This project involves fabrication and characterization of a series of deoxyribonucleic acid- cetyltrimethyl-ammonium (DNA-CTMA), DNA-CTMA biopolymer Nonlinear Optical (NLO) Chromophore and NLO Chromophore films by various methods of casting for use as components of photonic, electronic, nonlinear optical devices and nonlinear optical coatings. Films of varying properties will be fabricated by using different solvents and solvent systems to include butanol, ethanol and the varying ratios of toluene to dimethylsulfoxide (DMSO) solvent system at 30:70, 40:60, 50:50, 60:40 and 70:30 (Toluene : DMSO). Microscopic techniques will be used to characterize the variation of film surface structure, uniformity and morphology. Circular Dichorism will be used to understand the interaction between the DNA-CTMA and 4-(N,N- diethylamino)- $\beta$ -nitrostyrene (DEANST). Furthermore, linear optical and nonlinear optical properties of the films will be explored using various ground and excited spectroscopic methods as deemed appropriate.

## **Description of Research: 970-592-587-254**

In order to fabricate DNA-CTMA films, DNA must be complexed with CTMA to be able to dissolve in organic solvents. Marine salmon DNA was first dissolved in deionized water and after filtration and sonication, DNA was added via titration to CTMA. Upon the interaction of DNA and CTMA and filtration, DNA-CTMA is obtained which is dried and then dissolved in ethanol and ethanol soxhlet-dialysis is followed to purify the DNA-CTMA and is rotaevaporated to get rid of excess ethanol and dried in the oven. After processing of the DNA-CTMA, the appropriate weight is dissolved in the organic solvents to obtain the desired concentration and the solutions were both spin coated and solution casted on both quartz wafer and pyrex glass dishes and beakers respectively. Drying of the films was done through the use of a hot plate and a laboratory oven resulting in a film casted on quartz coverslip and free standing films as shown in figures 1 and 2. Thick films were characterized using a table-top scanning electron microscope (SEM) to measure thickness, circular dichorism (CD) of the DNA helix as a function of solvent polarity and Infrared-Scan (I-scan) to measure the two photon absorber character of the dye in

the DNA-CTMA films. Using the table-top SEM, the films were cut and placed on carbon tape and images of the cross section of the films were processed and the software was used to measure the thickness of the films and view the interlayer characteristics of the films. In the case of CD, due to the thickness of the films, data was not possible to be obtained to characterize the DNA-CTMA; therefore, the solutions were spin coated on a quartz wafer. Characterization of the thick films to non-linear optical properties was done with the use of the I-Scan with a laser of 785nm wavelength.

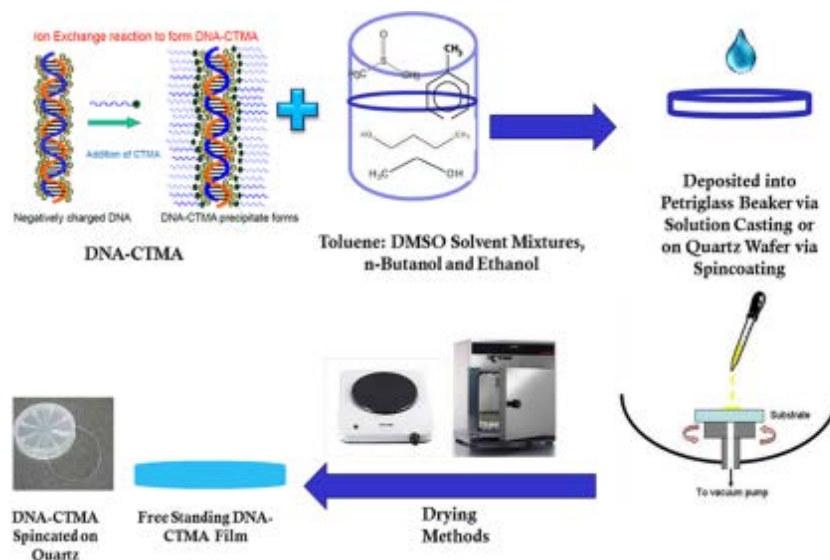


**Figure 31: Procedure for Making DNA-CTMA Films**

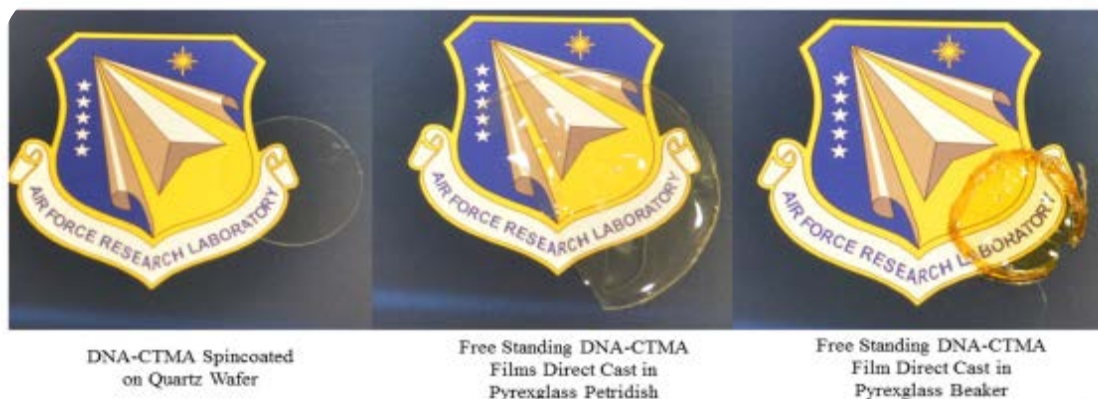


**Figure 32: DNA-CTMA Films**

## Results

Thickness profiles across all of the films that were produced using the toluene: DMSO solvent ratio ranged between 210-350 micrometer Figure 3. The interlayer profile gave an insight to the how the DNA-CTMA is intertwined in the films Figure 4.

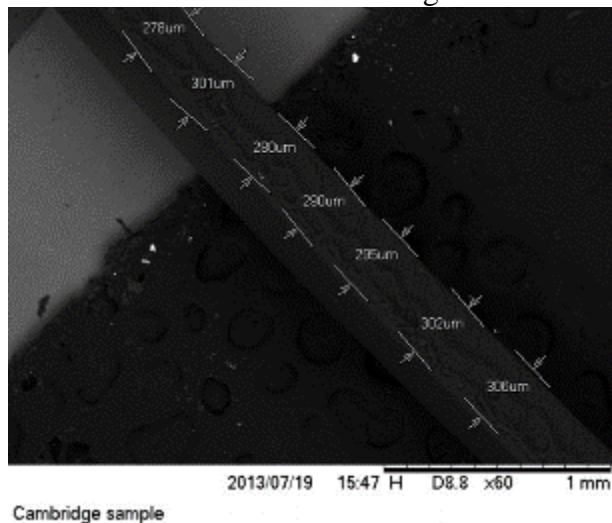


**Figure 33: Thickness Profile of 70 Toluene: 30 DMSO DNA-CTMA Film**

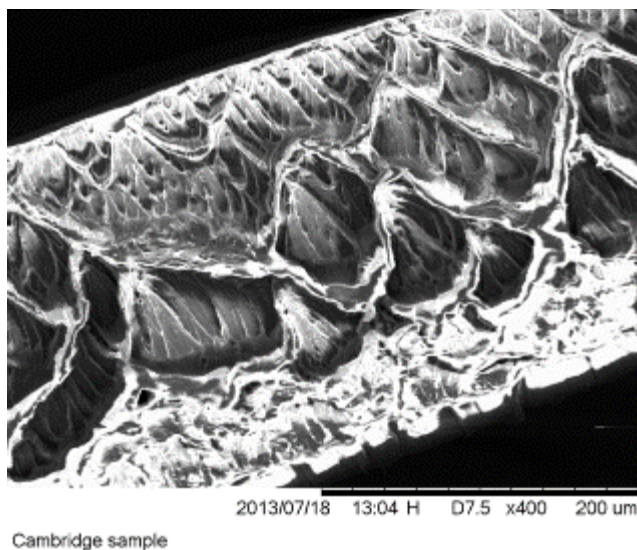


**Figure 34: Inter Layer View of 30 Toluene: 70 DMSO DNA-CTMA Film**

Using CD, a profile of the absorption of the films and helicity of DNA-CTMA was obtained, Figure 5 and Figure 6 respectively. A conclusion that could be made is that as the amount of toluene increased the polarity of the solvent system increased and therefore increasing the helicity of the DNA. On the other hand, others could argue that the thickness of the spin coated films or the interaction of the solvent with the DNA-CTMA while evaporating could also play a factor in the increase in helicity.

## Absorbance of DNA-CTMA/(T:DMSO) Spin Coated Films Acceleration of 5000 and RPM 3000

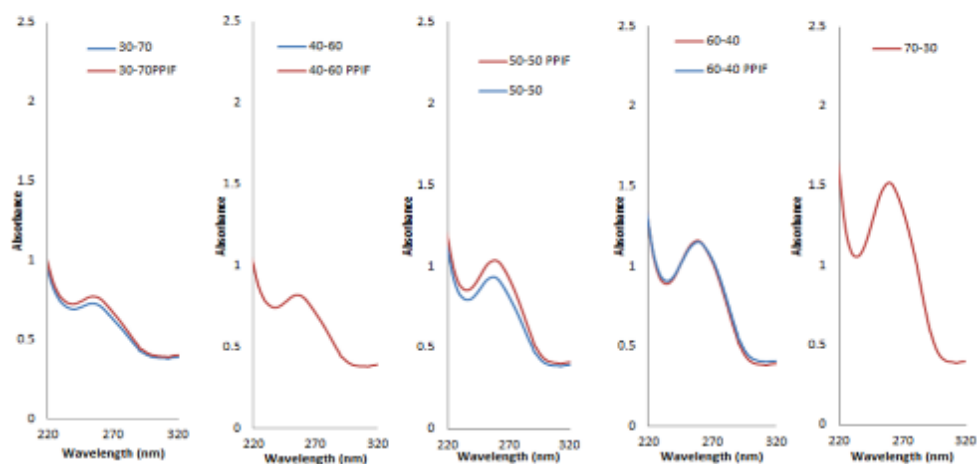


**Figure 35: Absorption Profile of Spin Coated DNA-CTMA Films**

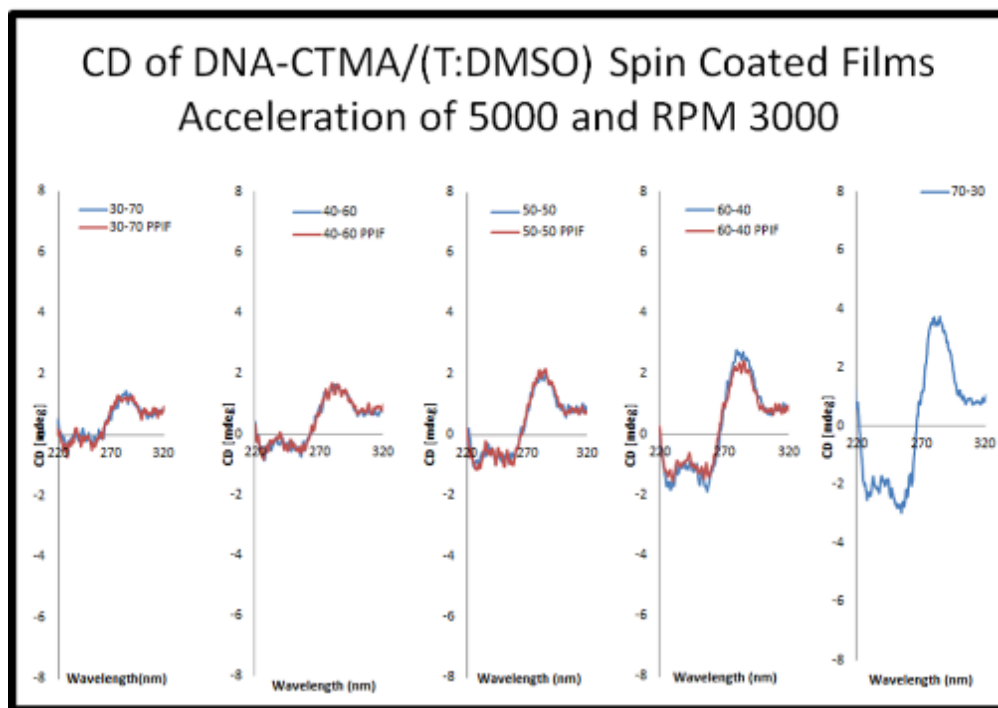


**Figure 36: Circular Dichorism of DNA-CTMA Films as Polarity Increases**

Using I-Scan, the DNA-CTMA and DNA-CTMA-Dye films were scanned and the films with and without the dye did not show any difference in their non-linear optical properties. This perhaps could be due to the low concentration of dye present. However, from this, it is concluded that the DNA-CTMA films without the dye exhibit non-linear optical properties. From Figure 7, the nonlinear transition of DNA-CTMA films, is traced. At the peak fluence of 1-10 J/cm<sup>2</sup>, the decrease in the transition energy crossing the nonlinear domain is due to the nonlinear activity and absorption of the film. Continuous decrease in transmission is a result of the nonlinearity breakdown of the DNA-CTMA films.

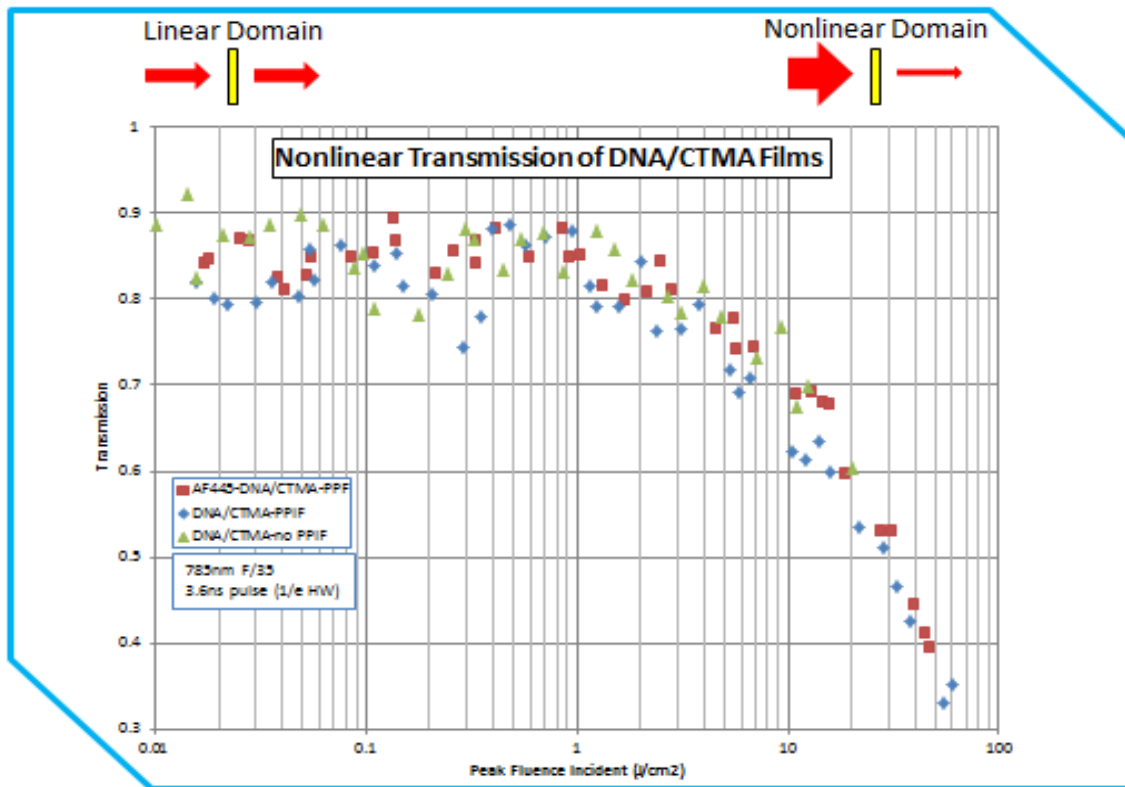


**Figure 37: Linear and Nonlinear Domain Transmission of DNA-CTMA Films**

Figure 8 shows the threshold damage of the DNA-CTMA films which correlate to Figure 7. At 11.1 J/cm<sup>2</sup>, the damage of the DNA-CTMA films as a cause of the nonlinear activity and absorbance of energy is indicated by the dark spots shown in the figure.

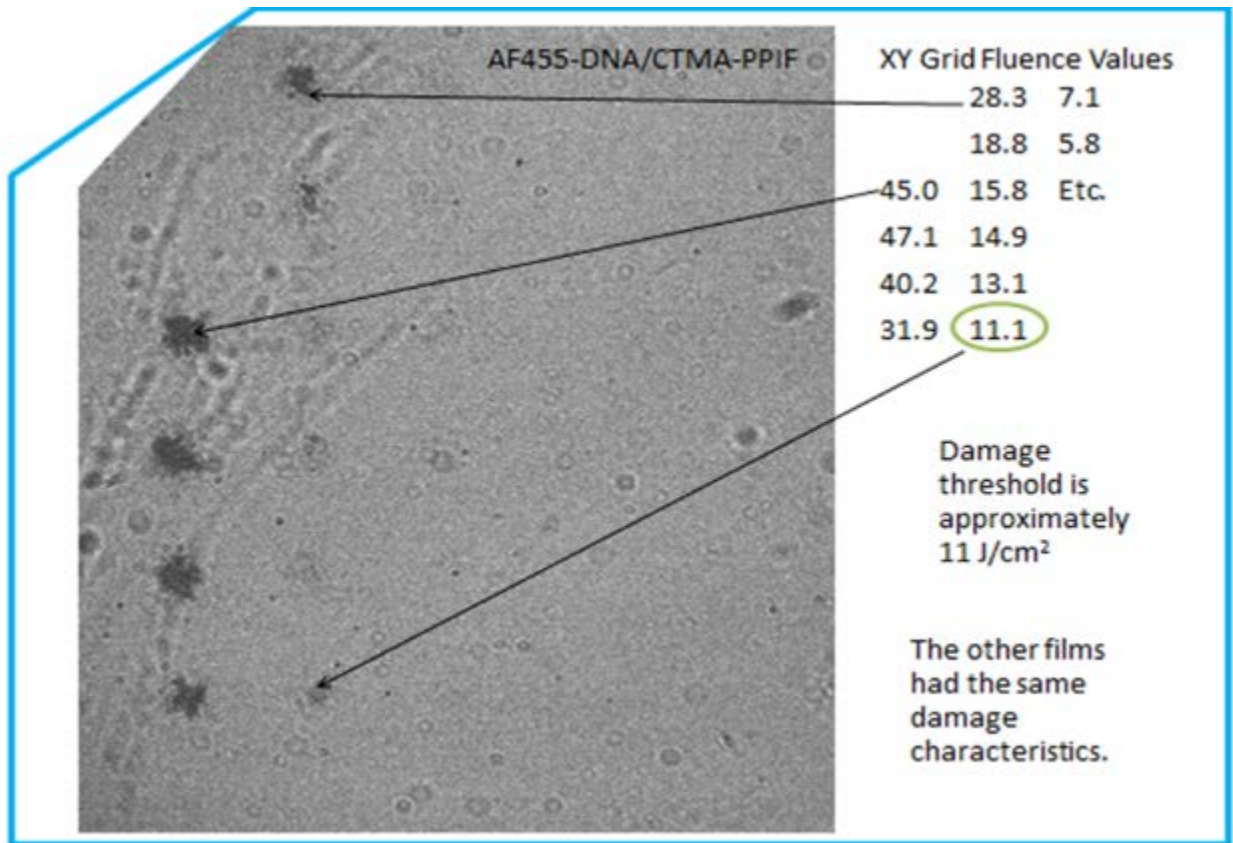


**Figure 38: Damage Threshold of DNA-CTMA Film**

Exploring other dyes and perhaps other solvents such as ethanol and n-butanol will hopefully answer some of the questions that are pondered upon with respect to the solvent effect on the DNA-CTMA. Furthermore, exploring the effect of the film variance in thickness and characterizing the solutions of the mixture of DNA-CTMA with other solvents will provide a greater insight on the behavior of the DNA-CTMA in the solid and liquid form.

COMPOSITE DAMAGE TOLERANCE AND PERFORMANCE

Project No. 0157

Mark D. Flores  
University of Texas at El Paso

31 August 2014

Government Project Leader  
Dr. David Mollenhauer  
AFRL/RXCC

Southwestern Ohio Council for Higher Education  
Student Research Program  
Agreement Number: FA8650-09-2-5800

## Acknowledgements

I would like to take the opportunity to acknowledge Dr. David Mollenhauer from Air Force Research Laboratory for working as a mentor in the process of obtaining my PhD and research. I would like to thank Dan Rapping for his continuous hard work throughout the project, which has allowed me to enhance my knowledge of composites. I would like to thank John Camping, Brian Smyers, Kevin Hoos, and Kevin Shively for helping the team set up experiments. Special thanks goes to Eric Lindgren and the RXSA group for providing non-destructive evaluation of the composites.

## General Description of Project

The use of polymer composite materials is continuously increasing in its application throughout industry. However, certification and damage tolerance is a growing concern in many aerospace, energy, and marine industries. Although, compression-after-impact and fatigue-after-impact have been studied thoroughly, determining a damage tolerance methodology that accurately characterized the failure of composites has not been established. A computational and experimental investigation will be performed to study the effect of stacking sequence, low-velocity impact response, and residual strength due to compression and fatigue. Five different stacking sequences are subjected to series of testing to understand the performance of IM7/977-3 carbon fiber composite unidirectional tape. Compression and fatigue tests will be performed on 6"x4" (154.2 mm x 101.6 mm) specimens to create a baseline strength of the composites. Separate tests will utilize a drop weight tower to perform a low-velocity impact using a hemispherical tupper. Then each of the specimens will undergo the latest non-destructive evaluation (CT-Scan, Thermography, Ultrasound) to determine the extent of the damage created by the impact event. Information from the non-destruction evaluation (NDE) will be used to create a more accurate representative model of the impacted specimen and numerical computations will be done on the post-impacted specimens to validate the compression-after-impact and fatigue-after-impact results from the experiments. Digital Image Correlation (DIC) will be used to capture the strains and deformation of the plate due to compression. The failure mechanisms such as fiber/matrix crack, delamination growth, and buckling differ between fatigue and compression. The results from this study provide comprehensive knowledge of the compression strength of plates, compression-after-impact, and fatigue-after-impact of composites. The final report per SOCHE contract outlines the methodology, preliminary experiments, and simulations.

## Description of Research

### 2.1 Materials

Carbon fiber reinforced polymer composites (IM7/933) were produced by Air Force Research Laboratory (AFRL/RXCC). Panels with 24 layers of unidirectional tape were produced with a nominal cured thickness of 1/8" (3.2 mm). Different layup sequences consisted of [-45/90/45/90/-45/0/45/90/90/-45/90/45]<sub>s</sub>, [-45/45/-45/45/0/45/90/-45/45/-45/45/-45]<sub>s</sub>, [-45<sub>3</sub>/90<sub>3</sub>/45<sub>3</sub>/0<sub>3</sub>]<sub>s</sub>, [-45/90/45/0]<sub>3s</sub>, [45/0/045/90]<sub>3s</sub>, where the 0 degree ply is the loading direction of the compression load. Each 24" by 24" panel were cut into smaller specimens with the dimension of 4" x 6" (101.6 mm x 152.4 mm) as required by the ASTM D 7137 "Standard Test

Method for Compressive Residual Strength Properties of Damage Polymer Matrix Composite Plates.”

## 2.2 Experimental Testing Methodology

Each stacking sequence will undergo a compression test using a loading rate of 0.05 in/min (1.27 mm/min). A MTS machine with a 50 kip load cell will be used to perform the compression test. The size of the specimen is determined by the ASTM 7136 and ASTM 7137 standards to get a baseline set of data for the compression tests and fatigue tests.

Although normal fatigue tests use the ASTM 3140 standards, it is being modified more towards the ASTM 7137 standards to make a side-by-side comparison of the static compression strength and fatigue strength of composite plates. Each specimen will use the same buckling fixture used in ASTM 7137, loaded up to 80% of the static compression strength, and compression-compression cyclic loading will be performed.

Impact damage will be introduced using an INSTRON drop weight tower setup. All samples were subjected to an impact using either a ½ in or 1 in hemispherical tupper. Each impact will be at the center of the specimen. Several energies will be used to assess the right amount of damage needed for residual testing to understand damage propagation patterns. CT-scans will be done to the impacted specimen to measure the area of damage the tupper caused. The statistical data will be used to create accurate analytical models using AFRL in house BSAM code.

Post-partum impacted specimens will undergo a compression test using a loading rate 0.05 in/min. A MTS machine with a 50 kip load cell will be used to perform the compression tests. Once the static compression residual strength is determined, separate compression-compression fatigue tests will be conducted. Similar to previous tests, impacted specimens will be loaded up to 80% of the static compression after impact strength, and cyclic loading will be performed.

## 2.3 Non-Destruction Evaluation

Each panel will be c-scanned. After each panel is cut into the proper specimen sizes, it will be c-scanned again to ensure that no damage occurred during the cutting process and verify the proper and correct fiber orientation of the composites prior to testing them.

After each impact, each specimen will be CT-Scanned to analyze the impact region. From this, the damaged area will be documented. Once the level of damage is assessed, the information will be used to pre-impose delamination and fiber cracks into the BSAM models. A liquid will be injected into the specimens and CT-scanned to determine the extent of the damage that occurred within the specimen.

After each compression and fatigue test, even post-partum impacted specimens, will be CT-scanned to analyze the fiber failures of the specimens.

## 2.4 BSAM – Finite Element Analysis

Using the ASTM 7137 dimensions and theoretical boundary conditions, laminated composite specimens were discretized into a BSAM model, which consisted of individual cracks and delaminations. Matrix cracking and delamination initiation, propagation, and interaction,

without any prior knowledge and/or meshing of the matrix cracking surfaces, is accomplished by combining stress and fracture mechanics-based constitutive modeling within a mesh independent crack-modeling framework[1]. To model pre-existing delamination between plies as a result of impact, a weak cohesive model was employed. Images from 3d X-ray scans provide the capability to model the cracks and plastic deformation as a result of impact. A continuum damage mechanics approach was implement to accurately model fiber failure.

A mesh sensitivity analysis was performed to analyze the accuracy of the model. Both linear and non-linear buckling schema was implemented into the model to take into consideration of large displacements. Compression models and compression after impact models were constructed as seen in Figure 2.4.1. The gray area in Figure 2.4.1 is the pre-imposed impact region of the model. Similar to isotropic materials, the damage progression of impact can be conical and the delamination was model as such. Experiments and x-ray CT scans will be conducted to create accurate models of the delamination and fiber cracks.

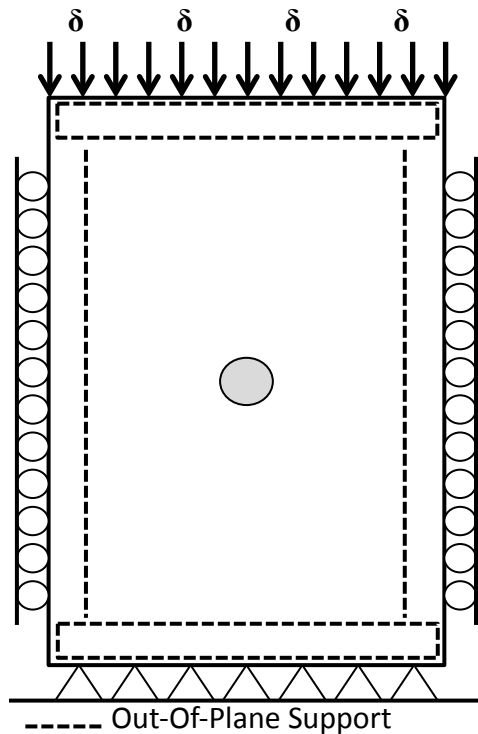


Figure 2.4.1 – Boundary Conditions of BSAM model

Table 2.4.1 IM7/977-3 Mechanical Properties

$E_{xx}$ (MPa)	164000
$E_{yy}, E_{zz}$ (MPa)	8977
$\nu_{xy}, \nu_{xz}$	0.32
$\nu_{yz}$	0.496
$G_{xy}, G_{xz}$ (MPa)	5000
$G_{yz}$	3500

## Results

During the manufacturing process, the  $[-45/90/45/90/-45/0/45/90/90/-45/90/45]_s$  panels were warped. Therefore it as stood as an excellent opportunity for preliminary studies to set up baseline experiments for the rest of the layups. Compression tests of the material were done. Using the drop weight tower, a steel ½” hemispherical tupper was lifted to approximately 1 foot above the specimen and released. Compression after impact tests was conducted on two impacted specimens. The experiments for the summer of 2014 were a preliminary analysis of capture future data for different layups and is outlined in this section.

### 3.1 Compression Tests

A compression test was performed on one specimen. Two strains gauges were put side by side on the front along the width and two strain gauges were put side by side along the length. Each of the strain gauges was approximately an inch away from the center of the plate. Figure 3.2.1 is a graphical representation of the compression test performed with the 50 kip MTS machine. The maximum force obtained was 62 kN and the static compressive strength of the material is 191 MPa. Figure 3.2.2 is a graphical representation of the strains of the composite structure. The slight deviation of the strains may be attributed due to the fact that the composite specimen was warped from the manufacturing process.

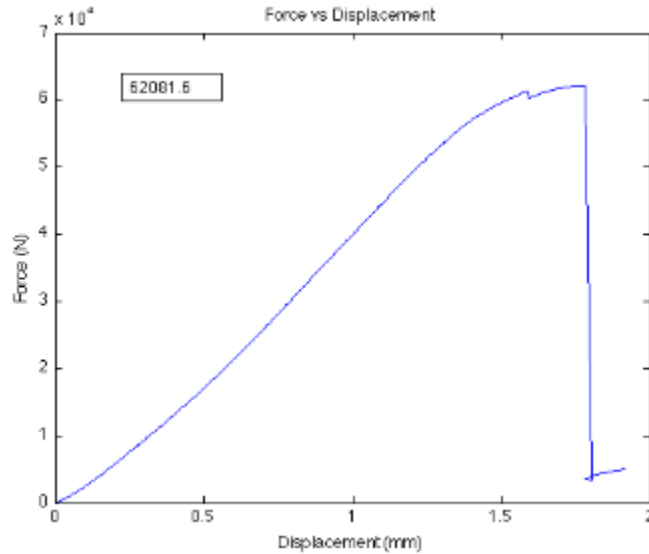


Figure 3.1.1 – Force vs Displacement Compression Test

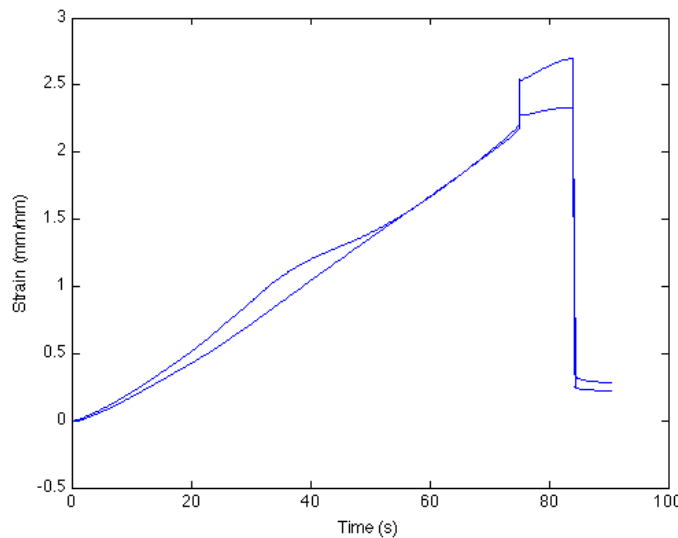


Figure 3.1.2 – Strain vs Time Compression Test

### 3.2 Impact Studies

Using an Instron drop weight tower, a steel ½” hemispherical tupper was released from a foot above the specimen. Two specimens were impacted. The first test specimen was impact in several regions as shown in ultrasound figure Figure 3.2.1. The ultra sounds of the specimens only show the amount of delamination that occurs within the composite place. The dark regions indicate the actually impacted area while the larger dark ring surrounding is the result of the base plate the composite lay on. The second specimen was impacted only once in the center of the composite. Figure 3.2.2 is an ultrasound of a specimen that was only impacted once. Similar the

dark region in the center of the composite is delamination. The ring is from the base plate where the composite was placed. The impact energy of the composite was around 8 lb-ft (10 J).

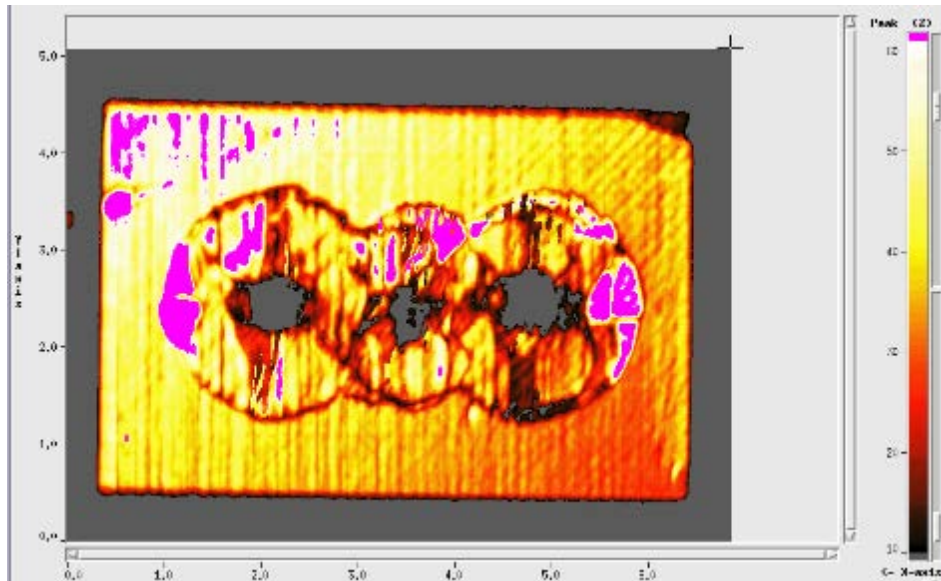


Figure 3.2.1 – Ultrasound of multiple impact on single specimen

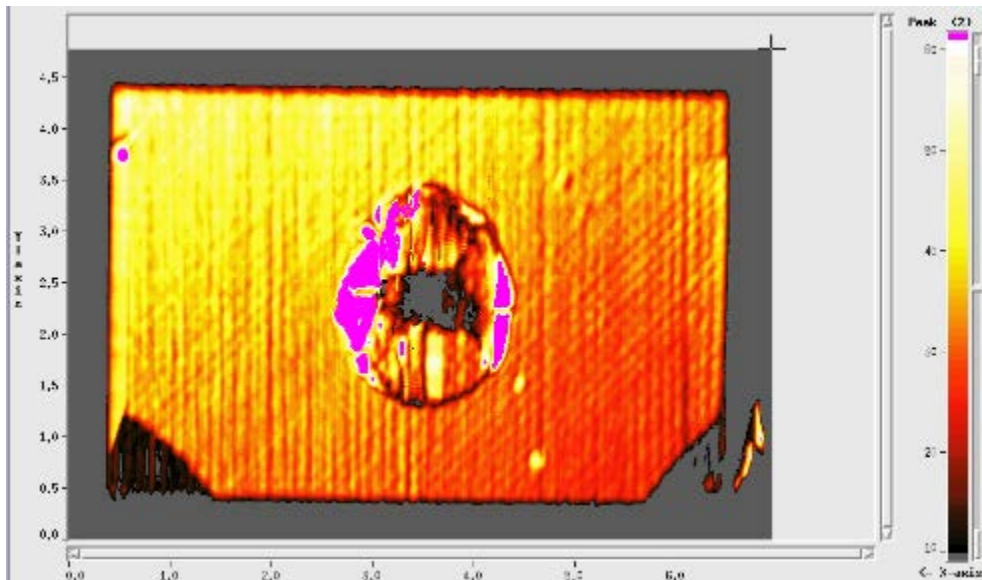


Figure 3.2.2 – Ultrasound of single impact on single specimen

### 3.3 Compression after Impact Studies

Using a 50 kip MTS machine, each of the post-partum impacted specimens were compressing with a loading rate of 0.05 in/min until failure. Digital image correlation was performed to measure the strain effects of the impacted regions. Two strain gauges were put in the back of the single impacted specimen. Figure 3.3.1 is a graphical representation of the digital

image correlation strain data at the time of failure for the multi-impacted specimen. Assessing damage for this particular test is difficult due to the amount of damage that from impact. However, post partum failure indicated that the final failure was global buckling on the top impacted region. The information that can gather from Figure 3.3.1 is the compression and tensile behavior of the strain surround each of the impacted regions. Figure 3.3.2 is a graphical representation of the strain data for the single impacted specimen. Although, these tests were a preliminary venture in the current technology capabilities, digital image correlation was able to capture displacement and strain quite accurately.

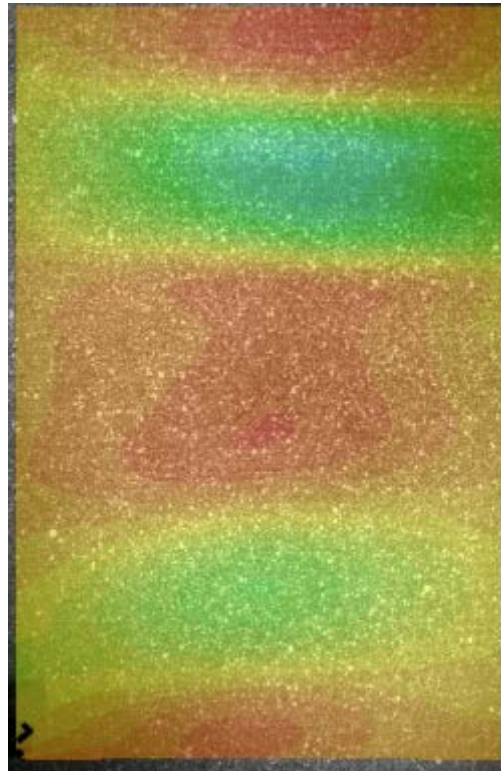


Figure 3.3.1 – Strain-YY data of multiple impacted specimen

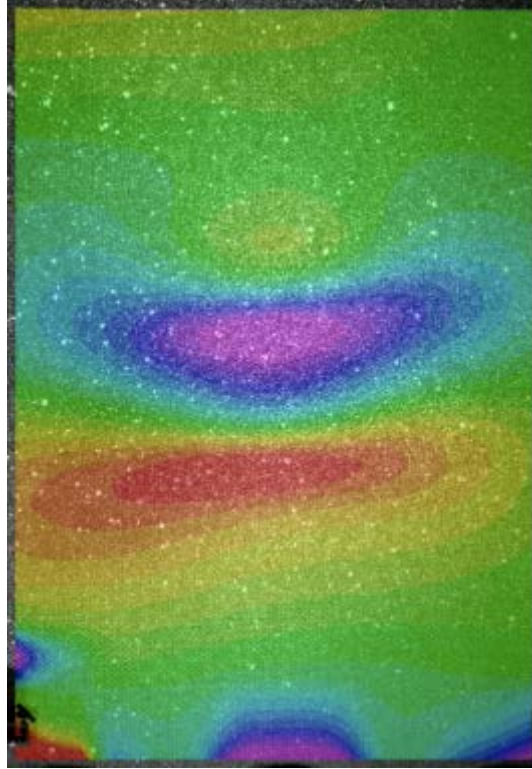


Figure 3.3.2 – DIC strain-yy data of single impacted specimen

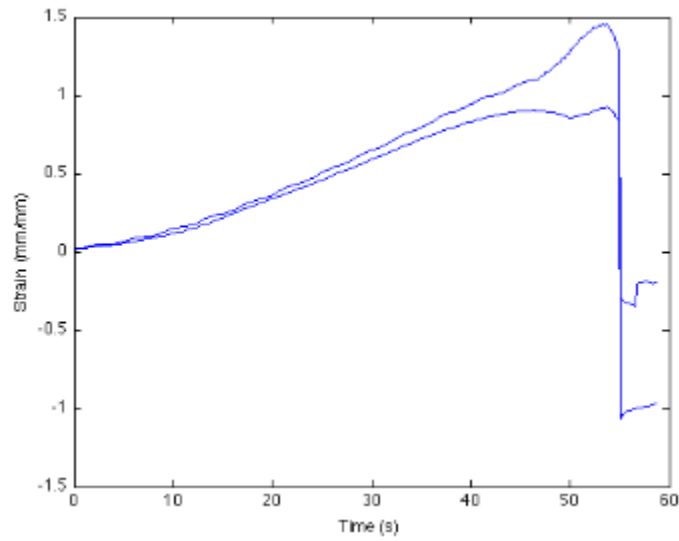


Figure 3.3.3 – Strain gauge data of single impacted specimen

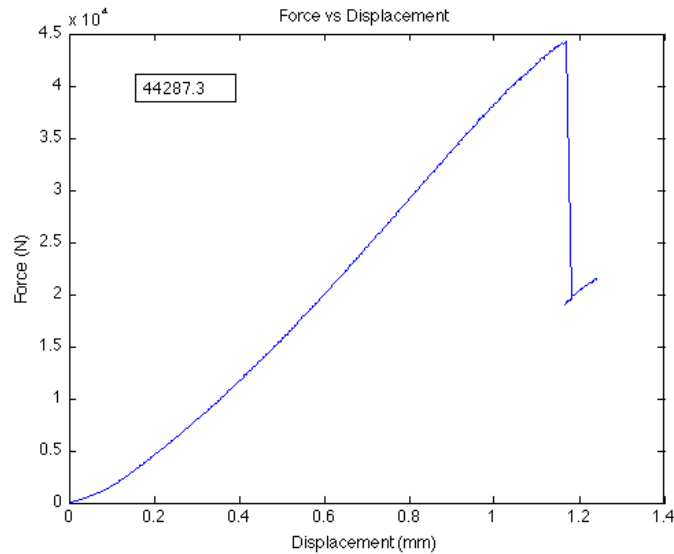


Figure 3.3.4 – Force vs displacement for single impacted specimen

### 3.4 BSAM Models

A course model was implemented to determine the theoretical static compression failure of composites. Two models were performed. One simulation used a compression linear continuum damage mechanics approach while the other used a nonlinear approach to account for large displacements and instabilities due to buckling. The static compressive strength was around 451 MPA, however, the damage it captured were entirely different. In the compression simulation, there were more fiber cracks, the delamination occurred at the center and edges, and the damaged elements were primarily in the center. In the buckling simulation, it appears there was less fiber cracks and the damage occurred at the top edges where the displacement was being applied. When assessing the average traction, a large increase and/or instability occurred in the compression simulation. When taking into account the nonlinear effects of the lamina, instabilities weren't as problematic as seen Figure 3.4.1. However, the nonlinear part of the code seemed to lack in its ability to predict cracks and damage seen in the compression simulation. The data in this report will be used to develop a series of experiments for a larger study to understand the composite performance of IM7/977-3 carbon fiber reinforced composite.

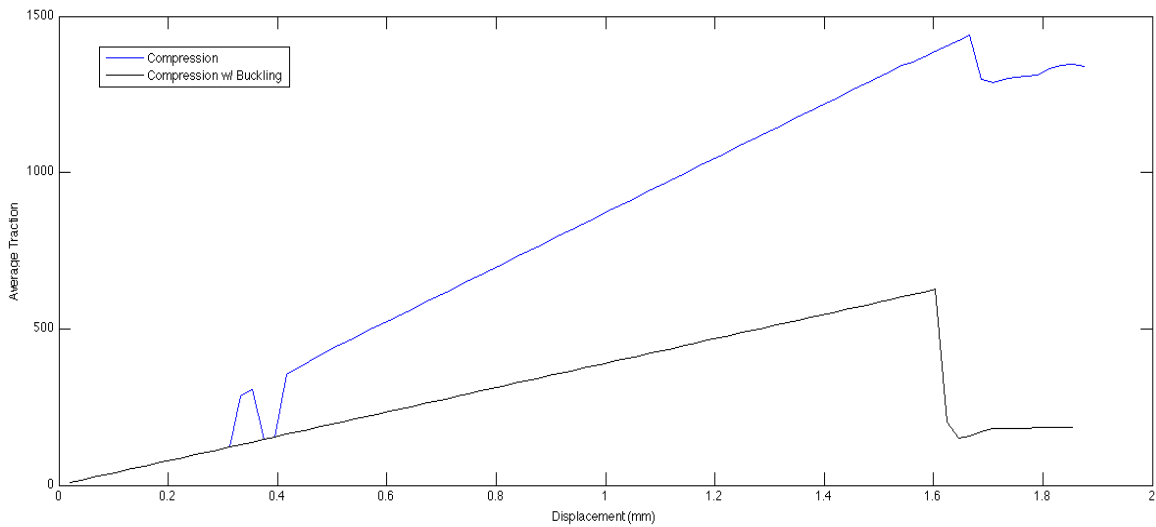


Figure 3.4.1 – Compression vs Buckling effects on Traction

## Conclusions

Several experiments are still needed to understand some of the damage mechanisms that occur with composite structures. The baseline data from the compression strength will be used for compression-after-impact and fatigue tests. Digital Image Correlation captured the displacement and strains in the compression after impact experiments and will be used in fatigue other future tests. Although, not much significance can be taken into account from a single data point, the compression after impact strength was 25% lower than the static compression strength. Strain data information from the digital image correlation and strain gauge will prove to be a useful tool to determine eccentric loadings in the specimens when compressed.

## Future Work

The warped panel provided information that could be used to design better experiments for the larger set of specimens. Eventually more layups will be experimented on including fatigue and validated with a computational investigation. Mesh sensitivity is currently being performed to ensure accurate results. Future work involves gathering data from CT-Scans, creating discretized models of damage using the CT-Scans and performing computational modeling. This would be a viable tool for operational maintenance when assessing damage on wings to an airplane to propellers of a windmill. The information from the paper will be used to creating better fracture, damage and fatigue resistant materials for the future.

## Works Cited

Mollenhauer D., Ward, L., Iarve, E. V., Putthanarat, S., Hoos, K., Hallett, S., Li, X., Simulations of discrete damage in composite Overweight Compact Tension specimens, *Composites: Part A* 43 (2012) 1667-1679

Iarve, E. V., Mesh independent modeling of cracks by using higher order shape functions, *International Journal of Numerical Methods in Engineering*, 2003, 56:869-882

Turon, A., Costa, J., Camanho, P. P., and Davila, C. G., Simulations of Delaminations in Composites Under High-Cycle Fatigue. *Composites Part A*, 2007, 38(11):2270-2282

Camanho, P. P., Turon, A. Davila, C. G., Costa, J., An Engineering Solutions for Mesh Size Effects in the Simulations of Delaminations using cohesive zone models. *Engineering Fracture Mechanics*, 2007, 74(10):1665-682

Iarve, E. V., Gurvich, M. R., Mollenhauer, D. H., Rose, C. A., Davila, C. G., Mesh-independent matrix cracking and delamination modeling in laminated composites. *International Journal for Numerical Methods in Engineering*, 2007, 88:749-773

ASTM Standard D7136M, 2012, "Standard Test Method for Measuring the Damage Resistance of a Fiber-Reinforced Polymer Matrix Composite to a Drop-Weight Impact Event," ASTM International, West Conshohocken, PA, 2005, DOI: 10.1520/C0033-03, [www.astm.org](http://www.astm.org).

ASTM Standard D7137M, 2012, "Standard Test Method for Compressive Residual Strength Properties of Damaged Polymer Matrix Composite Plates," ASTM International, West Conshohocken, PA, 2005, DOI: 10.1520/C0033-03, [www.astm.org](http://www.astm.org)

Wyzgoski, M. G., Novak, G. E. "An improved model for predicting fatigue S-N (stress-number of cycles of fail) behavior of glass fiber reinforced plastics", *Journal of Material Sciences*, (2008) 43:2879-2888

Olsson R., "Modelin of impact damage zones in composite laminates for strength after impact", *The Aeronautical Journal*, December 2012, 116:1186:1349-1365

MODELLING THE EFFECTS OF SHOT-PEENED RESIDUAL STRESSES AND  
INCLUSIONS ON MICROSTRUCTURE-SENSITIVE FATIGUE OF NI-BASE  
SUPERALLOY COMPONENTS

Project No. 0158

William D. Musinski  
Georgia Institute of Technology

4 April 2014

Government Project Leader  
Dr. Patrick J. Golden  
AFRL/RXCM

Southwestern Ohio Council for Higher Education  
Student Research Program  
Agreement Number: FA8650-09-2-5800

## **Acknowledgements**

Completion of this work could not have been possible without the immense support from multiple people throughout my graduate studies. First and foremost, I would like to thank my advisor, Dr. David L. McDowell for his patience, guidance, and encouragement throughout the completion of this work. I am truly grateful for the ability to pursue independent research under his direction. I have developed tremendously as a research professional and technical writer under his advisement which I will take with me for the rest of my life.

Prior to my start at the Air Force Research Laboratory (AFRL), I have a number of lab mates within the McDowell group that I would like to thank. When I first started at Georgia Tech, I appreciate the senior members who got me started in the right direction, including Rob Matthews, Dr. Craig Przybyla, Dr. Rajesh Prasannavenkatesan, Dr. Jason Mayeur, Dr. Garritt Tucker, and Dr. Nima Salajegheh. To all those who shared MRDC 3338, I enjoyed the deep discussions regarding research and other life happenings. Specifically, I would like to thank Dr. Jeff Lloyd, Dr. Brett Ellis, Dr. Gustavo Castelluccio, Jin Song, Sam Britt, Ben Smith, Shreevant Tiwari, Dr. Anirban Patra, Matthew Priddy, Shuozhi Xu, and Dr. Jagan Padbidri, who have certainly enriched my time at Georgia Tech.

I am extremely thankful for funding from multiple sources prior to my start at AFRL beginning with the Pratt and Whitney/Georgia Tech Center of Excellence under technical lead Bob Grelotti, fellowships provided by the George W. Woodruff School of Mechanical Engineering, and support from the Carter N. Paden, Jr. Distinguished Chair in Metals Processing held by Dr. David L. McDowell. I am also thankful for the last couple of years of support from the Air Force Research Laboratory in the form of a Southwestern Ohio Council for Higher Education (SOCHE) internship. There are many colleagues at AFRL that have provided technical and non-technical support in my research endeavors including Drs. Patrick Golden, Andy Rosenberger, Sushant Jha, Reji John, Dennis Buchanan, Jon Miller, Garth Wilks, and Christopher Crouse.

I am thankful for the computational resources provided by the Georgia Tech Partnership for an Advanced Computing Environment (PACE) and the U.S. Air Force Research Laboratory (AFRL) DoD Supercomputing Resource Center (DSRC) that supported many of the parametric studies performed in this work.

I would like to thank my parents and brothers who have all supported me throughout my career. Last and definitely not least, I owe a great deal of gratitude towards my wife, Melissa. Thank you for loving and supporting me throughout the difficult process of graduate school and finishing up the Ph.D. Dissertation.

## **Introduction**

The simulation and design of advanced materials for fatigue resistance requires an understanding of the response of their hierarchical microstructure attributes to imposed load, temperature, and environment over time. For Ni-base superalloy components used in aircraft jet turbine engines, different competing mechanisms (ex. surface vs. subsurface, crystallographic vs. inclusion crack formation, transgranular vs. intergranular propagation) are present depending on applied load, temperature, and environment. Typically, the life-limiting features causing failure in Ni-base superalloy components are near surface inclusions. Compressive surface residual stresses are often introduced in Ni-base superalloy components to help retard fatigue crack

initiation and early growth at near surface inclusions and shift the fatigue crack initiation sites from surface to sub-surface locations, thereby increasing fatigue life. To model the effects of residual stresses, inclusions, and microstructure heterogeneity on fatigue crack driving force and fatigue scatter, a computational crystal plasticity framework is presented that imposes quasi-thermal eigenstrain to induce near surface residual stresses in polycrystalline Ni-base superalloy IN100 smooth specimens with and without nonmetallic inclusions.

## Methodology

A microstructurally small crack (MSC) growth equation was developed that took into account (1) the tilt and twist character of the grain boundary, (2) the distance that the MSC was from the next grain boundary, and (3) an estimation of the evolution of driving force fatigue indicator parameter (FIP) with crack extension from initially uncracked simulations. This MSC growth model was fit to experiments (in both laboratory air and vacuum) for the case of 1D crack growth and then computationally applied to 3D crack growth from a focused ion beam (FIB) notch in a smooth specimen, from a debonded inclusion located at different depths from notched components containing different notch root radii, and from inclusions located at different depths from the surface in smooth specimens containing simulated shot-peened induced residuals stresses.

## Results

For the FIB notch studies, the MSC growth model successfully portrayed the scatter in experimental MSC  $da/dN$  versus  $\Delta K$  behavior of surface cracks. Using the square root of the projected area characterization method, the MSC model predicted the reduction in oscillation behavior of the MSC growth rate and the convergence toward linear elastic fracture mechanics (LEFM) response with crack extension; this reduced oscillation behavior was due to the crack front statistically sampling more grains with crack extension.

The calibrated MSC growth model was then used to study the effect of inclusion depth on fatigue life of notched components. It was found that inclusions located closer to the surface were statistically more detrimental than inclusions further into the bulk of the material. At the strain level tested, the predicted fatigue life behavior showed life-limiting phenomenon for only 1 to 2 out of 20 simulated instantiations. It was argued that more simulations should be performed to better characterize this life-limiting feature. However, the demonstration of the simulations as a tool to determine the relative effect of surface versus bulk fatigue crack formation and early growth seems promising. Indeed, once the simulated MSC penetrated the surface, the surface MSC growth rate versus range of stress intensity factor results tracked well with MSC experiments.

Next, a method for inducing shot-peened residual stresses within a computational crystal plasticity framework was presented. In this process, a distribution of quasi-thermal expansion eigenstrains was imposed on the finite element model resulting in a distribution of residual stresses. The eigenstrain distribution was first fitted to an experimentally-measured residual stress curve using an isotropic J2 plasticity material behavior and then applied within a crystal plasticity finite element method (CPFEM) model. Good correlation between computational and experimental values were obtained for (1) the initial residual stress profile, (2) the scatter in the initial residual stress profile among multiple instantiations, and (3) near surface residual stress relaxation trends for a single load/unload cycle.

The developed eigenstrain-based residual stress application technique was then used to investigate the effectiveness of residual stresses on near-surface suppression of fatigue crack initiation from non-metallic inclusions. The effect of compression was notable for determining the “debond life” for the inclusions within the region of highest compressive residual stresses. Once the inclusion was debonded from the matrix, it was simulated using an elastic/plastic compression/tension asymmetric material behavior given by the “cast iron plasticity” model in ABAQUS. This material behavior allowed for separate yield strengths and hardening behaviors in tension and compression. The MSC growth model from previous work was then extended to account for the effect of residual stresses on MSC growth. This modified MSC growth model was used in conjunction with an inclusion/matrix interfacial debond law and a crack incubation law of the Mura-Tanaka type to estimate the overall fatigue life of the simulated specimens with inclusions at different depths with and without initial residual stresses applied. The resulting estimated minimum life predictions correlated well with experimental trends, indicating the effectiveness of residual stresses in suppressing near-surface fatigue crack initiation within the transition fatigue regime between LCF and HCF.

The general framework presented in this work can be used to advance integrated computational materials engineering (ICME) by predicting variation of fatigue resistance and minimum life as a function of heat treatment/microstructure and surface treatments for a given alloy system and providing support for design of materials for enhanced fatigue resistance. In addition, this framework can reduce the number of experiments required to support modification of material to enhance fatigue resistance, which can lead to accelerated insertion (from design conception to production parts) of new or improved materials for specific design applications. Elements of the framework being advanced in this research can be applied to any engineering alloy.

## **Related Activities**

The following publications and dissertation are directly related to work summarized in this report:

- [1] Przybyla, C.P., Musinski, W.D., Castelluccio, G.M., and McDowell, D.L., (2013). Microstructure-sensitive HCF and VHCF simulations. *International Journal of Fatigue*, 57, 9-27.
- [2] Castelluccio, G.M., Musinski, W.D., and McDowell, D.L., (2014). Recent developments in assessing microstructure-sensitive early stage fatigue of polycrystals. *Current Opinion in Solid State and Materials Science*. In press, corrected proof. pp. 8. Doi: . <http://dx.doi.org/10.1016/j.cossms.2014.03.001>.
- [3] Musinski, W.D., Modeling the effects of shot-peened residual stresses and inclusions on microstructure-sensitive fatigue of Ni-base superalloy components. Ph.D. Dissertation, Georgia Institute of Technology, April 2014.

IMPROVE ENERGY TECHNOLOGIES

Project No. 0159

Rachel Smith  
Cedarville University

1 November 2013

Government Project Leader  
Mr. David Madden  
AFRL/RXSC

Southwestern Ohio Council for Higher Education  
Student Research Program  
Agreement Number: FA8650-09-2-5800

## **Acknowledgments**

I am thankful for the opportunity I had to work for AFRL/RXSC under Mr. Dave Madden this past year. I have gained useful information on various energy projects that our team is a part of. In particular, I would like to thank Mr. Dave Madden for his guidance on my project; he has provided much insight. In addition, Mr. Madden shared his interest in working with his students by arranging for me to work on a project that aligned best with my interests. I would also like to thank Ms. Andrea Mahaffey for all the work she did with me in conducting my questionnaire. She took the time to do her best to help me implement my project to its fullest. It has been a pleasure to work with Mr. Madden and his team for the time I was here.

## **General Description of Project**

Initial research was conducted on changing the culture in the workplace. In doing this, research focused on theories of behavior and attitude change. It was noted by Dave Madden that there seems to be a “cultural gap” between the older generations and the younger generations when it comes to willingness on saving energy. It was deemed necessary to gather data in order to assess the current workplace attitudes toward energy awareness.

The purpose of this research was to obtain a sample of data from the RX division of the Air Force Research Laboratory (AFRL) pertaining to beliefs about energy consumption and conservation. Several objectives were set when constructing the research method. Objective one included the creation of a standardized questionnaire in order to gather the baseline attitudes of the AFRL/RX workforce. The questionnaire aimed to collect two measures: demographics such as age and location as well as the attitudes and opinions of those surveyed. Furthermore, the questionnaire was not to be biased; the questions were to be parsimonious, and allowed for unambiguous and meaningful answers through close ended questions. Similarly, the questionnaire was to avoid leading questions, double-barreled questions, and vagueness. The sample of people used was to be an equivalent sample group due to the shared workplace of all participants. In order to assure validity, the questionnaire was given a pilot testing to an even smaller sample size that included the RXSC group. Through the pilot testing, the questionnaire was revised in order to more accurately measure the attitudes of AFRL/RX employees toward energy consumption and conservation. Objective two sought to implement the questionnaire to the sample selected: RX employees. The purpose of this research is to evaluate existing attitudes on energy awareness.

## **Description of Research**

Research was then conducted on how to properly gauge the current attitudes in the workplace. First, there was collaboration with Andrea Mahaffey, who holds the proper knowledge on administering a questionnaire to such a variety of people. It was agreed upon that the questionnaire would be administered to the RX directorate via the SharePoint site. Next, a template was set up through Andrea Mahaffey on the SharePoint site to enter the questionnaire in to. Once the questions were entered, there was the issue of how best to get the questionnaire out to the entire RX directorate. After collaboration with both Ms. Mahaffey and Mr. Madden, it was determined that the questionnaire would best be accepted through the Daily Dose email

distribution that is sent to RX members daily. Upon posting to the distribution, the questionnaire was readily accepted, which yielded a 34 person sample size.

Participants included 34 RX employees from various buildings throughout the complex. There were 12 females and 22 males who participated in this research. Demographics of the participants included 4 people from building 651; 10 people from building 652; 4 people from building 653; 8 people from building 654; 7 people from building 655; and 1 person from building 1661. There was also a variation in ages of participants: There were 7 people from the 20-29 age group, 4 people from the 30-39 age group, 9 people from the 40-49 group, 9 people in the 50-59 age group, and 5 people were 60 years or older. Overall, ages and buildings were pretty evenly distributed. The answers to the questionnaire were collected, and the data analysis phase ensued.

## **Results**

In order to best analyze the collected data, results were gathered into an excel spreadsheet. This data was then transferred into graphical form in order to compare results by building location, gender, and age group. Overall, reported attitudes within the RX directorate fall in the “aware” or “positive attitude” section. The results yielded encouraging results for the future direction of the RXSC group in particular. Due to the positive nature of attitudes reported from the questionnaire, future energy projects should be more readily accepted.

It is important to note that just because this questionnaire found overall positive attitudes among RX employees, does not mean that RX as a whole was accurately represented. It is questionable as to how generalizable these results actually are. Those who took the “Energy Awareness Questionnaire” may also be people who view energy in a more positive manner; those who may not view energy conservation as positive were probably underrepresented in this sample. In conclusion, the results obtained from this research are encouraging, but also possibly not generalizable to the entire RX population.

EVALUATION OF ALTERNATE FIBER FORMS FOR A HOT TRAILING EDGE  
STRUCTURE

Project No. 160

Daniel Reilly  
Wright State University

31 August 2014

Government Project Leader  
Dr. Brett Bolan  
AFRL/RXSA

Southwestern Ohio Council for Higher Education  
Student Research Program  
Agreement Number: FA8650-09-2-5800

## **Acknowledgments**

This report could not have been made possible without the combined efforts of a dedicated and talented RXSA team. I would like to thank Dr. Brett Bolan and Dr. Jim Mazza for making this internship possible. A special thanks goes out to Mr. Paul Childers for his technical support and knowledge of materials science.

## **General Description of Project**

The purpose of the Evaluation of Alternate Fiber Forms for a Hot Trailing Edge Structure project (1-007) is to demonstrate and transition a new higher temperature capable material form to an Air Force aircraft. Astroquartz-III/ AFR-PE-4 fabric prepreg was the first to be evaluated since many of the repairs to a HTE occur in the glass composite regions, the portion of the HTE that attaches to the body of the aircraft. The current polyimide material utilized behind the exhaust nozzle on the aircraft is in an environment that repeatedly undergoes thermal stresses which cause it to quickly degrade. The first task of this project required physical property testing of this graphite/ AFR-PE-4 material to see if it meets the Air Force requirements. This means testing both forms of the uncured fiber prepreg to the original equipment managers specified test methods for prepreg properties. Following this, cured forms of the composites were manufactured for laminate physical property testing while simultaneously assessing the plausibility of the carbon processability.

## **Description of Research**

Prepreg physical property evaluations consisted of tests for volatile content, resin content, fiber areal weight, and drape. All tests followed calculations and processes of the Northrop Grumman spec T-137B. Volatile content was found using 3"x3" squares of prepreg weighed to the nearest 0.005 grams. The specimens were exposed to a heat soak of 450°F for 10 minutes in order to cook volatiles out of the prepreg. The specimens were then reweighed to calculate the volatile content by weight percent. Resin content determination also used 3"x3" squares which were weighed initially then placed in Erlenmeyer flasks containing 250 ml of Acetone and agitated three separate times followed by a heat bath of 325°F. The goal was to dissolve the prepreg resin leaving behind just the fibers, and calculate the resin content by weight percentage. Using the same specimens, the fiber areal weight was calculated. Drape tests used a 3"x9" rectangular specimen which was attached to a drape fixture and inspected for fiber damage. All prepreg requirements can be found in Table 1. All collected data from prepreg physical properties can be found in Table 2.

Laminate physical property testing began with fabricating a carbon fiber AFR-PE-4 laminate. This began with cutting epoxy pre-impregnated fiber reinforcement. This type of carbon came in fabric rolls of various lengths which were subsequently cut into 12"x12" plies with an orientation stack up of  $[0, \pm 45, 90]_{2s}$  which were then stacked and vacuum debulked for 15 minutes in 4 ply books. The polyimide resin moved throughout the stacked plies of fiber during the debulk stage and the laminate became consolidated as air bubbles are removed which if left in, would result in porosity and possible laminate delamination. Once debulked, the panel was incorporated to AFRL's bagging sequence with the vacuum bag built around the laminate using porous Teflon, non-porous Teflon, fiberglass breather, and Kapton bagging material. The

goal was to create a vacuum seal around the laminate in order for the volatiles to be pulled out of the part through the vacuum hose and induce compaction pressure. The panel was then put in the



4'x2' AFRL autoclave where it was cured per AFRL's developed process. The elevated heat and

Figure 39 PE-4 Unidirectional Panel [0,±45,90]<sub>2s</sub>

pressure during the cure cycle initiates the chemical crosslinking in the resin resulting in a rigid laminate. This along with directional fibers gives the panel its strength. Once cured, the panel was taken to the non-destructive inspection team where the panel was ultrasonically scanned for defects (i.e. voids and delamination). The panel is shown in Figure 1. The panel passed the non-destructive inspection which means it had few discontinuities in the matrix and can be used for mechanical property testing.

## Results

Results show that graphite fiber/ AFR-PE-4 prepreg is an option for a HTE structure. Manufacturing the laminates shows the carbon fiber usage is plausible through means of the AFRL cure process. Non-destructive inspection on the panel shows minimal cavities in the matrix which means it will be useful for mechanical property testing. Prepreg physical property tests show that prepreg volatile content is consistently within 2 weight percent of requirements. Similarly, resin content meets requirements being in the  $35 \pm 3$  weight percent. Areal weight percent tests passed and were in the  $147 \pm 7$  region.

## Figures and Tables

Table 4 Unitape Prepreg Physical Property Requirements

Property	Requirement (Average)
Volatile Content, weight percent	$11.0 \pm 3.0$
Dry Resin Content, weight percent	$35 \pm 3$
Fiber Areal Weight, g/m <sup>2</sup>	$147 \pm 7$
Drape	Pass



Prepreg Volatile Content		
Specimen #		Value
<b>TVC-1</b>		
	Watch Glass Weight (Tared)	97.5952
	Specimen & Watch Glass Weight (Int)	99.1565
	Specimen Weight Int (WI)	1.5613
	Specimen & Watch Glass Weight (Post)	98.9304
	Specimen Weight Post (WF)	1.3352
	<b>Volatile Content</b>	14.48%
<b>Specimen #</b>		<b>Value</b>
<b>TVC-2</b>		
	Watch Glass Weight (Tared)	97.3332
	Specimen & Watch Glass Weight (Int)	98.7645
	Specimen Weight Int (WI)	1.4313
	Specimen & Watch Glass Weight (Post)	98.5625
	Specimen Weight Post (WF)	1.2293
	<b>Volatile Content</b>	14.11%
<b>Specimen #</b>		<b>Value</b>
<b>TVC-3</b>		
	Watch Glass Weight (Tared)	97.5031
	Specimen & Watch Glass Weight (Int)	99.0158
	Specimen Weight Int (WI)	1.5127
	Specimen & Watch Glass Weight (Post)	98.816
	Specimen Weight Post (WF)	1.3129
	<b>Volatile Content</b>	13.21%
<b>Prepreg Resin Content</b>		
<b>Specimen #</b>		<b>Value</b>
<b>TRC-1</b>		
	Watch Glass Weight (Tared)	97.627
	Specimen & Watch Glass Weight (Int)	99.061
	Specimen Weight Int (WI)	1.434

	Specimen & Watch Glass Weight (Post)	98.405
	Specimen Weight Post (WF)	0.778
	<b>Resin Content (Wet)</b>	45.75%
	<b>Resin Content (Dry)</b>	36.96%
	<b>Areal Weight</b>	134.1379
<b>Specimen #</b>		<b>Value</b>
<b>TRC-2</b>		
	Watch Glass Weight (Tared)	97.504
	Specimen & Watch Glass Weight (Int)	99.0586
	Specimen Weight Int (WI)	1.5449
	Specimen & Watch Glass Weight (Post)	98.3575
	Specimen Weight Post (WF)	0.06914
	<b>Resin Content (Wet)</b>	55.25%
	<b>Resin Content (Dry)</b>	48%
	<b>Areal Weight</b>	119.2
<b>Specimen #</b>		<b>Value</b>
<b>TRC-3</b>		
	Watch Glass Weight (Tared)	97.5834
	Specimen & Watch Glass Weight (Int)	99.144
	Specimen Weight Int (WI)	1.5606
	Specimen & Watch Glass Weight (Post)	98.4145
	Specimen Weight Post (WF)	0.8311
	<b>Resin Content (Wet)</b>	46.74%
	<b>Resin Content (Dry)</b>	38.12%
	<b>Areal Weight</b>	143.29

Table 5 Unitape Prepreg Physical Property Data

### Works Cited

McCray, Dan. "Evaluation of Alternate Fiber Forms of AFR-PE-4 for B-2 Hot Trailing Edge Structure." (2013): 1-17. Print.

HIGH TEMPERATURE SYNTHESIS OF LOW DIMENSION STRUCTURES

Project No. 0161

Emory Beck-Millerton  
University of Cincinnati

21 August 2014

Government Project Leader  
Dr. Shanee Pacley  
AFRL/RXAN

Southwestern Ohio Council for Higher Education  
Student Research Program  
Agreement Number: FA8650-09-2-5800

## **Acknowledgements**

I would like to give my deepest gratitude to Dr. Shanee Pacley, Mr. Adam Waite, Mr. John Bultman, Mr. Michael McConney, Dr. Michael Check, Dr. Michael Jespersen, Ms. Diana Carlin, Mrs. Rachel Naguy, Dr. Andrey Vovoedin, Dr. Raj Ganguli, Mr. Randall Stevenson, Mr. Jamie Gengler, Mr. Nicholas Glavin, Mr. Arthur Safriet, Mr. John Camping, Mr. Scott Apt, Mr. Gerald Landis, Mr. Douglas McFarland, and Dr. Fahima Ouchen for helping me with my research project.

## **General Project Description**

This project was to study and develop the Chemical Vapor Deposition (CVD) based growth procedure of the transition metal dichalcogenide, molybdenum disulfide ( $\text{MoS}_2$ ). It is generally used as a solid lubricant but has exhibited great potential in nano-electronics and optical applications. A procedure that would facilitate the transfer of this thin film was also developed. The purpose of this was to perfect the synthesis/growth of this dichalcogenide and eventually transfer it to flexible substrates and then to construct heterostructures using other 2D materials such as hexagonal boron nitride and graphene.

## **Research Description**

Research was performed on the growth and transfer of molybdenum disulfide ( $\text{MoS}_2$ ). This thin film dichalcogenide was grown using the chemical vapor deposition (CVD) process. The process was used to facilitate the sulfurization of molybdenum (VI) oxide (or molybdenum trioxide,  $\text{MoO}_3$ ) using sapphire as the target substrate. Initially, experiments were performed to determine the optimum growth conditions. These experiments were also performed on sapphire substrates of various dimensions: 0.25 in x 0.25 in, 0.5 in x 0.5 in, and 1 in x 1 in. It was discovered that a different amount of sulfur would be necessary depending on the dimensions of the target substrate.

$\text{MoO}_3$  was deposited on the sapphire substrates using magnetron sputtering in which plasma is created by reacting a molybdenum target with oxygen. The sample was then characterized using X-Ray Photoelectron spectroscopy (XPS) in order to verify the presence of  $\text{MoO}_3$  and calculate film thickness. (Figure 1)

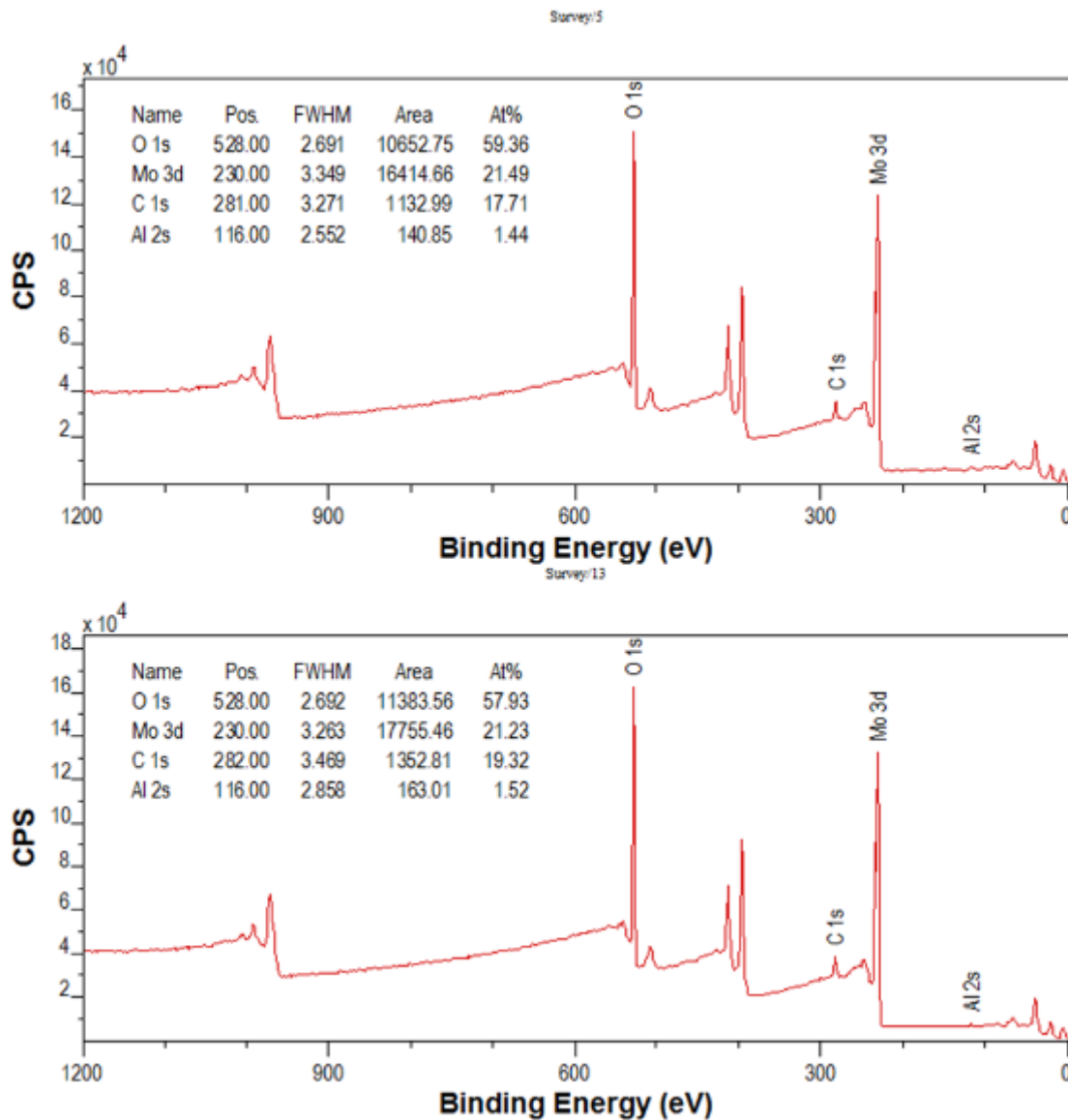


Figure 1. XPS data verifying the presence of MoO<sub>3</sub> on a sapphire substrate with the binding energy of molybdenum being around 230 eV and the binding energy of oxygen being around 528 eV.

The sample was then placed into an alumina boat. The sample was loaded into a quartz tube in one of the three zones of the CVD furnace. Sulfur was measured out according to the dimensions of the sapphire substrate (e.g. 2.0 g of sulfur for a 1 in x 1 in substrate) and placed into the quartz tube but outside of the furnace. The sapphire substrate was heated up to 750 °C in two steps (to 550 °C at 20 °C/min and then to 750 °C at 5 °C/min) a mixture of Ar/H<sub>2</sub> gas was used at 64.8 sccm, under a vacuum pressure of 5 Torr. Once the furnace reached 750 °C the sulfur was moved inside the quartz tube. The transfer of heat throughout the furnace allowed for the sulfur to evaporate and be carried by the Ar/H<sub>2</sub> gas, causing a reaction with the MoO<sub>3</sub>. The MoO<sub>3</sub> sublimed at 750 °C and thus reduced to MoO<sub>2</sub> which then reacted with the sulfur atoms and converted to MoS<sub>2</sub>. The furnace was then allowed to cool off throughout the remainder of the

work day with the Ar/H<sub>2</sub> still flowing through the furnace. The variables that were changed during experimentation period were the vacuum pressure, amount of sulfur needed for the various substrate sizes and the dwell time necessary for the sulfur to evaporate.

After the furnace cooled down, the sample was taken out to have Raman characterizations performed on it. The Raman spectra for MoS<sub>2</sub> shows peaks at (or around) 383 cm<sup>-1</sup> (E<sub>2g</sub>) and 408 cm<sup>-1</sup> (A<sub>1g</sub>). (Figure 2) The purpose of this was to quickly verify the presence of MoS<sub>s</sub> on the sapphire substrate. Also, the data acquired was one of ways used to determine the quality of the MoS<sub>2</sub>. The E<sub>2g</sub> peak represents in-plane vibration and the A<sub>1g</sub> peak represents the out-plane vibration. The ratio of these two values is the lateral coherence of the material and thus the quality indicator with high values meaning good quality. Further confirmation was acquired by taking optical images of the sample. (Figure 3) Once the sample was confirmed to have a MoS<sub>2</sub> film on it, Atomic Force Microscopy (AFM) was performed on the sample. The purpose of this characterization procedure was to determine the roughness of the MoS<sub>2</sub> film. (Figure 4) XPS was performed after AFM in order to determine the thickness of the MoS<sub>2</sub> and its stoichiometry. (Figure 5) The thickness helped determine how many layers of MoS<sub>2</sub> the film consisted of and the stoichiometric amount showed whether the reagent (sulfur) was totally consumed.

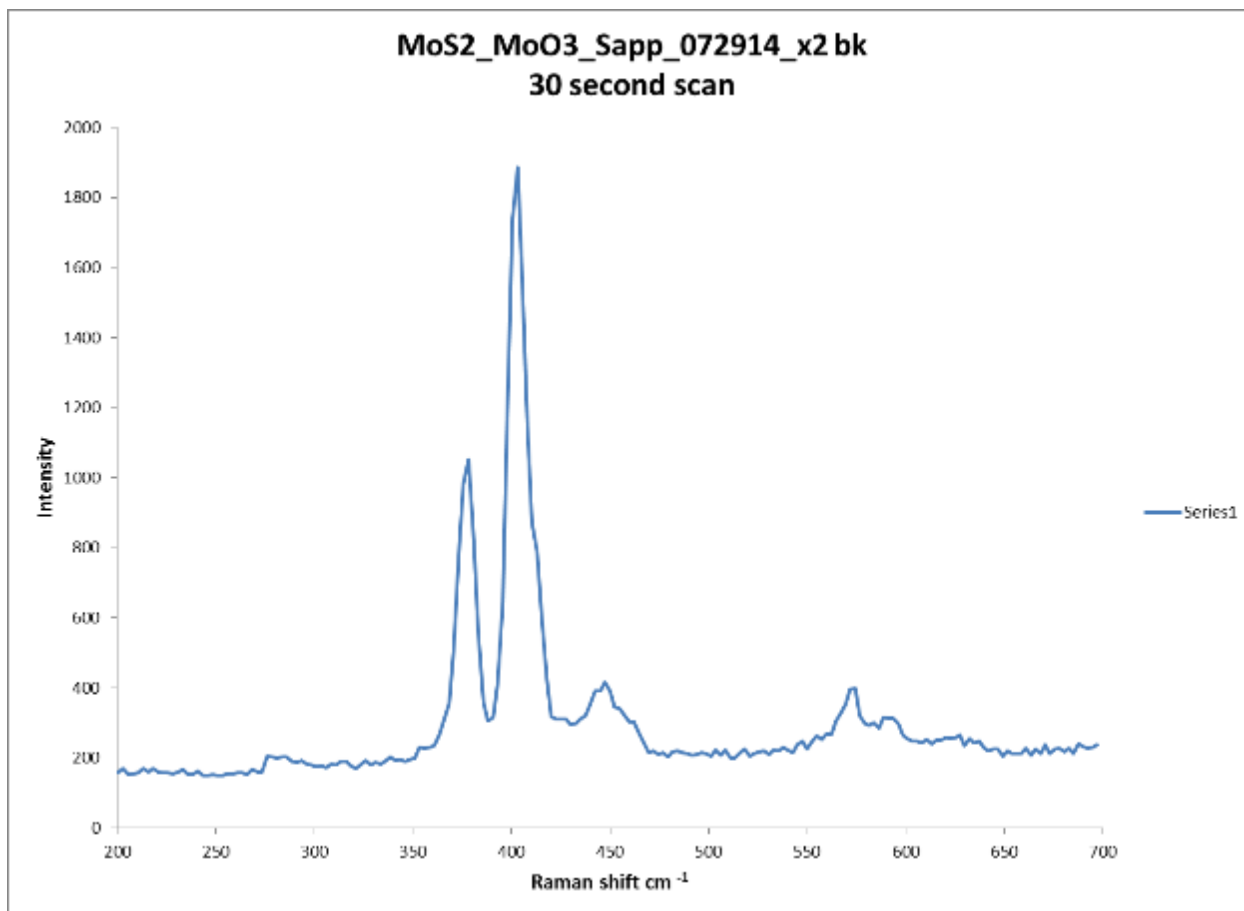


Figure 2. Raman spectra of MoS<sub>2</sub> grown on sapphire. The peaks indicative of MoS<sub>2</sub> are fairly intense here with a relative intensity value of ~0.94.



Figure 3. Optical Image of MoS<sub>2</sub> on a sapphire substrate. The ‘scratches’ on the sample is actually excess sulfur that coalesced on the substrate during the final stages of the growth process. These were burned off during XPS without damaging the sample.

RMS Roughness: 13.0nm

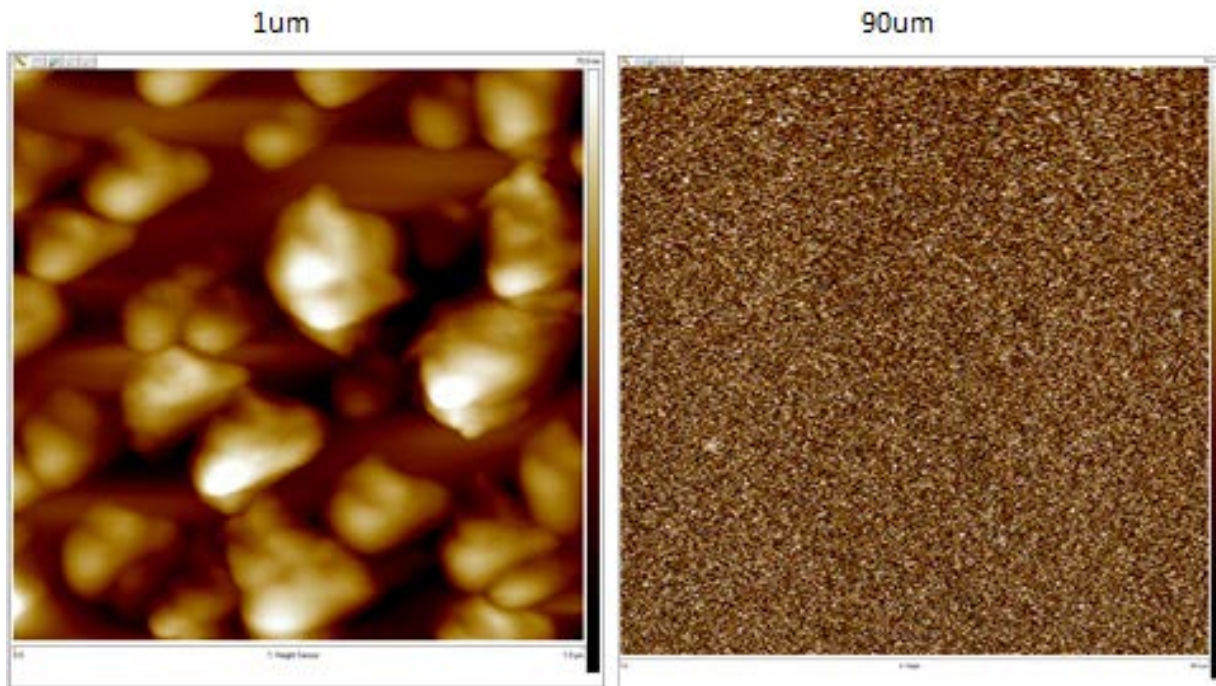


Figure 4. Topographic AFM scan of MoS<sub>2</sub> grown on sapphire. Scan is at two different magnifications on a portion of the sample. It shows a roughness of 13 nanometers. (nm)

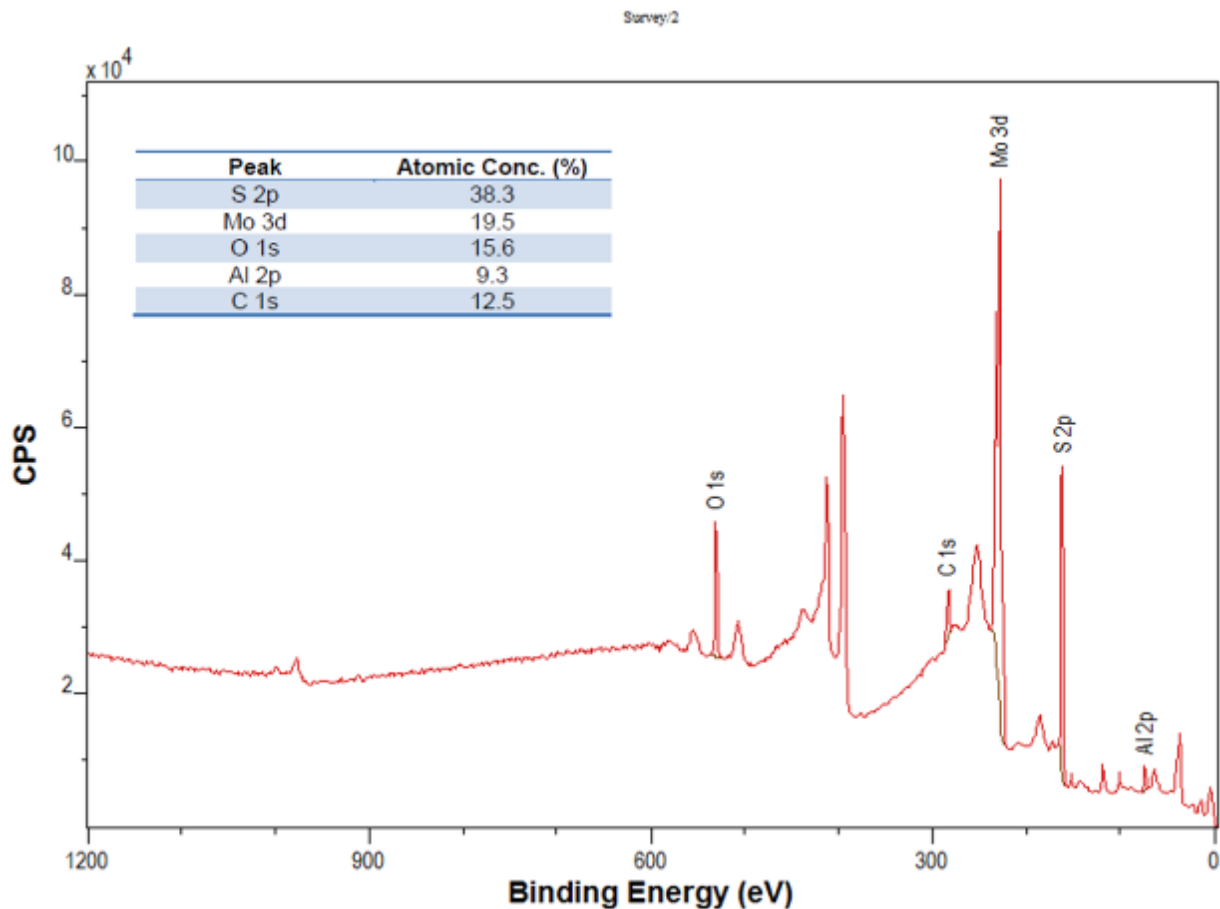


Figure 5. XPS survey scan of MoS<sub>2</sub> grown on sapphire. Atomic concentration values are shown which can be used to calculate the stoichiometry ratio of sulfur and molybdenum. This particular sample has a ratio of 1.96. This is good because 2 is the optimum value (S: Mo → 2:1).

Once the MoS<sub>2</sub> sample was confirmed to be of good quality, the sample was then subject to transfer onto a different substrate, potentially for further characterization. The target substrates for MoS<sub>2</sub> transfer were silicon dioxide (300 nm on silicon, SiO<sub>2</sub>/Si) and transmission electron microscopy (TEM) copper grids. Initial ideas for a transfer involved a process that utilized a sodium hydroxide (NaOH), hydrogen peroxide (H<sub>2</sub>O<sub>2</sub>), and de-ionized water solution (the ratio being 1:1:3) to loosen the film from the sapphire substrate. (Lin, et al. 2012) Poly(methyl methacrylate) (PMMA) was spin-coated onto the sample to provide a solid hold for the film to be maneuvered. Afterward, the sample was placed into the NaOH solution for 15 minutes while heated to 100 °C. The sample is then placed into de-ionized water. This step allowed the film to de-laminate for 5 to 15 minutes. The film was then ‘fished’ out and placed onto the target substrate. Next, the MoS<sub>2</sub> sample was baked at 100 °C for 10 minutes. Acetone, isopropyl alcohol (IPA), de-ionized water, and then chloroform were all used to dissolve the PMMA. (Lin, et al. 2012) This process was tested but did not yield satisfying results. Thus the process was changed multiple times with the same basic structure and the results have improved with each change. The changes made to this process were the following: use ammonium hydroxide (NH<sub>4</sub>OH) instead of NaOH, baking the sample at 180 °C for 2 to 3 minutes following the

depositing of the PMMA, keeping the solution at room temperature as opposed to heating to 100 °C, allowing the sample to remain in the solution until the MoS<sub>2</sub> starts to lift (usually 5 minutes), air drying the sample after 'fish' out, using acetone and IPA to remove the PMMA, and drying the sample by lightly spraying it with nitrogen gas.

## Results

It was discovered that the amount of sulfur used, and the vacuum pressure at which the growth occurred, were both important components to the growth of continuous MoS<sub>2</sub> on sapphire substrates. Detailed information about the characterization procedures used was also learned, along with how to interpret the data received. The transfer procedure changed because of the discoveries made about the differences between the NaOH and the NH<sub>4</sub>OH. Work on this procedure must still be done in order to transfer the films consistently.

The data obtained from the raman spectra, optical images, topographic AFM scans, and the XPS scans have shown that the MoS<sub>2</sub> grown using the final growth conditions have been very good for all of the proposed sample sizes. In conclusion, MoS<sub>2</sub> can be grown by reacting sulfur with MoO<sub>3</sub> that has been deposited onto sapphire substrates of various sizes by heating the MoO<sub>3</sub> to its sublimation temperature of 750 °C and varying the amount of sulfur. Also, transferring MoS<sub>2</sub> to arbitrary substrates can be performed by breaking the bond between the MoS<sub>2</sub> film and its original substrate. The film is then placed onto a different substrate for further characterization.

## Works Cited

- 1) Lin, Yu-Chuan, Wenjing Zhang, Jing-Kai Huang, Keng-Ku Liu, Yi-Hsien Lee, Chi-Te Liang, Chih-Wei Chu, and Lain-Jong Li. "Wafer-scale MoS<sub>2</sub> Thin Layers Prepared by MoO<sub>3</sub> Sulfurization." *Nanoscale* 4 (2012): 6637-641. *Nanoscale - Royal Society of Chemistry*. 29 Aug. 2012. Web. 8 Jan. 2014.

EFFECT OF MICROSTRUCTURE ON SMALL CRACK GROWTH IN TI-6AL-4V

Project No. 0162

Alec Blankenship  
Wright State University

31 August 2014

Government Project Leader  
Dr. Reji John  
AFRL/RXCM

Southwestern Ohio Council for Higher Education  
Student Research Program  
Agreement Number: FA8650-09-2-5800

## Acknowledgments

This project was guided by the government researchers Dr. Reji John, Dr. Sushant Jha, Dr. Chris Szczepanski, Dr. Mike Caton, and Eric Burba. I wish to express gratitude to these individuals who have provided their time and support both on and off this project.

## General Description of Project

This project aims to explore the life limiting behavior of fatal flaws commonly associated with materials used in aerospace applications. A more accurate prediction of the lifetime will allow engineers to utilize the full lifetime potential of these materials which could assure safety and increase affordability. Material fatigue has resulted in catastrophic failures in the past and remains a major concern for engineers moving forward. It has been shown in AFRL/RXCM that the majority of life-limiting fatigue failures are caused by the initiation of microstructure scale cracks and their resulting propagation.

Cracks usually initiate due to flaws in alloy casting processes. Depending on the flaw, the cracks will propagate through the three regimes as shown in figure 1. The figure is a log-log plot of the propagation rate ( $\frac{da}{dN}$ ) and the stress intensity factor range ( $\Delta k$ ).

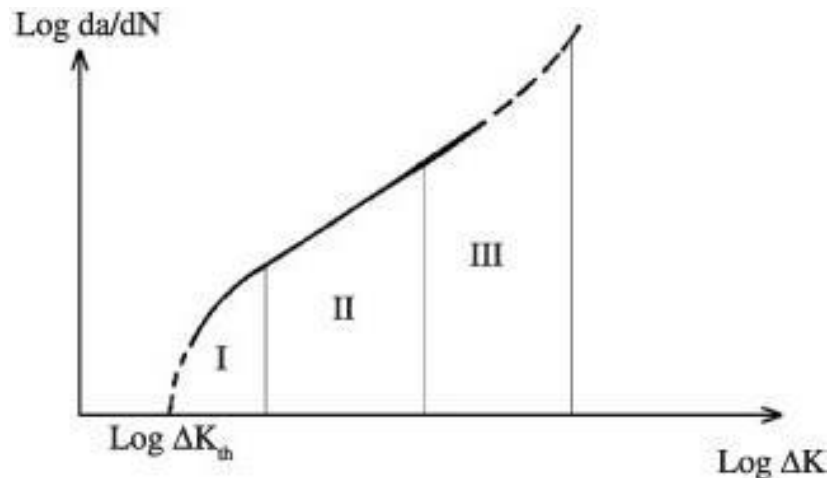


**Figure 40: Three regimes of crack growth (*Materials Research - Crack Propagation under Constant Amplitude Loading Based on an Energetic Parameters and Fractographic Analysis - 2014*)**

In the first regime the cracks are very sensitive to the microstructure around them. The size and orientation of the grain microstructure around the crack can impede or stimulate the cracks propagation. This variability is very important as it can have a dramatic effect on the fatigue lifetime. The second regime shows steady crack growth behavior which has proven to be fairly repeatable in a laboratory environment. In the final region of crack growth the crack is at the end of its lifetime and rapidly grows causing fracture as indicated by the plot.

For this project the titanium alloy Ti-6Al-4V was tested under constant loading conditions. The samples used had random microstructures at the crack initiation sites to allow for the collection of crack growth population data for this particular alloy. Because the microstructures are slightly different locally around the cracks, the area of interest is the small crack growth found under the first regime as illustrated in the plot above. As mentioned previously, this regime is where the microstructure has the most affect on the crack propagation properties. The goal of this project is to collect a population of data and quantify the performance of each specimen based on crack propagation rates.

### Description of Research

The project uses a group of Ti -64 dogbone specimens that were loaded into an MTS load frame designed to provide tensile stress along the vertical axis of the sample. Prior to testing the titanium specimens were electropolished after low stress grinding to provide a uniformly smooth surface that is suitable for replication methods and observation. Once the samples were completely polished, a 30 micron width notch was inscribed using focused ion beam (FIB) microscopy. This notch was used to initiate the crack site and was placed such that the local microstructure was random for each specimen. Ideally the random microstructures will provide the data with a good statistical distribution for further population based analysis. A pictorial description of the specimen can be seen in figure 2 below.

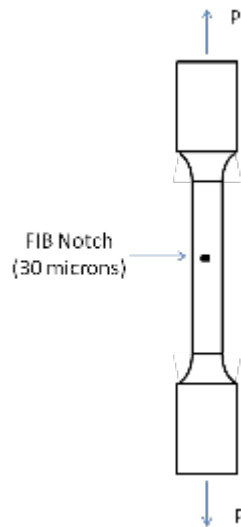


**Figure 41: Diagram of FIB notched specimen used**

Once the specimens were loaded they ran for a defined number of cycles before being interrupted to perform the standard acetate replication method. Each specimen was approximately 4mm in diameter and was run at the conditions found in Table 1 below.

**Table 6: Test Parameters**

Max Stress ( $\sigma_{max}$ )	690 MPa
Stress Ratio (R)	0.1
Cycling Frequency ( $\nu$ )	20 Hz
Temperature (T)	23 C – Room Temp

Once the sample failed, optical microscopy was used to inspect each replication and quantify the length of the crack at each cyclic interval. Scanning electron microscopy (SEM) would later be used to image the fracture surface of the specimens and obtain high magnification and high resolution images of the initiation site at the fracture surface. Since this is an ongoing project, the data, images, and qualitative information will continue to be used to characterize the crack growth properties in this titanium alloy.

### Results

Several specimens have been tested thus far and have each yielded similar looking data as one would expect from the same type of material. The plot in figure 3 below shows the curve that relates the crack length to the number of cycles the specimen has undergone.

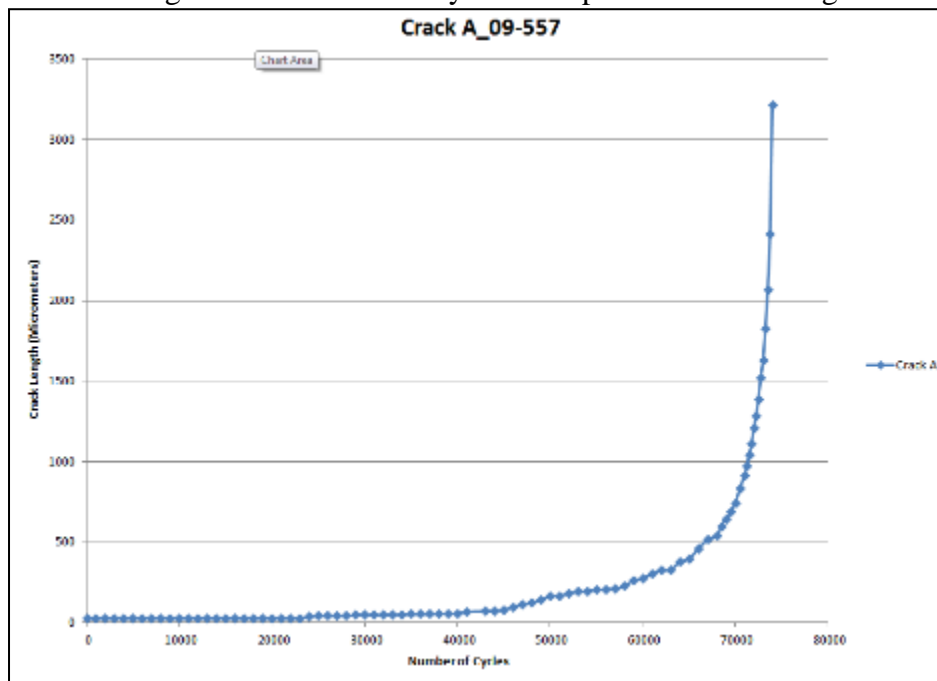


**Figure 42: Crack Length vs Cycle Number curve**

The figure shows that initiation occurred after 20000 cycles and maintained small crack behavior until the rate of change in the crack length begins to increase with every cycle. This

data was then used to create the log-log plot of the propagation rate ( $\frac{da}{dN}$ ) and the stress intensity factor range ( $\Delta k$ ) as shown previously.

High resolution and high magnification images were also taken at the fracture surface of each specimen. This imaging technique is called fractography and is used to observe the fracture surface and characterize the internal microstructure around the crack initiation site. Figures 4-6 are samples of the fractography images that are used in this project. Note that these images do not all come from the same fractured sample.

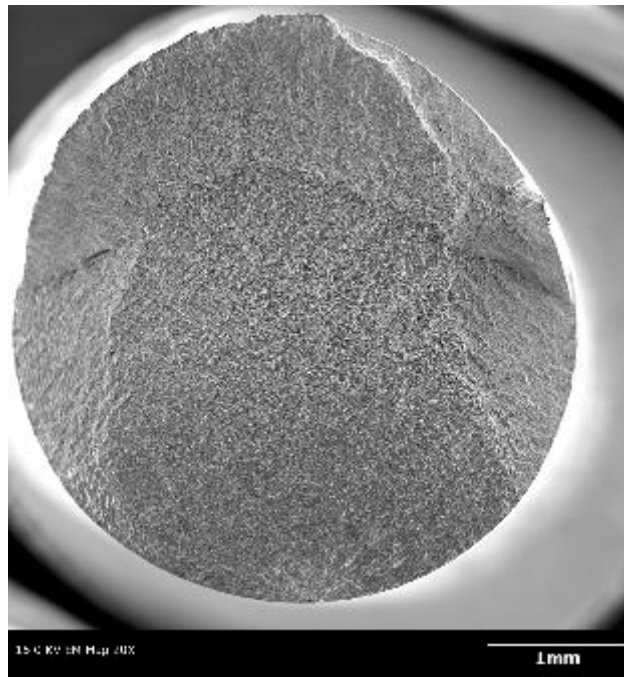


**Figure 43: 20x image**

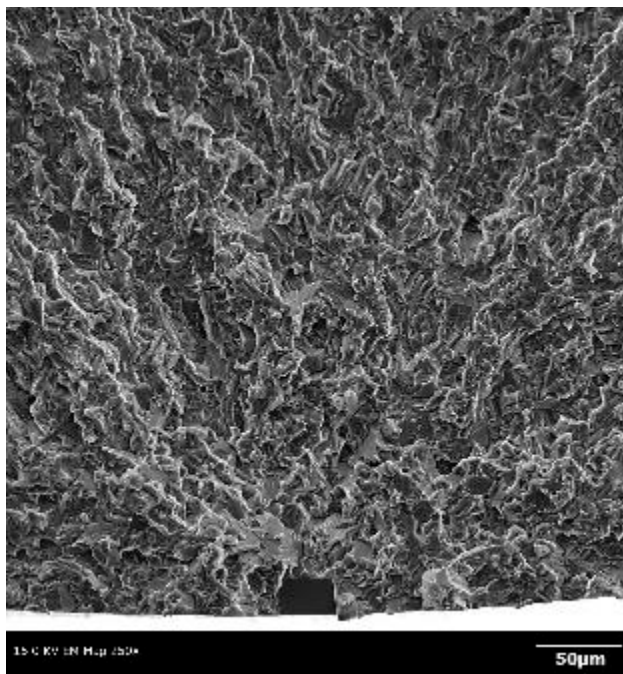


**Figure 44: 250x image**

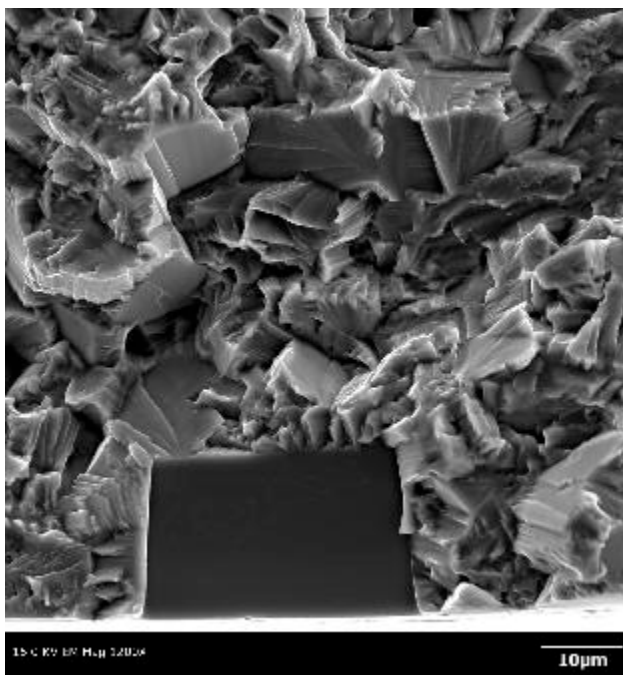


**Figure 45: 1200x image**

Figure 4 shows the square FIB notch as well as the depth that the surface crack penetrated through the diameter of the sample. From the images in figures 5 and 6 the fracture lines created by the crack show to be coming from the FIB notch meaning that is where the crack initiated, the goal from the beginning. The images and data that were collected will continue to be used to characterize the crack growth properties of the Ti-64 alloy.

### Works Cited

- Jha, Sushant K., Reji John, and Larson M. James "Incorporating Small Fatigue Crack Growth in Probabilistic Life Prediction: Effect of Stress Ratio in Ti-6Al-2Sn-4Zr-6Mo." *International Journal of Fatigue* (2013): 83-95. Web
- Jha, Sushant K., Szczepanski J. Chris, and Larson M. James "Reducing Uncertainty in Fatigue Life Limits of Turbine Engine Alloys." *International Journal of Fatigue* (2013): 103-12. Web.
- Materials Research - Crack Propagation under Constant Amplitude Loading Based on an Energetic Parameters and Fractographic Analysis*. N.p., n.d. Web. 29 Aug. 2014.

LIQUID METAL FOR TUNABLE CONFORMAL ANTENNAS

Project No. 0163

Brad Cumby  
University of Cincinnati

11 April 2014

Government Project Leader  
Dr. Christopher Tabor  
AFRL/RXAP

Southwestern Ohio Council for Higher Education  
Student Research Program  
Agreement Number: FA8650-09-2-5800

## Acknowledgments

I would like to thank SOCHE for financial support, for without this support, the project and work reported herein would not be possible. I would like to thank Dr. Christopher Tabor for taking the initiative to lead this project, without his support and collaboration with the University of Cincinnati this work would not be possible. I would like to thank my advisor, Dr. Jason Heikenfeld, for he has played an important role in guiding the scope of the research reported herein. I would like to thank Dr. David Mast for providing a collaborative effort, laboratory equipment, and expertise.

## General Description of Project

Present day electronics are now taking on small form factors, unexpected uses, adaptability, and other features that only a decade ago were unimaginable even for most engineers. To optimize electronics a growing trend has been to both minimize the physical space taken up by the individual electronic components as well as to maximize the number of functionalities in a single electronic device, forming a compact and efficient package. To accomplish this challenge in one step, many groups have used a design that has reconfigurable electromagnetic properties, maximizing the functionality density of the device. Having multiple or reconfigurable electromagnetic capabilities within a single device is highly desirable, however, typical devices are limited in reconfigurability [1] compared to actual physical rearrangement of metal conductors to modify apertures, resonance lengths, etc. There is also increasing interest in physically flexible or conformal electronics [2] which can improve user ergonomics and facilitate integration into applications where a rigid substrate is not possible.

The work reported herein involves reconfigurable pressure-actuated liquid metal devices (Figure 1) with fundamental electromagnetic capabilities within the GHz regime spanning tunable dipole antennas, switchable shielding with 35 dB attenuation, ~30 dB polarizer attenuation, and ~40 degree diffraction from a linear grating. These devices consist of inherently flexible materials, use non-toxic GaInSn (68.5% Ga, 21.5% In, and 10.0% Sn ) alloy, employ non-alloying/corrosion-resistant electrodes, and are implemented in a sealed closed system (Figure 1) with oxide-preventing reducing-vapor background since the GaInSn forms a sticky oxide. The devices all rely on a similar construction (Figure 1) and operation. With <10 pounds per square inch (psi) vacuum applied to two flexible films, one film having a network of microreplicated trenches (between spacers), the channel height between the films collapses, radius of curvature of the liquid metal residing between these two films decreases, increasing Laplace pressure (Laplace pressure is inversely proportional to radius of curvature for a liquid surface) driving the liquid metal into the trenches [3]. Upon release of vacuum, the channel height returns to its original position, erasing the liquid metal pattern as surface tension dewets the liquid metal into droplets that compacts to 10-100x less area than when in the trenches.

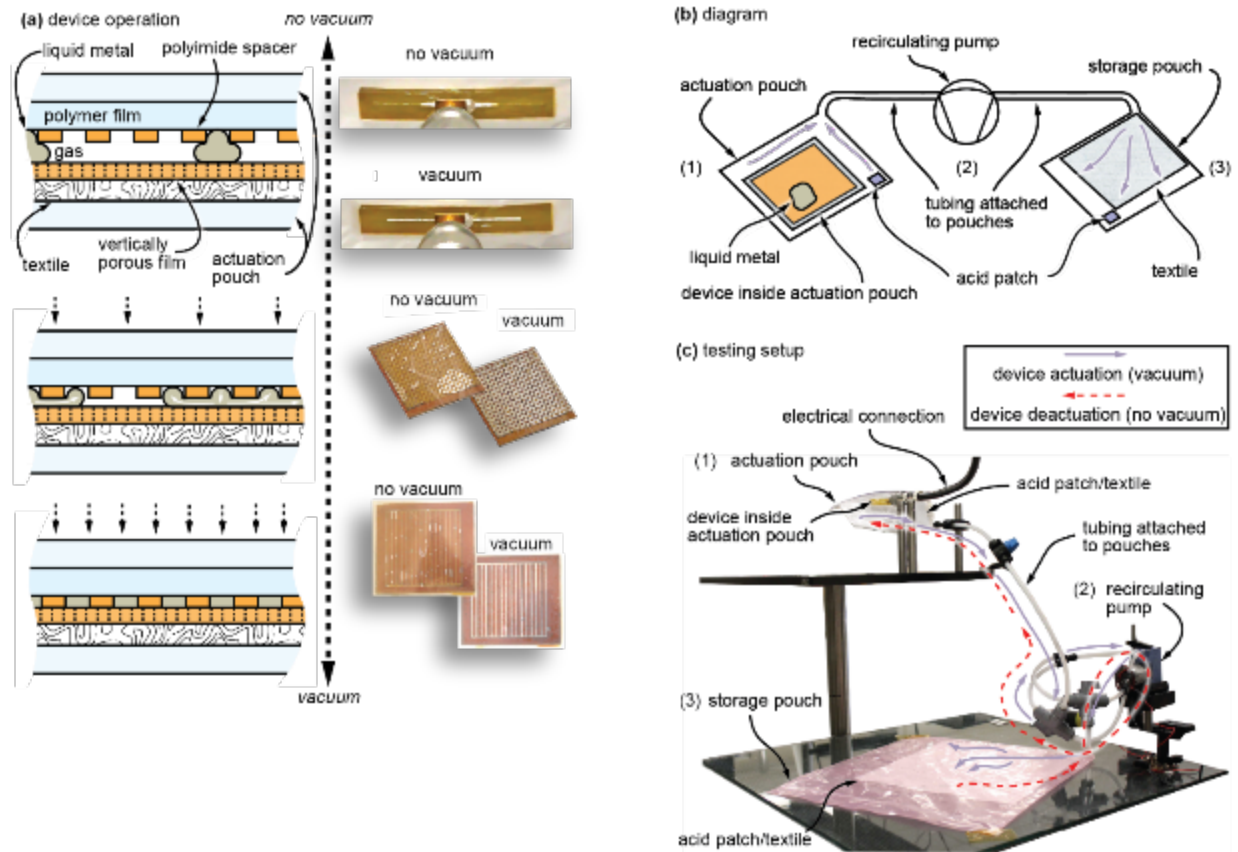


Figure 1. Diagram of a reversible vacuum pressure-actuated liquid metal device (left) and photographed examples including antennas, shields and polarizers (middle-left, top to bottom). (b) Diagram and (c) photograph of the system used for the experiments shown herein. The system is easily miniaturized (not shown).

## Description of Research

A tunable dipole antenna was assembled using components shown in Figure 2. The polydimethylsiloxane (PDMS) superstrate was formed using Dow Corning Sylgard 184 and has a specific geometry for promoting analog control of the liquid metal actuation (more pressure results in an equal increase in length of each dipole arm Figure 2). To provide radio-frequency (RF) electrode connections that are non-alloying with the liquid metal, a conductive carbon ink protective coating was added (Henkel, Acheson Electrodag PF-407C). The coated RF electrode tips were then inserted through two vias that were laser ablated through the device pouch as well as placed through the vias formed in the PDMS superstrate. Lastly, the adhesive perimeter was achieved using 101.6  $\mu\text{m}$  thick double-sided polyimide adhesive tape (Kapton). Two liquid metal droplets were dosed under the retraction domes and then the superstrate pressed against the adhesive layer. The device is then placed into the actuation pouch (Figure 1b). The RF connector is connected to a coaxial cable which is then connected to a network analyzer (Agilent 8753D) and the resonant frequency of the dipole antenna was measured as a function of length as

the device is cycled (actuated/deactuated, see Figure 1c). The resonant frequency is approximated by a dielectrically loaded dipole antenna by:

$$f = \frac{2 \cdot c}{L \sqrt{\epsilon_{eff}}}, \quad (1)$$

where  $c$  is the speed of light,  $L$  is the length of the dipole (Figure 2) and the effective dielectric,  $\epsilon_{eff} \sim 2.0$ . This resonant frequency vs length was measured (network analyzer), calculated (Eqn. 1) and simulated (Agilent ADS) and is plotted in Figure 2.

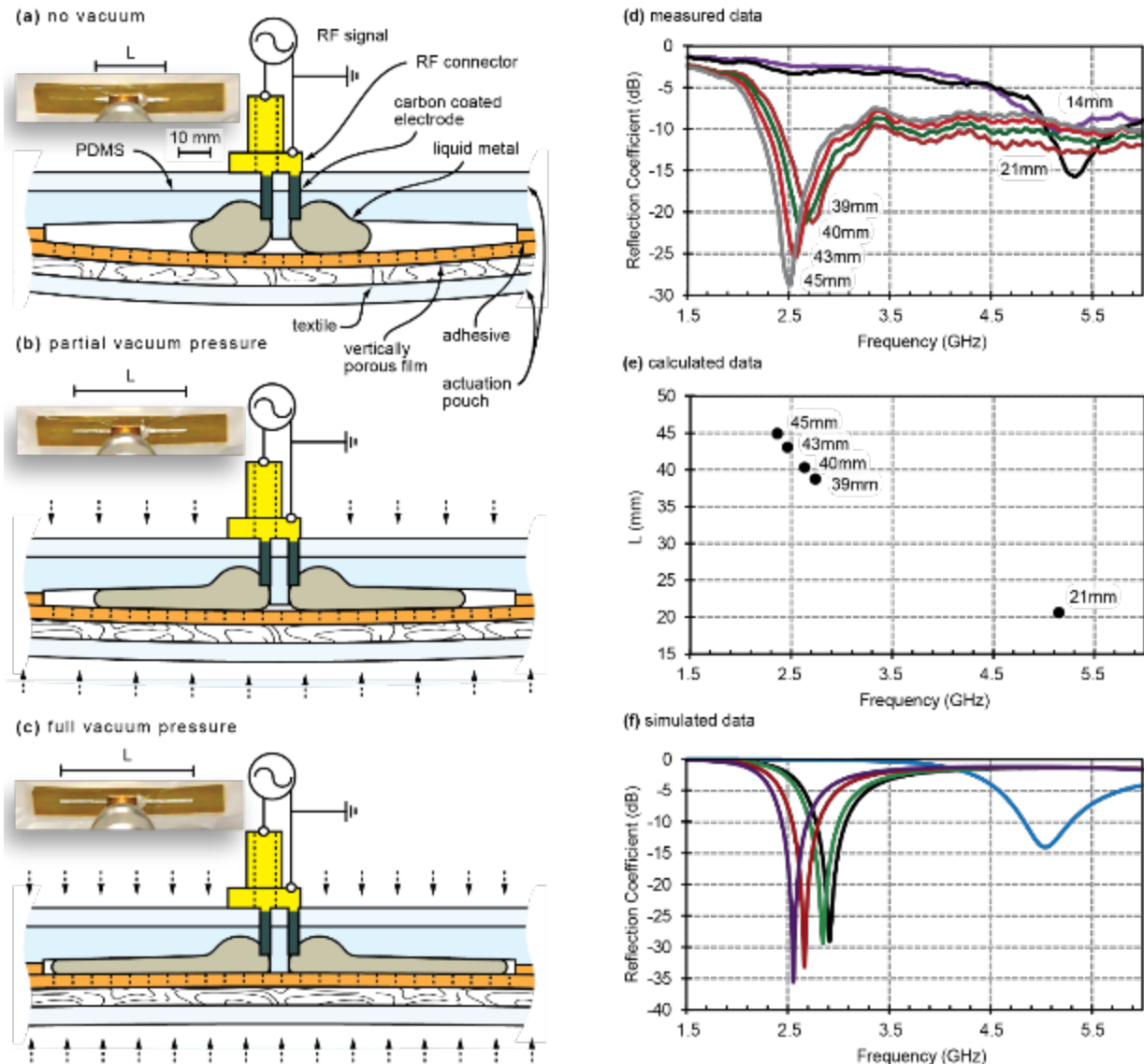


Figure 2. Dipole operation diagrams and experimental photographs (left) including labeling of the combined dipole length ( $L$ ). Dipole device data (right) as vacuum pressure is

applied and dipole length is varied as (d) measured, (e) calculated, and (f) simulated using Agilent ADS.

A switchable electromagnetic shield, polarizer and diffraction grating was created using flexible materials similar to those shown in the diagrams of Figure 1. The laser-ablated polyimide spacers determines the shape that the liquid metal takes when the device is actuated. In regards to the shield these were circular spacers ~0.9 mm in diameter, 50  $\mu\text{m}$  in thickness, and spaced center-to-center at 3.0 mm in an irregular hexagonal lattice, and carried by a polyethylene terephthalate (PET) substrate 254  $\mu\text{m}$  in thickness. Linear spacers 0.94 mm wide, height 100  $\mu\text{m}$ , length of 43.0 mm, and spaced 1.673 mm apart as well as 4.0 mm in width, 0.73 mm in spacing, 50  $\mu\text{m}$  in thickness, and 43.0 mm in length in regards to the linear polarizer and diffraction grating respectively. When actuated the shapes taken were: liquid metal film with circular apertures and a plane consisting of parallel liquid metal lines, for the shield and both the linear polarizer and grating respectively. Like the dipole antenna, a double-sided Kapton tape adhesive boarder was used to seal the substrate carrying the polyimide spacers to the vertically porous film. The sealed device was placed on top of a textile and then placed inside the actuation pouch. The transmission was measured as each device was placed between: rectangular waveguides and horn antennas for both the shield and polarizer and grating respectively.

The switchable shield reconfigures between multiple compact droplets to a reticulated network that attenuates incoming microwaves. The transmission loss or shielding effectiveness (S.E.) of the shield was approximated using [4]:

$$\text{S. E.} = 20 \log \left( \frac{3ab\lambda_0}{2\pi d^3} \right) + \frac{32t}{d} - 20 \log \left( \frac{1}{\cos \theta_i} \right) \quad (2)$$

$$b = a/2 \tan \theta. \quad (3)$$

Where  $a$  is the spacing from center to center of the apertures (polyimide spacers),  $\theta$  is a 45 degree angle between rows of apertures,  $d$  is the diameter of the spacers,  $\theta_i$  is the incident angle of the microwaves,  $\lambda_0$  is the free space wavelength and  $t$  is the thickness of the shield. The data shown in Figure 3 (b,c) shows the amount of power measured in both actuated and non-actuated states of the shield. The simulated data in Figure 3 (f) is completed by using a 2-D simulation (COMSOL) of the shield setup with only one row of liquid metal/polyimide spacers as a unit cell. The results were then modified according to [5]:

$$\text{S. E.}_{net} = \text{S. E. (simulated)} - 20 \log \sqrt{n}, \quad (4)$$

where  $n$  is the largest number of consecutive apertures formed in a straight line within an array of total length that is less than half a wavelength.

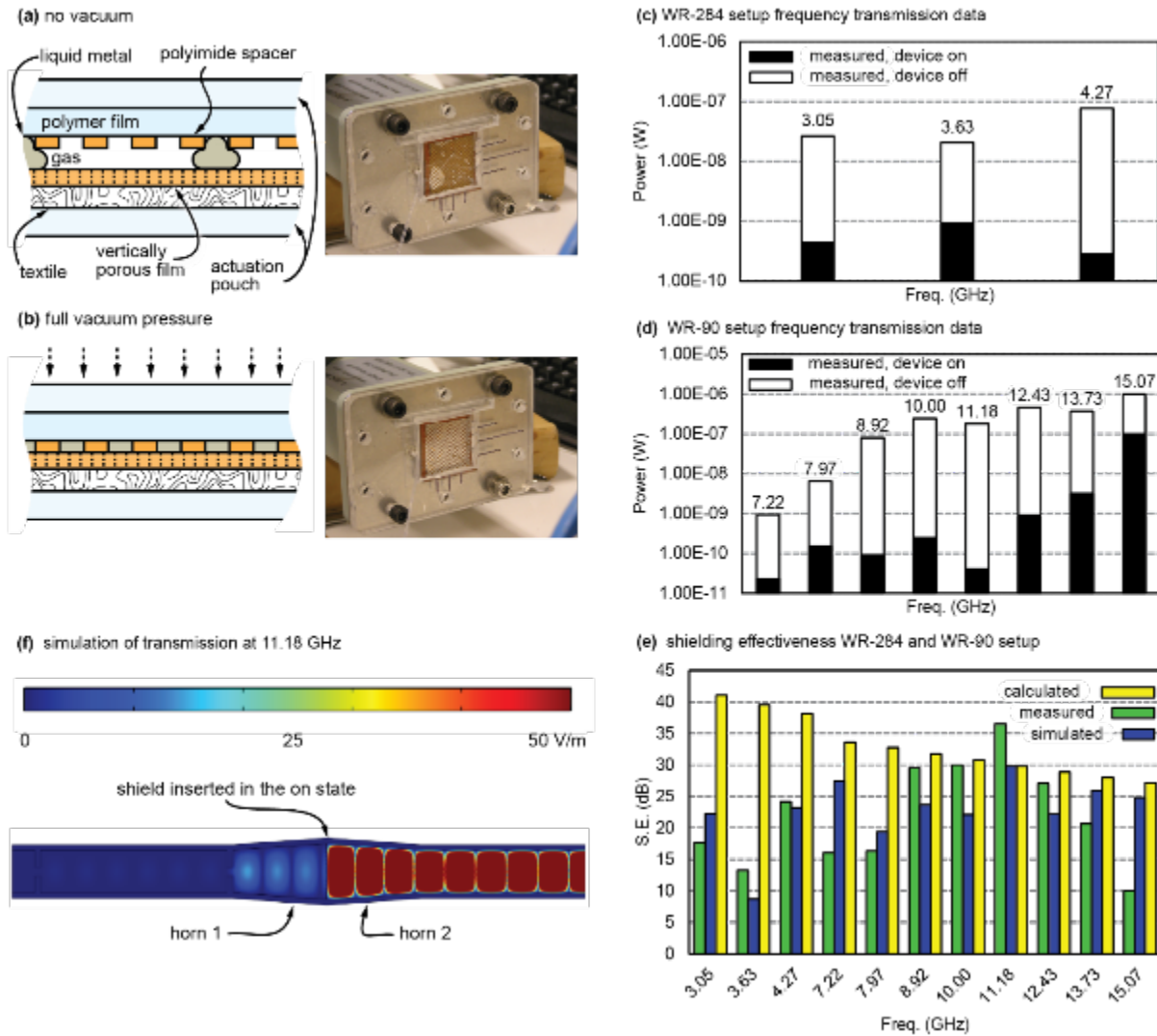


Figure 3. Shield operation diagrams (top-left) and experimental photographs. (c,d) Measured power attenuation of the switchable shield in on and off states. (e) Calculated, measured and simulated (COMSOL) results of the switchable shield. Simulation (f) of shield in WR-90 setup displays strong resonance resulting in a potential decrease in shielding effectiveness.

The polarizer reconfigures between multiple compact droplets to metallic lines attenuating the microwaves based upon the orientation of the lines relative to the incoming microwaves. The coefficients of transmission for parallel and perpendicular orientations relative to the incoming electric field can be approximated by [6]:

$$T_{\parallel} = \frac{k^2 d^2 \ln^2 \left[ \sin \frac{\pi a}{d} \right] / \pi^2}{1 + k^2 d^2 \ln^2 \left[ \sin \frac{\pi a}{d} \right] / \pi^2} \quad (5)$$

$$T_{\perp} = \frac{1}{1 + k^2 d^2 \ln^2 \left[ \cos \frac{\pi a}{d} \right] / \pi^2} \quad (6)$$

where  $k$  is the propagation constant  $2\pi/\lambda$ ,  $a$  is the width of the metallic lines and  $d$  is the spacing between adjacent metallic lines. The transmission loss of the calculated and measured results, waveguide setup and experimental images are shown in Figure 4. The measured results of the setup with no device inserted, the device inserted in the off state as well as the device inserted in the perpendicular/on state are shown directly below the calculated data.

The diffraction grating reconfigures from multiple compact droplets to metallic lines. While in droplet form the microwaves are slightly impeded and in linear form the microwaves is diffracted and was calculated by the well-known equation:

$$d \sin \theta = m\lambda \quad (7)$$

Where  $d$  is the center to center distance of the spacing between adjacent metallic lines,  $\theta$  is the angle between the central maximum and the maximum at the order  $m$ ,  $m$  is the  $n^{\text{th}}$  maximum and  $\lambda$  is the wavelength of the source.

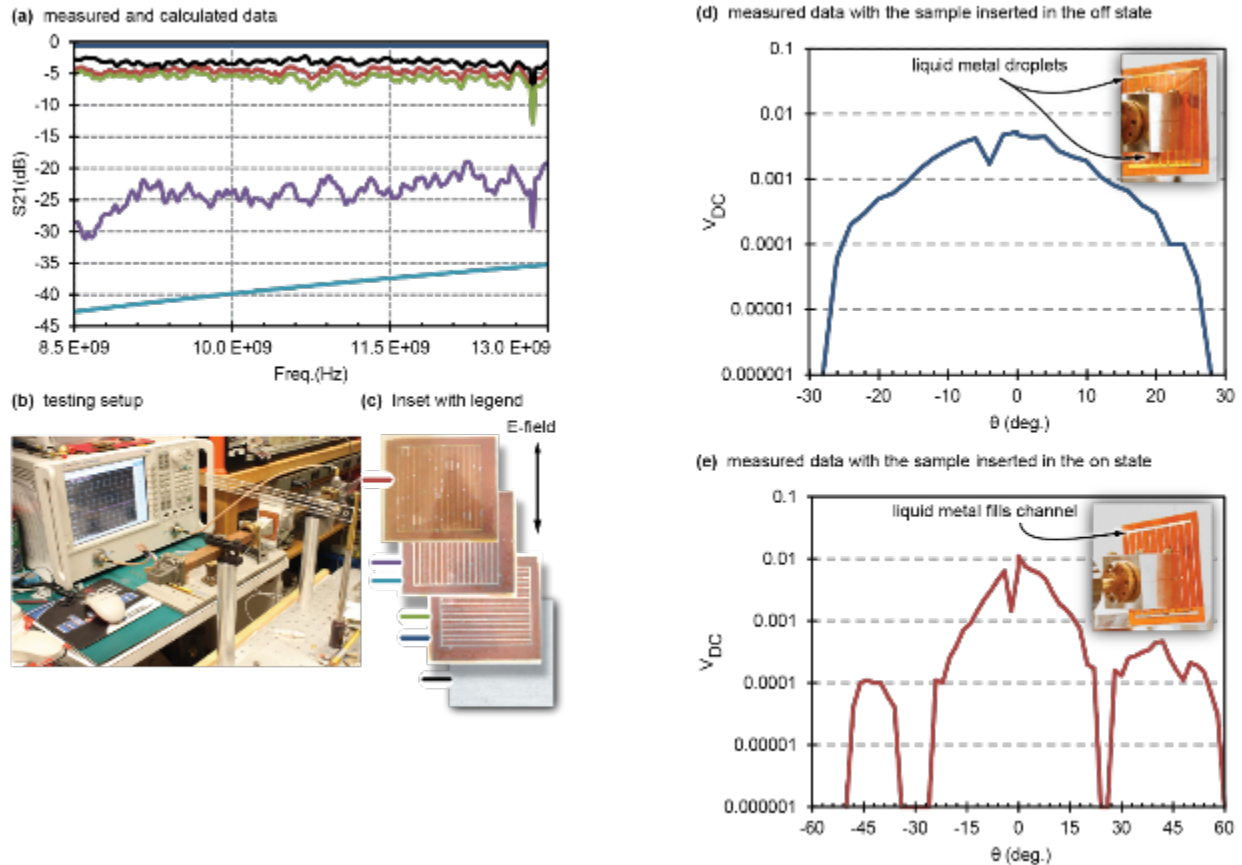


Figure 4. Polarizer measured and calculated results as the device is in different orientations (with respect to the microwave polarization) and device actuation states. See inset with legend (c), from top to bottom: parallel/off state — (measured); parallel/on state — (measured) — (calculated); perpendicular/on state — (measured) — (calculated);

no device inserted — (measured). Measured diffractive results as a function of angle of the diffraction grating setup and their associated experimental photos when (d) the device is inserted in the off state and (e) the device is inserted in the on state.

## Results

As can be seen in Figure 2, the experimentally measured data (Network Analyzer), calculated data (Eq. 1), and simulated data (Agilent ADS), are all in excellent agreement. Several finer observations are worth mentioning. The dipole data shown in Figure 2 shows that as the resonant frequency increases the matching of the dipole decreases. This may be due to several factors including: surrounding metallic objects and their coupling, i.e. the impedance of the dipole increases closer to the theoretical  $73 \Omega$  as the distance above the ground plane. This matching could be improved with a common impedance matching network, optimizing the height of the dipole above the ground plane.

The shield data shown in Figure 3 varies as a function of frequency but not in a way that is normally predicted by a conventional shielding equation (shielding steadily decreases as a function of frequency). In regards to the waveguide setup, since the shield covers the iris with a new conductive boundary this may cause the resonator at certain frequencies to be more/less efficient due to the reflections from the face of the shield (shifted resonance, decreasing the shielding during certain frequencies).

As shown in the polarizer data it can be seen there is slight attenuation already with no device inserted. The alignment of the two waveguides is not ideal and can cause a slight loss in transmission. Although there is a deviation, it is only slight and could be decreased if the alignment were optimized. The last two sets of data are the measured and calculated results when the device is in the on state and oriented parallel to the E-field. Although there is a larger deviation between this set of data, the trend is approximately parallel (transmission loss decreases as freq. increases). This deviation is attributed to the fact that the calculations used herein are under the assumptions that the metal is a perfect conductor and the wave is propagating in free space. The experiment is in the near field zone which will change the coupling of the incoming microwaves through the shield. Although there is a deviation, the magnitude can be determined by applying a more robust theory, which was not the intent of this setup. The expected trend was more important so that the fundamentals could be shown as well as an estimated result predicted.

Concerning the diffraction grating, the calculated angle for the first order maximum is  $40^\circ$ . The measured diffractive data is shown in Figure 4. As can be seen the first maximum is in close agreement to the expected  $40^\circ$ . However, there are dips in the central maximum as well as variance in the widths of the first maxima. This is most likely due to the imperfect filling of the channels with liquid metal as well as the undesired displacement of liquid metal into the region outside the channels.

Reported herein were pressure-actuated liquid metal demonstrations that targeted real-world challenges with a complete system-level design, including: non-toxic GaInSn (68.5% Ga, 21.5% In, and 10.0% Sn) alloy; employing non-alloying/corrosion-resistant electrodes; a closed system with oxide-preventing reducing-vapor background. Experimental data for the devices was coupled with theoretical calculations, which confirms that they can be specifically designed and perform as expected for various reconfigurable electromagnetic applications. In conclusion, this work provides both the theoretical evidence, and the applied breakthroughs, needed for real-

world application of reconfigurable liquid-metal electromagnetic devices.

## Works Cited

- [1] F. B. Gross. Frontiers In Antennas: Next Generation Design and Engineering, 92nd ed. New York: McGraw Hill Professional, 2011, pp. 277–703.
- [2] T. Someya, “Bionic Skin for a Cyborg You - IEEE Spectrum,” September 2013, pp. 50–56.
- [3] B. L. Cumby, G. J. Hayes, M. D. Dickey, R. S. Justice, C. E. Tabor, and J. C. Heikenfeld, “Reconfigurable liquid metal circuits by Laplace pressure shaping,” Appl. Phys. Lett., vol. 101, 2012.
- [4] T. Y. Otoshi and K. Woo, “Further Studies of Microwave Transmission Through Perforated Flat Plates,” Deep Sp. Netw. Prog. Rep. Oct. 1971, pp. 125–129.
- [5] H. W. Ott, Electromagnetic Compatibility Engineering. New York: John Wiley & Sons, 2009.
- [6] K. T. McDonald, “Wire Polarizers.” [Online]. Available: <http://www.physics.princeton.edu/~mcdonald/examples/polarizer.pdf>.

## Related Activities

This work has been submitted to IEEE Transactions on Antennas and Propagation and is currently under review. The work reported herein has been submitted to the International Symposium on Antennas and Propagation and USNC-URSI Radio Science Meeting to be held in July 2014. During my Ph.D. at the University of Cincinnati I have collaborated with the Air Force Research Lab at Wright-Patterson AFB, Ohio and lead initiatives to expand their group working on subjects of liquid metal electronics resulting in an ongoing project beyond my graduation.

ELASTOMERS SUPPORT

Project No. 0164

Michael Morris  
Wright State University

31 December 2013

Government Project Leader  
Mr. Alan Fletcher  
AFRL/RXSA

Southwestern Ohio Council for Higher Education  
Student Research Program  
Agreement Number: FA8650-09-2-5800

## **Acknowledgements**

I would like to thank the amazing people at AFRL and the ACE team for giving me the opportunity to work with them on a lot of their projects and I wish them all the best on finishing them. I would also like to thank Mr. Alan Fletcher, my boss, for how much he has taught me about engineering, and also business. This has been a great learning experience for me and I am very proud to have been a part of the ACE team. My team has taught me to think outside the box and sometimes the answer is as easy as it may seem. They also taught me a lot of the professionalism that I am going to need after I graduate and go looking for a job. I'd like to thank all of the members of my team for all that they have taught me during my stay.

## **General Description of Project**

A wide variety of research was conducted during this project. The projects ranged from developing and testing new leak-detecting-fuel-tank-tape to characterizing fuel bladder materials.

## **Description of Research**

The work done with fuel-detection-tape is applied to an aerial refueling aircraft known as the KC-135. Five types of tape were used in the testing conducted, three specialized tapes and two types of duct tape. Each type of tape was aged in two conditions, room temperature and 180°F, both for one week. After all had been aged, two tests were conducted on each type of tape. One of the tests is known as the drip test, which is simply a burette dropping a fixed amount of jet fuel on the tape for a fixed amount of time. After that test was finished, peel tests were conducted using a machine known as the instron. Engineers use peel test data to assess materials and determine if those materials have the required strengths. Tapes one through three are developed so that when a hydrocarbon, such as jet fuel, comes into contact with the tape; dyes are released turning the point of impact blue. This blue area allows technicians to locate and repair the targeted leaks.

## **Results**

The two types of duct tapes performed effectively but left heavy residue. The three other types of tapes weren't as effective in either condition but are still being developed. Tapes one through three are being developed further for reduction in residue left on the panel and peel strength. Each of the tapes needs to be developed further before real world application can be considered.

ELASTOMER SUPPORT

Project No. 0165

Michael A. Rybak  
Wright State University

20 December 2013

Government Project Leader  
Mr. Alan Fletcher  
AFRL/RXSA

Southwestern Ohio Council for Higher Education  
Student Research Program  
Agreement Number: FA8650-09-2-5800

## **Acknowledgments**

Through the privilege of working for SOCHE at Wright-Patterson Air Force Base, I have been honored with working within the best division, and for team ACE (Adhesive, Composites, and Elastomers). Alan Fletcher, my boss, is a world renowned engineering who is highly respected within the elastomers community, and provided me with knowledge, connections, guidance, and more. Working for team ACE has been a dream come true, and the best work experience and guidance for how I will be as an engineer.

## **General Description of Project**

During the past year research has been conducted on various types of materials in RXSA. One of the projects currently being worked on is "Standard Contaminant". Standard Contaminant is a project that focuses on the different kind of environments that any of the Air Forces aircrafts could possibly come into contact with, mainly pertaining to a factory and field environment. The Standard Contaminant is needed, so the Air Force can properly test various kinds of cleaning solvents to make sure that the cleaning solvents can and will truly clean the surface of any contaminant.

## **Description of Research**

Methods that are currently being used to make a proper Standard Contaminant are first determining what kinds of contaminant the Air Forces aircrafts are coming into contact with. Focusing on the field and factory settings we were able to come up with a blend of chemicals that seemed to constantly come into contact with the aircrafts. The fluids in the Standard Contaminant consisted of engine oil, deicers, hydraulic fluid, fuel, grease, petrolatum, and coconut oil.

After determination of the chemicals that would be represented in the Standard Contaminant, the next step consisted of making the Standard Contaminant and combining all of the chemicals determined. To determine if the Standard Contaminant actually was a proper blend an FTIR and a Surface Analyst was used to give actual data on what kinds of contaminants were on the different substrates used.

## **Results**

Standard Contaminant is still in testing, and much more work is to come. The data that has been collected thus far has provided very good information of how to further the future testing of Standard Contaminant. The further the project goes the more in depth the testing becomes and the more interest the project gets from the Air Force.

I have learned an unforgettable amount here at Wright-Patterson Air Force Base, varying from life lessons, and engineering lessons but all are equally important. With this job I have obtained a better understanding of how I should pursue different problems that need to be solved as an engineer. I have failed in tasks that have been given to me, and I have succeeded, but most importantly I have never stopped learning and that is something that is truly priceless.

LABORATORY FACILITY ENGINEERING SUPPORT PROJECT

Project No. 0166

Tyler Rammel  
Wright State University

31 August 2014

Government Project Leader  
Mr. Steve Reichard  
AFRL/RXOE

Southwestern Ohio Council for Higher Education  
Student Research Program  
Agreement Number: FA8650-09-2-5800

## **Acknowledgements**

I would like to thank the whole Operations Facility (RXOF) branch team for all the experience and guidance they have provided; especially Wade Brower, Steven Reichard, Jesse Genetin, Rodney Flowers and Chris Lawler. I know that their knowledge they have passed on to me has shaped me into a confident and dependable engineer and over-all hard worker.

## **Description of Research**

The Heraldic Device was the main area of research over this work term at Wright Patterson Air Force Base. The research was created from a project that was given to all of AFRL as a competition to create the next Heraldic Device, which is presented at the Heraldic Dinner, to all the major generals here as well as those who are off of the base. Once given the chance to create this project, many steps were used to create a final project with the research group. The first step was to brainstorm and come up with various ideas that would or could be incorporated into the final design. The second was the creation of many ideas in Solidworks to make the ideas more of a reality. This was followed by a selection process to narrow down ideas and choose just one. From there building the device was the final step which led to many other issues along the way. However, the results and lessons learned from working on this project will be vastly incorporated into future projects and problems with other engineering positions. The position also involved ensuring compliance with AF regulations for Occupational Health and Safety, as well as real property building maintenance.

## **Description of Research**

The amount of research put into the Heraldic Device was immense. It began with brainstorming including the utilization of vast amounts of CAD and Solidworks to come up with a final design submission. Once awarded with the honor of designing and being able to construct the device, the ideas began to change. The first design was simplistic. It began with three bases, wood, aluminum, and carbon fiber, showing the stages that AFRL has made in flight research through materials. Followed by four pillars that all connected to give symbolism of the Air Force monument. Then attached to the pillars held rings holding a dodecahedron with faces of the many important engineers and scientists that have been a part of the Air Force Research Laboratories. However, more needed to be done to create a final design, thus a second design was created. In this design the main additions were included. These included a famous quote by Henry "Hap" Arnold as well as having a three pillar design, instead of four pillars from before, which completely matches that of the Air Force monument. For this project many pieces of large equipment were used. Such equipment includes the bandsaw, CNC mill, various saws and drills, CNC lathe, and various amounts of other equipment. Through these types of equipment the data was able to be analyzed by measuring for exactness so that the assembly would match up to perfection. Overall there was a lot of work and learning in implementing a final design and a finished project.

## **Results**

This project was able to teach many important lessons that will be needed for future engineering positions. The first lesson was how to completely work through a project from cradle to grave. This taught the importance of bringing together people with different areas of expertise to help teach and enable others to learn more about an area in which one may lack experience. The second lesson to learn is that not everything is as easy as it might seem. This project that was once thought of as an easy project turned into being a nightmare at times, but through hard work and perseverance the research was able to be accomplished. The final thing that was learned in doing this research is to never give up; there is always a way to get through the problems that might be faced. Lastly this project provided a great opportunity to improve as an engineering student and learn from all of the mistakes made in order to create something from the research that was done to provide a final product.

EVALUATION OF ALTERNATE FIBER FORMS FOR A HOT TRAILING EDGE  
STRUCTURE

Project No. 0168

Clint Hirtzinger  
Wright State University

31 August 20014

Government Project Leader  
Dr. Brett Bolan  
AFRL/RXSA

Southwestern Ohio Council for Higher Education  
Student Research Program  
Agreement Number: FA8650-09-2-5800

## **Acknowledgments**

I would like to thank all of the members of RXSA that have helped out on this project. A special thanks to Dr. Brett Bolan and Dr. Jim Mazza for giving me the opportunity to intern for them and Mr. Paul Childers for teaching me everything I need to know to work on this project.

## **General Description of Project**

The Goal of the Evaluation of Alternate Fiber Forms for a Hot Trailing Edge Structure was to transition AFR-PE-4 to a HTE by performing a few tasks. The first task was to obtain AFR-PE-4 prepregs with addition fiber forms (i.e. graphite) and verify that they meet the Original Equipment Manufacturers (OEM's) material specification requirements. The next task was to verify that the previously developed AQIII/AFR-PE-4 Quartz fiber manufacturing process will work with other fiber forms and thicker structures. If it does not, then modify the manufacturing process to allow fabrication of these thicker structures using the alternate fiber forms. After standardizing the manufacturing process a limited set of data had to be generated using each prepreg and layup to determine if the graphite fiber/AFR-PE-4 met the OEM's specifications.

## **Description of Research**

The prepreg physical properties were tested first. This was done on uncured material. The four properties tests were Volatile Content, Dry Resin Content, Fiber Areal Weight, and a Drape test. All test followed the procedures and calculations found in the OEM's specification. The prepreg Volatile Content Test is performed by cutting the prepreg into three 3"x3" squares and measuring the initial weight to the nearest 0.005 grams. Then an air circulation oven was preheated to 450°F ± 10°F. Using a tared watch glass, each specimen was placed into the oven for 10 ± 0.5 minutes. The specimens are then cooled in a desiccator for at least 15 minutes. The final weight is then measured to the nearest 0.005 grams and the volatile content is calculated. Prepreg Resin Content Test is performed by cutting three more 3"x3" square specimens and measuring the initial weight to the nearest 0.005 grams. The specimens were then placed in a 500 milliliter (mL) Erlenmeyer flask, with 250 mL Acetone and agitated for 5 ± 0.5 minutes using a wrist action shaker at room temperature. The solvent is then disposed of and the process is repeated three times. An air circulated oven was then preheated to 325°F ± 10°F and the specimens were placed into the oven for 15 ± 0.5 minutes. The specimens were then cooled in a desiccator for 15 ± 0.5 minutes, removed and measured to find the final weight to the nearest 0.005 grams from which the resin content was then calculated. The Prepreg Fiber Areal Weight is found from the resin content and the area of the specimen. The Drape test was performed by cutting the prepreg into a 3"x9" rectangular specimen, bending the specimen over a ¼" radius corner and inspected for any additional damage to the fiber or resin.

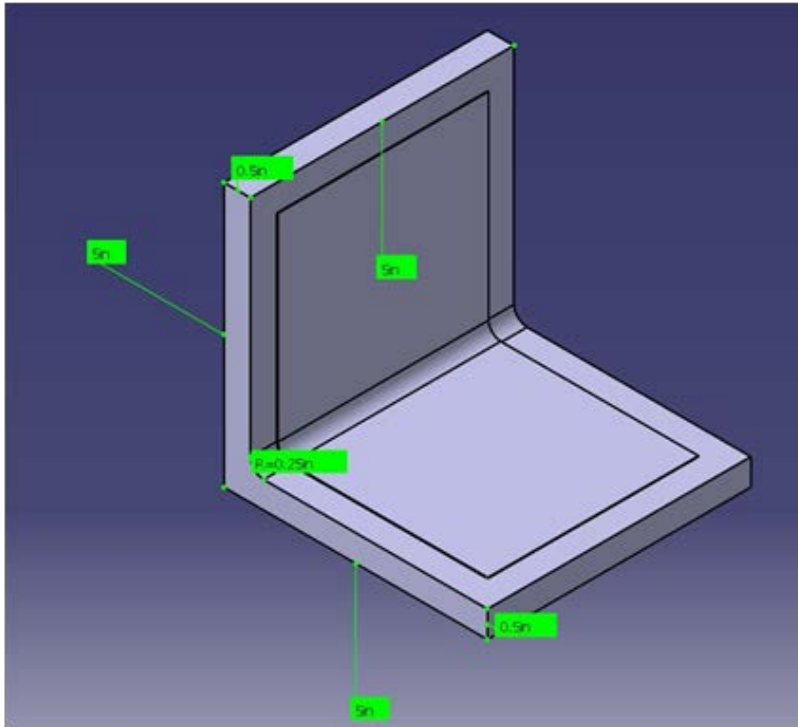


Figure 46. NGC Tack and Drape Fixture

The next set of tests that were conducted were to determine the laminate physical properties. To test these properties the prepreg has to first be cured. To do this the material has to be cut to a specific size. The size is determined by the number and amount of specimens that are needed for testing. The two most common sizes were 12”x12” and 18”x18”. After the material is cut and stacked according to the specified ply orientation, they are then placed on a caul plate and covered in a vacuum bag assembly (Figure 1).

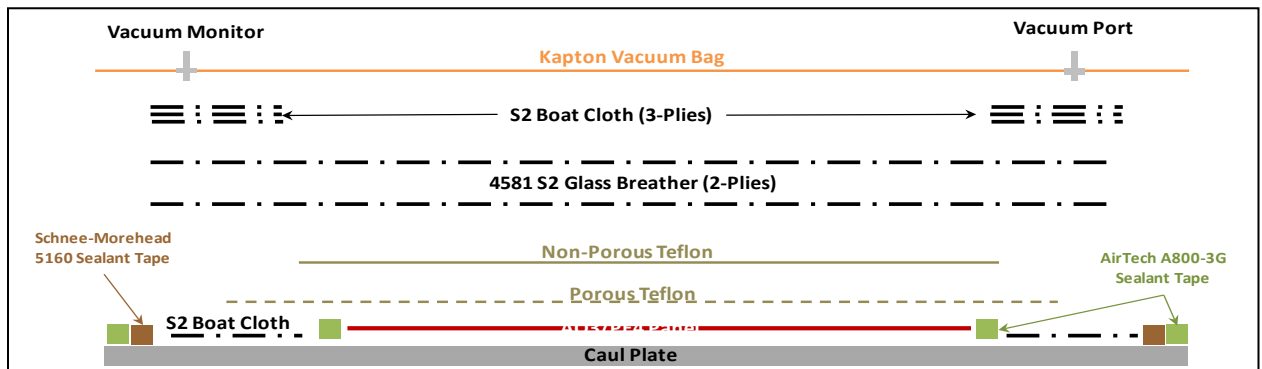


Figure 47

The laminates vacuum bag were then placed in an autoclave and cured per AFRLs previously developed procedures for AFR-PE-4 composites shown in (Table 1). Once the material has been cured the edges were then trimmed and the part was cleaned. The cured part was then sent to be nondestructively scanned to see if the part had any flaws in it. If there were any flaws they were cut out of the laminate and not used so the test specimens were all from an acceptable quality laminate.

Step	Procedure
1	Apply full vacuum and debulk parts for 12 hours
2	Reduce vacuum to 5 inches Hg
3	Ramp 0.5°F per minute to 350°F
4	Apply full vacuum at 215°F
5	Hold at 350°F for 1 hour
6	Ramp 2.0°F per minute to 500°F
7	Hold at 500°F for 2 hours
8	Ramp 2.0°F per minute to 585°F
9	Hold at 585°F for 30 minutes
10	Apply 10 psi per minute to 180 psi
11	Ramp 2.0°F per minute to 700°F
12	Vent vacuum when 20 psi is achieved
13	Hold at 700°F for 4 hours
14	Cool to 550°F at 2.0°F per minute then 4.0°F per minute to 70°F

Table 7

## Results

The prepreg physical properties results are shown in (Table 3) and requirements in (Table 2). The average volatile content was within the required specification requirements, but two of the three tests failed to meet this requirement, however the margin was so close that it was determined that these would be considered within the Specifications. With the dry resin content two out of the three tests were within specification requirements. The one test that did not meet the requirements was so far off that it can be considered an outlier and be disregarded. After testing the AFR-PE-4 Unitape we found that it was able to be produced with thicker structures (Figure 3).

Table 8

### *PE-4 Unitape Prepreg Physical Property Requirements*

Property	Requirement (Average)
Volatile Content, weight percent	11.0 ± 3.0
Dry Resin Content, weight percent	35 +4, -3
Fiber Areal Weight, g/m <sup>2</sup>	147 ± 7

Table 9

Prepreg Volatile Content		
<b>Specimen # TVC-1</b>		<b>Value</b>
	Watch Glass Weight (Tared)	97.5952
	Specimen & Watch Glass Weight (Int)	99.1565
	Specimen Weight Int (WI)	1.5613
	Specimen & Watch Glass Weight (Post)	98.9304
	Specimen Weight Post (WF)	1.3352
	<b>Volatile Content</b>	<b>14.48%</b>
<b>Specimen # TVC-2</b>		<b>Value</b>
	Watch Glass Weight (Tared)	97.3332
	Specimen & Watch Glass Weight (Int)	98.7645
	Specimen Weight Int (WI)	1.4313
	Specimen & Watch Glass Weight (Post)	98.5625
	Specimen Weight Post (WF)	1.2293
	<b>Volatile Content</b>	<b>14.11%</b>
<b>Specimen # TVC-3</b>		<b>Value</b>
	Watch Glass Weight (Tared)	97.5031
	Specimen & Watch Glass Weight (Int)	99.0158
	Specimen Weight Int (WI)	1.5127
	Specimen & Watch Glass Weight (Post)	98.816
	Specimen Weight Post (WF)	1.3129
	<b>Volatile Content</b>	<b>13.21%</b>
<b>Prepreg Resin Content</b>		
<b>Specimen # TRC-1</b>		<b>Value</b>
	Watch Glass Weight (Tared)	97.627
	Specimen & Watch Glass Weight (Int)	99.061
	Specimen Weight Int (WI)	1.434
	Specimen & Watch Glass Weight (Post)	98.405
	Specimen Weight Post (WF)	0.778
	<b>Resin Content (Wet)</b>	<b>45.75%</b>
	<b>Resin Content (Dry)</b>	<b>36.96%</b>
	<b>Areal Weight</b>	<b>134.1379</b>

Specimen # TRC-2		Value
	Watch Glass Weight (Tared)	97.504
	Specimen & Watch Glass Weight (Int)	99.0586
	Specimen Weight Int (WI)	1.5449
	Specimen & Watch Glass Weight (Post)	98.3575
	Specimen Weight Post (WF)	0.06914
	<b>Resin Content (Wet)</b>	55.25%
	<b>Resin Content (Dry)</b>	48%
	<b>Areal Weight</b>	119.2
Specimen # TRC-3		Value
	Watch Glass Weight (Tared)	97.5834
	Specimen & Watch Glass Weight (Int)	99.144
	Specimen Weight Int (WI)	1.5606
	Specimen & Watch Glass Weight (Post)	98.4145
	Specimen Weight Post (WF)	0.8311
	<b>Resin Content (Wet)</b>	46.74%
	<b>Resin Content (Dry)</b>	38.12%
	<b>Areal Weight</b>	143.29

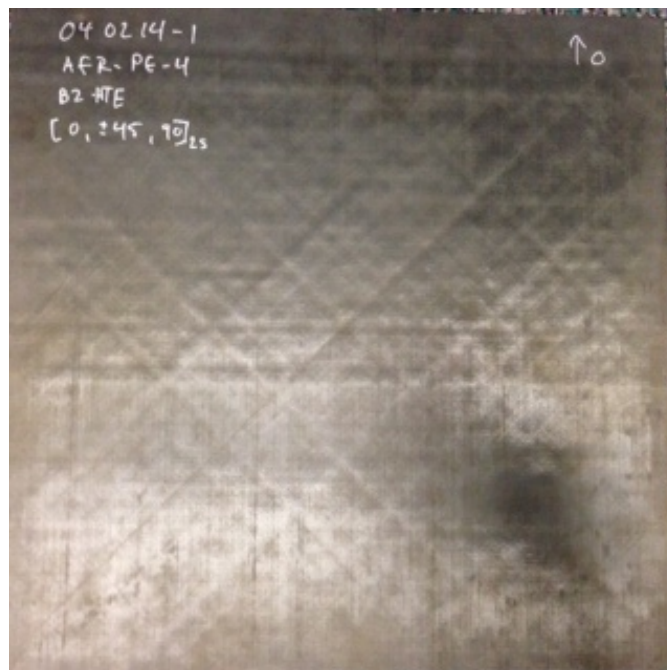


Figure 48

## Works Cited

McCray, Dan. "Evaluation of Alternate Fiber Forms of AFR-PE-4 for B-2 Hot Trailing Edge Structure." (2013): 1-17. Print.

PULSED LASER DEPOSITION FOR GLASS DIELECTRICS

Project No. 0169

Jason Anders  
Wright State University

30 November 2013

Government Project Leader  
Mr. Charles E. Stutz  
AFRL/RXAN

Southwestern Ohio Council for Higher Education  
Student Research Program  
Agreement Number: FA8650-09-2-5800

## Acknowledgements

I would like to thank Charles E. Stutz for allowing me the opportunity to work on base. I have learned a tremendous amount during my time at RXAN. I would like to thank my advisor, Dr. Gregory Kozlowski, for his help and support in the development of the system. I would like to thank Dr. John Jones for his help and expertise. I also would like to thank Brittany Edwards and SOCHE for allowing me to be on base.

## General Description of Project

Pulsed laser deposition was used to create thin films, using dielectric target material. This material was characterized in terms of surface morphology, grain size, and electrical properties.

## Description of Research

Thin films of  $\text{Sr}_y\text{Ca}_{1-y}\text{Zr}_{1-x}\text{Ti}_x\text{O}_3$  (SCZT) with  $x = 0.8$ ,  $y = 0.01$ ,  $\text{CaHf}_{1-x}\text{Ti}_x\text{O}_3$  (CHT) with  $x = 0.8$ , and  $x\text{BiScO}_3 - (1-x)\text{BaTiO}_3$  with  $x = 0.36$  (BSBT(36/64)) showing a high permittivity are useful both in capacitor applications. These dielectric thin films with a  $\text{SrRuO}_3$  (SRO) conductive bottom electrodes were prepared by using pulsed laser deposition on  $\langle 100 \rangle$   $\text{La}_{0.3}\text{Sr}_{0.7}\text{Al}_{0.65}\text{Ta}_{0.35}\text{O}_3$  (LSAT) single crystal substrates. In a search of optimal conditions to achieve epitaxially grown SCZT, CHT, BSBT(36/64), and SRO thin films, different substrate temperatures (600 C, 650 C, 750 C, and 800 C) and different partial pressures of oxygen (50 mTorr, 100 mTorr and 300 mTorr) in the chamber were used during deposition onto LSAT substrates. The optimized deposition conditions for conductive buffer layer of SRO film required 300 mTorr of oxygen partial pressure and substrate temperature of 750 C. The thorough structural and chemical studies of SCZT, CHT and BSBT(36/64) films were done by using SEM (scanning electron microscopy), AFM (atomic force microscopy), and XRD (X-ray diffraction) measurements. Sputtered gold top electrodes were added to the samples, along with etching to the SRO conductive buffer layer. These conductive electrodes were used to generate an AC electric field between the top electrodes and conductive buffer layer. Electrical characterizations of thin films such as complex permittivity, resistance and capacitance of grains and grain boundaries were performed using AC impedance spectroscopy, with curve fitting using Z-View software.

## Results

Our study suggested that the best dielectric films of SCZT, CHT, and BSBT(36/64) fabricated by PLD in terms of the smallest roughness of the surface and the largest grains were obtained at 700 C deposition temperature and at 50 mTorr oxygen partial pressure.

These results concluded the initial part of our work. We were able to determine the deposition parameters that led to the largest grain size in our materials. We were also able to correlate larger grain size in the materials with smoother surface roughness of the films.

In the second part of our work, we began the initial investigation into the dielectric properties of the films using impedance spectroscopy. A comparative analysis of BSBT(36/64) for two grain sizes showed a higher value for the dielectric constant for the larger grain. Using the equivalent circuit model suggested by literature for the shape of our Cole-Cole impedance

data, we were able to fit physical parameters for the grain and grain boundary (resistance and capacitance). These values closely matched the approximations based on a second and independent method, curve fitting of the semicircle plot. These fitting parameters were important tools to extract tangible values about the grain and grain boundary, from the complicated real and imaginary components involved in impedance only measurements.

Future work will involve a more detailed theoretical evaluation of the capacitance and resistance of the grain and grain boundaries for all thin films fabricated by PLD system in AFRL. Our current results show a higher contribution of both resistance contributions for smaller grain size, and a higher capacitive element for larger grain size. Important topics to be covered will be determining the activation energies of the grain boundaries, and their contributions toward resistance to conduction through the dielectric on one end, and possible contribution to accumulation of space charges leading to anisotropy in the overall polarization, on the other. These electrical effects based on film morphology will be important in understanding pulsed laser deposition's contribution to the development of thin film dielectrics.

ORIENTATION-PATTERNED GALLIUM NITRIDE FOR QUASI PHASE-MATCHED  
NONLINEAR OPTICS

Project No. 0170

Katherine Hitchcock  
Wright State University

31 August 2014

Government Project Leader  
Dr. Kent Averett  
AFRL/RXAP

Southwestern Ohio Council for Higher Education  
Student Research Program  
Agreement Number: FA8650-09-2-5800

## **Acknowledgments**

I would like to thank the Air Force Research Laboratory for the opportunity they have provided me to gain experience within my major. I would like to thank Kent Averett for challenging me and teaching me an abundance of new things, which will be described in the following report. I would like to thank him for his patience as I learn these new things. I would also like to acknowledge Kurt Eyink for talking through problems with me and providing input that many times leads me to a solution for my problem. I would like to thank Larry Grazulis for teaching me about atomic force microscopy (AFM). There have been many others along the way that have helped as well and I am thankful for each of their contributions.

## **General Description of the Project**

Through this internship has provided areas for the development of a plethora of skills (or have at least begun to develop, there is still much to learn). This range includes: AFM, Filmetrics, Ellipsometry, Sample and Substrate cleaning, vacuum chamber procedures, Field emission, and the application of LabView programming.

## **Description of Research**

AFM utilizes a cantilever with a small tip on the end, referred to as a probe. The probe moves along the surface and provides an image of the surface morphology through the interaction of forces. The interaction between the probe and the surface is one of Van der Waals forces. For GaN, the AFM is typically run in tapping mode which makes the tip oscillate as it interacts with the surface moving along in a line. A typical scan consists of 512 lines that are traced and retraced to ensure accuracy. The AFM is a very sensitive measurement so the system is set up on an air table to prevent noise from skewing the data. In the figure below, the AFM system is illustrated with the tip on the cantilever interacting with the surface. This interaction is measured by the laser and photodiode. Figure 2 provides an example of an AFM scan on GaN completed by the researcher.

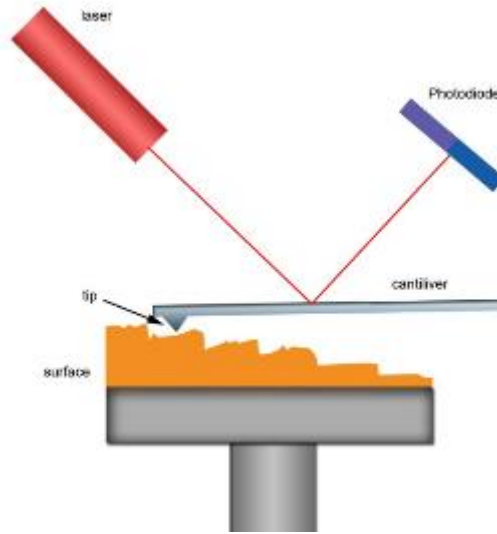


Figure 49: Illustration of a typical AFM setup

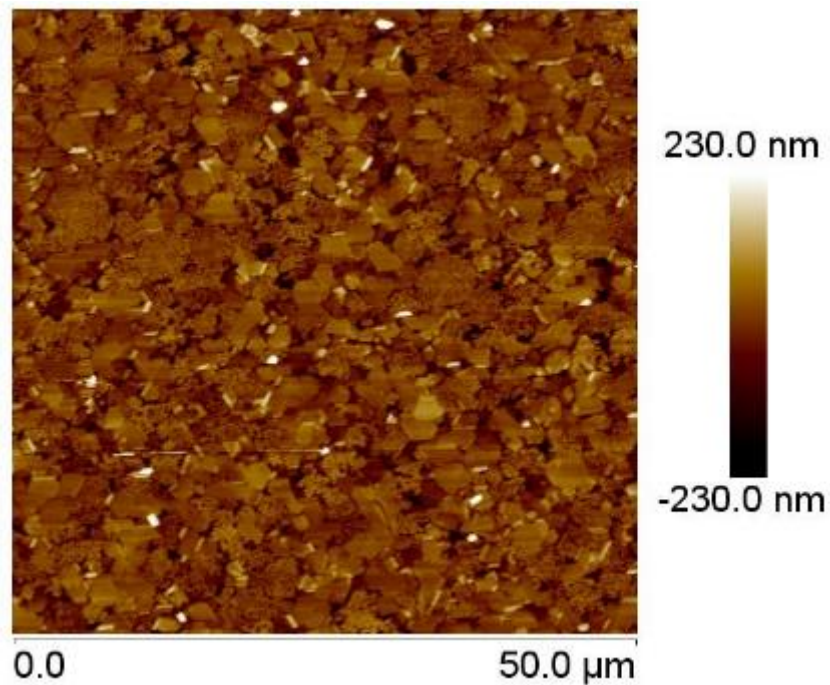


Figure 50: 50micron AFM for B295

Another system for measuring the surface of the samples is the Filmetrics system. Unlike the AFM which is typically used post-growth, the Filmetrics system can be (and typically is) used for both pre-growth and post-growth. The Filmetrics system measures the thickness of each sample using optical properties. Both surface maps and single points can be measured with this system. Surface maps allow the uniformity of a sample be determined. Below is an image

collected for a map of a surface of a sapphire substrate. This image provides an example of how the sample height can be analyzed and mapped for particular area of a substrate.

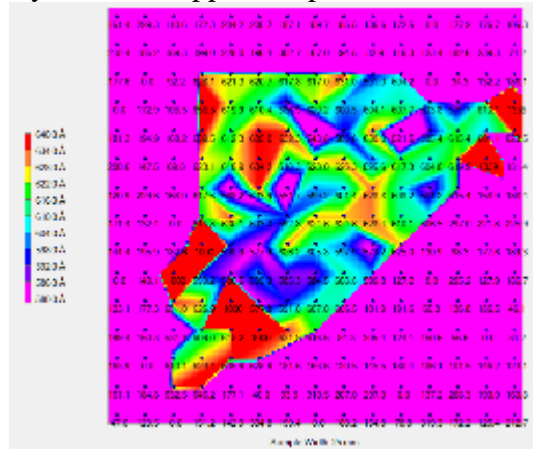


Figure 51: Map of a Sapphire substrate using the Filmetrics system (non-uniform)

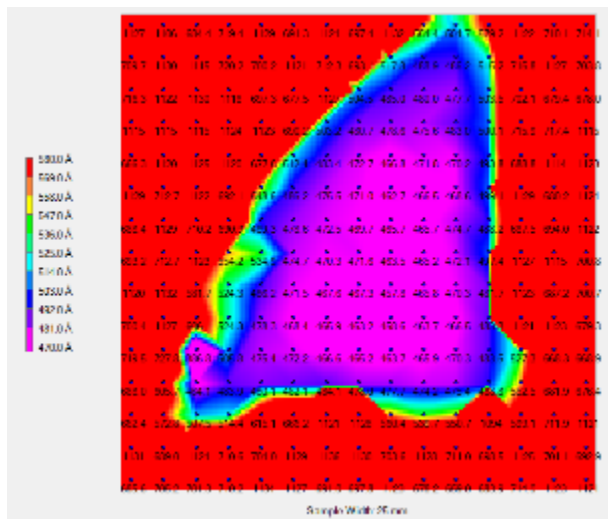


Figure 52: Map of a Sapphire substrate using the Filmetrics system (uniform)

These are just two detailed examples of the focused skill set. Vacuum chambers require a very meticulous set of skills to ensure that the system continues to run optimally. This includes cleaning the samples to remove any oils or dust that would cause the system to become dirty and out-gas. This would prolong the research efforts if the system has to out-gas for longer. Labview programming is currently being updated for the shutters and temperature controllers in the chamber. Labview programming is also being used for the field emission system to develop the Approach Curve Method.

## Results

The AFM analysis has allowed for growth conditions to be altered to produce different surface structures. It also has aided in determining the success of step flow growth for GaN samples (the ultimate goal). Step flow growth is ultimate goal because it allows for a smooth thin film to be grown over top. The Filmetrics data allowed for the best deposition methods for sapphire to be determined. It also provided an insight into the uniformity of the deposition. The map depicted in Figure 4 shows a uniform surface. This is characterized by a single color throughout the surface, representing heights that are all within a certain range.

HAIRY NANO-PARTICLES: GENERAL BRUSH ARCHITECTURE

Project No. 0171

Vernecia Person  
Clark Atlanta University

31 July 2013

Government Project Leader  
Dr. Rajiv Berry  
AFRL/RXAS

Southwestern Ohio Council for Higher Education  
Student Research Program  
Agreement Number: FA8650-09-2-5800

## Acknowledgments

I would like to express my deepest appreciation to Dr. Rajiv Berry, Dr. Hilmar Koerner, Dr. Elizabeth Opsitnick, and Dr. Stephen Barr for their contributions of skill, and encouragement that helped me to develop this project.

## General Description of Project

This project focused on the synthesis and characterization of Hairy-Nanoparticle systems. Over several decades, the combined use of inorganic-nanoparticles and organic-polymers has led to the production of a number of advanced materials which include polymer nanocomposites (PNCs). These materials are of interest since the presence of the inorganic filler enhances the thermal, barrier, mechanical, and electrical performance of polymer composites. The enhancement of these properties has been found to be strongly dependent on the dispersion characteristic of the nanoparticles in the polymer matrix, which relates to the issue of structure control in PNCs.

Structure control can be achieved with careful processing techniques. It's scalability and reliability can be improved if the desired structure and dispersion were intrinsically stable properties of the material itself. Conventional polymer nano-composites have a tendency to aggregate and form phase separated domains which cause the desired properties of the material to either diminish or vanish altogether. When polymer chains are grafted to the inorganic particle and there is a high enough coverage of chains about the particle, the inorganic material becomes sterically stabilized allowing for enhanced dispersion and mixing into the polymer matrix. The desired properties associated with the material are thereby enhanced, and several advantages of this material become very apparent. Because hairy-nanoparticles are composed of an inorganic core (i.e. silica particle) and an organic corona (polymer chains, polystyrene), the combined properties of the material can be utilized; such as the band gap and dielectric properties of the inorganic core, and the processibility and mechanical properties that are associated with the organic corona. But again, the dispersion characteristics of HNPs is strongly dependent on the degree of polymerization, grafting density, and molecular weight of the organic corona (polymer). The design of interface- or surface active polymer modifiers lacks crucial molecular scale information about the behavior and structure-property relationships of the brushes.

In the present work, the synthesis of polymer chains was accomplished via Atom Transfer Radical Polymerization. Next, the chains were tethered to inorganic particles (silica particles) via Click Reaction. The resulting materials were experimentally characterized to determine their properties ( $T_g$ , fragility, enthalpic relaxation time, etc.) as a function of molecular weight distribution, grafting density, and particle size.

Molecular modeling was utilized to gain a theoretical understanding of the HNP at the molecular level. Simulation of the nano-composite systems was conducted to evaluate the ability of computational models to predict fragility as a function of structure. The Hairy-Nanoparticle systems are simulated using a method called MARTINI-Coarse-Graining to evaluate structural and dynamical properties of the brush, with special focus on the trajectories of the chain ends.

The results of this study will allow for the possible production of high energy density capacitors based on thermal and mechanical, and electrical studies.

## Description of Research

The simulation of various Polystyrene Hairy-nanoparticle systems in solvent free environments was accomplished via MARTINI-Coarse Graining. The structural and dynamical properties of the brushes were analyzed with special focus on the trajectories and chain ends, which can be functionalized.

Each of the monomers in the HNP systems are represented by four beads; with the B beads representing the Carbon and Hydrogen atoms located on the backbone of the polymer, and the R beads representing the benzene rings (Figure 1).

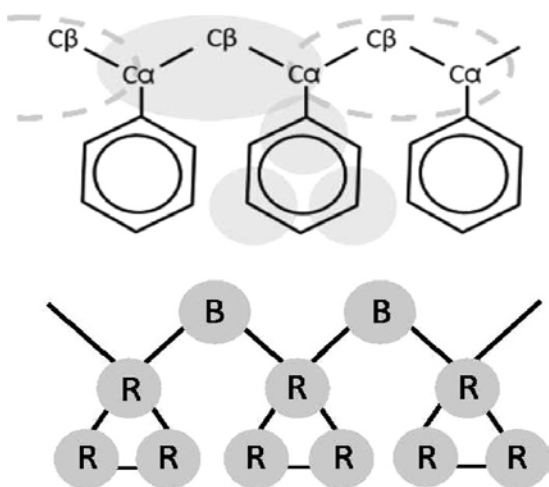


**Figure 1.** In the top image, gray areas on top of the atomistic description represent CG beads. In the CG molecule, at the bottom, backbone, and ring beads are called B and R beads, respectively. (Rossi, Elliott, Al-Nissila, and Faller, *Macromolecules*, 2012)

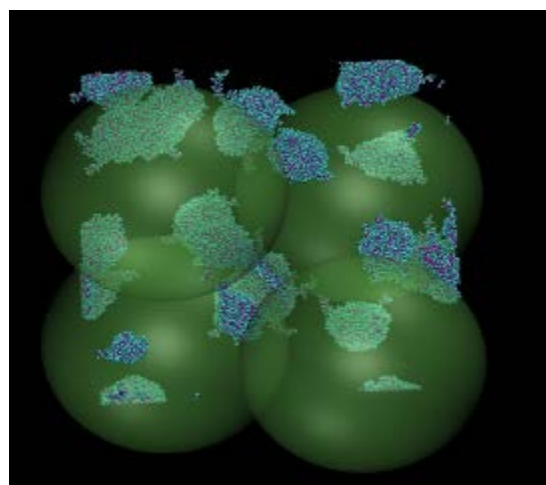


**Figure 2.** MARTINI-COARSE GRAINED Polystyrene Hairy-Nanoparticles: Molecular weight 20K, graft density .01chains/nm<sup>2</sup>, 200mers/chain

This degree of coarse-graining allows for retaining the backbone-ring structure of polystyrene. Nine HNP systems consisting of three molecular weights: 20K, 60K, and 100K were simulated. Three grafting densities, 0.01, 0.05, and 0.10 chains/nm<sup>2</sup> were chosen for each molecular weight. The three specified molecular weight correspond to 200, 600, and 1000 mers/chain, respectively. The number of beads in each system ranged from 64K to 3200K. Silica particles of 26nm diameter were simulated.

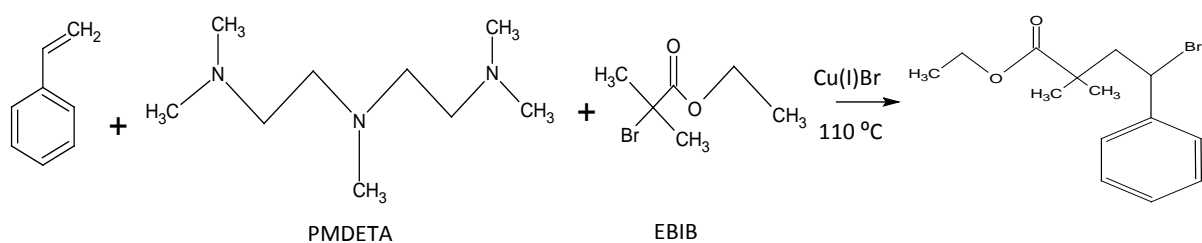
**Table 1.** Hairy-Nanoparticle systems at various molecular weights, graft densities, chains per particle, monomers per chain, and number of beads in each system.

MW	Graft Density (chains/nm <sup>2</sup> )	Chains/ particle	Mers/ Chain	Nbeads/ system
20K	0.01	20	200	64K
	0.05	100		320K
	0.10	200		640K
60K	0.01	20	600	192K
	0.05	100		960K
	0.10	200		1920K
100K	0.01	20	1000	320K
	0.05	100		1600K
	0.10	200		3200K

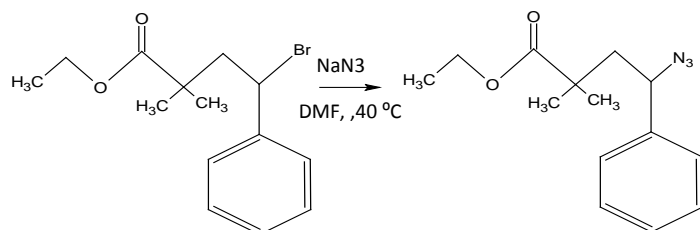
The experimental component of this investigation began with the synthesis of the polymer chains. The styrene monomer was synthesized via Atom transfer radical polymerization (ATRP). The ligand N,N,N',N'',N''-Pentamethyldiethylenetriamine (PMDETA) and initiator Ethyl  $\alpha$ -bromoisobutyrate (EBIB) were added to a schlenk flask containing the styrene monomer and a magnetic stir bar. The flask was placed under vacuum while being frozen in a nitrogen bath. After the solution was completely frozen, the flask was put under an argon blanket and allowed to thaw to room temperature. This procedure, known as freeze-pump-thaw was repeated 2 more times. On the third cycle, the flask was placed under an argon blanket while still frozen. Cu(I)Br was added to the flask while frozen, and placed under vacuum for 10 minutes. The flask was then put under an argon blanket and allowed to thaw to room temperature before being transferred to an oil bath at 110°C overnight. The polymer was then precipitated, dried and reacted with sodium azide (in dimethylformamide, DMF) in order to produce polystyrene chains functionalized with a reactive azide terminus.

**Scheme 1.** Synthesis of polymer chains (Polystyrene), and the conversion of the chains to azide.

### ATRP



## Conversion to Azide

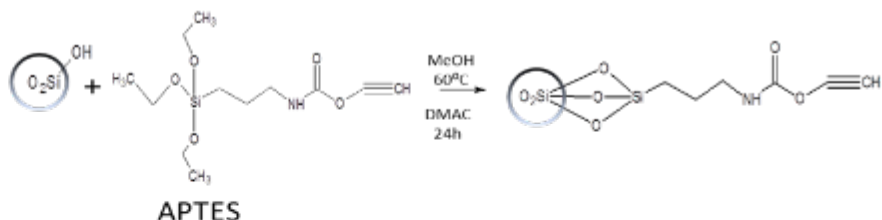


The silica particles were obtained as a Ludox solution (40wt% solution). This solution was diluted to a 5wt% solution in water. DMAC was added to the 5%wt solution and water was evaporated out of the solution at a temperature of 110°C for a few hours. The silica solution (in DMAC) was then reacted with APTES (in MeOH) at a temperature of 60°C for 24 hours. The reaction of the silica particle with APTES produced particles with alkyne termination. The alkyne moieties were the active sites for the attachment for polymer chains. The click reaction was accomplished by drop wise addition of the polystyrene solution (consisting of copper sulfate pentahydrate and sodium ascorbate in water) to the silica particle (in DMAC) resulting in the production of the Hairy-nanoparticles.

### Scheme 2. Ludox Reaction and Click Reaction

- Ludox Reaction**

  - ❖ Dilute Ludox (40wt%) solution to 5wt% in water
  - ❖ Add DMAC to solution



### Click Reaction



Differential scanning calorimetry (DSC) was used to analyze the free polymer chains and hairy-nanoparticles. The method employed for characterization on the DSC is called physical aging. Physical aging, also known as structural relaxation, occurs when a material is kept at a temperature below its glass transition temperature, or when the cooling rate of the polymer is varied from its melting temperature to a temperature below  $T_g$ . Such materials are not in their true thermodynamical equilibrium state and many of their properties change such as free volume, the enthalpy, and other properties change with time until equilibrium is achieved.

Physical aging of the HNPs and Free Polymer systems were performed at fixed cooling rates. The samples were heated at 10°C/min and then cooled at a max cooling rate (super cooling) to a fixed temperature below  $T_g$ . (75, 85 and 95°C). The cooling rate was fixed in order to ensure that the sample did not relax upon cooling.

## Results

As mentioned earlier, the HNP models were simulated in a solvent free environment. In such an environment, the polymers tend to aggregate in clumps. When the grafting density increases, stripes or wormlike micelles begin to form about the particle.

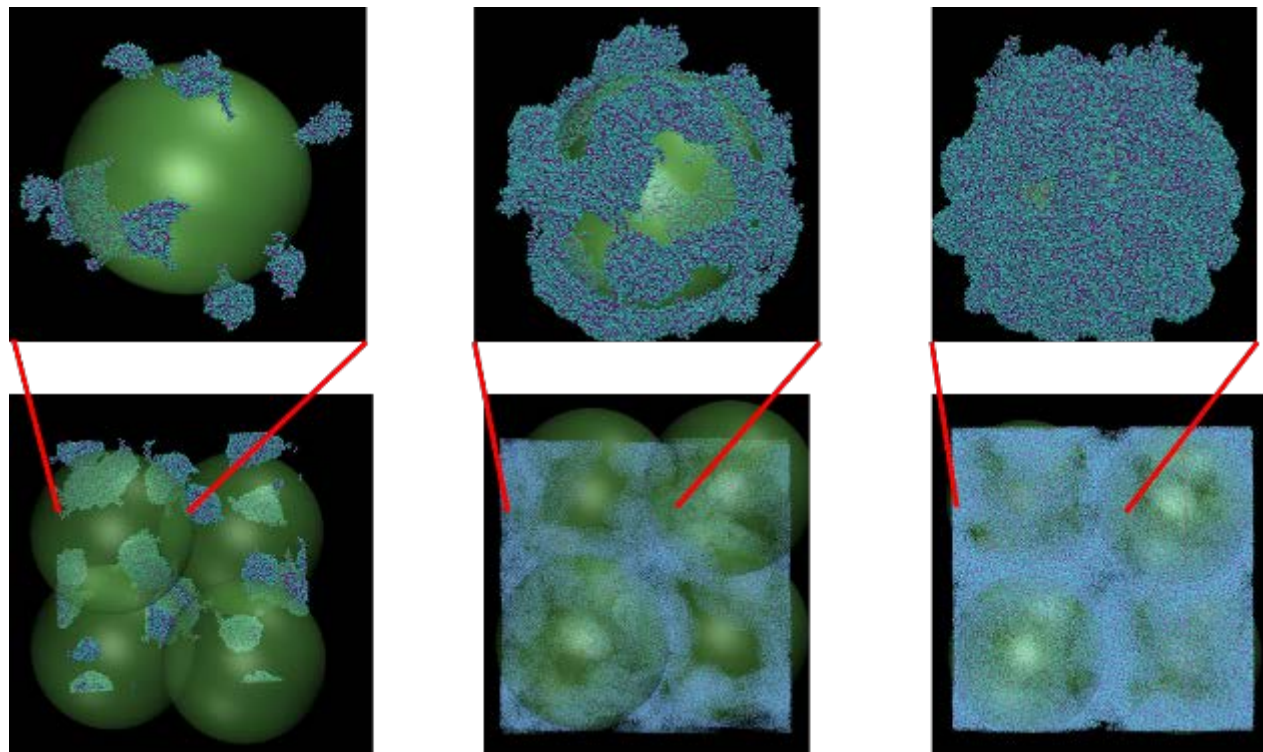
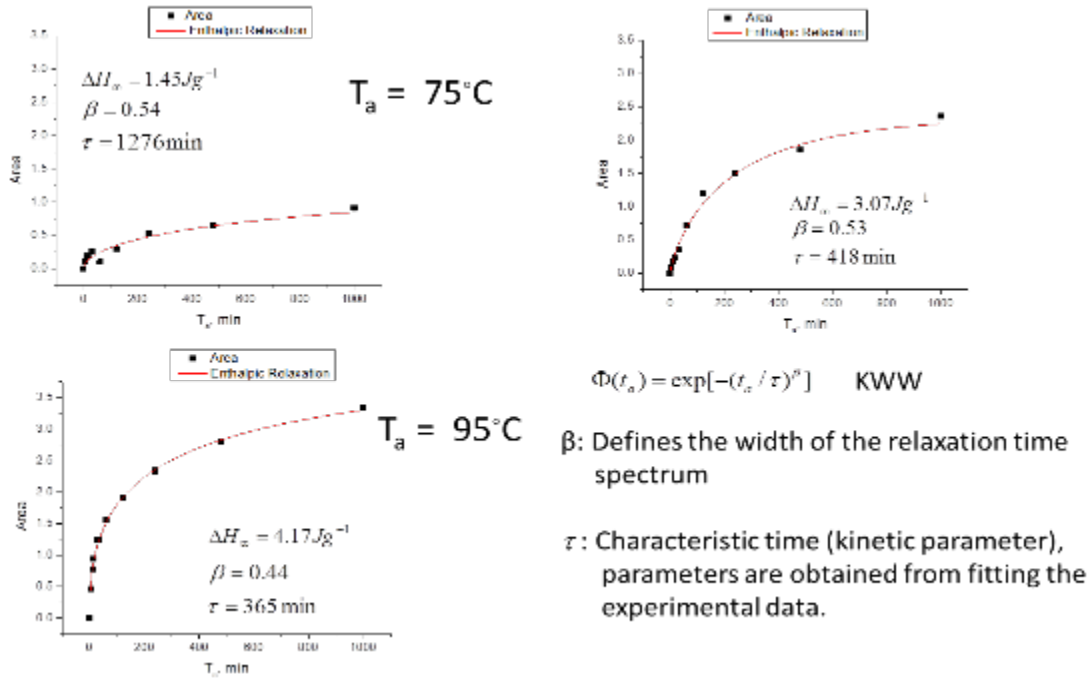


**Figure 3.** MARTINI-COARSE GRAINED Polystyrene Hairy-Nanoparticles: Single bead representation of HNP and model of HNP represented by 4 beads, in a box. Molecular weight 20K, graft density: .01chains/nm<sup>2</sup>, .05chains/nm<sup>2</sup>, .10chains/nm<sup>2</sup> 200mers/chain

At higher graft densities one begins to observe something that looks like uniform coverage. The conclusion of the computational results was that at higher graft densities a uniform dispersion of polymer chains was achieved about the particle.

The evolution of endothermic peaks has been explained in the literature as a reduction in the molecular chain mobility. Physical aging processes lead to densification of chain packing and reduction in chain mobility. The distribution of chain mobility can be affected by parameters such as chain length distribution, graft density, and whether chains are covalently bonded or not. The distribution is expected to be broader for HNPs since the chains are covalently attached to the particle. At low graft densities, the distribution can also be broader due to particle size distribution and patchiness.

**Figure 3.** Enthalpic Relaxation plots at three different annealing temperatures



The experimentally determined area of the endothermic peaks (see Figure 3) should increase with increased annealing time. This data was then fitted with the KWW equation to obtain the parameters  $\beta$ ,  $\tau$ , and change in enthalpy. The parameter of greatest interest is the  $\beta$  value. This parameter defines the width/broadness of the spectrum of relaxation time. The lower the  $\beta$  value, the broader the distribution of the relaxation times, and vice versa, the higher the  $\beta$  value, the narrower the distribution of the relaxation times.

**Table 2.**  $\beta$  and  $\tau$  value comparison for Free Polystyrene and HNP systems

	$\beta$		$\tau$ , min	
	Free	HNP	Free	HNP
52K	Free	HNP	Free	HNP
T <sub>a</sub> = 75	0.93	0.54	401	1276
T <sub>a</sub> = 85	0.75	0.53	190	418
T <sub>a</sub> = 95	0.30	0.44	35	365

There observed trends for the  $\beta$  and  $\tau$  values for the free PS and HNP systems are summarized in Table 2. As the annealing temperature increases, the  $\beta$  and  $\tau$  values decrease. A conclusion that can be made from this data is that the relaxation modes for the HNP are much broader and slower due to the fact that the chains are restricted to the surface of the particle.

The material needed to make high energy density capacitors must be tough. If the material being used has a broad distribution of relaxation modes, as well as a slow relaxation time, it will become tougher. Energy storage plays a major role in the development of high energy density capacitors as well. Again, it is known that physical aging leads to densification of the material. The result of this process will enhance the mechanical properties associated with the material, and in turn increase its modulus. The ability to store energy will also increase per volume.

In summary, it has been shown that increasing the grafting density of HNPs leads to a uniform distribution/coverage of polymer chains about the inorganic particle; and the relaxation modes of HNP systems are much broader than those of the free polymer systems due to the polymer chains being tethered to the surface of the particle.

### Works Cited

- Liquid Crystal Polymers: A DSC Investigation of the Enthalpy Relaxation, *Macromolecules* 2002, 35, 9049-9056
- C. Chevigny, D. Gigmes, D. Bertin, J. Jestin, and F. Boue: Polystyrene grafting from silica nanoparticles via Nitroxide-Mediated-Polymerization (NMP): synthesis and SANS analysis with contrast variation method
- N. Doulache, M. Khemici, A. Gourari, and M. Bendaoud: DSC Study of Polyethylene Terephthalate's Physical Ageing
- B. Frieberg, E. Glynos, G. Sakellariou, P. Green: Physical Aging of Star-Shaped Macro Letters, *Macro Letters*, 2012, 1, 636-640
- G.G. Vogiatzis and D. Theodorou: Structure of Polymer Layers Grafted to Nanoparticles in Silica-Polystyrene Nanocomposites, *Macromolecules* 2013
- N. Fernandes, H. Koerner, E. Giannelis, R. Vaia: Hairy nanoparticle assemblies as one-component functional polymer nanocomposites: opportunities and challenges
- Rossi, Elliott, Ala-Nissila, and Faller: Molecular Dynamics Study of a MARTINI CoarseGrained Polystyrene Brush in Good Solvent: Structure and Dynamics, *Macromolecules*, 2012

COMPOSITE MATERIALS SUPPORTABILITY

Project No. 0172

David Cossey  
Louisiana Tech University

31 August 2014

Government Project Leader  
Dr. Rajiv Berry  
AFRL/RXAS

Southwestern Ohio Council for Higher Education  
Student Research Program  
Agreement Number: FA8650-09-2-5800

## **Acknowledgments**

I would like to acknowledge the DOD Supercomputing Resource Center for their support and use of the DOD supercomputers. Without their resources, this project never would have made the progress it has. I would also like to thank Dr. Gary Kedziora for his support and technical expertise with high level density functional theory (DFT) and initial studies of DFT functionals. Lastly, none of this would have been possible without the financial support of the Southwestern Ohio Council for Higher Education.

## **General Description of Project**

The primary focus of this project was to validate the work previously done by Aerial Camden (Camden, et al., 2013). Higher level density functional theory (DFT) calculations were performed on the S66x8 benchmark dataset (Rezac, et al., 2011) to evaluate the validity of non-bonded interaction energies predicted by the forcefield used in previous work (Camden, et al., 2013). The S66x8 benchmark dataset is a group of 66 molecular structures consisting of dimers of various common molecules. Each of the 66 molecular structures consists of its optimized MP2 geometry and seven other points along its dissociation curve freezing the geometry of each monomer. DFT calculations are usually more accurate than classical molecular dynamics forcefields; however, they are more computationally expensive and not suitable for large systems. This study will establish the accuracy of the TEAM forcefield (TEAM-FF) and determine if corrections to the forcefield would be necessary.

## **Description of Research**

This study focuses on using the S66x8 benchmark dataset to calculate interaction energies from DFT and TEAM-FF for comparison against complete basis set coupled cluster (CCSD/CBS) reference energies (Rezac, et al., 2011). Figure 1 below display a small sample of the dimer structures from the S66x8 benchmark set. Density functional theory uses functionals of the electron density to approximate solutions for the Schrödinger equation of a many-body system. This allows for the determination of all ground-state properties of a system, and in turn yields the total energy of a system. Classical molecular dynamics (MD) calculates energy by summing all the contributions from bonded and non-bonded interactions. Bonded interactions (bonds, angles, and torsions) are treated as harmonic oscillators, while non-bonded interactions are calculated using Lennard-Jones potentials and electrostatic energies. Interaction energies for these systems were acquired by subtracting the energies of the monomers from the energy of the dimer.

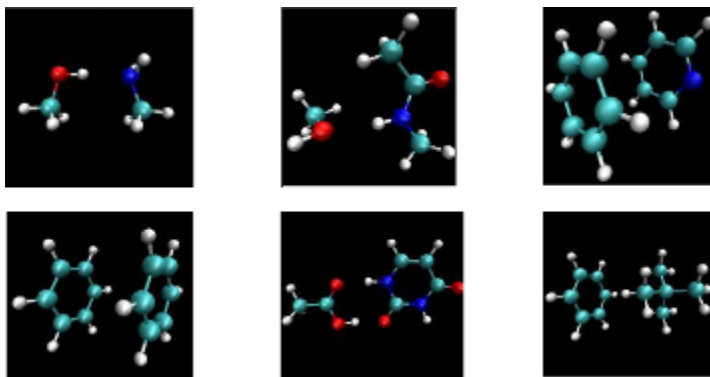


Figure 1. Sample of dimer structures from the S66x8 data set.

DFT calculations were performed using the CP2K software freely available (VandeVondele, et al., 2005). The revPBE DFT functional with Grimme D2 (Grimme, 2006) dispersion corrections paired with the double zeta valence (DZVP) basis set was used for calculating the DFT energies for this study. For efficiency, an orbital transformation method was implemented to reduce the computational time for these DFT calculations (VandeVondele & Hutter, 2003). Calculating interaction energies for TEAM-FF involved assigning forcefield parameters to each system using Direct Force Field 7.0.10 and calculating the energies using Sandia National Laboratories' LAMMPS software (Plimpton, 1995). Since, the TEAM-FF was specifically designed for non-bonded adsorption of biological molecules onto surfaces, it is not widely known in the classical MD community. For this reason, the CHARMM forcefield was also used in this study for comparison against the TEAM-FF. Applying the CHARMM forcefield and calculating the interaction energies of the benchmark set required using Discovery Studio 4.0 (Ref. Accelrys Software Inc., 2013).

## Results

Figure 2 below shows the difference between the energy predicted by the CCSD reference on all the dimers in the S66x8 database and each of the three methods listed above. The difference for most dimers is found to be within 4 kcal/mol. A large deviation is observed for dimer systems that include Uracil, for those cases revPBE provides acceptable values.

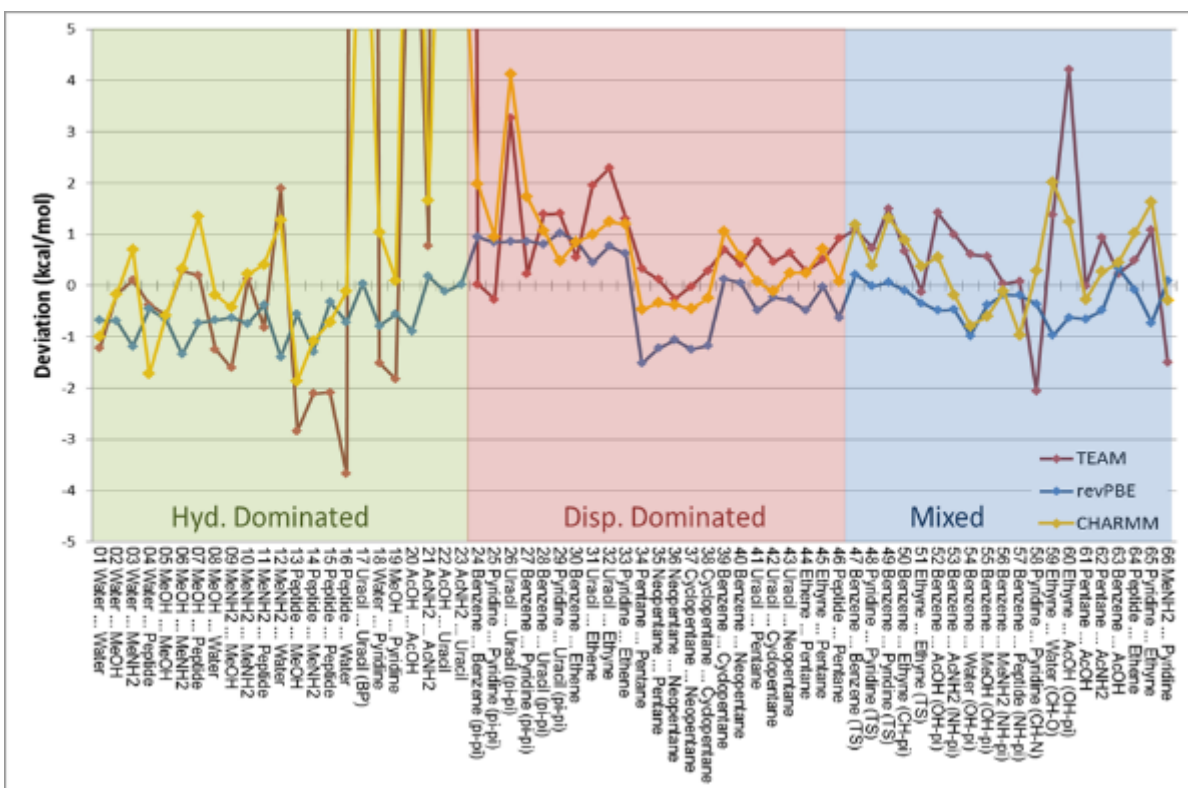


Figure 2. Energy deviations from the CCSD reference energies for the optimized equilibrium structures of the S66x8 benchmark dataset.

However, both force fields produce extremely large errors. Direct Force Field 7.0.10 fails to provide accurate TEAM-FF parameters for the Uracil molecule. CHARMM uses its special parameters for Uracil; however, these do not reliably predict the non-bonded hydrogen interactions between Uracil and other molecules.

Table 1. S66 Energy Statistics (kcal/mol) for the entire data set

	revPBE-D2	TEAM-FF	CHARMM
Mean Error	-0.42	0.22	0.52
Mean Absolute Error	0.60	1.06	0.99
RMSE	0.71	1.86	2.03
MARE	16%	22%	21%

Table 1 above shows the overall accuracy of interaction energies compared with the CCSD/CBS reference energies. RevPBE agrees with the reference within less than 1 kcal/mol. TEAM force field provides interaction energy errors that are comparable to CHARMM, although it shows a lower overall root mean squared (RMSE) deviation, yet a slightly greater mean absolute (MAE) error and greater relative error. This shows that CHARMM, while having a smaller MAE, CHARMM tends to have more statistical outliers. From the average error it can be observed that while revPBE slightly over predicts the binding energy from the mean error

(ME), both force fields under predict interactions with TEAM-FF showing a more balanced distribution. We can break these interactions down further to their dominant type of interaction: hydrogen, dispersion, or mixed.

In order to further analyze the data and determine the best method for a particular system, molecular systems were grouped according the dominant type of interaction in the dimer. Three groups were considered, hydrogen bond dominated, dispersion dominated, and mixed interaction. Tables 2 through 4 below summarize the results where molecular systems with Uracil are removed from the averages, as the deficiencies in the force fields would skew the statistics. RevPBE shows excellent results on all the three categories, with MAE's all below 1 kcal/mol. This agreement highlights the good properties of the dispersion corrections incorporated into this functional. Given the diversity of molecules in the set, we can conclude the revPBE with the Grimme D2 dispersion corrections does a good job in general.

Table 2. S66 Energy Statistics (kcal/mol) for the systems dominated by hydrogen bonded interactions.

	revPBE-D2	TEAM-FF	CHARMM
Mean Error	-0.72	-0.21	0.63
Mean Absolute Error	0.72	1.64	1.42
RMSE	0.79	2.75	3.14
MARE	12%	21%	14%

Table 3. S66 Energy Statistics (kcal/mol) for the systems dominated by dispersion interactions.

	revPBE-D2	TEAM-FF	CHARMM
Mean Error	-0.23	0.33	0.50
Mean Absolute Error	0.76	0.41	0.75
RMSE	0.87	0.54	0.92
MARE	30%	18%	30%

Table 4. S66 Energy Statistics (kcal/mol) for the systems with a mixture of hydrogen bonded and dispersion interactions.

	revPBE-D2	TEAM-FF	CHARMM
Mean Error	-0.27	0.58	0.42
Mean Absolute Error	0.36	0.96	0.74
RMSE	0.44	1.32	0.90
MARE	11%	26%	22%

Comparing the two force fields, it is observed that TEAM FF and CHARMM both produce rather acceptable results with average errors of less than 2 kcal/mol. When hydrogen bonded interactions are dominant, both force fields yield about the same magnitude of error, while TEAM FF outperforms CHARMM when dispersion interactions dominate. For mixed interactions, CHARMM produced results slightly more accurate than TEAM FF.

The next step was to calculate the interaction energies of the dissociation curves in the S66x8 set. The S66x8 dataset uses the minimum geometries from the S66 dataset as a reference distance and varies the distance between the dimers with an expansion factor from 0.90 to 2.00. As before, the statistics are calculated without the systems containing Uracil.

Table 5. S66x8 Energy Statistics (kcal/mol) for the entire data set.

	revPBE-D2	TEAM-FF	CHARMM
Mean Error	-0.39	0.26	0.53
Mean Absolute Error	0.50	0.94	0.97
RMSE	0.65	1.77	2.34
MARE	19%	30%	37%

Table 5 shows again that revPBE predicts acceptable values over the entire S66x8 dataset with errors less than 1 kcal/mol. TEAM-FF shows a better agreement over the S66x8 dataset than CHARMM. This suggests that TEAM-FF more accurately calculates non-bonded interactions over the varying distances along the dissociation curve even though CHARMM shows slightly better agreement at the minimum distances in the optimized MP2 geometries.

Table 6. S66x8 Energy Statistics (kcal/mol) for systems dominated by hydrogen bonded interactions.

	revPBE-D2	TEAM-FF	CHARMM
Mean Error	-0.68	-0.14	0.68
Mean Absolute Error	0.68	1.35	1.37
RMSE	0.76	2.40	3.39
MARE	22%	65%	84%

Table 7. S66x8 Energy Statistics (kcal/mol) for systems dominated by dispersion interactions.

	revPBE-D2	TEAM-FF	CHARMM
Mean Error	-0.23	0.35	0.42
Mean Absolute Error	0.56	0.42	0.61
RMSE	0.77	0.75	1.04
MARE	33%	31%	57%

Table 8. S66x8 Energy Statistics (kcal/mol) for systems with a mixture of hydrogen bonded and dispersion interactions.

	revPBE-D2	TEAM-FF	CHARMM
Mean Error	-0.22	0.59	0.46
Mean Absolute Error	0.28	0.93	0.84
RMSE	0.38	1.57	1.66
MARE	12%	36%	39%

As before, Tables 6 through 8 break down the interaction energy errors to their respective dominant traits. RevPBE shows excellent accuracy over all categories with mean absolute errors of  $\sim 0.5$  kcal/mol and RMS errors of less than 1 kcal/mol. TEAM-FF provides better or comparable statistical errors across the board in each category against CHARMM. TEAM-FF shows a noticeable difference of  $\sim 1$  kcal/mol better RMS error and standard deviation than CHARMM in hydrogen dominated interactions.

The final objective, however, is to be able to relate the bulk properties (or at least systems larger than a few molecules) to small dimer molecules. It would be more efficient to study small systems rather than running massive lengthy simulations to just choose the best method for a particular system. To compare bulk properties against the small molecule dimer systems, it is necessary to predict the density, self-diffusion coefficients, and atomic spacing of known liquids.

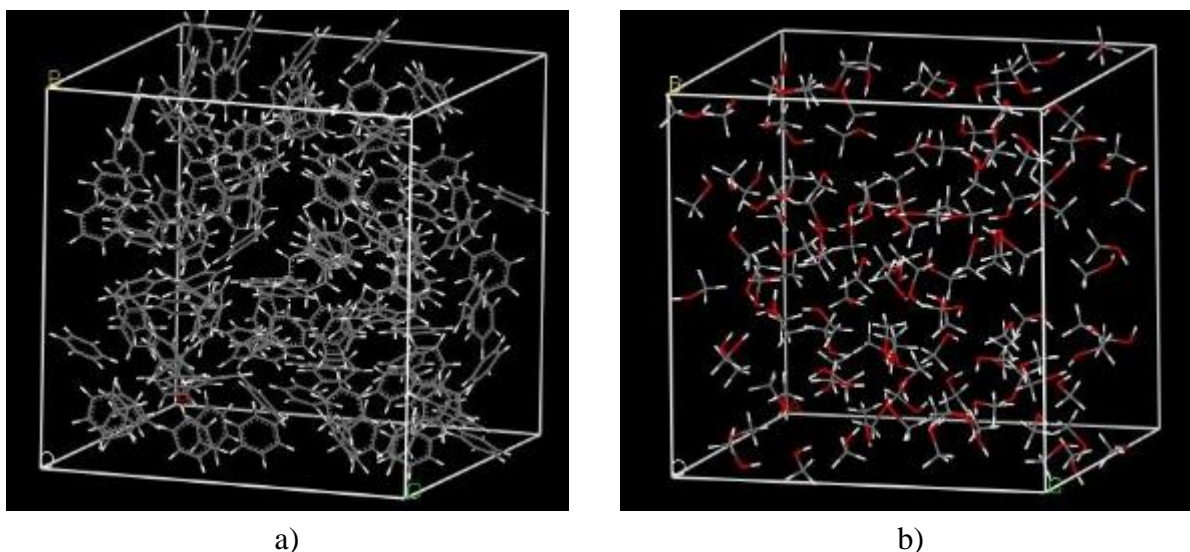


Figure 3. Molecular systems built to experimental liquid densities at 25 C for a) benzene and b) methanol.

Liquid methanol and benzene systems were created at their respective experimental densities for this comparison as seen in Figure 3. For each force field, the simulations were run approximately 4 ns to reach equilibrium and an additional 100ns for statistical data on liquid densities. From these simulations, densities were calculated and shown in Table 9 below.

Table 9. Simulated Densities of liquid benzene and liquid methanol compared against experimental densities a) (Parkhurst Jr. & Jonas, 1975) and b) (NIST webbook).

(g/cm <sup>3</sup> )	Experimental	TEAM FF	CHARMM	revPBE
Benzene	0.8765 ± 0.01 <sup>[a]</sup>	0.8017 ± 0.02	n/a	0.8454 ± 0.02
Methanol	0.7918 ± 0.01 <sup>[b]</sup>	0.8137 ± 0.01	n/a	0.8234 ± 0.01

Both TEAM-FF and revPBE predict densities lower than the experimental density for benzene; however, revPBE is within the statistical error of the experimental density. For methanol, both methods predict higher than experimental density, but TEAM-FF is close to being within statistical error for liquid methanol. Examining the radial distribution function (RDF) for the benzene-benzene center of mass in Figure 4, gives some insight for this lower density.

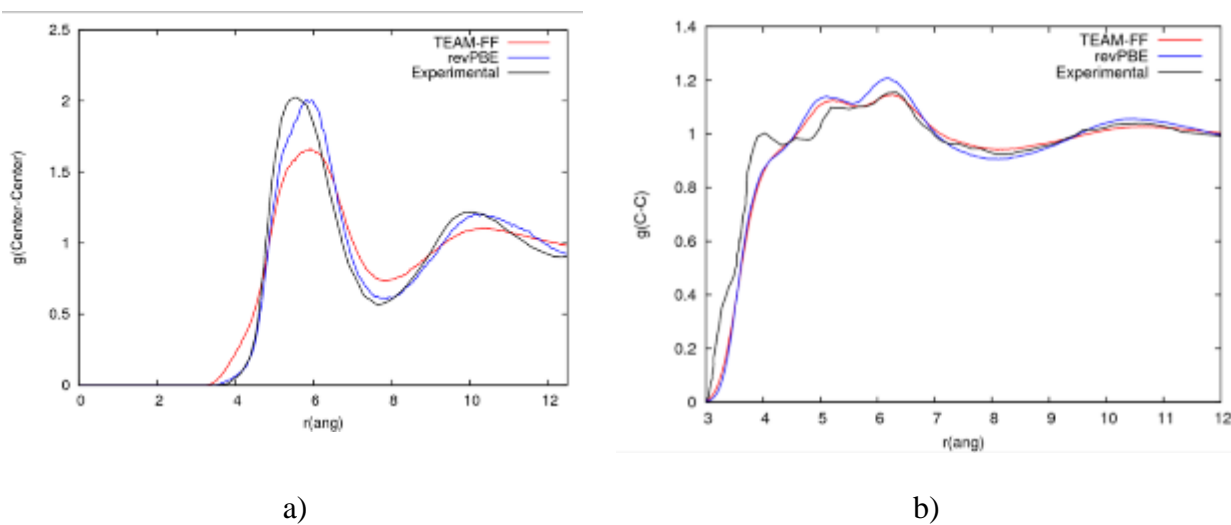


Figure 4. Radial Distribution of liquid benzene for a) center of masses and b) C-C distances compared against experimental results (Narten, 1977).

Both revPBE and TEAM-FF show the first peak for the center-of-mass to be shifted further away. TEAM-FF also shows a broader, less intense peak for the first shell of benzene rings as well as the peak being shifted ~0.5 angstroms. This shows a wider variation in distances over the simulation time for the first shell of benzene rings for TEAM-FF. RevPBE shows comparable peak intensities and widths to that of experimental data; however, the peaks for revPBE are shifted ~0.5 angstroms. In the RDF of C-C distances, both methods show a reduced first peak and a broad peak spanning the second and third peaks. This can be attributed to greater rotation and less defined structure for the first shell of benzene rings and can be partly contributed to by the weaker Pi-Pi dispersion interactions from Figure 5a for revPBE and weaker Pi-H interactions from Figure 5b for TEAM-FF. This weak initial peak is a trend continued for the C-H and H-H RDFs in Figure 6a and Figure 6b.

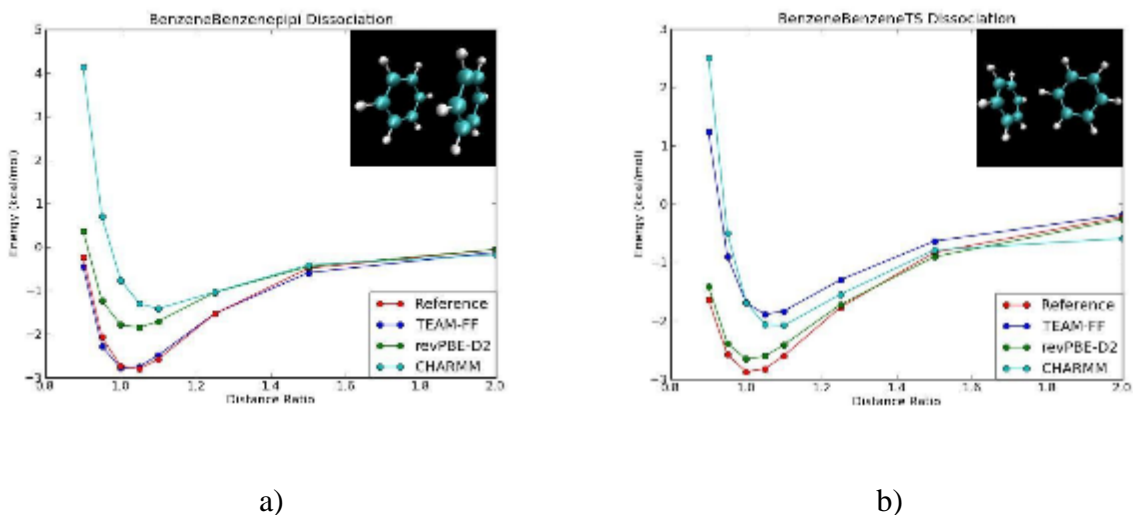


Figure 5. S66x8 dissociation curve of Benzene-Benzene in a) PiPi configuration and b) T-shaped configuration.

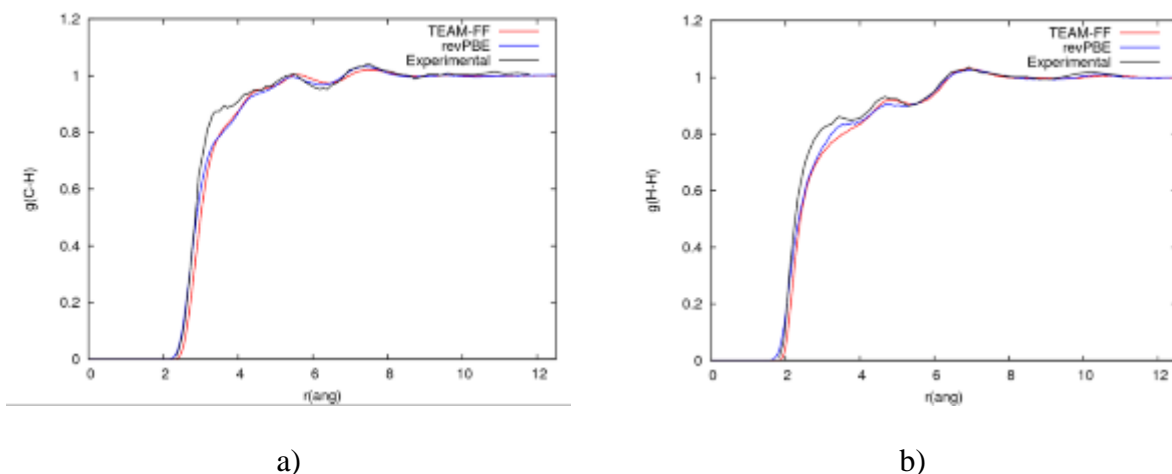


Figure 6. RDF for liquid benzene at 25 C for a) C-H and b) H-H distances.

Using this benchmark dataset, we have established the accuracy of different computational methods compared against what is considered the standard reference method for small to medium molecule systems. TEAM-FF is shown to have less statistical outliers than CHARMM over the entire S66x8 dissociation dataset even though it does not always have a lower mean absolute error. In most cases, TEAM-FF outperforms CHARMM; in cases where CHARMM shows better statistics, TEAM-FF has comparable results. The DFT functional revPBE outperformed the force fields except in the cases with dispersion dominated interactions. Even in these cases, the errors shown by the revPBE functional were less than 1 kcal/mol. There still isn't enough data to accurately predict liquid properties from small dimers. Further study is needed to make any concrete conclusions in that area.

## Works Cited

- Camden, A. N., Barr, S. A. & Berry, R. J., 2013. Simulations of Peptide-Graphene Interactions in Explicit Water. *Journal of Physical Chemistry B*, 117(37), pp. 10691-10697.
- Grimme, S., 2006. Semiempirical GGA-type density functional constructed with a long-range dispersion correction. *Journal of Computational Chemistry*, 27(15), pp. 1787-1799.
- Krack, M. & Parrinello, M., 2000. All-electron ab-initio molecular dynamics. *Physical Chemistry Chemical Physics*, Volume 2, pp. 2105-2112.
- Narten, A. H., 1977. Xray diffraction pattern and models of liquid benzene. *Journal of Chemical Physics*, 67(5), p. 2102.
- Parkhurst Jr., H. J. & Jonas, J., 1975. Dense liquids. II. The effect of density and temperature on viscosity of tetramethylsilane and benzene. *Journal of Chemical Physics*, 63(6), p. 2705.
- Plimpton, S., 1995. Fast Parallel Algorithms for Short-Range Molecular Dynamics. *Journal of Computational Physics*, Volume 117, pp. 1-19.
- Ref. Accelrys Software Inc., 2013. *Discovery Studio Modeling Environment, Release 4.0*. San Diego: Accelrys Software Inc..
- Rezac, J., Riley, K. E. & Hobza, P., 2011. S66x8: Dissociation curves for the S66 dataset. *Journal of Chemical Theory and Computation*, 7(8), pp. 2427-2438.
- VandeVondele, J. & Hutter, J., 2003. An efficient orbital transformation method for electronic structure calculations. *Journal Chemical Physics*, Volume 118, p. 4365.
- VandeVondele, J. et al., 2005. Quickstep: fast and accurate density functional calculations using a mixed Gaussian and plane waves approach. *Computational Physics Communication*, Volume 167, p. 103.

CERAMICS GROUP LABORATORY TECHNICIAN

Project No. 0173

Travis Tidball  
Wright State University

31 August 2014

Government Project Leader  
Michael Cinibulk  
AFRL/RXCC

Southwestern Ohio Council of Higher Education  
Student Research Program  
Agreement Number: FA8650-09-2-5800

## **Acknowledgements**

I would like to acknowledge Randy Hay, Randy Corns, Matt O'Malley, Geoff Fair, and Mark Cridge.

## **General Description of Project**

The goal of this project was to assist the Ceramics division of the Air Force Research Laboratory. This was done with numerous tasks including preparation and polishing of samples for transmission electron microscopy (TEM), preparation and polishing of samples for scanning electron microscopy (SEM), single filament tensile testing of ceramic fibers, push-in and push-out testing of fibers in a ceramic matrix, and setting up a system in order to steam treat ceramic fibers. SEM and TEM prep were done in order to analyze coatings on various fibers. Single filament testing was done in order to acquire the peak stress of the sample being tested. The system to steam treat the fibers is being done in order to see how the fibers react to a steam environment completely saturated in silicic acid. The SEM and TEM prep was done using a tripod polisher on diamond films. Single filament testing was done using a MTS testing machine. Lastly, the system to steam treat fibers was done using a steam generator, a pre-heater, and a furnace.

## **Description of Research**

The SEM and TEM preparation was done in order to analyze coatings on various fibers. Researchers were interested whether or not coating was present and also the thickness and chemical makeup of the coatings. The equipment used for the SEM and TEM polishing was a South Bay Technology Inc. tripod polisher and diamond films from Buehler and Allied. The data was analyzed using a Quanta scanning electron microscope and a Titan transmission electron microscope.

Single filament tests of ceramic fibers were done in order to determine the peak stress and load that a fiber can withstand. Tests were done on fibers that were heat treated in various environments and that had coatings applied to them. Fiber diameters were measured for each fiber tested using a laser diffraction method. The fiber tests were done using an MTS tester.

Push-in and Push-out tests were done in order to determine the bond energy between the fibers and the matrix. These tests were done with a variety of fibers that were heat treated and that contained numerous coats. The tests were done on an indenting machine that was built in house. The machine has indenters in sizes ranging from 5 micrometers to 100 micrometers and is capable of pushing a single fiber out of a matrix, or compress a fiber that is already in the matrix, depending on the setup.

Lastly, work has been done in order to steam treat fibers. The methodology is to saturate the steam with an outside substance, and then allow the saturated steam to flow over the fibers for varying lengths of time. The hypothesis being tested is that the substance that is saturated in the steam will lead to a decrease in the mechanical properties of the fibers. The equipment used consists of a steam generator, a pre-heater, and a furnace (figure 1). The data was analyzed through single filament tensile tests, SEM, and TEM.

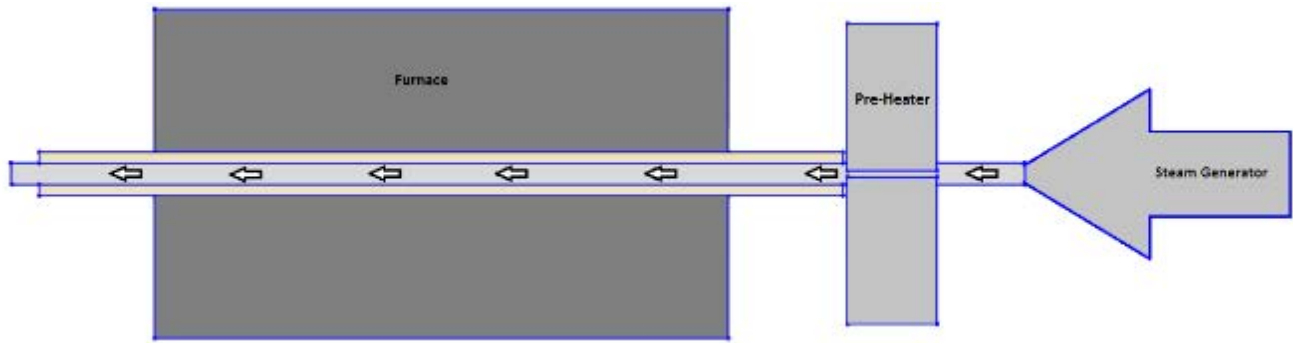


Figure 53. Fiber steam treating system.

## Results

The results from the SEM and TEM preparation were that fiber dense tows were returned to the researcher with a desirable thickness. These samples were then ready to either be looked at under a SEM or further processed to be looked at under a TEM. A successful process to create fiber dense tows without compromising the fiber coatings was discovered.

Single filament test yielded an apparent relation between the environment that the fibers were exposed to and mechanical properties of the fibers. As the temperature and length the fibers were treated in increased, the peak stress of an individual fiber decreased.

Due to numerous setbacks, fibers have not been treated in saturated steam yet. Thermal profile analysis has shown that the system is capable of achieving desirable conditions. The current hurdle in the project is developing a method to keep the saturating substance in the path of the steam. Figure 2 depicts the current thermal profile of the system with the saturating substance placed in the system from thirteen inches deep to twenty-two inches deep.

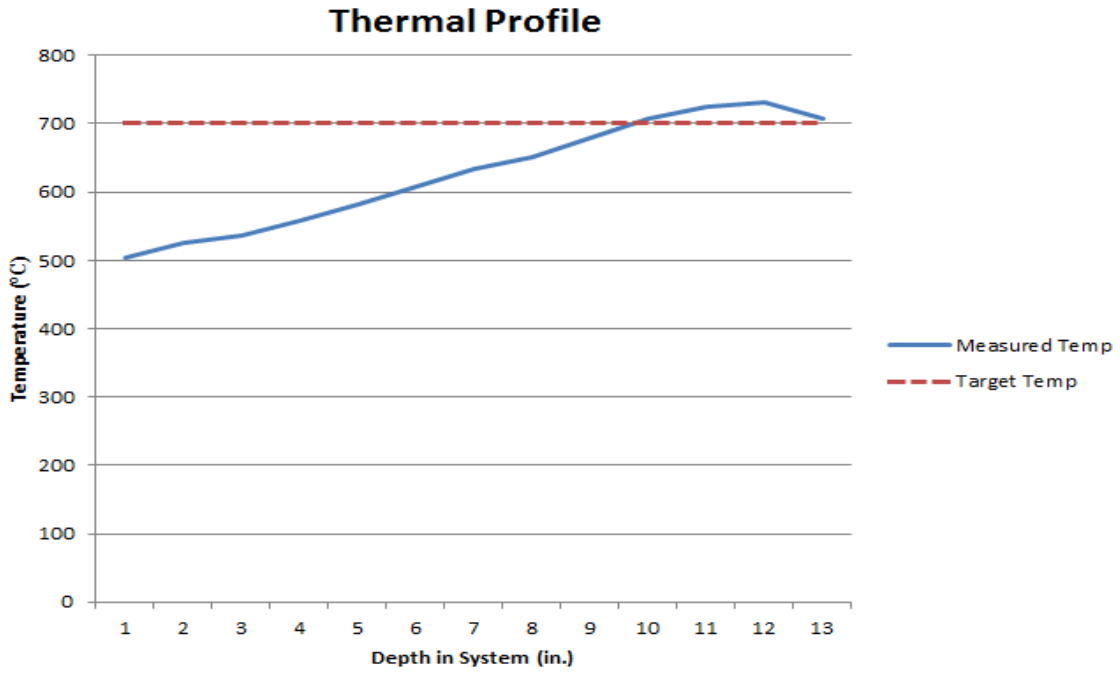


Figure 54. Thermal profile of the steam treatment system.

PHASE EVOLUTION FOR STRUCTURAL MATERIALS

Project No. 0174

Tinuade Daboiku  
Wright State University

31 August 2014

Government Project Leader  
Dr. Jaimie Tiley, Ph.D.  
AFRL/RXCM

Southwestern Ohio Council for Higher Education  
Student Research Program  
Agreement Number: FA8650-09-2-5800

## **Acknowledgments**

Dr. Jaimie Tiley played a significant role throughout this project, not only as government project leader but also as a professional mentor. I am tremendously appreciative for the opportunity to have hands-on experience in materials research. Mike Velez and Bob Lewis (UES, Inc.) provided the necessary laboratory training to complete the research as well as many other members of the Materials Characterization Facility. Finally, I would like to thank my fellow SOCHE student researchers for their help along the way.

## **General Description of Project**

Structural materials in aerospace applications need to be lighter and stronger to meet the ever-growing demands for better fuel consumption, higher flight velocities, and thus higher operating temperatures. Titanium alloys have been studied to fill this need; the alloy boasts high specific strength and good fatigue properties. Many researchers have studied this material at high temperatures and have found microstructure greatly impacts the mechanical properties of titanium. For example, crystallographic orientation affects fatigue strength and tensile ductility. Also, oxygen diffusion at high temperatures reduces ductility but increases wear resistance and microstructural hardness.<sup>1</sup>

In the present work, the dependency of high temperature oxygen ingress on crystallographic orientation was investigated for Ti-6Al-2Sn-4Zr-2Mo+Si (Ti-6242S). Ingress depth was estimated and simulated.

## **Description of Research**

Ti-6242S samples were produced by ATI and subsequently solutionized to increase the beta-phase grain size. Samples were then oxidized in a box furnace to produce the oxygen-rich layer and cooled in air. Analysis preparation included sectioning the sample and polishing via standard metallographic procedures. The samples were then etched to reveal the oxygen-rich layer under optical microscope and measured. Backscattered electron (BSE) images were taken of unetched samples with a scanning electron microscope (SEM) to characterize local crystallographic orientation. Thin films were milled and evaluated by an electron probe microanalyzer (EPMA) and energy dispersive spectroscopy (EDS). Microhardness was also used to estimate oxygen ingress in conjunction with electron backscatter diffraction (EBSD) to determine crystallographic orientation at the microhardness indentation sites.

## **Results**

It was determined that ingress through the microstructure depends on the alpha-phase grain orientation with respect to ingress direction. Figure 1a illustrates the crystallographic orientation relative to ingress direction. Figure 1b shows the oxygen layer brightened by etching under an optical microscope.

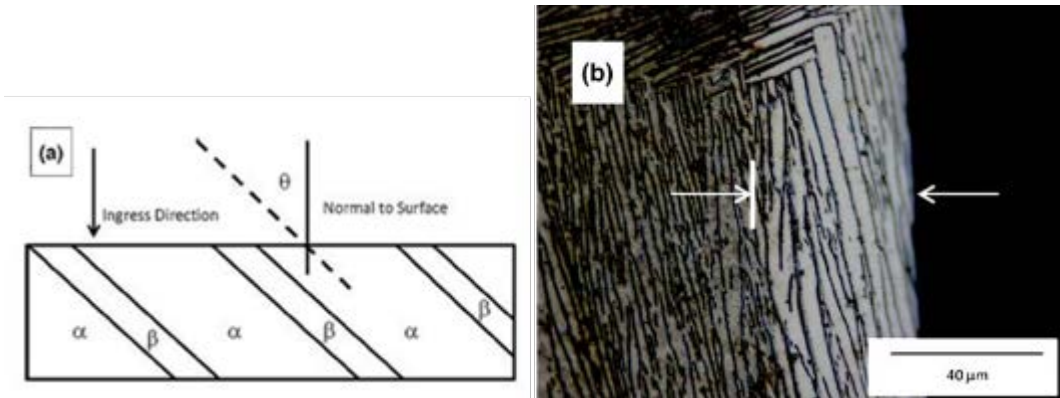


Figure 1—(a) Schematic of crystallographic orientation, ingress direction and inclination angle  $\theta$ ; (b) optical image of etched sample showing ingress layer.

Oxygen counts by EPMA (Figure 2) show high oxygen concentration near the sample surface and decreases toward the bulk material. The measured microhardness of oxidized samples shows significantly higher values than unoxidized samples near the surface (Figure 3). Both EMPA and hardness measurements share a common trend through the oxygen-rich layer indicating that the ingression does in fact harden the materials surface, possibly benefitting some mechanical properties.

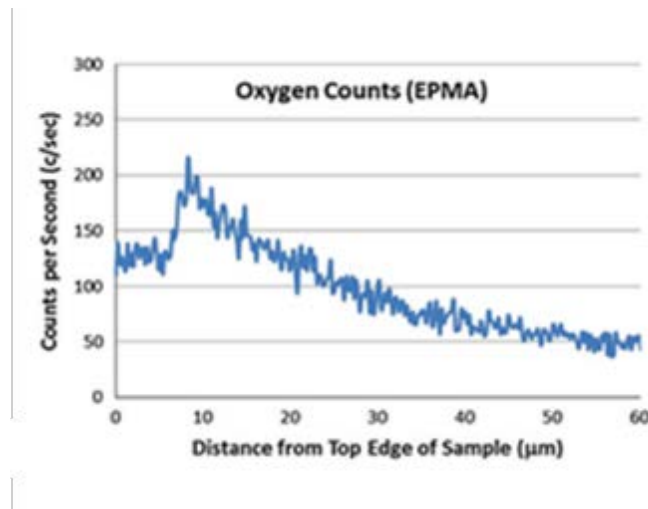


Figure 2—EPMA measured oxygen count as a function of distance from sample edge. Values below 10  $\mu\text{m}$  are the result of beam interaction.

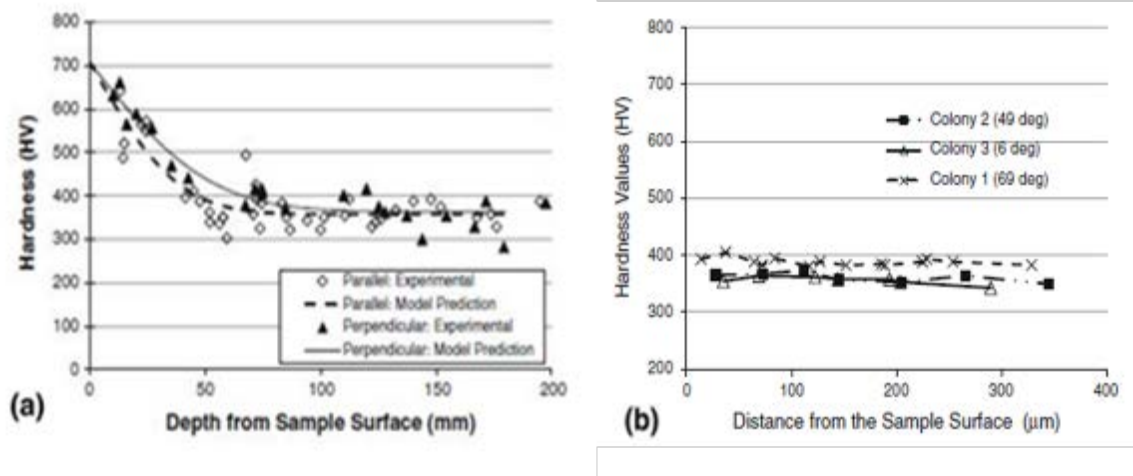


Figure 3—(a) Measured and modeled microhardness as a function of distance from sample surface and grain orientation ; (b) measured microhardness of unoxidized sample for alpha grains at three inclination angles.

Modeled microhardness predictions of the oxidized material with parallel and perpendicular alpha grains proved viable. The modelling method used the exposure temperature and measured microhardness of unoxidized and oxidized material to fit an effective diffusion coefficient to each inclination angle. This may benefit future efforts to link processing, microstructure, and mechanical properties.

### Conclusion

Ti-6242S is an excellent candidate for aerospace applications, however, thermomechanical processing and microstructure greatly influences the material's mechanical properties. Hardness measurements and microstructural information allow a feasible estimation for effective diffusivity through multi-phase titanium thus providing essential insight on the microscopic to macroscopic properties relationship.

### Works Cited

1. Tiley, Jaimie, et al. "The Effect of Alpha Lath Orientation on Oxygen Ingress in Titanium Alloys." Meta Trans A 45A (2014): 1041-1048.

EVALUATION OF ALTERNATE FIBER FORMS OF AFR-PE-4 FOR B-2 HOT TRAILING  
EDGE STRUCTURE

Project No. 0175

Austin T. Christopher  
Wright State University

31 August 2014

Government Project Leader  
Dr. Brett Bolan  
AFRL/RXSA

Southwestern Ohio Council for Higher Education  
Student Research Program  
Agreement Number: FA8650-09-2-5800

## **Acknowledgments**

I would not have had this opportunity if it wasn't for Kara and Tara Storage for getting my foot in the door and helping me get the edge up to receive this internship. I would also like to thank Paul Childers for working with Dan Reilly, Clint Hirtzinger and me and showing us how to do our job correctly and to the best of our ability. Jim Mazza and Brett Bolan also deserve an acknowledgment for helping our group with research needed to complete the projects we were assigned.

## **General Description of Project**

The purpose of the Evaluation of Alternate Fiber Forms for a Hot Trailing Edge (HTE) Structure (# 1-007) is to demonstrate and ultimately transition a new higher temperature capable material form which compresses the section of the HTE that attaches to the aircraft. These new materials are needed because the current polyimids HTE, which is situated in the engine exhaust, quickly degrades in this thermally stressed environment. In this evaluation the physical and mechanical properties of this new material were tested to determine if they met Air Force specifications. This same methodology is also used to ensure prepreg material beyond its stated shelf life can be validated for additional usage.

## **Description of Research**

The beginning step of the Evaluation of Alternate Fiber Forms for a Hot Trailing Edge Structure (# 1-007) project was to cut the correct amount of plies in the right direction and to the correct size from a roll of prepreg (e.g. 12"x12" or 18'x18" and then stacked up accordingly to make panels of the following orientation  $[0/\pm 45/90]_{25}$  or  $[0]_{30}$ . This is done by hanging up a large roll of material on a rack, using a razor blade and a metal cutting template to cut out the plies. This speeds up the process and makes sure that all plies are the same size. Once all the plies have been cut and the aluminum caul plate has been prepared the building of the vacuum bag begins. This is started by laying up and stacking the plies that were just cut in the correct orientation for the panel being fabricated. The laminate is then covered with porous (breathable) and non-porous teflon. Then around the outer edges of the caul plate Schnee-Morehead 5160 and Air Tech A800-3G Sealant Tapes (tacky-tape) are placed so that when the vacuum bag is placed over top of their arrangement an airtight bag can be formed. Inside the vacuum bag there are two other materials, S2 Boat Cloth and 4581 S2 Glass Breather. Both of these materials help provide a breath path through the bag so the trapped gases volatiles generated during the curing of the laminate can escape through the vacuum hoses. Once the panel is cured, using an Air Force specified cure cycle (Table 1), the panels are removed from the vacuum bag and trimmed so they can be sent to be nondestructively inspected for quality. This entails the utilization of ultrasonic waves sent throughout the panel while it is underwater. If there is a defect in the panel, then the affected area cannot be used for the mechanical properties tests because the composite laminate will not meet the required Air Force specification for this material. The mechanical properties tested are to check if the material can withstand the stresses it is expected to experience while in operational flight. The physical properties tests are to check if the prepreg, as received, meets Air Force specifications (i.e. volatile content, resin content, and fiber content).

## Results

The physical properties tests are the only tests that have been completed at the moment because the mechanical properties tests are still waiting to be done. By the numbers that were gained from the physical properties tests the prepreg material is still within specifications and can still be used. The curing process for the panels has also been standardized so that laminate panels can be consistently made without defects in them or weak points.

## Figures & Tables

**Table 1 Unitape Prepreg Physical Property Requirements**

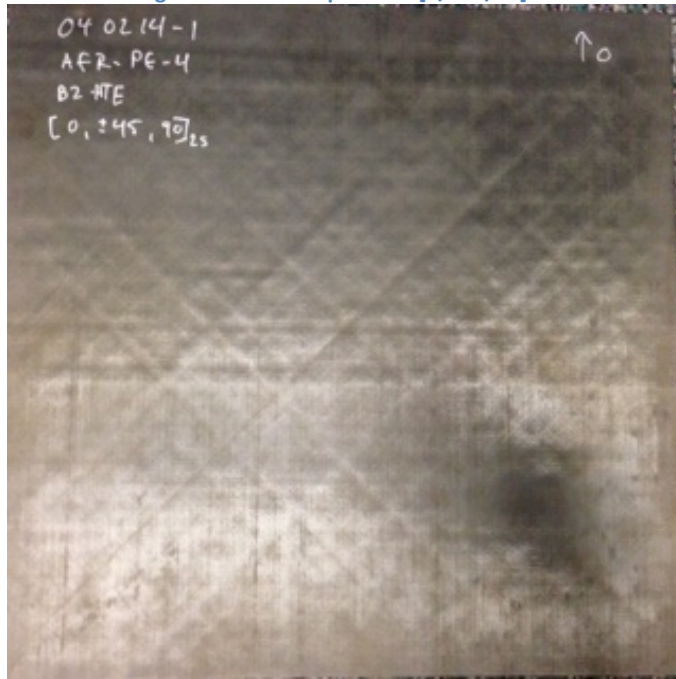
Property	Requirement (Average)
Volatile Content, weight percent	11.0 ± 3.0
Dry Resin Content, weight percent	35 +4, -3
Fiber Areal Weight, g/m <sup>2</sup>	147 ± 7

**Table 2 Unitape Physical Properties Results**

PE-4 Uni Tape		
Prepreg Volatile Content		
Specimen #		Value
TVC-1	Watch Glass Weight (Tared)	97.5952
	Specimen & Watch Glass Weight (Int)	99.1565
	Specimen Weight Int (WI)	1.5613
	Specimen & Watch Glass Weight (Post)	98.9304
	Specimen Weight Post (WF)	1.3352
	<b>Volatile Content</b>	<b>14.48%</b>
TVC-2	Watch Glass Weight (Tared)	97.3332
	Specimen & Watch Glass Weight (Int)	98.7645
	Specimen Weight Int (WI)	1.4313
	Specimen & Watch Glass Weight (Post)	98.5625
	Specimen Weight Post (WF)	1.2293
	<b>Volatile Content</b>	<b>14.11%</b>
TVC-3	Watch Glass Weight (Tared)	97.5031

	Specimen & Watch Glass Weight (Int)	99.0158
	Specimen Weight Int (WI)	1.5127
	Specimen & Watch Glass Weight (Post)	98.816
	Specimen Weight Post (WF)	1.3129
	<b>Volatile Content</b>	13.21%
<b>Prepreg Resin Content</b>		
<b>Specimen # TRC-1</b>		<b>Value</b>
	Watch Glass Weight (Tared)	97.627
	Specimen & Watch Glass Weight (Int)	99.061
	Specimen Weight Int (WI)	1.434
	Specimen & Watch Glass Weight (Post)	98.405
	Specimen Weight Post (WF)	0.778
	<b>Resin Content (Wet)</b>	45.75%
	<b>Resin Content (Dry)</b>	36.96%
	<b>Areal Weight</b>	134.1379
<b>Specimen # TRC-2</b>		<b>Value</b>
	Watch Glass Weight (Tared)	97.504
	Specimen & Watch Glass Weight (Int)	99.0586
	Specimen Weight Int (WI)	1.5449
	Specimen & Watch Glass Weight (Post)	98.3575
	Specimen Weight Post (WF)	0.06914
	<b>Resin Content (Wet)</b>	55.25%
	<b>Resin Content (Dry)</b>	48%
	<b>Areal Weight</b>	119.2
<b>Specimen # TRC-3</b>		<b>Value</b>
	Watch Glass Weight (Tared)	97.5834
	Specimen & Watch Glass Weight (Int)	99.144
	Specimen Weight Int (WI)	1.5606
	Specimen & Watch Glass Weight (Post)	98.4145
	Specimen Weight Post (WF)	0.8311
	<b>Resin Content (Wet)</b>	46.74%
	<b>Resin Content (Dry)</b>	38.12%
	<b>Areal Weight</b>	143.29

Figure 1 PE-4 Unitape Panel [0/±45/90]2S



FIBER VOLUME FRACTION ANALYSIS WITH CERAMIC MATRIX COMPOSITES

Project No. 0176

Talion Grace  
Central State University

6 June 2014

Government Project Leader  
Dr. Eric Jones  
AFRL/RXCC

Southwestern Ohio Council for Higher Education  
Student Research Program  
Agreement Number: FA8650-09-2-5800

## **Acknowledgements**

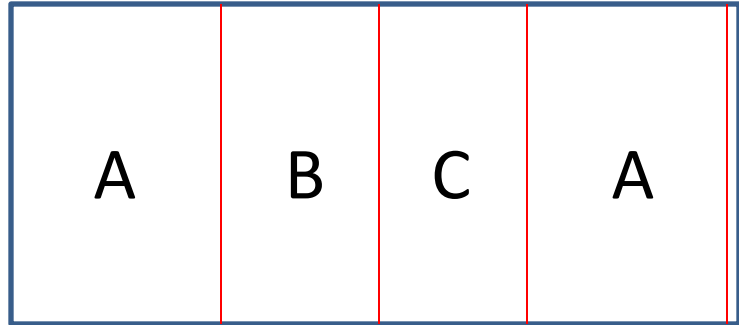
I would like to acknowledge the general faculty and staff on behalf of the students for giving us this opportunity to grow in the careers we are trying to pursue. I personally would like to acknowledge Ms. Brittany Edwards and the Southwestern Ohio Council for Higher education for giving me the opportunity to work at AFRL. I also want to thank Dr. Eric Jones for the leadership and positive mentorship he has provided for me throughout my duration here as an employee. Dr. Jones has helped grow professionally and he has enhanced my character on becoming a better person and a better engineer. I would also like to acknowledge Mrs. Jenny Pierce. Jenny has done a tremendous job mentoring me as well and training me with the lab equipment. She has also provided me with the tools and resources that I need to perform my projects. I would last like to acknowledge Dr. Darnell Diggs. Dr. Diggs and I didn't spend much time together from a technical standpoint, but he has helped me grow professionally. He has been a mentor for me since I first started here and he has helped me make the right decisions to better my character and my personal life.

## **General Description of Project**

The overall objective of this project was to verify the fiber volume fraction (FVV) of several non-oxide ceramic matrix composites (CMCs). The fiber volume fraction is a critical parameter in terms of understanding the strength and behavior of CMCs. We also like to see the behavior of the fibers in these CMC's to see the difference in their structures and to view their properties. The structures in these CMC's are different because the materials have different properties. The difference in properties enable the performance of the materials to also be different. It's important to understand the behavior of the fibers in the material because we can further determine how long these materials will last in aircraft applications before maintenance is required. The knowledge of the longevity of the aircraft applications for these materials is essential because it eventually increases part life, improves reliability, and reduces operating and maintenance costs of aircraft applications such as exhaust nozzles, and jet engines. The behavior of these fibers is determined through fiber volume fraction analysis.

## **Methodology and Procedures**

In order for the fiber volume fraction analysis to be performed, images of the fibers needed to be taken. The materials were put through a process in order to prepare them for the images. First the materials were cut using a Diamond Wafering Series 15LC Blade. The materials were sectioned out according to the diagrams that were given. The diagram required us to section the samples into four pieces labeled A, B, C, and D. A and D were 10mm in length and the other two samples were 5mm in length. Red lines indicated the side that was going to be polished.



After the samples were cut and sectioned, they were mounted on the buehler machines. The mounting process is required because it compacts the materials with heat and pressure to stop air from getting in contact with them. If too much air gets in contact with the materials, they become damaged and that prevents us from taking images. Samples are ran at these settings on the machine:

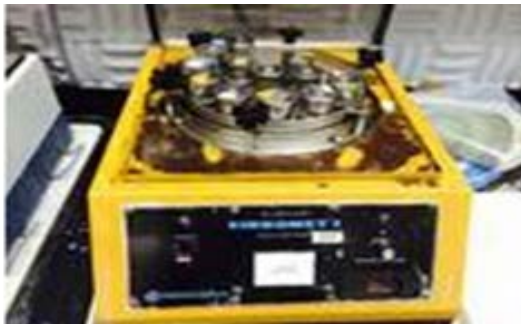
- $\frac{3}{4}$  Coarse Polyfast
- $\frac{1}{4}$  Fine Polyfast
- $\frac{1}{8}$  Epomet
- Temperature- 180 degrees Celsius
- Pressure Load-170
- Settings-Thermoset
- Heating Time-10min
- Cooling Time-8min

After the samples are mounted, they have to be polished. Polishing is required because the samples have to be flattened in order to see the fibers under the microscope. The 6 and 1 micron diamond is used to rub up against the surface of the samples to flatten and produce the fibers. The samples are placed in holders and the polishing machine is ran according to these settings:

- Time-8 cycles Avg (30min per cycle) depends on the material
- Base-60
- Head-120
- Water-off
- Load-7lbs (For 3 samples or less, the load should be 5lbs)

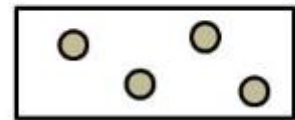
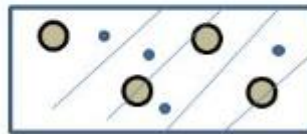


After the samples are polished, they are placed on the vibromet. The vibromet is a machine that does extensive cleaning to remove any additional scratches or dirt from the materials. This is what the sample is supposed to look like under the microscope after it has been on the vibromet.

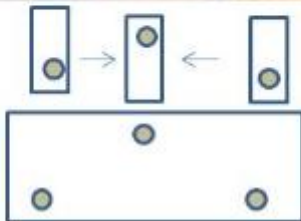


**Dirty Sample**

**Clean Sample**



Now the samples are clean and they are ready to be imaged. The Zeiss Microscope is what was used to create montage images for the samples. The microscope can take images of different parts of the sample and put them together to create one full image. Here is a picture of what the montage image is supposed to look like.



Once these images are taken, we are now ready to do the volume fraction analysis.  $V_v = (\sum A_i) / A_t$  is the equation for determining the analysis. This requires you to take the area of each particle size and add them all together. Each particle is an ellipse and the area of an ellipse is  $3.14(AB)$ . The A and B letters represent the length and width of the particle. Next you divide by the test area which is essentially the area of the printed document paper the images are on. Once you compute that answer, you multiply by 100.

**Results:**

The samples that I was given, have already been analyzed. I was required to perform the analysis again to see if my results were accurate with the results of the manufacturers of the materials. I was given five different materials and the results of the manufacturers from each one. My results were as follows:

<b>Material</b>	<b>Measured Fiber Volume Fraction</b>	<b>Manufacturer Fiber Volume Fraction</b>	<b>Percentage Difference with Manufacturer</b>
S200H	53.7%	54.3%	0.6%
N720/AS	35.3%	35.6%	1.3%
S400 C/SIC	59.3%	59.7%	0.4%
A500	56.4%	56.9%	0.5%
HYPR	51.2%	51.6%	0.4%

In conclusion, the numbers that were determined were close to the numbers that were determined by the manufacturers of the materials. We learned that fibers give CMC's strength, and they're a source of variability for the materials behavior. This fiber volume fraction analysis is essential because it helps us determine the behaviors and responses of fibers in given materials. The measured numbers were consistently low compared to the manufacturers. The average percentage difference between all of the numbers was 0.64%. Our goal was to have our results as accurate as possible to the results of the manufacturer. There are other methods that can be used to find the Fiber Volume Fraction. Different methods are useful because they can give you better accurate results. The method that was used in this project was called the Areal Analysis. Another common method that was used was the Point count Method. This method consists of counting how many times one of the fiber particles hits an intersection. After that, you take the area of the grid lines and find the quotient between the two. This analysis was also performed to see if the percentage differences would decrease. When the Point Count method was completed, the results were the same as the Areal Analysis. Even though we couldn't determine why there was a 0.64 average percentage difference in both methods, it still shows that there are different methods that can be used to produce the same result.

METALLOGRAPHIC RESEARCH ON ADVANCED CERAMICS FOR ELECTRON  
CHARACTERIZATION

Project No. 0177

Dontrel Reynolds  
Alabama A&M University

1 August 2014

Government Project Leader  
Dr. Eric Jones  
AFRL/RXCC

Southwestern Ohio Council for Higher Education  
Research Collaboration Program  
Agreement Number: FA8650-09-205800

## **Acknowledgements**

I would like to thank SOCHE for the opportunity to intern this summer at AFRL. I would also like to give a special thanks to Dr. Eric Jones, Dr. Travis Whitlow, Dr. Jennifer Pierce, Nick Engel and Mike Scott for their contribution to the research project. The knowledge and guidance that they provided was instrumental to me in accomplishing my project.

## **General Description of Project**

The focus of this project is to investigate the initiation and development of damage in Ceramic Matrix Composites (CMCs) during mechanical testing (monotonic & cyclic loading) using acoustic emission (AE). AE are sound waves that are produced during damage growth within a material, in this case matrix cracks and fiber breaks are two damage modes that are producing the waves. The project will include working with engineers in the Composites Branch to monitor damage development and determine failure location during mechanical testing and to modify or develop new metallographic procedures for preparing these samples for optical imaging. Damage evolution is an important characteristic because it gives insight of how the material's microstructure plays a critical role in the failure location. Acoustic emission is used to locate the development of any matrix cracks or fiber breaks in the specimen. To examine the damage in these CMCs, an effective metallographic procedure for cutting, mounting, and polishing was utilized. The metallographic techniques developed were applicable to several current projects in the Composite Performance Research Team. A four point bending fixture was designed and used to open cracks in the sample. This will enable the researchers to calculate the matrix crack density (MCD). This characterization is utilized to quantify the damage in the CMCs in an specific area.

## **Description of Research**

In this project, CMCs were mechanical tested using monotonic and bi-cyclic loading methods on MTS Test Frame. The bi-cycle loading was a load, unload, and reload process. During the mechanical test, sound waves are initiated by matrix cracking and/or fiber breaks which are detected by wide band piezoelectric sensors. The individual sound waves are measured as AE events. In order to detect these sound waves, three sensors were clamped along the gage section of the specimen to detect the crack growth. The signals that are detected by the sensors are sent to the Wave Explorer Software for analysis. This software provides waveforms that are used to interpret the crack growth that is being detected by the sensors. Researchers are in continuous study to understand the extensional and flexural waveforms. Other measurements that are being taken during the test are strain; researches receive strain information by using an extensometer which is displayed in figure 2.

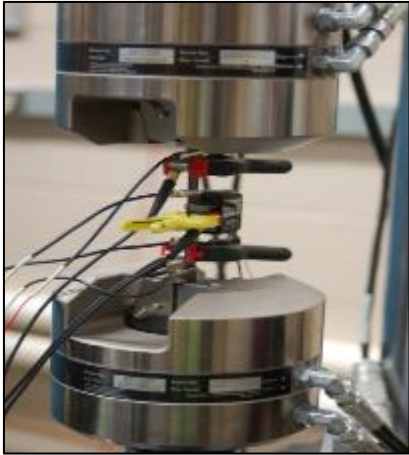


Figure 1: MI-SiC HiNicalon CMC loaded into the MTS Test Frame for mechanical and AE testing

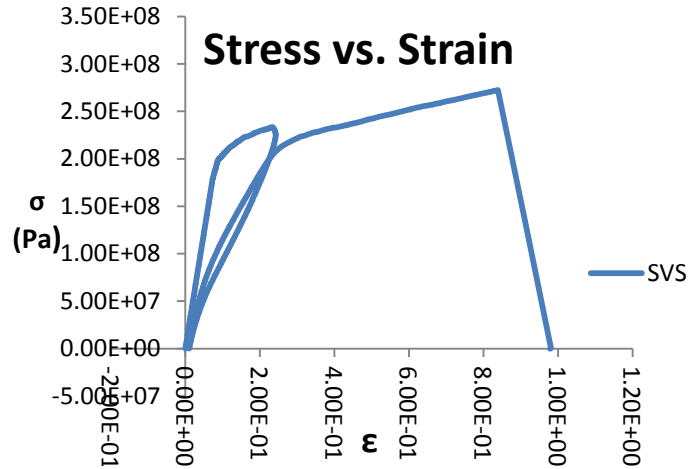


Figure 2: Stress Strain curve from cycling fatigue test

Next, have to analysis of the wave data received from the AE events during the test is done. The waves are characterized by their extensional and flexural modes. The extensional wave is a higher velocity wave mode and is detected before the flexural. Figure 4 shows the loading profile of the sample (load, unload, and reload) and the location of AE events that were detected within the gage section by the sensors. This information is used to determine the location of the damage. More analysis is needed to confirm the indication of AE events determine the final failure location.

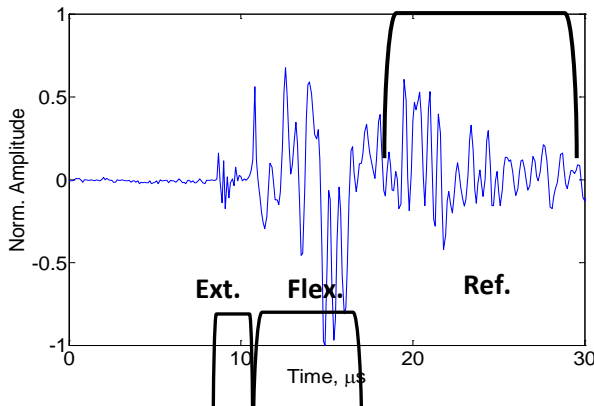


Figure 3: Typical wave form displaying extensional and flexural region of wave. Reflections were also detected

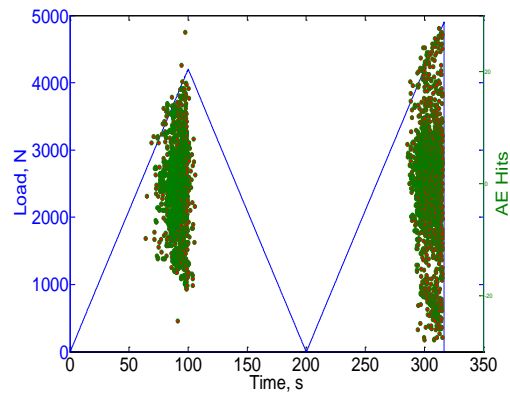


Figure 4: Loading profile of fatigue test overlapped with the location of AE events within the gage section

The next step in the project was to develop/modify a metallographic procedure to cut, mount, polish, and un-mount the CMC. A diamond blade saw was used to cut a 25mm section from the tested specimen. Next, an acrylic cold mount was used to mount the sample for polishing. The polishing procedure began with a Gold Label abrasive polishing cloth with a 9 micron diamond suspension. The purposes for these materials were to remove any mounting material from the face of the sample and to provide a flat polishing surface so that the sample will polish evenly.

Once a flat surface has been achieved, the polishing cloth and diamond suspension are changed to a White Label cloth and 6 micron suspension which is less aggressive and provides a fine polish. The final polishing step is to continue with the White Label cloth and used a 1 micron suspension to buff out any scratches from previous polishing steps. Polishing is complete when the matrix can clearly be seen under an optical microscope for damage observations. Now, the polished sample can be soaked in a beaker of acetone for two hours so that it can be removed from the acrylic mount.



Figure 5: Specimen after cut (left) mounted and polished sample (right)

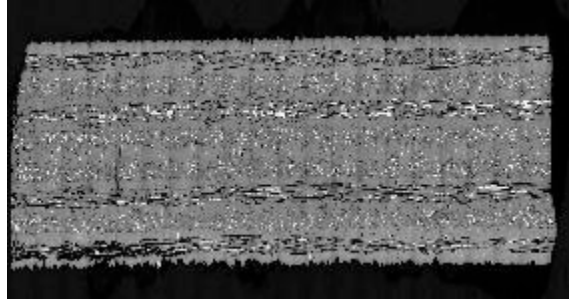


Figure 6: Microstructure of polished CMC at 100x

The final approach taken in this project is to calculate the matrix crack density. Before this could be done, a four point bending fixture was designed. The purpose of the fixture is to apply a small load onto the sample to open cracks. The material is so dense that cracks are not visible when there is no load. Once the specimen is loaded in the fixture, optical images will be taken in a 10mm section of the sample. Within the 10mm, the number of cracks counted will determine the matrix crack density of that area.



Figure 7: Four point bending fixture

## Results

This research was successful in detecting crack initiation and growth using AE. Location of AE events gave indication of final failure region, but more analysis needed in this area. A metallographic procedure was modified to use for future references to clearly see matrix for optical imaging and to calculate the matrix crack density.

EXPLORATORY STUDIES IN THIN FILM OPTICAL COATINGS

Project No. 0178

Regina Gallagher  
The Ohio State University

3 January 2014

Government Project Leader  
Dr. Neil Murphy  
AFRL/RXAP

Southwestern Ohio Council for Higher Education  
Student Research Program  
Agreement Number: FA8650-09-2-5800

## **Acknowledgments**

I would like to thank Neil Murphy, Dr. Lirong Sun, Dr. Rachel Jakubiak, Dr. John Jones, and Dr. Elizabeth Steenbergen for giving me the opportunity to work with them and for all their help. I really appreciated the knowledge they shared and time they spent helping me understand new ideas and concepts. I would also like to thank Dr. Angela Campbell and the Southwestern Ohio Council for Higher Education for giving me the chance to experience research.

## **General Description of Project.**

Uniformity measurements of test grade silicon substrates were taken. Alpha SE Ellipsometry was used to measure thickness and native oxide thickness of silicon wafers. Stress measurements were taken for the silicon substrates before and after semiconductor films (e.g. Rhenium Oxide, Germanium Oxide) were deposited. Data was analyzed using Microsoft Excel. The purpose of the measurements were to evaluate the uniformity of wafers used when depositing semiconductor thin films so that the effects of thickness uniformity and stress in substrates on the films deposited could then be evaluated. The use of test grade wafers could then be validated or rejected.

## **Description of Research**

The first step of the project was to determine qualities in silicon substrates that would most affect the quality of thin films deposited on the surface. Factors that were determined to have a significant effect on thin film quality were native oxide thickness, thickness uniformity, and stress in silicon wafers used. Test grade silicon wafers were measured in order to either justify or reject their use in thin film deposition. Cleaning methods for test grade silicon substrates were also investigated.

Native oxide thickness, and thickness uniformity measurements were taken using Alpha SE tabletop Ellipsometry. The data was analyzed using Alpha SE software and then exported into Microsoft Excel for statistical analysis. Stress measurements of wafers were taken with the Tencor FLX 2320. This data was plotted using built in 3D analysis software. Stress plots were made and then exported as images. Average, maximum, and minimum stress values were recorded and analyzed in Microsoft Excel.

After initial substrate uniformity tests were performed, semiconductor thin films were deposited on the substrates using DC Magnetron Sputtering. The films were deposited under high vacuum conditions. During deposition films were analyzed using in-situ ellipsometry. The native oxide and substrate thickness measurements initially taken were used to fit data for the growth of the thin films. After deposition, the thickness of the semiconductor films were verified using a stylus profilometer. Next, a second set of stress measurements were taken using the Tencor FLX. These stress measurements were compared to the original measurements from the substrate alone. The built in 3-D analysis software used the contour plots from before and after deposition to create a stress profile for each of the wafers tested.

Additionally, research was done on silicon wafer cleaning. Different methods of cleaning were considered for use on the test grade silicon substrates. After considering the benefits and difficulties of multiple cleaning methods including, but not limited to basic chemical rinsing, sonication, and hydrofluoric acid rinse, it was decided that an effective and practical cleaning method to try for deposition purposes would be an acetone rinse followed by a methanol rinse.

After a cleaning method was decided upon the benefits of cleaning the wafers were evaluated by using the Alpha SE ellipsometer to take native oxide thickness measurements of recently unpackaged silicon wafers in comparison to wafers that underwent the chosen cleaning process.

## Results

It was discovered that the test grade wafers had a significant amount of non-uniformity in native oxide thickness and in stress measurements. Figure 1, shown below shows native oxide thickness measurements across four different test grade wafers from the same package.

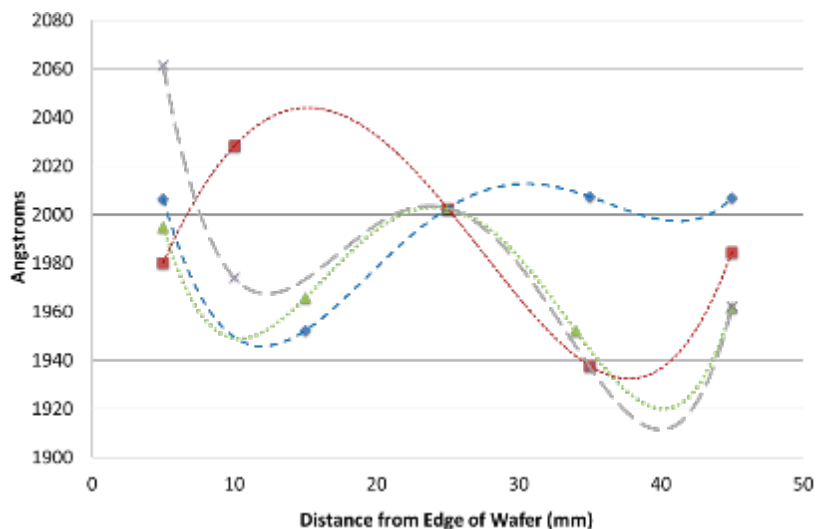


Figure 55. Plot of native oxide thickness across the surface of 4 different test grade silicon wafers. Plot made in Excel.

The deviation in native oxide thickness across the surface of the test grade wafers was high. This could lead to irregularities in films deposited on wafers which could cause error when analyzing and comparing semiconductor thin films deposited on different silicon wafers or even across a single wafer.

The stress measurement data also showed high variance across the silicon wafers and even across the surfaces of individual wafers. Contour plots of bare test grade silicon wafers differed dramatically. Films deposited under the same conditions but on different silicon wafers sometimes exhibited very different stress profiles, some of which ranged from tensile to compressive under the exact same conditions. The effect of the non-uniformity of native oxide thickness and stress profiles in the silicon substrates on the deposited films was considered to be of enough concern to reject the use of test grade silicon wafers for thin film deposition and justify the use of higher grade wafers.

The native oxide thickness measurements of wafers that underwent the chosen cleaning process of an acetone rinse and methanol rinse were compared to the measurements from before cleaning. It was found that the chosen cleaning method made no significant improvement on the

uniformity of the native oxide thickness. Therefore the chosen cleaning method was not justified or rejected.

#### **Related Activities**

During my time at AFRL with Southwestern Ohio Council for Higher Education I was able to gain experience in another lab where I learned to prepare samples by thinning them for Fourier Transform infrared spectroscopy (FTIR) with a diamond grinder. I also learned to take FTIR measurements and Photoluminescence (PL) measurements of the samples. I used OriginPro Software to analyze the data from FTIR and PL to determine the transparency and band gap of samples.

PREDICTION OF MATERIAL PROPERTY DISTRIBUTIONS WITH SMALL  
PROBABILISTIC MICROSTRUCTURAL MODELS

Project No. 0179

Daniel M. Sparkman  
University of Texas at San Antonio

31 December 2013

Government Project Leader  
Dr. Patrick Golden  
AFRL/RXCM

Southwestern Ohio Council for Higher Education  
Student Research Program  
Agreement Number: FA8650-09-2-5800

## **Acknowledgments**

I am grateful for the wonderful opportunity to work with the AFRL Materials and Manufacturing Directorate as a part of SOCHE. The people and resources I was given access to enabled me to finish my dissertation and now I'll graduate with a PhD. in Mechanical Engineering this spring.

I thank my AFRL mentors for their support and encouragement - Dr. Patrick Golden and Dr. Reji John. I also thank Dr. Chris Sczcepanski, Dr. Sushant Jha, Dr. Robert Brockman, and Dr. Mike Groeber for the helpful discussions. I am very grateful to Dr. Adam Pilchak for providing the EBSD data used in this work, as well as his invaluable experience and expertise. I thank my fellow AFRL interns Eric Burba, Alec Blankenship, and Eric Tipps for their support.

I thank Dr. Angela Campbell for her role in the Minority Leaders Program and for her encouragement along the way. I also thank Brittany Edwards with SOCHE for all of her help.

## **General Description of Project**

Probabilistic methods were developed for the characterization of microstructural features important to the deformation and failure of titanium alloys. This project was completed in parallel with efforts within RX to characterize regions of material with a preferred crystallographic orientation, called microtexture regions. In this project, a statistical model of the crystallographic orientation distribution function was developed for a titanium alloy from electron back scatter diffraction data provided by RX. Methods from spatial statistics were applied to characterize the spatial configuration and size of the regions. Statistically equivalent microstructures containing microtextured regions were simulated. The statistical model developed and calibrated with data enables the quantitative comparison of the microtextured regions present in different materials. The model also enables the prediction of bulk material properties such as yield strength and fatigue life through simulation with a crystal plasticity model.

## **Description of Research**

The thermomechanical processing of titanium alloys has been observed to produce regions within the material with alpha particles that have a preferred crystallographic orientation. [1, 2, 6, 7, 8] These regions are called microtextured regions (MTRs), macrozones, or "ghost structures". [2] The presence of microtextured regions can result in significant reductions in dwell fatigue life [8], fatigue life [9], and low cycle fatigue life [6, 10], and affect yield strength. [6]

Electron back scattered diffraction (EBSD) with a scanning electron microscope is used to determine the crystallographic orientation in the form of Euler angles ( $\phi_1$ ,  $\Phi$ ,  $\phi_2$ ) at each spatial location (x,y) on the surface of a test specimen. EBSD data for several Ti-alloys was provided by RX and an inverse pole figure map for billet Ti-6242 is presented in Figure 1. In this sample, MTRs are present as evidenced by many local regions of similar color (orientation). The regions are of varying shapes and sizes, and have a predominantly vertical elongation.

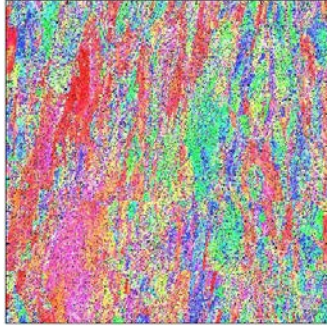


Figure 1. Microtextured Regions – The inverse pole figure map from an EBSD scan shows many MTRs are present as evidenced by many local regions of similar color (orientation). The dimensions of this area is 5mm x 5mm.

Despite the role MTRs play in structurally important material properties, only a few efforts have been made to quantitatively characterize their shapes or sizes. No standard method exists, but some researchers have employed a linear intercept method on inverse pole figure maps[1], used the TiZone software to segment out the MTRs[73], and used 2-point correlation functions[11,12]. Only one technique has been published for the statistical simulation of microtexture using quantiles of neighbor fractions at specified misorientation angles[3,4].

The project involved the development of a statistical framework for the characterization and simulation of polycrystalline materials containing microtextured regions. The framework explicitly takes into account the spatial nature of the microtextured regions.

The microtextured regions were statistically characterized by first decomposing the macro-texture crystallographic orientation distribution function (ODF) into component ODFs with a finite mixture model using the Expectation-Maximization (EM) algorithm [13] as in Figure 2. The model was formulated such that each microtextured region has orientations that belong to a single component ODF.

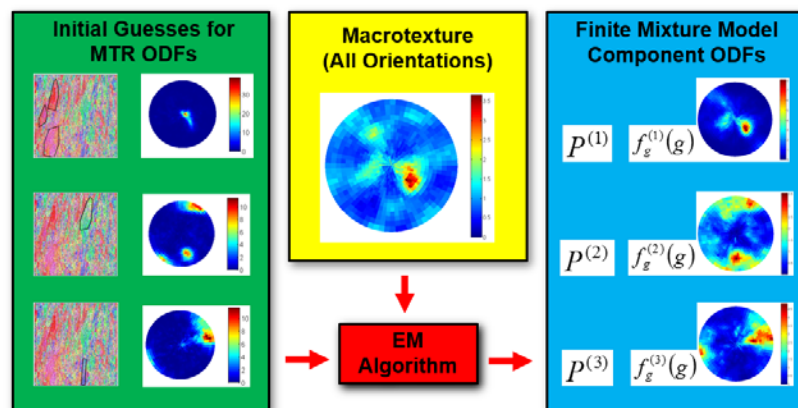


Figure 2. Estimated Component ODFs with the EM Algorithm – The MTR ODFs found from each of the regions outlined by black polygons ‘evolved’ with the EM algorithm to give the finite mixture model component ODFs that describe all of the orientation data.

Each location in the microstructure was assigned to an MTR ODF based on its orientation. This transformed the data from a field of orientation data (Euler angles) to the field of categorical data (assigned component ODF index) in Figure 3.

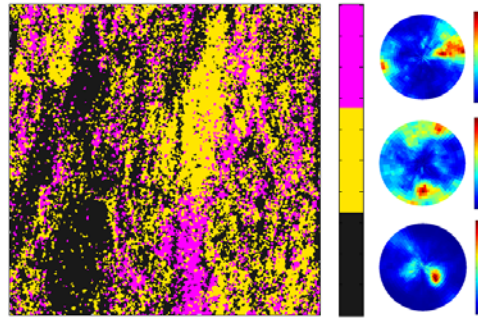


Figure 3. Component ODF Assignment Map – Each spatial location was assigned to one of the 3 component ODFs shown. MTRs appeared as large regions of a single assignment.

A summary statistic called an empirical indicator semivariogram was developed from the assignment data. It provides a global quantitative description of the spatial features within the data, enabling comparison of materials containing MTRs.

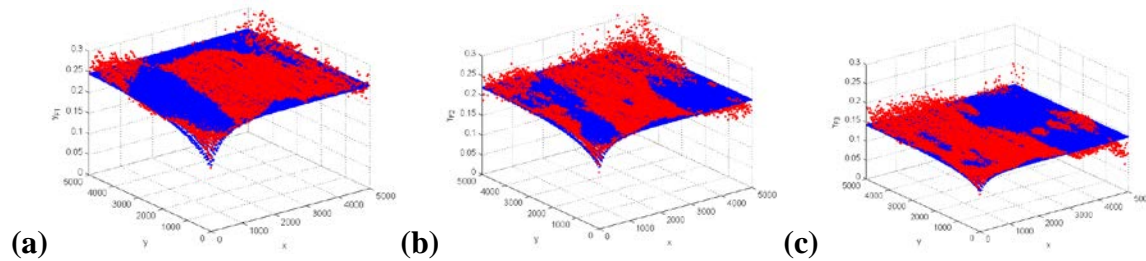


Figure 4. Component ODF Empirical and Theoretical Semivariograms – The theoretical semivariogram (blue) fit to the empirical semivariogram (red) is plotted for component MTR ODF 1 in (a), 2 in (b), and 3 in (c).

A plurigaussian model was fit to the empirical semivariogram using a weighted least squares scheme as seen in Figure 4. The model consists of a set of underlying gaussian random fields that are thresholded according to an assignment rule[5].

Microtextured regions were simulated with the fitted statistical model by first simulating the underlying gaussian random fields as in Figure 5.

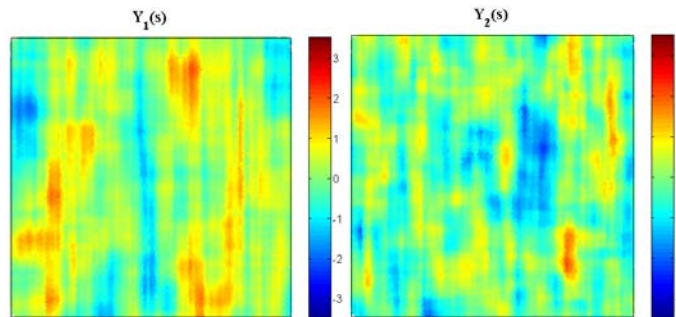


Figure 5. Plurigaussian Simulations – The GRFs were simulated with parameters estimated by least squares.

The assignment rule in Figure 6a is a set of thresholds that were applied to the simulated random fields to produce the categorical field in Figure 6b. To complete the simulation, a crystallographic orientation for each spatial location was simulated according to its assigned component ODF. The resulting simulated MTRs are presented in the inverse pole figure map in Figure 6c.

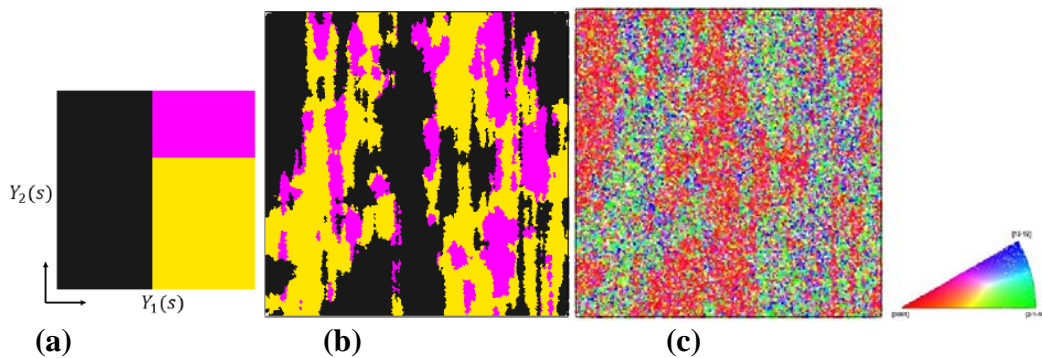


Figure 6. Simulated MTRs – The assignment rule in (a) produced the simulated assignment map in (b). Crystallographic orientations were simulated according to the component ODFs to produce the simulated MTRs in (c).

## Results

A statistical model was developed for the characterization and simulation of microtextured regions using a finite mixture model for the ODF and plurigaussian methods for the description of the spatial features. The methodology was applied to experimental data for a titanium alloy. It was found that the model captured some of the spatial characteristics present. The empirical semivariograms for each of the components exhibited a larger practical range in the y-direction than the x-direction, corresponding to visually observed elongation of MTRs in the y-direction. Simulated microtextured regions also contained vertically elongated MTRs.

The empirical semivariograms enable quantitative comparison of the MTRs in different materials. The simulated MTRs can be used with a crystal plasticity model to predict bulk material properties. Future efforts may use this model to modify material processing parameters to produce materials optimized for some desired perfor.

## Works Cited

- [1] Bhattacharjee, A., et al., Correlating Ultrasonic Attenuation and Microtexture in a Near-Alpha Titanium Alloy. *Metallurgical and Materials Transactions A*, 2011. **42**(8): p. 2358-2372.
- [2] Biavant, K.L., S. Pommier, and C. Prioul, Local texture and fatigue crack initiation in a Ti-6Al-4V titanium alloy. *Fatigue and Fracture of Engineering Materials and Structures*, 2002. **25**: p. 527-545.
- [3] Groeber, M., Ghosh, S., Uchic, M.D., and Dimiduk, D.M., "A framework for automated analysis and simulation of 3D polycrystalline microstructures Part 1: Statistical characterization," *Acta Materialia*, Vol. 56, 2008, pp. 1257-1273.
- [4] Deka, D., Joseph, D., Ghosh, S., and Mills, M., "Crystal Plasticity Modeling of Deformation and Creep in Polycrystalline Ti-6242," *Metallurgical and Materials Transactions*, 37A, 2006.
- [5] Armstrong, M., et al., *Plurigaussian Simulations in Geosciences*. 2003, Berlin: Springer.
- [6] Szczepanski, C.J., S.L. Semiatin, and J.M. Larsen, *The Role of Microtexture of Fatigue Lifetime Variability and Crack Initiation Mechanisms*. Report AFRL-RX-WP-TP-2011-4369. 2011.
- [7] Bridier, F., Villechaise, P., and Mendez, J., "Analysis of the different slip systems activated by tension in a  $\alpha/\beta$  titanium alloy in relation with local crystallographic orientation," *Acta Materialia*, Vol. 53, 2005, pp. 555-567.
- [8] Woodfield, A.P., et al., *Effect of Microstructure on Dwell Fatigue Behavior of Ti-6242. Titanium '95: Science and Technology*, 1995: p. 1116-1123.
- [9] Lindemann, J. and L. Wagner, *Microtextural effects on mechanical properties of duplex microstructures in (a+b) titanium alloys*. *Materials Science and Engineering: A*, 1999. **263**(2): p. 137-141.
- [10] Pilchak, A.L., et al., *The Influence of Microstructure and Microtexture on Fatigue Crack Initiation and Growth in a+b Titanium*, M.a. Manufacturing, Editor. 2011: Wright-Patterson Air Force Base, OH.
- [11] Morawiec, A. and J. Pospiech, *Functions Describing Orientation Correlations in Polycrystalline Materials*. *Textures and Microstructures*, 1992. **19**: p. 67-74.
- [12] Lee, P.S., et al., *Texture Clustering and Long-Range Disorientation Representation Methods: Application to 6022 Aluminum Sheet*. *Metallurgical and Materials Transactions A*, 2002. **33**(3709-3718).
- [13] Dempster, A.P., Laird, N.M., and Rubin, D.B., *Maximum Likelihood from Incomplete Data via the EM Algorithm*. *Journal of the Royal Statistical Society*, 1977. **39**: pp. 1-38.

## Related Activities

The work corresponding to this project went into my dissertation, which I successfully defended this December. I am preparing a paper on this work to submit for publication and to present at a conference.

DEVELOPMENT OF HIGH TEMPERATURE FULL FIELD METHODS TO UNDERSTAND  
THE BEHAVIOR OF STRUCTURAL MATERIALS FOR AIR FORCE APPLICATIONS

Project No. 0180

Brittanie Rooths  
University of Dayton

31 August 2014

Government Project Leader  
Dr. Eric Jones  
AFRL/RXCC

Southwestern Ohio Council for Higher Education  
Student Research Program  
Agreement Number: FA8650-09-2-5800

## Acknowledgements

There are several people would like to thank for their involvement with my project. First and foremost, I would like to thank my government project leader, Dr. Eric Jones for his mentorship and guidance. I would also like to thank several others for their assistance and contribution to my project: Kevin Hoos, David Mullenhauer, Sirina Safriet, Mark Kistner, Art Safriet, Mike Braginsky, Craig Pryzbyla, George Jefferson, and James Scott.

## General Description of Project

Ceramic matrix composites (CMCs) are used for high temperature applications (1000-1500 °C) and are potential candidates for uses such as gas turbine engine components and thermal protection systems (TPS) for hypersonic vehicles. The out-of-plane, or through-thickness, properties of CMCs are an order of magnitude lower in strength than the in-plane properties. High interlaminar (out-of-plane) stresses and low interlaminar strength of CMCs causes delamination that could propagate, resulting in a reduced load-carrying capacity or overall failure of the component. Although there are tests capable of measuring the in-plane properties of CMCs at application temperature, the current test used to measure the interlaminar tensile strength of CMCs presents some flaws. The weakest properties of CMCs lie between the plies (through thickness). Therefore, measurement of these properties is essential in order to optimize the use of CMCs. A test that is capable of measuring the interlaminar strength of CMCs at application temperatures is needed.

This work proposes a new method to measure the interlaminar properties using micro digital image correlation (DIC). DIC was used to measure localized displacements to determine the feasibility of the new test methodology. However, DIC only provides information for surface defects. Computed tomography (CT) scans were used to acquire detailed images of internal structures of the CMC samples. The results from both the micro DIC test and the CT scans were then compared.

## Description of Research

### *High Temperature Interlaminar Tension Sample*

The sample used throughout the project was an Oxide CMC, specifically, Nextel 720 fiber/ Alumino-Silicate matrix (N720/AS) 18 ply (0/90)s layup. The new test method proposed will test CMCs at their potential application temperature using the test sample geometry to generate interlaminar tensile failure within the center of the sample (gauge section) as load is applied. Figure 1 shows the distribution of stress and the effects of load to the stress within the ample and at crack initiation, respectively. As a load is applied to the sample, the tabs cause compression directed toward the outside of the gauge section. This initiates a tensile load within the center of the gauge section. The test relies on balance within the test fixture and sample in order to re-create the results in the finite element model. Figure 2 shows the high temperature interlaminar tensile (HTILT) sample in the load fixture. Micro digital image correlation was used to validate the FE model by measuring the full field deformation of the CMC sample and providing localized displacement and strain information

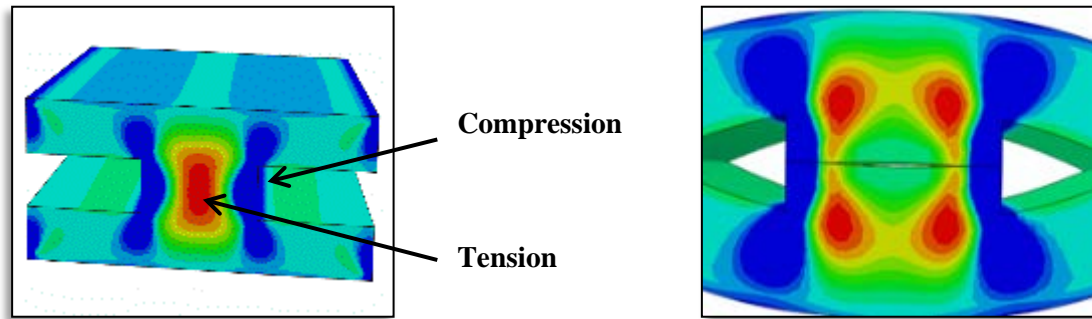


Figure 1: Computational model of interlaminar stress a) before crack, b) after crack initiation.

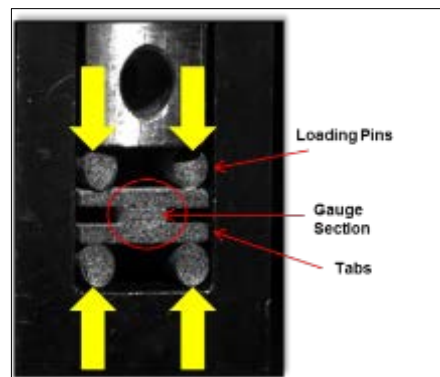


Figure 2: HTILT sample in loading fixture. The yellow arrows identify the direction of the load application.

### *Micro Digital Image Correlation*

Micro digital image correlation is used to capture the real-time deformation images of the test. It is a non-interferometric optical method used in experimental mechanics. DIC is capable of capturing the real-time surface effects of the test, even at the application temperature needed for CMCs. Currently, tests using DIC have only been conducted at room temperature. However, if the test can be successfully run under ambient temperatures, ideally, the test should be successful at much higher temperatures (1000-1500°C).

DIC uses a random speckle pattern on the surface of a sample to track displacement from each image based on an initial reference image. The DIC software, VIC 3D, discretizes each image based on the subset (or facet) size. Then, it compares sub-regions throughout the image to obtain a full field measurement. DIC is non-contact and provides localized displacement and strain measurements. As load is applied to the sample, two charged-coupled devices (CCD cameras) capture surface deformation by obtaining images throughout the test. The images are then correlated using computer software for further analysis. The CCD cameras used for this test were from Point Grey Research, Inc. (Richmond, BC, Canada). Figure 3 is a schematic of the materials used to run a micro DIC test.

After the images are correlated, 2D and 3D contour plots are available in VIC 3D. Several variables are available for post-processing analysis, including position, displacement and strain.

For this test, analysis is focused on displacement and strain along the Y-axis (V), which provide data for the interlaminar properties. Using the 2D contour plots, displacement and strain may be measured using the inspector tools. To calculate the displacement of the specimen's surface, section lines and points may be used. Strain was measured using virtual extensometers. The numerical data from the displacement lines, points, and extensometer may be extracted from VIC 3D for further analysis.

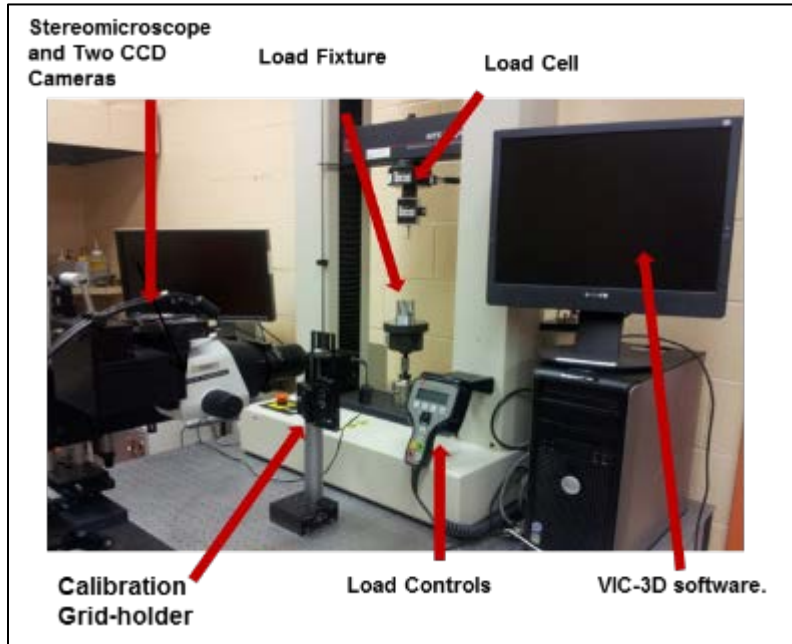


Figure 3: Schematic of micro DIC setup

### *Computed Tomography*

Micro DIC is limited to providing information only on surface defects on the HTILT samples. For this reason, computed tomography (CT) scans were used to acquire images of the internal structures of the samples. Pre and/or post-test scans were run on some of the samples. This helped correlate visible cracks seen in the DIC with any pre-existing defects. The additional data provided with the CT scans prompted additional CT tests to be used. 2D and 3D in-situ load tests will be performed on HTILT samples in the CT. However, because of the size of the samples, a new fixture had to be designed and machined in order to test the sample in the CT, which is shown in Figure 4.

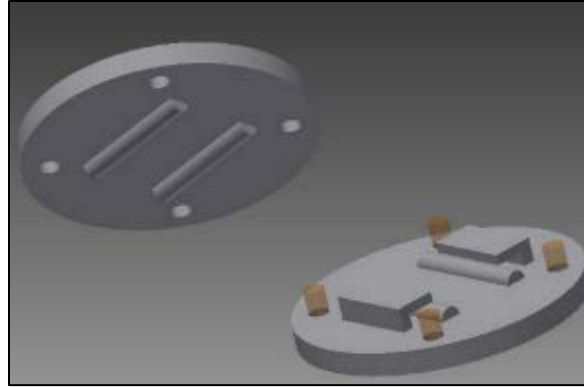


Figure 4: Drawing of fixture designed for HTILT samples to be tested in CT.

## Results

### *Digital Image Correlation*

Based on the computational model, the HTILT samples, the most stress should be in the center of the gauge section and should therefore fail in that region. However, experiments show the most stress to be directed in various other locations, which can be seen in the results of sample 7 in Figure 5 and Figure 6. Possible reasons for differences are stress concentrations from machining and unbalanced loading due to misalignment in test fixture.

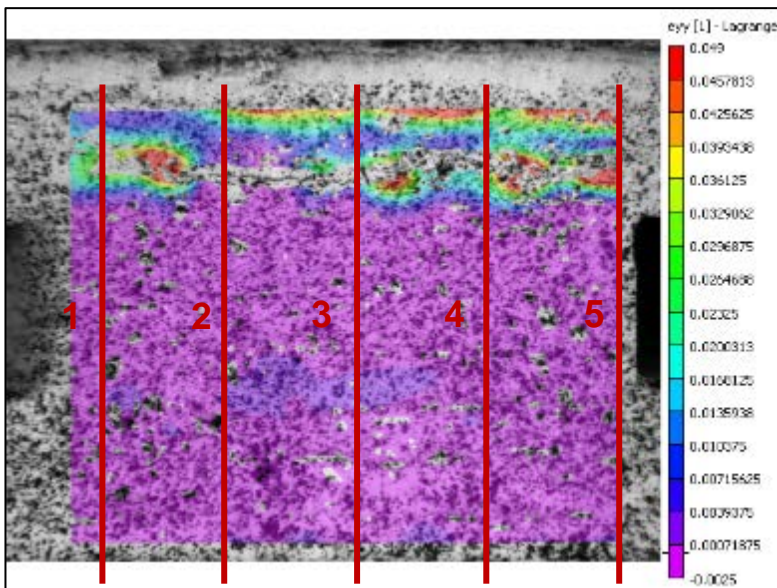


Figure 5: Strain contour map over HTILT sample 7 at stage (image) 289, indicating highest stress locations around crack which formed at the top of the gauge section. Also shows location of virtual extensometer lines in VIC 3D software.

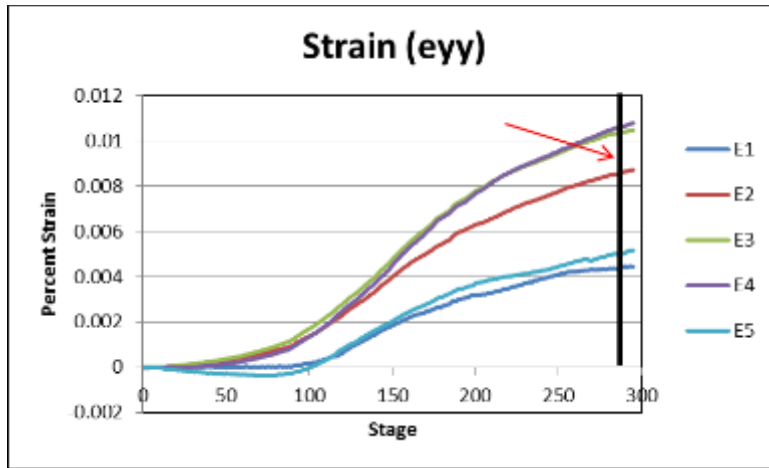


Figure 6: Plot of data extracted from the five virtual extensometer lines at stage 289 in VIC 3D. At this stage, the highest stress was located at the fourth extensometer line.

### Computed Tomography

A post-test CT scan was run on sample 7. The scan validated the crack seen in DIC and also revealed whether it originated on the edge of the sample or within the center of the gauge section (Figure 7).

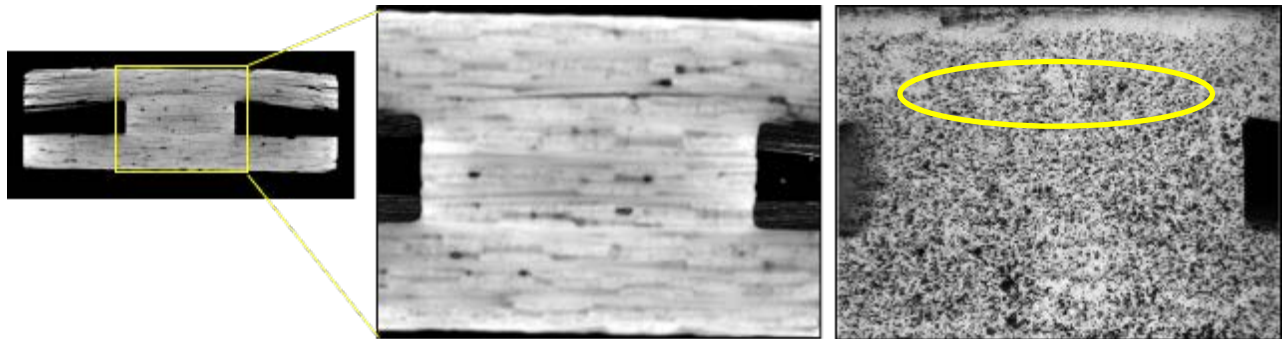


Figure 7: CT image with visible crack originating from edge of sample 7 and DIC image of sample 7 with visible crack.

A pretest CT scan was run on HTILT sample 8. 2D surface images were taken of the sample as well as 3D. It revealed expected pre-existing flaws within the sample (Figure 8) as well as the orientation of the fibers (Figure 9).

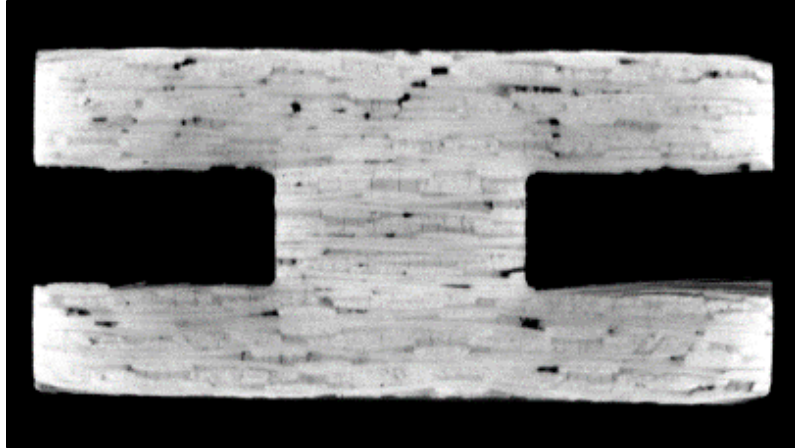


Figure 8: Visible pre-existing defects shown in CT image including porosity of sample and micro-cracks.

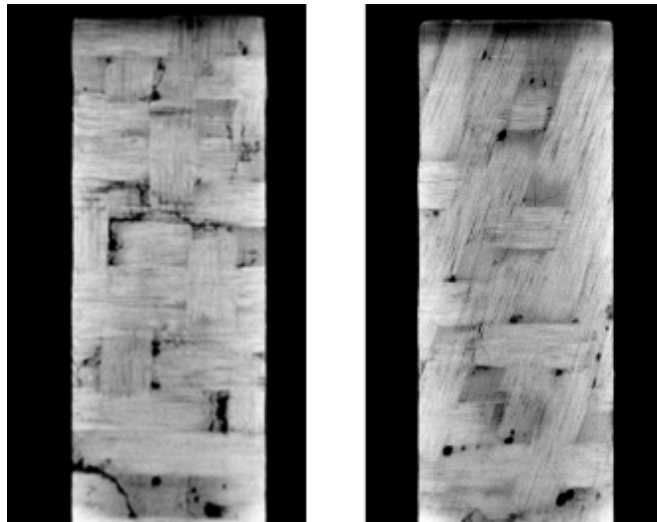


Figure 9: An off axis ply was discovered in CT image.

### *Summary*

The computational model suggests results that have not been able to be duplicated. Defects in sample may dominate its deformation. Although this test method may not be viable, the information gained from the experimentation/characterization is valuable. We also saw that the CT data may provide evidence of failure process.

### *Future Work*

CT will be used to examine HTILT sample 8 after DIC test and to correlate pre-existing defects found with crack initiation during DIC test. 2D continuous load test and 3D constant load tests will be performed on future samples using the fixture machined in Figure 4. Additional DIC tests will also be run on other HTILT samples.

INVESTIGATION OF NONLINEAR OPTICAL MATERIALS

Project No. 0181

Sarah Barnes  
University of Dayton

6 December 2013

Government Project Leader  
Dr. David Zelmon  
AFRL/RXPS

Southwestern Ohio Council for Higher Education  
Student Research Program  
Agreement Number: FA8650-09-2-5800

## **Acknowledgements**

When first investigating opportunities for internships I contacted Dr. Elhamri Said, a professor at the University of Dayton, because he worked at Wright-Patterson Air Force Base part time. I would like to thank him for giving my resume to my POC and helping me obtain a job at the Air Force Base. I would also like to thank Dr. David Zelmon. I cannot thank him enough for this opportunity. It gave me work experience in a professional working laboratory. He taught me about the basics of nonlinear optics. He knew I had no knowledge on this topic, so he gradually introduced me to this material. The tasks Dr. Zelmon gave me had enough responsibility, which encouraged me to learn, but were not overwhelming. Once again I would like to thank Dr. Zelmon for making this a great first internship that will help me in my future as an engineer.

## **General Description of Project**

During this work term the goal was to investigate nonlinear optical materials. The primary task was characterization of optical material to establish their efficiency in lasers and other optical devices. To do so, measurements of refractive index, thermo-optic coefficient, and absorption measurements, need to be taken on various materials. The main focus was on the refractive indexes of different doped materials. The index of refractive is a number that describes how light propagates through different material. For example, if a laser is traveling through air, it produces an initial incident ray at some angle ( $\alpha$ ). If continuing on, the angle would stay linear, but if the laser hits a new substance, for example water, the new ray is produced at a difference angle ( $\alpha_2$ ), which is the refracted ray. Refractive characterization enables the study of non-linear optics. Thermo-optic coefficients are in correlation to the refractive indexes except the material is heated to different temperatures ( $dn/dt$  measurements).

Lastly, "The absorption coefficient determines how far into a material light of a particular wavelength can penetrate before it is absorbed". "In a material with a low absorption coefficient, light is only poorly absorbed, and if the material is thin enough, it will appear transparent to that wavelength" (Honsberg and Bowden). The absorption coefficient depends on the material and also on the wavelength of light, which is being absorbed. After taking these measurements, analysis was done to determine how the material behaves in optical devices.

## **Description of Research**

Prisms were sent with an array of chemicals, doping's, and properties to be analyzed for optical properties (stated above). The core of the worked involved running the Moller-Wedel Divided Circle spectrometer, which measured the average refractive indexes data. Three different setups were used to find refractive indexes in the: Visible light (wavelengths at .380-.700  $\mu\text{m}$ ), Near Infrared (wavelengths at .78-3 $\mu\text{m}$ ), and Low and Mid Infrared (wavelengths at 3-50 $\mu\text{m}$ ) wavelengths. After these measurements some prisms needed thermo-optic coefficients measurements. For this process a small hole, about 1mm wide, need to be drilled into the prism so a thermal couple could be placed inside to measure the temperature and a heating plate was placed underneath to adjust to different temperatures. Then the refractive indexes could be measured. In addition to running the Moller-Wedel Divided Circle spectrometer, another instrument was the Cary 5000 UV-VIS-NIR spectrophotometer a machine that measured the

absorption of the chemical doping on materials. All of these testing took place in a lab based setting. After running the tests graphs would be compiled of the data collected into a computer program called Kaliedagraph. The graphs were used to comprehend analyses on multiple aspects such as, relationships between different refractive indexes versus temperatures ( $dn/dt$  measurements), percentage of doped materials versus their refractive indexes, and the exponential function of refractive indexes in general.

## Results

The knowledge gained about nonlinear optics was an experience builder. In the thermo-optic measurements ( $dn/dt$ ) the refractive index is exponential with respect to wavelength vs. refractive indexes, and the difference between these temperatures is small but noticeable, concluding the refractive index does change with respect to temperature. When testing the refractive indexes with a constant temperature the results depended what the prisms chemical components were. Most prisms tested exponentially decreased as the wavelength increased. In conclusion, the refractive index does change with respect to wavelength.

Being in a research environment was a great learning experience. It became evident that in a lab based setting diligent records and an organized work place is key for experiments to fully run. One key aspect of research learned was that testing the material is relevant, but how one interprets or analyzes data is more relevant. Without good analytical skills the data is meaningless. Running all these data tests also showed that testing is very time consuming and can be very tedious. Most solutions or theories are not developed over night; it takes diligence, time, knowledge, money and effort to produce results.

## Work Cited

Honsberg, Christian A., and Bowden, Stuart. "Absorption Coefficient." *PVEducation*. N.p., n.d. Web. 19 Dec. 2013.

INVESTIGATION OF NONLINEAR OPTICAL MATERIALS

Project No. 0181.1

Emily Erdman  
University of Dayton

31August2014

Government Project Leader  
Dr. David E. Zelmon  
AFRL/RXPS

Southwestern Ohio for Higher Education  
Student Research Program  
Agreement Number: FA8650-09-2-5800

## Acknowledgements

I would like to thank Dr. Said Elhamri from the University of Dayton, who gave my name as a recommendation to my current government supervisor, Dr. David E. Zelmon. I would also like to thank my supervisor Dr. Zelmon for giving me an opportunity to gain valuable experience in the realm of experimental fiber optics.

## General Description of Project

The focus of the work was measuring a critical property of optical materials, called the refractive index measurement. Refractive index measurements lead to several important conclusions about the applicability of different optical materials. The main application for the different optical materials studied was for high-powered lasers. When trying to understand what materials would be best suited to be placed within a high-powered laser, one needs to place an optical material that can withstand high temperatures and not have extreme refractive index variations as the temperature drastically increases. In this way, the work of measuring the refractive index is crucial in determining materials for high-powered laser application.

### Description Of Research

The figure below depicts what occurs as light passes through a prism (Figure 1). An incident ray  $i_1$  enters a prism at an angle with the normal  $N_1$ . The ray  $i_1$ , as it enters the new medium, is refracted. The emergent ray,  $i_2$ , leaves the prism at an angle between itself and the normal  $N_2$ . Using the law of refraction (Snell's Law) and geometry, the equation relating refractive index to the apex angle ( $\alpha$ ) and minimum deviation angle ( $\epsilon_{min}$ ) was determined to be

$$n = \frac{\sin[\frac{1}{2}(\epsilon_{min} + \alpha)]}{\sin(\frac{1}{2}\alpha)} \quad (\text{Born and Wolf, 1999}).$$

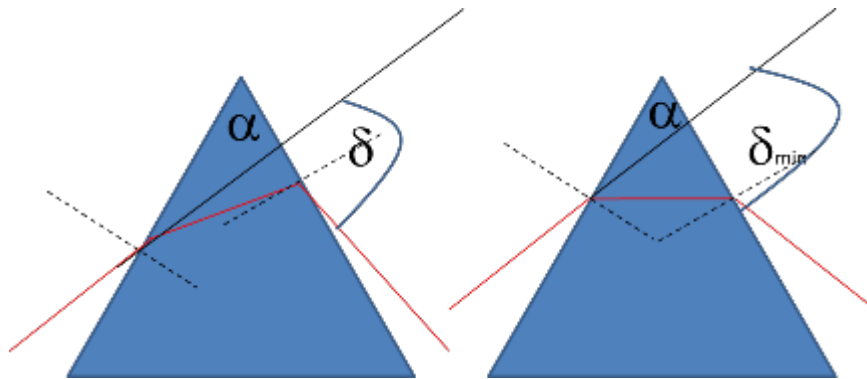


Figure 1. Minimum Deviation Angle of a Prism (Born and Wolf, 1999).

The apex angle is the first measurement taken in order to determine the refractive indices for different optical materials. The apex angle is obtained using an autocollimator which projects an image at the surface of the sample. By measuring the normal position on two sides of the prism, the apex angle can be determined. The Moller-Wedel divided circle spectrometer can measure these angles to plus or minus .001 degrees. After that measurement, light produced by a Mercury Xenon source or an infrared source is coupled into a monochromator with wavelengths ranging from .4046 to 5.2 microns and then transmitted through a small prism consisting of a

sample optical material. The angle of minimum deviation is found by rotating the prism until minimum deviation is reached. Different cameras are used to detect the refracted light depending on the spectral range.

## Results

Phase velocity and consequently refractive index are not constants for a given medium; refractive index varies with the wavelength of light that passes through a material. The variation of refractive index with wavelength is known as *dispersion*. The explicit dependence of the refractive index on frequency was found to be  $\frac{n^2-1}{n^2+2} = \frac{4\pi}{3} N\alpha = \frac{4\pi}{3} N \frac{e^2}{m} \sum_k \frac{f_k}{\omega_k^2 - \omega^2}$  where  $Nf_k$  is the number of electrons corresponding to the resonant frequency.

By approximating  $n \sim 1$  and using the substitution  $\rho_k = N \frac{e^2}{\pi m} f_k$  and  $v = \frac{\omega}{2\pi} = \frac{c}{\lambda}$ , it is possible to rewrite the above equation in the form  $n^2 - 1 = 4\pi N\alpha = \sum_k \frac{\rho_k}{v_k^2 - v^2} = \sum_k \frac{\rho_k}{c^2} \frac{\lambda^2 \lambda_k^2}{\lambda^2 - \lambda_k^2}$ .

Using the identity  $\frac{\lambda^2}{\lambda^2 - \lambda_k^2} = 1 + \frac{\lambda_k^2}{\lambda^2 - \lambda_k^2}$ , the simplified equation relating refractive index to

wavelength is  $n^2 - 1 = a + \sum_k \frac{b_k}{\lambda^2 - \lambda_k^2}$  which is known as Sellmeier's dispersion formula (Born

and Wolf, 1999). After data is obtained by experimenting with the Moller-Wedel divided circle

spectrometer, the refractive indices of the material being analyzed are fitted to Sellmeier's

dispersion formula using a range of different algorithms.

The most recent data collected were refractive indices of potassium titanyl phosphate (KTP), ranging in wavelength from .4046 to 1.4 microns. KTP is used in optical frequency conversion devices such as frequency doubling and optical parametric oscillators. Below is a table depicting the measured refractive indices of KTP for each given wavelength.

Table 1. Refractive Indices of KTP

Wavelength (Microns)	nx	ny	nz (x-cut)	nz (y-cut)**
0.4046	1.82423	1.84077	1.96236	1.96244
0.42001	1.81543	1.83073	1.94788	1.94789
0.43998	1.80591	1.81994	1.93243	1.93249
0.45999	1.798	1.81107	1.91985	1.9199
0.48	1.79141	1.80369	1.90942	1.90946
0.5	1.78575	1.79741	1.90063	1.90066
0.51998	1.78095	1.79198	1.89302	1.89307
0.53999	1.77667	1.7873	1.88657	1.88655
0.56002	1.77291	1.78316	1.88081	1.88081
0.58002	1.7696	1.77956	1.87576	1.87585
0.59999	1.76666	1.77637	1.87141	1.87145
0.61999	1.76402	1.77352	1.86743	1.86747
0.64	1.76164	1.7709	1.86387	1.8639
0.65999	1.75944	1.76851	1.86064	1.86069
0.68	1.75742	1.76636	1.85773	1.85777
0.7	1.75576	1.76451	1.85529	1.85531
0.75001	1.75191	1.76034	1.84962	1.84958
0.8	--	1.75696	--	--
0.85	--	1.75409	--	--
0.90002	1.74384	1.75172	1.83791	1.83787
0.94995	1.74184	1.74962	1.83526	1.83515
0.99999	1.74016	1.74779	1.83274	1.83273
1.05004	1.73856	1.7461	1.83052	1.83054
1.09998	1.73714	1.74458	1.82853	1.82858
1.15001	1.73584	1.74323	1.82674	1.82678
1.20004	1.73466	1.74196	1.82507	1.82515
1.25003	1.73347	1.74074	1.82352	1.8236
1.3	1.73239	1.73958	1.82206	--
1.35004	1.73133	1.73848	1.82065	1.81516
1.40004	1.73035	1.73741	1.81929	1.80831

The Sellmeir equations derived from the refractive indices of Table 1 were determined.

Below, they are displayed in Table 2.

Table 2. Sellmeir Formulas for KTP

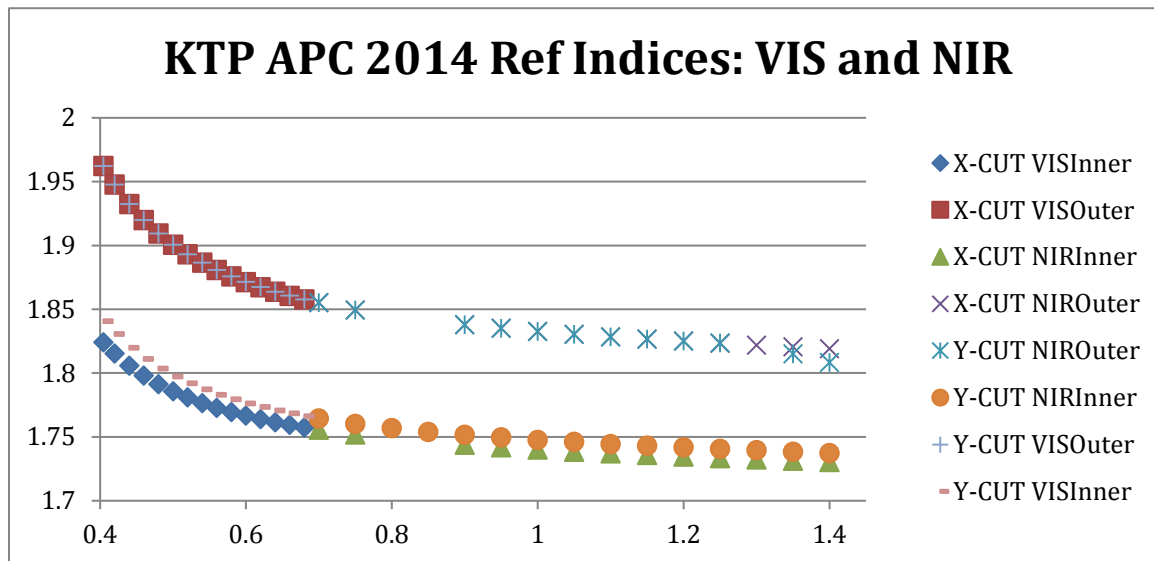
$$n_x^2 = 2.07428 + \frac{0.92623\lambda^2}{\lambda^2 - .20717^2} - .0139\lambda^2$$

$$n_y^2 = 2.13902 + \frac{.88566\lambda^2}{\lambda^2 - .21872^2} - .01442\lambda^2$$

$$n_z^2 = 2.20372 + \frac{1.11109\lambda^2}{\lambda^2 - .23117^2} - .01852\lambda^2$$

A graphical representation of the corresponding refractive indices to different wavelengths of KTP from Table 1 is displayed below in Figure 2.

Figure 2. Graphical Representation of the Refractive Indices of KTP



### Works Cited

Born, M., & Wolf, E. (1999). *Principles of Optics* (7th ed., pp. 95-193). New York, NY: Cambridge University Press.

CHEMICAL/ENVIRONMENTAL ENGINEERING SOCHE STUDENT

Project No. 0182

Matthew Shea  
University of Dayton

5 August 2014

Government Project Leader  
Mr. Wade W. Brower  
AFRL/RXOE

Southwestern Ohio Council for Higher Education  
Student Research Program  
Agreement Number: FA8650-09-2-5800

## **Acknowledgements**

I wish to thank numerous people for my experiences at Wright-Patterson Air Force Base. The first being Wade Brower, for giving me this experience that allowed me to learn and expand my knowledge in areas which I lacked experience in predominantly with hands on experience. I also wish to thank Tyler Rammel, Chris Lawler, Josh Brown, along with the whole Select Tech team for helping me continue with my studies and teach me everything I know.

## **Description of Research**

The Heraldic Device was the main area of research over the work term at Wright-Patterson Air Force Base. The research was created from a project that was given to all of AFRL as a competition to create the next Heraldic Device, which is presented at the Heraldic Dinner, to all the major generals here and off of the base. Once given the chance to create this project many steps were used to create a final project with the research group. The first step was to brainstorm and coming up with various ideas that would or could be incorporated into the final design. The second was the creation of many ideas into Solidworks to make the ideas more of a reality. This was followed by a selection process to narrow down ideas to choose just one. From there building the device was the final step which led to many other issues along the way. However, the results and lessons learned from working on this project will be vastly incorporated into future projects and problems with other engineering positions. The second area of research involved in was research with the Integrated Environmental, Safety Occupational Health or ESOH team. The RX AED program, which includes developing, participating in and documenting quarterly exercises, establishing procedures for training, was the second area of research covered. This was done to create a better understanding of the organizational aspect of engineering and upkeep that is involved in keeping things operational throughout the year. This will always be a program to learn from to use in the future to help promote better organizational skills in future positions in my engineering career.

## **Description of Research**

The amount of research put into the Heraldic Device was immense. It began with brainstorming including the utilization of vast amounts of CAD and Solidworks to come up with a final design submission. Once awarded with the honor of designing and being able to construct the device, the ideas began to change. The first design was simplistic. It began with three bases, wood, aluminum, and carbon fiber, showing the stages that AFRL has made in flight research through materials. Followed by four pillars that all connected to give symbolism of the Air Force monument. Then attached to the pillars held rings holding a dodecahedron with faces of the many important engineers and scientists that have been a part of the Air Force Research Laboratories. However more needed to be done to create a final design, thus a second design was created. In this design the main additions were included. Such as, a famous quote by Henry "Hap" Arnold and instead of four pillars from before the new design now includes only three to completely match that of the Air Force monument. For this project many pieces of large equipment was used. This includes the bandsaw, CNC mill, various saws and drills, CNC lathe, and various amounts of other equipment. Through these types of equipment the data was able to be analyzed to through measuring for exactness so that the assembly would match up to

perfection. Overall there was a lot of work and learning in implementing a final design and or finished project.

## **Results**

This project was able to teach many important lessons that will be needed for future engineering positions. The first lesson was how to completely work through a project from cradle to grave. This taught the importance of using people with different areas of expertise to help teach and enable oneself to learn more about an area in which one may lack experience. The second lesson to learn is that not everything is as easy as it might seem. This project that was once thought of as an easy project turned into being a nightmare at some times, but still through hard work and perseverance the research was able to be accomplished. The final thing that was learned in doing this research is to never give up there is always so way to get through the problems that might be faced. Lastly this project provided a great opportunity to improve as an engineering student and learn from all of the mistakes made in order to create something from the research that was done in order to provide a final product.

MECHANICAL ENGINEERING SOCHE STUDENT

Project No. 0183

Victoria Hutten  
University of Dayton

2 May 2014

Government Project Leader  
Mr. Stephen Reichard  
AFRL/RXOE

Southwestern Ohio Council for Higher Education  
Student Research Program  
Agreement Number: FA8650-09-2-5800

## **Acknowledgements**

I greatly appreciate the opportunity to work for RXOE branch within AFRL. I extend much appreciation to one of my supervisors, Mr. Wade Brower, for teaching me important lessons on management and quality of work. I want to thank Dan O'Brian for helping with the electronic portion of the Heraldic Device, Mary Ann Klos for her work on the dodecahedron pictures, and George, the machinist, for his help as well. I also appreciate the hard work of my team members, Tyler Rammel and Matt Shea, who shared the work load with me. I have learned a lot by working on this trophy and I believe it will help me become a better engineer.

## **General Description of Project**

The Mechanical Engineering SOCHE Student began work on the AFRL Heraldic Device Competition began immediately after hire involving the creation of a SolidWorks model of the design. This was an important step in the design process because it allowed the team to finalize the design of the Heraldic Device before the physical build. After the completion of the 3D model, these drawings helped the team devise a step-by-step build process. This process was annotated with Microsoft Office Project which illustrated a day-to-day flow chart of the tasks necessary to complete the Heraldic Device. Several pieces of equipment were used during the build of the Heraldic Device which included the 600W cutting laser, wood working equipment, CNC mill, and the CNC lathe.

## **Description of Research**

Research involved the use of SolidWorks for the 3-dimensional model, Microsoft Office Project for the plan of action, and back shop equipment for the final build of the Heraldic Device. Equipment used included extensive use of the 600W cutting laser, drill press, CNC mill, wood working equipment, power tools, and a soldering iron for the lighting circuits. The 600W laser was used mainly to create prototypes throughout the design process.

These prototypes were created to provide a physical work-up of the design of the struts before they would be cut on the CNC mill with expensive aluminum. The drill press was used extensively for the application of connecting each part to one another with bolts. Soldering was a new task for the students. This technique was necessary to connect all of the LED lights on a single switch. The CNC mill was used to make the first set of aluminum struts and the three circular bases, including the lettering on the wood base.

## **Results**

Because this project took about a year to complete, it is important to realize that things do not always go as planned. For bigger projects, it is important to be organized from the start. The use of Microsoft Office Project helped to keep tasks organized in a logical order. It was a great resource for tracking specific tasks with an estimated completion date. Another issue was communication. Often, tasks were overlooked because of the lack of communication between different members of the team, such as dividing up the tasks among the group members. This problem was corrected by having weekly meetings and updates on the progress of the Heraldic Device build.

BIOPOLYMER BASED MACH ZEHNDER ELECTRO-OPTIC MODULATORS

Project No. 0184

Emily Fehrman Cory  
University of Dayton

31 March 2014

Government Project Leader  
Dr. James Grote  
AFRL/RXAS

Southwestern Ohio Council for Higher Education  
Student Research Program  
Agreement Number: FA8650-09-2-5800

## Acknowledgements

I would like to thank SOCHE for supporting the completion of my doctoral research in preparation for my dissertation at the University of Dayton Electro-Optics program. I would also like to thank my government project leader, Dr. James Grote, for his support, along with my research advisor, Dr. Emily Heckman and my research group including Dr. Carrie Bartsch, Dr. Fahima Ouchen, Dr. Roberto Aga, Dr. Perry Yaney, and Cpt. Jack Lombardi.

## General Description of Project

The purpose of this research project was to develop a Mach Zehnder modulator as a test bed device to demonstrate the unique optical and electrical properties of the DNA-CTMA biopolymer as a cladding material for poled electro-optic polymers. Toward this goal, a method for applying the nanoimprint lithography (NIL) technique was developed for direct patterning of the deoxyribonucleic acid biopolymer DNA-CTMA. As an intermediate goal towards fabrication of the Mach Zehnder device, a DNA-CTMA clad inverted ridge waveguide was demonstrated at wavelengths of 633 nm and 1550 nm, the structure of which was patterned directly in the DNA-CTMA cladding by NIL. Additionally, electro-optic modulation was demonstrated in a slab waveguide structure with DNA-CTMA cladding and SEO110 electro-optic polymer core. Independent demonstration of optical modulation in a slab waveguide structure, together with waveguiding in an inverted ridge waveguide presents the case for the feasibility of the DNA-CTMA clad Mach Zehnder modulator.

## Description of Research

Since DNA-CTMA is a new material for the NIL patterning technique, a significant effort was spent developing a suitable NIL recipe for patterning inverted ridge waveguide and Mach Zehnder device designs in the DNA-CTMA biopolymer film. The NIL recipe was developed using the Nanonex NX-2600 Air Cushion Press NIL tool. The NX-2600 T-NIL process that was developed for the DNA-CTMA biopolymer involves four steps: 1) the chamber pump down, 2) pre-imprint step, 3) imprint step, and 4) the chamber vent (Figure 56).

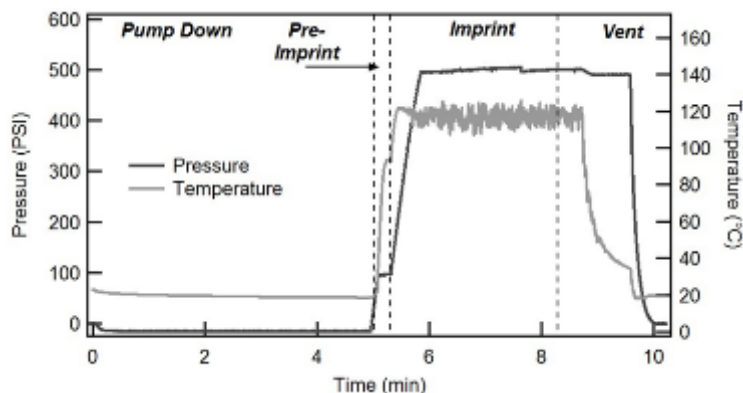


Figure 56. The Nanonex NX-2600 NIL recipe developed for DNA-CTMA biopolymer films.

A combination of SEM imaging, traditional microscopy, and ultimately waveguide performance, was used to characterize the imprinted patterns. A qualitative classification method of *excellent*, *good*, or *poor* was used to describe the NIL pattern quality (Figure 57, Table 10). *Excellent* indicates a 1:1 pattern transfer with straight sidewalls, minimal roughness, and fully developed corners. For *excellent* pattern transfer, the pattern appears to be complete and uniform along the full length of the waveguides (2 – 3 in.). *Good* transfer indicates approximately correct imprint depth but with overly rounded corners and rough sidewalls due to incomplete filling of the stamp pattern. *Poor* indicates that the DNA-CTMA film adhered to the sidewalls or other features of the stamp resulting in tearing of the film.

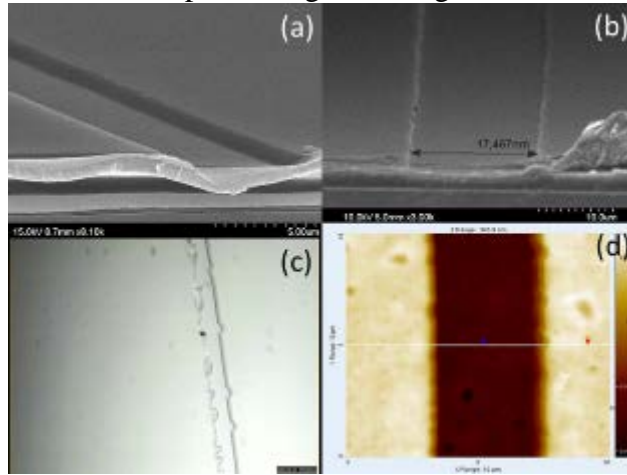


Figure 57. NIL pattern transfer quality for imprinted channels in DNA-CTMA, (a) excellent imprint quality (SEM image), (b) good imprint quality (SEM image), (c) poor imprint quality (microscope), and (d) good imprint quality (AFM image)

Table 10. Qualitative assessment of the NIL pattern quality in a DNA-CTMA biopolymer film.

NIL System	Stamp Material	Release Coating	Substrate	Recipe	Imprint Quality
NX-2600	Si	FDTS	Si/Chrome/Gold	150 °C, 500 psi, 5 min	<i>Good</i>
NX-2600	Si	NXT-130	Si/Chrome/Gold	150 °C, 500 psi, 5 min	<i>Good</i>
NX-2600	Si	FDTS	Si/HMDS	150 °C, 500 psi, 5 min	<i>Good</i>
NX-2600	SiO <sub>2</sub>	NXT-130	Si/Chrome/Gold	120 °C, 500 psi, 3 min	<i>Excellent</i>
NX-2600	SiO <sub>2</sub>	SigmaCote	Si/Chrome/Gold	120 °C, 500 psi, 3 min	<i>Excellent</i>

The NIL patterned DNA-CTMA inverted ridge waveguides were tested by fiber end coupling at the visible (red) wavelength of 633 nm (Figure 58) and at the infrared, telecom wavelength of 1550 nm (Figure 59). This test was done to ensure that the NIL pattern quality was sufficient for waveguiding and as an intermediate step towards the waveguide-based Mach Zehnder modulator device.

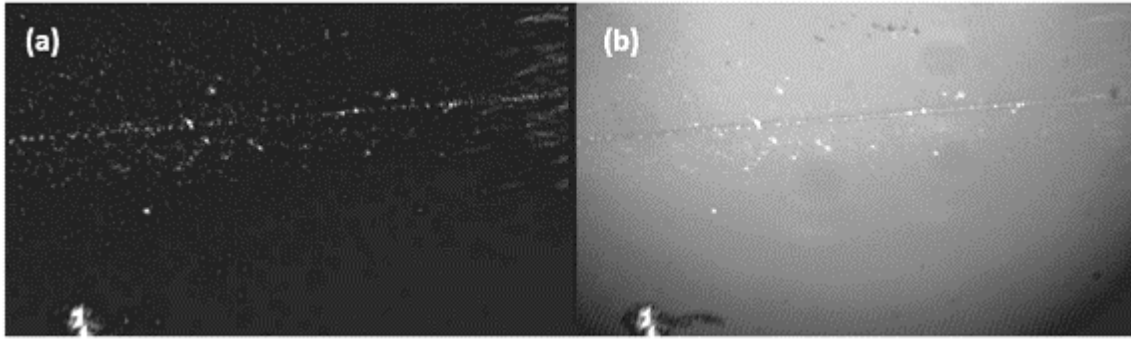


Figure 58. DNA-CTMA ridge waveguide performance at 633 nm. (a) Top down view of light coupled into the DNA-CTMA clad inverted ridge waveguide. (b) Image from (a) superimposed with a microscope image of the NIL patterned inverted ridge waveguide.

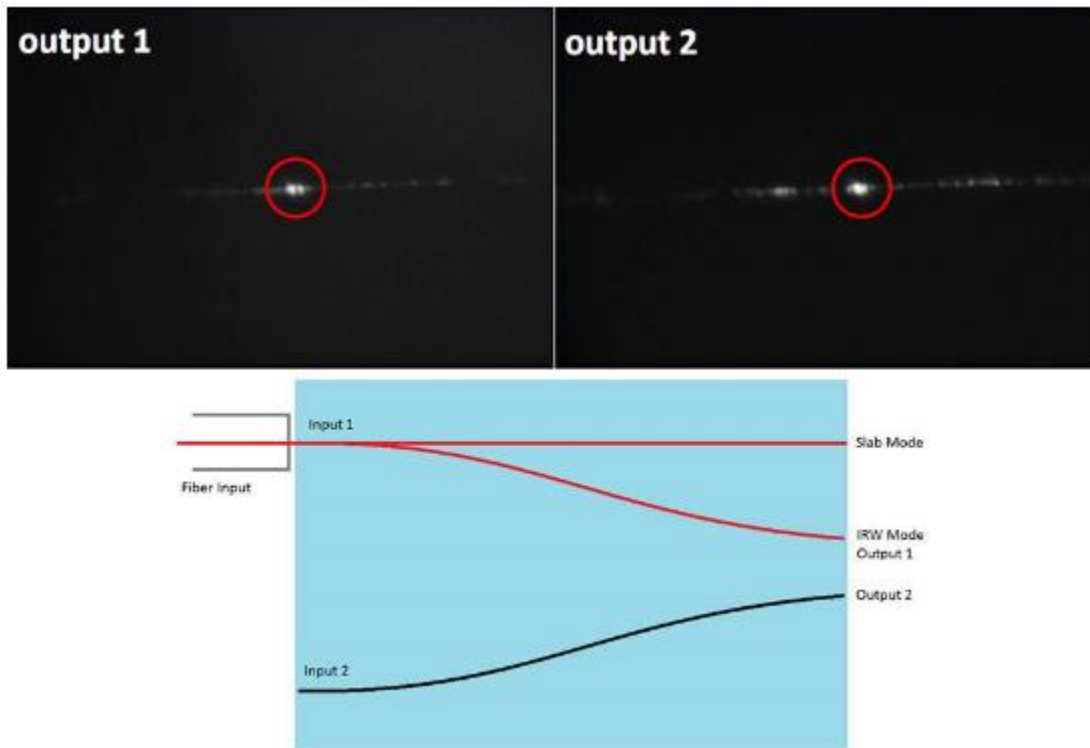


Figure 59. Cross-sectional (end on) view of the inverted ridge waveguide coupled at 1550 nm.

A small section of the Y-splitter of the large dimension MZ modulator was used to test the functioning of the inverted ridge waveguide. The diagram illustrates how the images were collected.

In addition to the NIL patterned ridge waveguides, a slab waveguide device consisting of the same polymer layer structure as the NIL patterned Mach Zehnder device was fabricated to measure the  $r_{33}$  electro-optic coefficient and to show electro-optic modulation in a DNA-CTMA

clad waveguide device. The transverse planar waveguide phase modulator (TPM) was used to measure the electro-optic coefficient in the 3-layer slab waveguide device. The effective electro-optic coefficient for the 3-layer device was measured to be 53 pm/V.

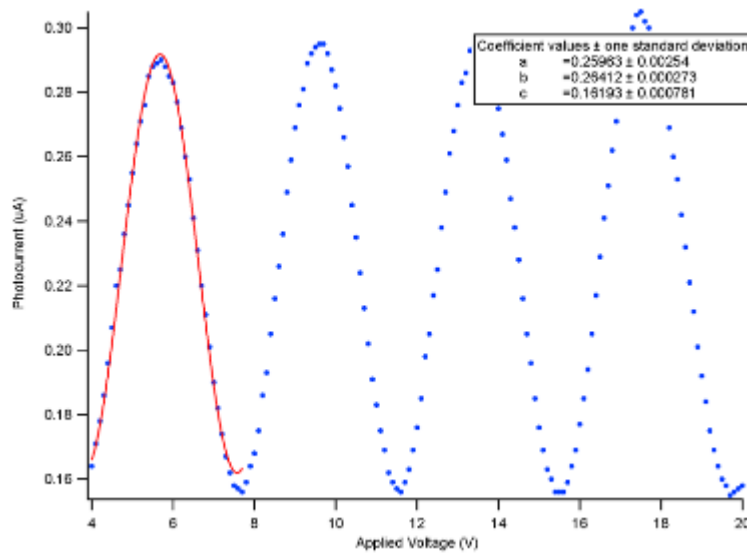


Figure 60. Transverse phase modulation results and curve fitting for the  $r_{33}$  measurement, taken

while increasing the voltage applied and resulting in a measured  $r_{33}= 53$  pm/V.

## Results

The primary contribution of this work was the development of a non-photolithographic; NIL method of patterning the biopolymer DNA-CTMA for use in fully patterned electro-optic devices, such as the Mach Zehnder modulator. This contribution opens the door for not only modulator devices, but a host of other waveguiding devices based on DNA-CTMA. This work has shown that the quality of the NIL pattern in DNA-CTMA is sufficient to function as an inverted ridge waveguide at both 633 nm and 1550 nm. Additionally, DNA-CTMA was used as a successful cladding material for a slab waveguide based modulator in the TPM experiment. While the Mach Zehnder modulator was not realized in this work, the two contributions of waveguiding in a NIL patterned inverted ridge waveguide and optical modulation in a DNA-CTMA clad slab waveguide modulator indicate that future work should be able to produce a functional polymer Mach Zehnder modulator with NIL patterned DNA-CTMA as a cladding material.

### **Works Cited**

Cory, Emily M. Fehrman, et al. "Nanoimprint lithography of deoxyribonucleic acid biopolymer films." *Journal of Micro/Nanolithography, MEMS, and MOEMS* 12.4 (2013): 040501-040501.

### **Related Activities**

Work completed as a part of this research project was published in the Journal of Micro/Nanolithography, MEMS, and MOEMS.

Cory, Emily M. Fehrman, et al. "Nanoimprint lithography of deoxyribonucleic acid biopolymer films." *Journal of Micro/Nanolithography, MEMS, and MOEMS* 12.4 (2013): 040501-040501.

ELECTRONIC CHARACTERIZATION FOR GLASS AND CERAMIC DIELECTRICS

Project 0185

Jessica Hendricks  
Wright State University

31 January 2014

Government Project Leader  
Mr. Charles E. Stutz  
AFRL/RXAN

Southwestern Ohio Council for Higher Education  
Student Research Program  
Agreement Number: FA8650-09-2-5800

## Acknowledgements

I want to thank Mr. Ed Stutz for giving me this opportunity. Dr. Steven Smith was of great assistance for the equipment and software use. And a thanks to Dr. Gregory Kozlowski for introducing me to Mr. Stutz and his work as my advisor.

## General Description of Research

The objective of this project was to make various electronic characterization measurements. The measurements included impedance, capacitance, and the loss tangent. The materials in the project produced on site include pulsed laser deposited materials and glass samples. Penn State University also provided high voltage ceramic capacitors for measurement.

## Description of Research

Impedance and capacitance measurements were made for pulsed laser deposition (PLD) samples, glass samples, and ceramic samples provided by Penn State University. The measurements were made using The Micromanipulator Model Number 6000 for contact with the sample, Solartron 1296 Dielectric Interface, SI 1260 Impedance/Gain-Phase Analyzer, and the SMaRT software. The data was then processed using Microsoft Excel.

The impedance is defined as

$$Z = R + i(\omega L - 1/(\omega C))$$

where R is the resistance, L is the inductance, C is the capacitance,  $\omega$  is the angular frequency, and  $i$  is the imaginary number. The capacitance is defined as

$$C = \epsilon_0 \epsilon_r A/d$$

where  $\epsilon_0$  is the permittivity of free space,  $\epsilon_r$  is the relative permittivity of the material, A is the area of the capacitor plates, and d is the thickness of the material. The capacitance is a complex value because the relative permittivity is a complex value. The relative permittivity is defined as

$$\epsilon_r = \epsilon' + i\epsilon''$$

where  $\epsilon'$  is the real part and  $\epsilon''$  is the imaginary part. Another important measurement in this project was the loss tangent or  $\tan\delta$ .  $\tan\delta$  is defined as

$$\tan\delta = \frac{\epsilon''}{\epsilon'}$$

The  $\tan\delta$  value is expected to be less than one. A high value indicates the material is very lossy, or loses energy. It could also indicate a short circuit in the system.

## Results

The Penn State University ceramics were not able to be measured. The system was not able to produce voltage high enough to test them. The PLD and glass sample results are shown in Figures 1 and 2.

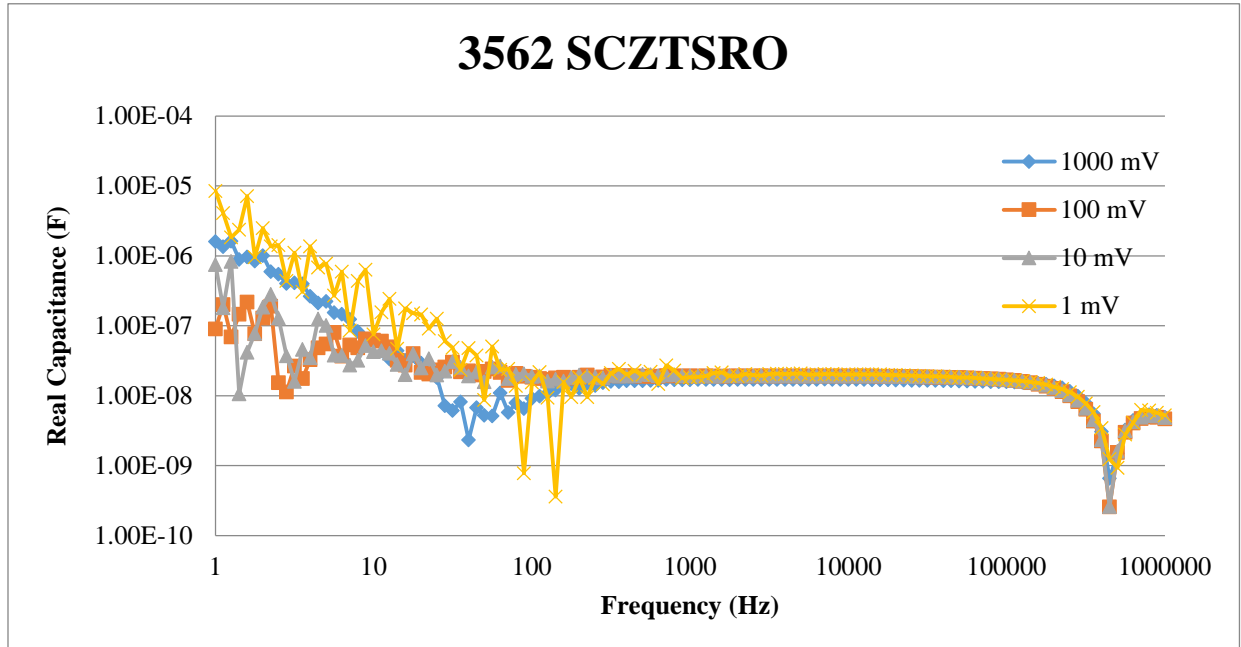


Figure 61. Capacitance vs. Frequency for PLD Sample

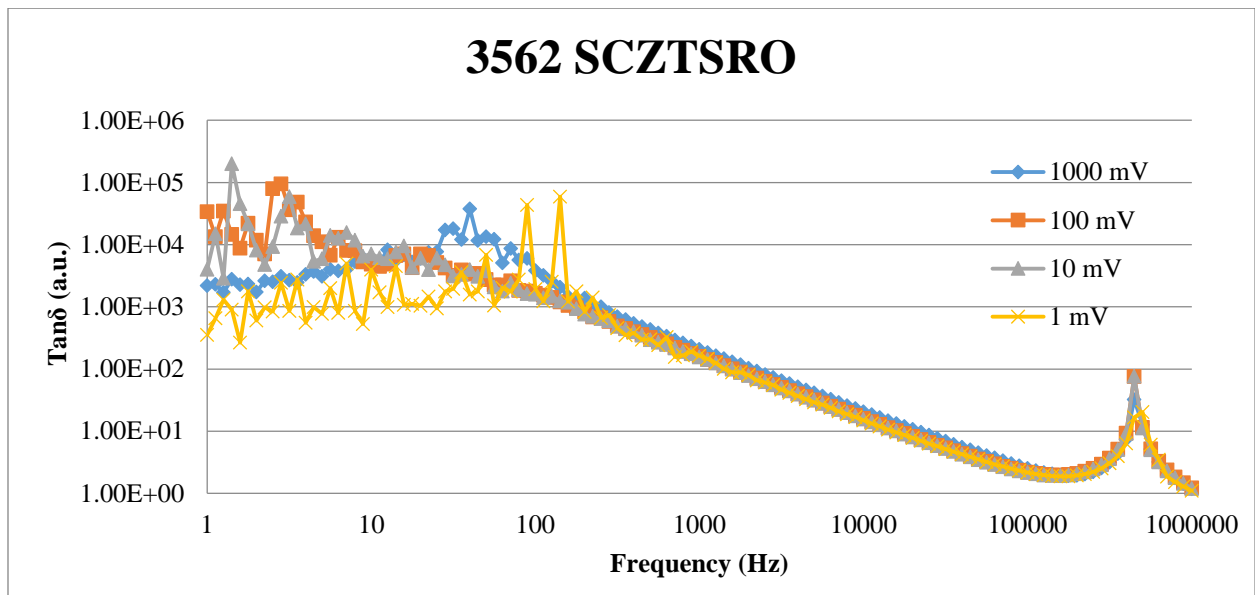
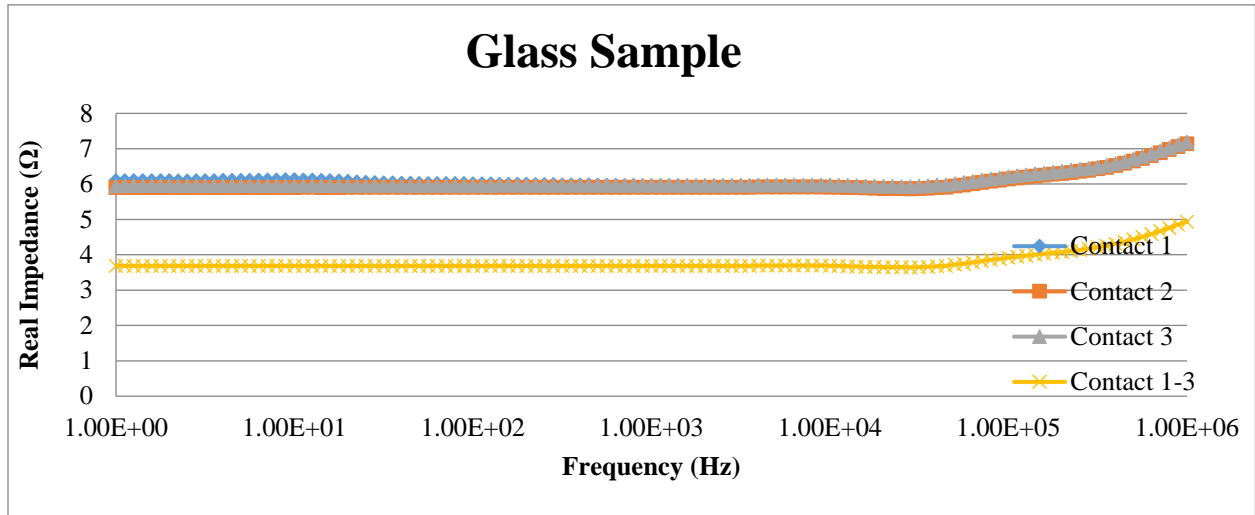
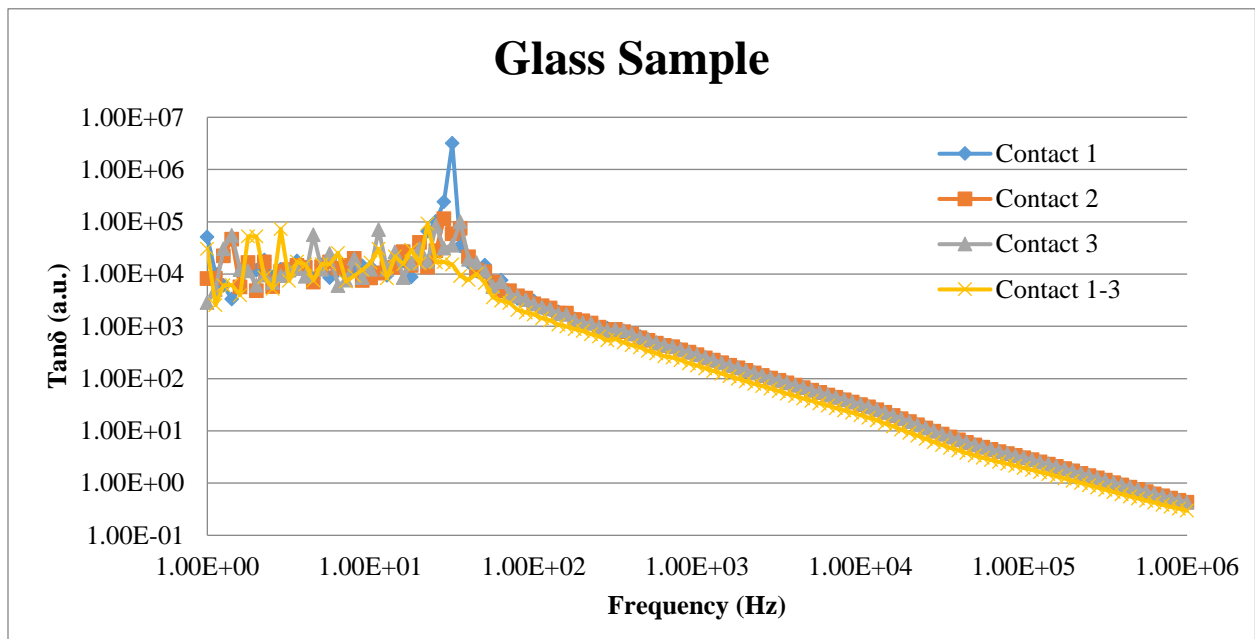


Figure 62. Tan $\delta$  vs. Frequency for PLD Sample

The extremely high values for  $\tan\delta$  indicates there is a short circuit in the system. The data is not reliable. The sample needs to be checked to see if the contacts are connected. The results for the glass sample are displayed in Figures 3 and 4.



**Figure 63. Real Impedance vs. Frequency for Glass Sample**



**Figure 64.  $\tan\delta$  vs. Frequency for Glass Sample**

The results here are similar to the PLD samples. There is an obvious short circuit in the system. The gold contacts deposited on both samples must be making contact with the gold bottom contact.

ELECTRICAL CHARACTERIZATION OF SEMICONDUCTOR MATERIALS

Project No. 0186

Arthur Siwecki  
University of Dayton

31 August 2014

Government Project Leader  
Dr. Shin Mou  
AFRL/RXAN

Southwestern Ohio Council for Higher education  
Student Research Program  
Agreement Number: FA8650-09-2-5800

## Acknowledgments

I would like to thank Dr. Said Elhamri for his guidance and help with this project. I would like to thank Dr. Shin Mou, and Dr. Gail Brown for their guidance as well, and for providing the opportunity for me to help with the research project.

## General Description of Project

This project characterizes semiconductor materials using Hall effect measurements and other forms of electrical measurement. The data is taken at various temperatures and room temperature. The project involves mounting samples in cryostats to take the data, as well as using probe stations. The information gained from these measurements represents electrical characteristics of the samples. This project also involves developing a database in Microsoft Access to allow previous data to be easily accessed and organized.

## Description of Research

The Van der Pauw method was used to characterize the semiconductor materials. In this method a current is forced through the sample and the resulting voltage drop is measured. This is repeated for all sides of the sample and the opposite current (Figure 1). This is used to determine the resistivity of the sample.

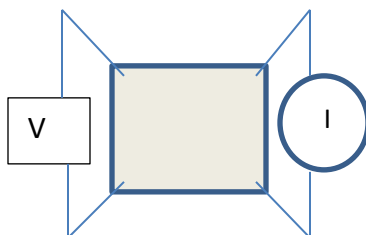


Figure 1. The current is forced through one side of the sample and the voltage drop is measured across the other side of the sample.

The next stage of the process forces a current diagonally through the sample under a magnetic field perpendicular to the sample. This creates a Hall voltage which is measured on the other diagonal of the sample. This process is repeated for both diagonals of the sample under a positive and negative magnetic field (Figure 2). This step of the measurement is used to determine the carrier density of the sample.

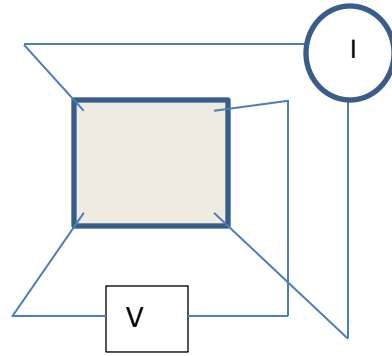


Figure 2. The current is forced across one diagonal under a magnetic field perpendicular to the sample and the resulting Hall voltage is measured across the other diagonal.

Using the resistivity and the carrier density of the sample, the carrier mobility and the carrier type are calculated.

A probe station was also set up to allow for faster measurement of samples. A Microsoft Excel spreadsheet was set up to calculate the values from the data provided by the probe station.

A database was also developed during this project with Microsoft Access and Visual Basic for Applications, a programming language built into Microsoft Access. Forms were designed in Microsoft Access, and the Visual Basic was used to enhance the functionality of the forms to allow the end user to easily search for a desired entry in the database.

### Results

It was determined that Microsoft Access is a suitable platform for developing the database desired for this project. It does have some shortcomings in some areas, but overall it is quite adequate and functional for the intended purposes. Visual Basic for Applications is a language that works very well with Microsoft Access. It allows for the programmer to access almost every aspect of the Microsoft Access database. It also makes accessing data entered via a form in Microsoft Access to be easy to access for use in querying the database. Another use for Visual Basic for Applications is to control different aspects of the form which allow for the form to respond differently for different types of input. Other features of Microsoft Access, such as macros, are also helpful for certain operations that are not complex enough to write a program in Visual Basic for Applications.

The Van der Pauw method was used extensively in this project. How this method works, and how the raw data is used to calculate the values were learned during the course of this project. Also the proper procedures for taking Hall data were learned in addition to the proper procedures to be followed in the laboratory.

INVESTIGATION OF LIQUID CRYSTAL DISPERSIONS AND PHOTSENSITIVE  
SURFACES

Project No. 0187

Aubrey Steele  
University of Dayton

31 August 2014

Government Project Leader  
Dr. Jonathan Vernon  
AFRL/RXAP

Southwestern Ohio Council for Higher Education  
Student Research Program  
Agreement Number: FA8650-09-2-5800

## **Acknowledgements**

I would like to thank Jonathan Vernon for choosing to take me in to work alongside him to achieve his project aspirations. I appreciated his patience for always taking the time to listen to me and explain the topic matter and his expectations. Most of all I thank him for his humor. Another vital person to my project was Timothy White. Without the use of his lab, none of this could have taken place. Many thanks go to Vincent Tondiglia for always stopping what he was doing in order to help me. For his mind and his kindness, I want to thank Kyungmin Lee. For accepting me in the lab and always answering my questions, be it sarcastic or not, I want to thank Taylor Ware, Bradley Worth II, Chad Keister, Andrew Harbach, Mariacristina Rumi, and Michael Mcconney. Lastly, I want to thank my professor and friend Christopher Muratore for pushing me to pursue a job with AFRL and helping me to get a foot in the door.

## **General Description of Project**

The motivation for liquid crystal microparticle production and its reorientation in a moderately conductive fluid host has been studied, tested, and successfully presented to the scientific community (Kosc 96-102 and Trajkovska-Petoska 217-222). One may ask what the need was to continue this area of research. The goal was to repeat the current state-of-the-art experiments already set in place and improve upon such methods and procedures.

The basis of the project reflected the work already done by Anka Trajkovska-Petoska, et al. In one experiment, they tested the reorientation time of polymer cholesteric liquid crystals that were used to produce microparticles from a polydimethylsiloxane (PDMS) mixture in a silicon wafer. In the first trial, the microparticles were rectangular with varying aspect ratios ranging from 1:1 ( $40\mu\text{m} \times 40\mu\text{m} \times 4\mu\text{m}$ ) to 4:1 ( $80\mu\text{m} \times 20\mu\text{m} \times 4\mu\text{m}$ ). They applied an AC electric field at a low frequency due to the ability to study the shape difference in the microparticles as opposed to a higher frequency which caused sub second response times that could not be recorded. Figure 1 shows the  $40\mu\text{m} \times 40\mu\text{m}$  squares completely reorient under the low frequency electric field (Trajkovska-Petoska, 221). They noted the time it took for these microparticles to completely reorient and found that the microparticles with an aspect ratio of 1:1 responded 33% slower than microparticles with an aspect ratio of 4:1 at 100 and 150 Hz proving that the size and surface area of the particle does impact the reorientation time (Trajkovska-Petoska, 221).

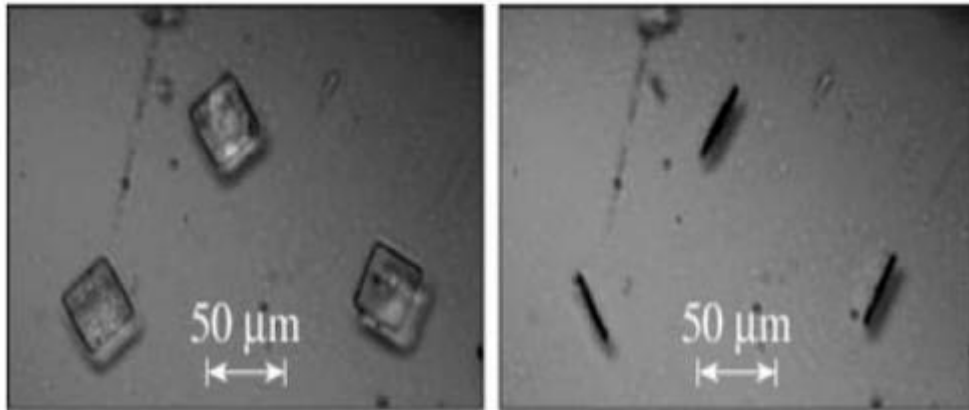


Figure 1. The before and after reorientation of square flakes ( $40\mu\text{m} \times 40\mu\text{m} \times 4\mu\text{m}$ ) under an applied field ( $35\text{mV}/\mu\text{m}$  at  $100\text{Hz}$ ).

In another experiment, Tanya Kosc et al. used commercial polycyclosiloxane ( $520\text{nm}$ ) microparticles ranging in size from  $20\text{-}50\mu\text{m}$  (Kosc, 97). The microparticles were suspended in a moderately conductive fluid host (propylene carbonate) and placed in an electrically conductive cell where an AC field would then be applied (Kosc, 97). Ideally, the microparticles would lie parallel to the substrates and appear green due to the reflective index of the liquid crystal used to make the microparticles. As the electric field was applied at low frequencies, the microparticles reoriented from a parallel to perpendicular position in the cell. He noted that the larger microparticles ( $\sim 35\text{-}50\mu\text{m}$ ) reoriented faster than the smaller microparticles ( $<35\mu\text{m}$ ). Another observation to note was that the relaxation time of the microparticles was measured as minutes as opposed to the seconds it took to reorient (Kosc 98). This experiment correlated with the previous experiment on aspect ratios. Tanya Kosc et al. theorized that the motion of the microparticles was due to the Maxwell-Wagner effect (Kosc, 100-101).

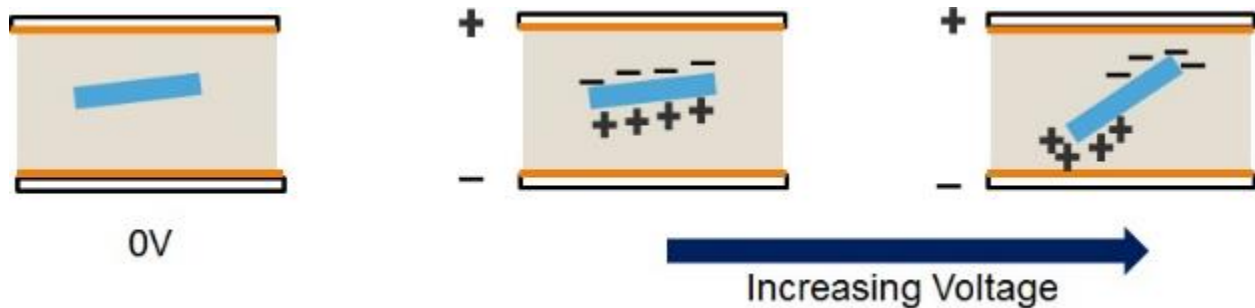


Figure 2: The Maxwell Wagner effect explains that when an electric field is applied to an uncharged particle, a dipole is created. The field exerts a force on the dipole causing the particle to reorient

The Maxwell-Wagner polarization results from the charge accumulation between two interfaces, i.e. host fluid and microparticles, that when an electric field is applied, it causes a dipole on the surface of the uncharged particles. When the current and charge are increased, the electric field exerts a force on the effective dipole, causing the particles to reorient (Kosc 101). Figure 2 is a visual of the Maxwell Wagner effect on an uncharged particle. Tanya Kosc et al. explained that as the microparticle size increased, the dipole would also increase; causing the

microparticle to reorient must faster than the smaller microparticles. This theory could also be applied to the Anka Trajkovska-Petoska, et al. article because the increased size and aspect ratio caused the microparticles to reorient up to 30% faster than the microparticles with a smaller aspect ratio (Trajkovska-Petoska, 221). By using this idea as the baseline, the project was to repeat Tanya Kosc, et al. work and improve upon it by suspending particles of a reduced size into different dielectric liquid crystal hosts, which exhibit various dielectric anisotropies. Monodispersed microparticles with controlled boundary conditions were studied in both liquid crystal and propylene carbonate hosts to evaluate the particles reorientation.

### Description of Research

The first task at hand was to produce smaller microparticle. Figure 4 shows a schematic of the microparticle production. Countless cells were needed in order to start the process of making microparticles. They were made with one piece of glass and one #0 coverslip: both cleaned, coated with elvamide, rubbed, and glued with 5 micron spacers. The empty cells were then filled with an RMM 691 mixture (i.e. 691,E7 liquid crystal, and S811 chiral dopant) that had an initial notch at or above 650 nm. After the filling process, the cells were then photo polymerized under a UV light (~365 nm) for 9-10 seconds at 9% (~11-14000 mW/cm<sup>2</sup>) under a photomask that contained a pattern of several 10µm x 10µm squares approximately 100µm apart as shown in Figure 3. After the polymerization process, the coverslips were then removed from the cell and placed in a vial of hexanes (for 1 hour) that dissolved the monomer film and isolated the newly made microparticles.

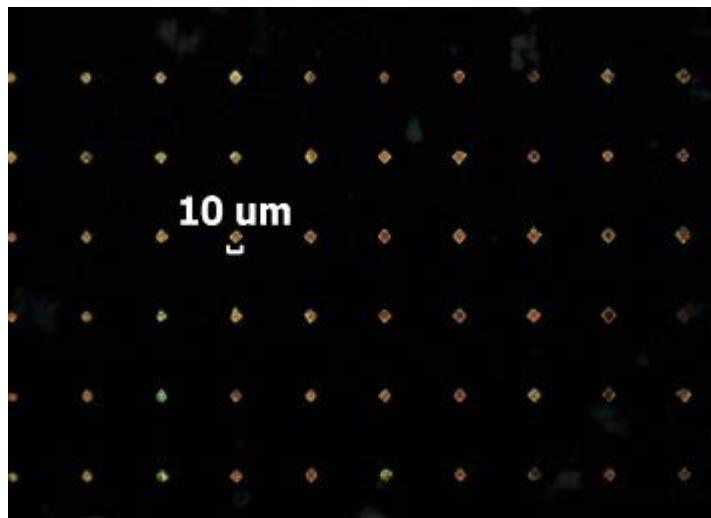


Figure 3: 10 x 10µm squares made with 85-90% RM 691, 5-7% S811, and 5-7% E7. The squares have a nice red color, shape, and size to them.

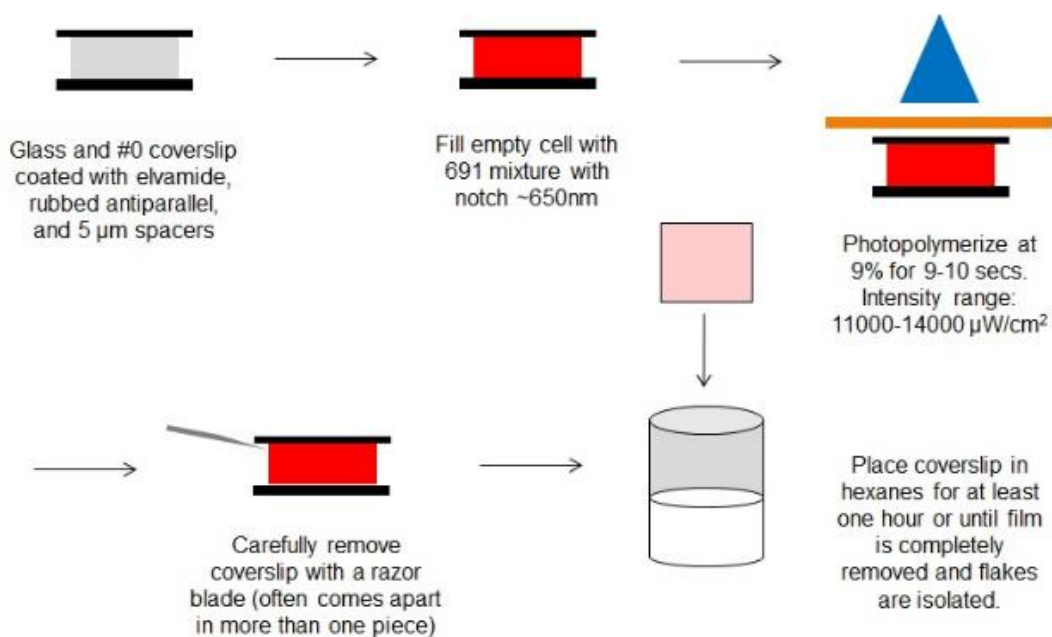


Figure 4: A schematic showing the steps for cell and microparticle production

The next step in the process was to harvest the microparticles. After validating that the coverslips only contained nice red, square shaped, 10 micron microparticles, approximately 8-10 coverslips were placed in another vial containing methanol to dissolve the elvamide alignment layer. Next, the vial was placed in a sonicator that assisted in the microparticle removal process. The vial was checked periodically every hour until the coverslips were clean and the microparticles completely suspended in methanol. The methanol was then driven off and evaporated until a thin layer of the methanol particle mixture remained. That mixture was pipetted into separate tubes and spun down in the centrifuge for 2 minutes at 14,000 rpms. The excess methanol was removed and the microparticle conglomerations were broken up. Clean methanol was added back into the mixture, which was then spun down again at the same setting. This rinsing/washing was repeated three times to successfully clean and rinse the microparticles from unwanted elvamide. After centrifugation, the mixture was pipetted into a weighed vial and set on a hot plate (40°C) that allowed the methanol to completely evaporate. After this process was complete, 70-100  $\mu\text{L}$ s of hexanes were added to the dry microparticles and returned to the hot plate until the hexanes were driven off. Finally, the vial was weighed once more to note the weight of the microparticles and a desired amount of liquid crystal was added. Figure 5 shows a visual of the stages of microparticle harvesting.

## Results

Before using the newly produced microparticles to test the mechanism, Tanya Kosci et al. work had to be duplicated. Chelix commercial microparticles (532 nm), similar to those of used in Marshall's second experiment (20-80  $\mu\text{m}$ ), were suspended in a moderately conductive host fluid (propylene carbonate) and tested in a conductive cell under an applied voltage at low frequencies. Comparable results were noted as the larger microparticles reoriented faster than the smaller microparticles and took minutes to relax when the field was turned off. Figure 6 shows the flakes lying parallel to the substrate then completely reorienting at an applied field and low frequencies under cross polarizers. Since the experiment was successfully duplicated, the next step was to test the same commercial microparticles in a liquid crystal.

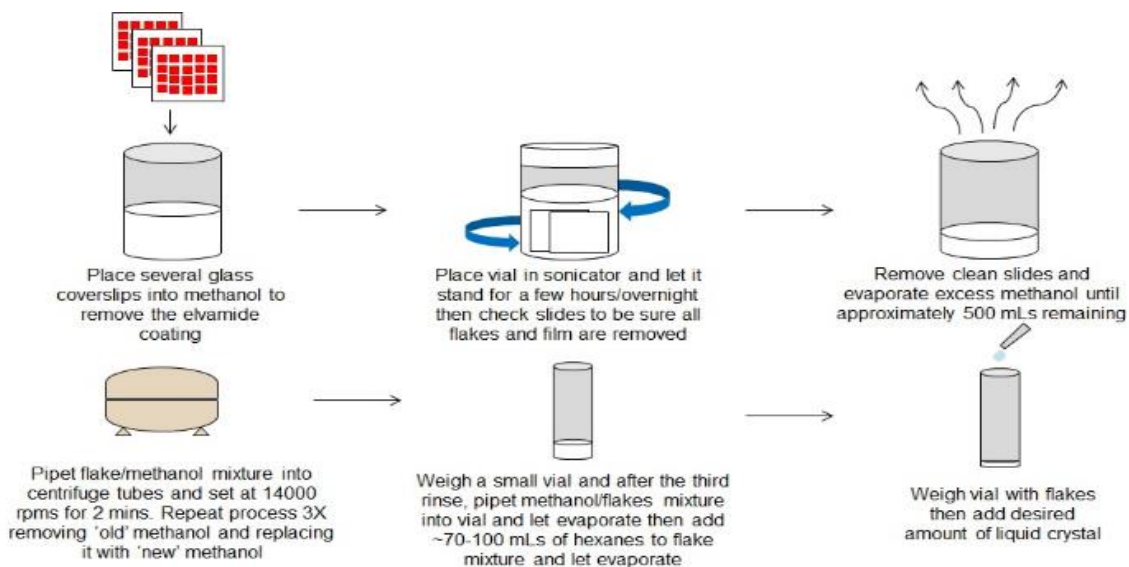


Figure 5: A schematic showing the flow of the harvesting process for the microparticles.

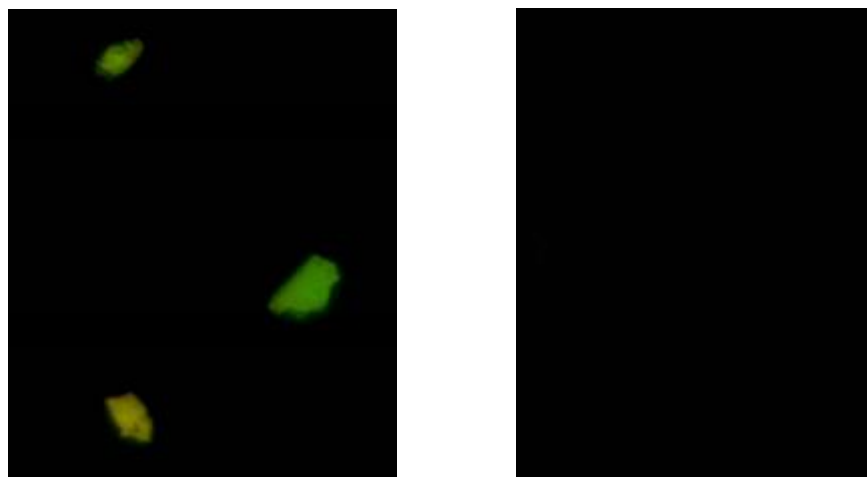


Figure 6: The Chelix commercial green flakes before and after an electric field ( $.23\text{V}/\mu\text{m}$  & 100Hz) is applied. A complete reorientation of the flakes has occurred.

The microparticles were suspended in a positive dielectric liquid crystal (E7) and placed in a planar aligned cell so the microparticles would lie parallel to the substrates. An electric field was applied at low voltages and frequencies and the particles reoriented. The microparticles took seconds to reorient as expected but only a few seconds to completely relax. Because the microparticles reoriented before the Fréedericksz transition (only applicable in dielectric liquid crystals as opposed to the crossover frequency dual frequency liquid crystals) of the liquid crystal, there was evidence to deduce that the Maxwell-Wagner effect was the driving force, but the quick relaxation time was also theorized to have been due to the controlled boundary conditions of the liquid crystal. While keeping these observations in mind, the next step was to test the newly produced 10 x 10  $\mu\text{m}$  microparticles.

The small microparticles were tested both in the propylene carbonate and the E7 host. The microparticles were unable to be seen in the propylene and very hard to find in the E7 due to their small size. Nonetheless, a field was applied to both cells and nothing was seen in the propylene and noticeable changes were seen in the E7. The fine particles found in the E7 were switching with the field, but there was no way to tell if it was just the liquid crystal moving or possible microparticles. After several trials, it was deduced that the microparticles were too hard to find and a new proposition was made to try and make bigger microparticles in order to continue testing the mechanism.

Despite the downfall with the small microparticles, the plan is to continue testing the various hosts to determine the driving force behind the mechanism. Larger microparticles should work for viewing the specific reorientation and relaxation times as noted in the Anka Trajkovska-Petoska, et al. article. The red notch of the microparticles should assist in measuring the spectra notch as the microparticles reorient. There are still many properties of the liquid crystal hosts that can be discovered through this microparticle reorientation. The future work will be to test each liquid crystal host and see how the microparticles react under an applied electric field.

There have been a few notable accomplishments to mention of the research done thus far. The experiment performed by Tanya Kosc et al. was reviewed, copied, and verified. The smallest 10x10  $\mu\text{m}$  microparticles were produced and tested. The commercial flakes were successfully implemented into the propylene carbonate and E7 hosts and reoriented as anticipated. From the commercial flakes, comparisons between the two hosts were formulated to start breaking down the mechanism behind each reorientation. There is still much to study and learn from this project, but each day brings a new discovery.

### Works Cited

- Kosc, Tanya, Ken Marshall, Stephen Jacobs, and John Lambropoulos. "Electric Field Induced Rotation of Polymer Cholesteric Liquid Crystal Flakes: Mechanisms and Applications." *Liquid Crystals VI* 4799 (2002): 96-102. Print.
- Trajkovska-Petoska, Anka, Rupal Varshneya, Tanya Kosc, Kenneth Marshall, and Stephen Jacobs. "Enhanced Electro-Optic Behavior for Shaped Polymer Cholesteric Liquid-Crystal Flakes Made Using Soft Lithography." *Advanced Functional Materials* 15.2 (2005): 217-22. Print.

NANOSCALE SURFACE TOPOGRAPHY CHARACTERIZATION

Project No. 0188

Rachel (Smith) Naguy  
University of Dayton

31 August 2014

Government Project Leader  
Dr. Andrey Voevodin  
AFRL/RXAN

Southwestern Ohio Council for Higher Education  
Student Research Program  
Agreement Number: FA8650-09-2-5800

## **Acknowledgements**

I am thankful for the opportunity I have to work for AFRL/RXAN under Dr. Andrey Voevodin this past year. I have gained useful information on Atomic Force Microscopy as well as the chance to use various different microscopes throughout the complex. In particular, I would like to thank Dr. Michael McConney for his guidance on my project; he has provided much insight on microscopy. In addition, Dr. McConney has shared his interest in working with his students by arranging for me to work on a project that has allowed for a new learning opportunity. Furthermore, I would like to thank the rest of my team members for providing me with new knowledge of this field as well as their continued patience to teach me about numerous materials.

## **General Description of Project**

Nanoscale Surface Topography Characterization involves understanding and learning how to use several different microscopes. The primary method used on these microscopes is Atomic Force Microscopy. In addition to Atomic Force Microscopy, the following methods have been used: Conductive Atomic Force Microscopy and Kelvin Probe Force Microscopy. The aforementioned techniques are used to determine the topography, morphology, adhesion, and electrical properties of the nanomaterials. One specific project was interested in molybdenum disulfide (MoS<sub>2</sub>) growth and whether there was a scalable approach for uniform growth of continuous two-dimensional (2D) transition metal dichalcogenides (TMD) films on substrates >4 cm<sup>2</sup>. One of the approaches used in this project was Atomic Force Microscopy.

## **Description of Research**

The Atomic Force Microscope (AFM) consists of a cantilever with a sharp tip (probe) at its end that is used to scan the material's surface. The cantilever used for this specific project was Silicon Nitride with a tip radius curvature of ~10nm. When the tip is brought into proximity of a sample surface, forces between the tip and sample lead to a deflection of the cantilever. This deflection is measured using a laser spot reflected from the top surface of the cantilever into an array of photodiodes. The movement of the cantilever on the photodiode deflects the laser correspondingly, and this creates an image or produces other data about the surface of the sample. Figure 1 shows a visual image of how the AFM works.

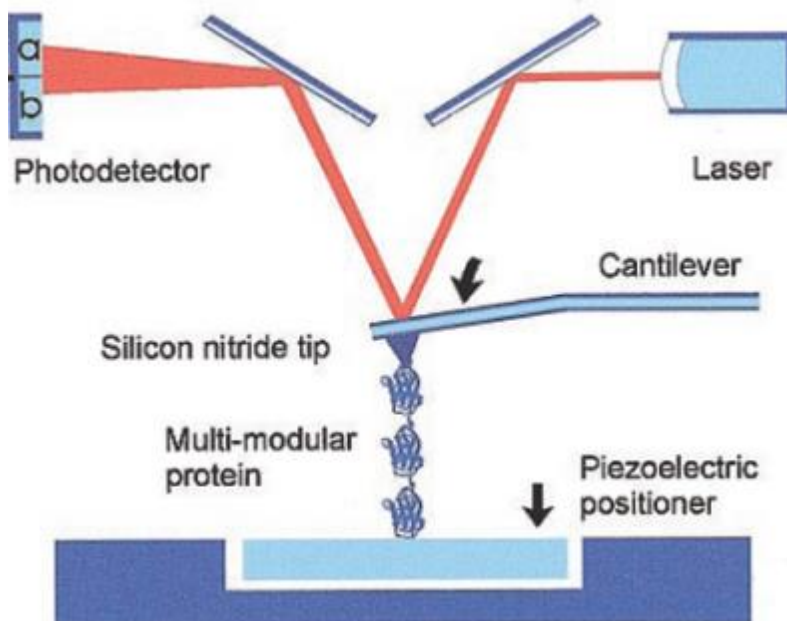


Figure 1. Basic operation of the AFM. As the AFM cantilever probes the surface by moving its tip along its contours, the movement of the cantilever is detected with a laser beam that is focused to the head of the cantilever and refracts into a photodetector (Paul Hansma Research Group).

In this particular project, PeakForce Quantitative Nanomechanical Property Mapping (QNM) mode was used. This mode allows for adhesive data to be collected while simultaneously imaging sample topography at higher resolutions. This technology records force response curves at every pixel in the image. Furthermore, this technique allows for longer probe life and improved sample integrity by using a low setpoint (<20mV) during sample engagement and throughout imaging thereby preserving the tip shape.

The microscope used to run the PeakForce QNM technique is the Bruker MultiMode. This microscope allows for fast, high-resolution mapping of nanomechanical properties. The images in figures 2-6 were gathered from Advanced Surface Microscopy, Inc., 2005.



Figure 2. The MultiMode AFM consists of a Base (B), a Scanner (S), and an optical head (H).



Figure 3. Vertical Engage Scanner. This makes work easier and faster. It is faster and more secure to adjust for differences in sample thickness. With a top view optical microscope, it can target a specific area and engage the probe tip at that spot.

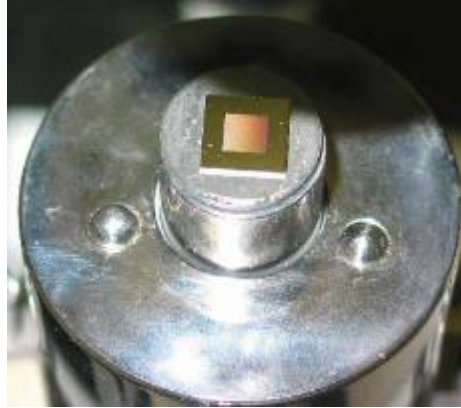


Figure 4. Sample on Vertical Engage Scanner. The sample is 8x8mm on a 15mm diameter steel disk.



Figure 5. MultiMode AFM with sample in place, ready to scan.

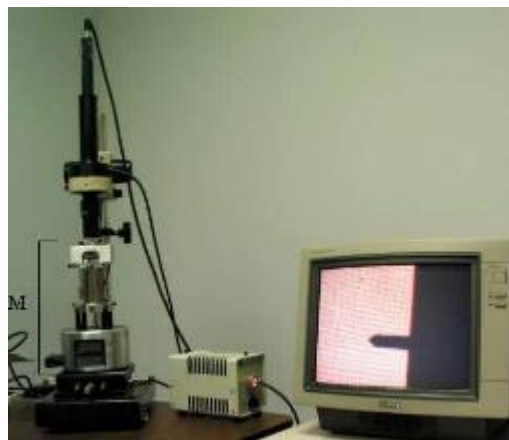


Figure 6. Full view of MultiMode setup. The magnification on the optical lens is approximately 450x.

## Results

The results show that the MoS<sub>2</sub> films on silicon oxide (SiO<sub>2</sub>) yielded layer by layer growth without island formation in Atomic Force Microscopy. The MoS<sub>2</sub> film was made with magnetron sputtering at a high temperature of 350°C using MoS<sub>2</sub> as a target. The RMS roughness of the MoS<sub>2</sub> film was approximately 0.58 nm compared to 0.26 nm of the SiO<sub>2</sub> substrate. Figure 7 shows that the film has nanocrystalline domains, as opposed to MoS<sub>2</sub> samples made with chemical vapor deposition (CVD). The films made via CVD have micro-scale domains (see Figure 8). This magnetron growth process is a scalable approach that enables uniform growth of nanocrystalline continuous 2D transition metal dichalcogenides films on large substrates (cm scale).

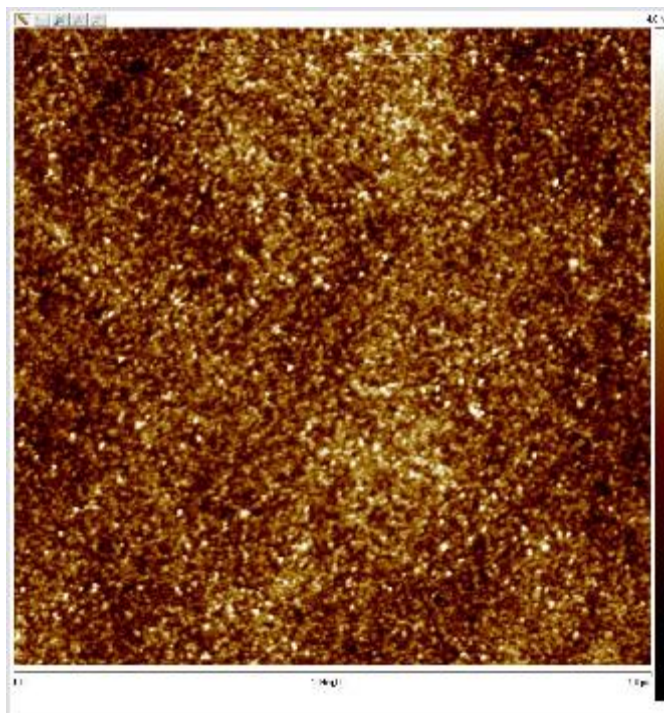


Figure 7. AFM scan of 3 layer MoS<sub>2</sub> on SiO<sub>2</sub> substrate grown with Magnetron Sputtering (Muratore *et al*, 2014).

A high resolution AFM image is presented in Figure 8 of CVD grown MoS<sub>2</sub>. The CVD process involves using a precursor film exposed to high temperatures and introduction of a reactive gas to the chamber. In this case, sulfur gas is introduced to the molybdenum trioxide (MoO<sub>3</sub>) which was used as a precursor film and heated to 750°C. The RMS roughness of the MoS<sub>2</sub> grown on MoO<sub>3</sub> is 5.44nm compared to 0.3nm of the Sapphire substrate. As can be seen in the AFM image, the MoS<sub>2</sub> crystals are quite large compared with the magnetron sputtered MoS<sub>2</sub>, but are not continuous and pin-hole free. CVD and magnetron sputtering offer different material properties and thus they complement each other. These two techniques can also be used to create other 2D TMD's such as tungsten diselenide (WSe<sub>2</sub>).

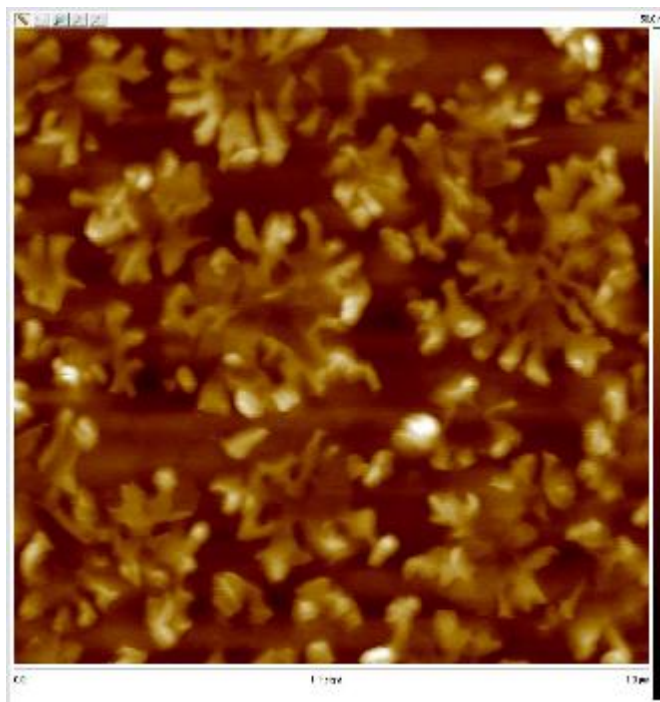


Figure 8. AFM scan of MoS<sub>2</sub> grown on a sapphire substrate via CVD.

Figure 9 shows a high resolution AFM image of a WSe<sub>2</sub> film on SiO<sub>2</sub> grown with magnetron sputtering. As one can see, this film also grows via layer by layer growth as opposed to island growth. The RMS roughness of the WSe<sub>2</sub> film deposited onto SiO<sub>2</sub> substrate taken from a 1 x 1 μm<sup>2</sup> image was 2.53nm. This serves as a demonstration that the growth techniques developed in the lab can be applied to other materials.

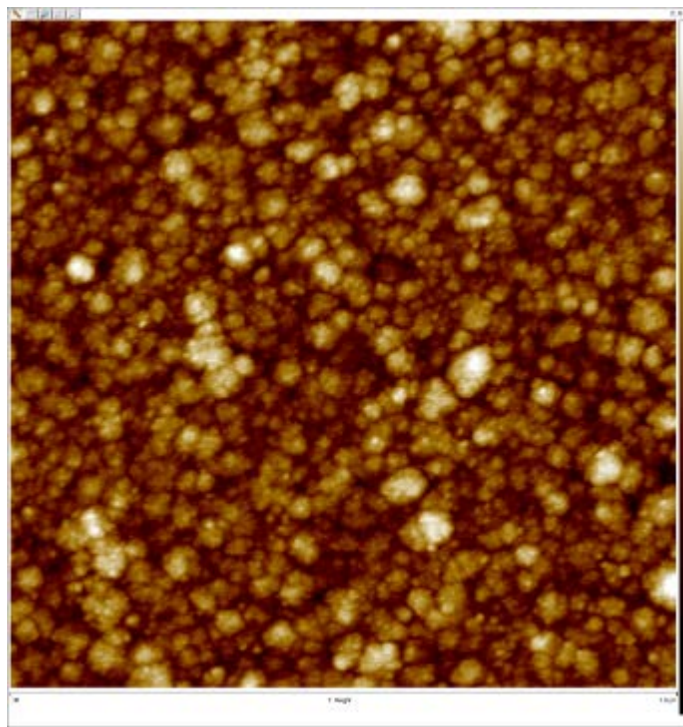


Figure 9. AFM scan of WSe<sub>2</sub> on SiO<sub>2</sub> substrate grown with Magnetron Sputtering.

In conclusion, in this project, thin film deposition was studied alongside materials scientists and characterization of their films were analyzed through the use of an Atomic Force Microscope. This allowed for characterization of the roughness and approximate domain size of the resulting films, which then provided the materials scientists with important feedback regarding the growth of their films. In addition, advanced electrical-based scanning probe microscopy techniques such as Kelvin Probe Force Microscopy (KPFM) and Conductive Atomic Force Microscopy (C-AFM) were utilized.

#### **Works Cited**

- "Advanced Surface Microscopy, Inc. - AFM page." N.p., 2005. Web.  
<<http://www.asmicro.com/equipment/multimodeafm.htm>>.
- Muratore, Chris, et al. "Continuous ultra-thin MoS<sub>2</sub> films grown by low-temperature physical vapor deposition," *Applied Physics Letters* 104 (2014): 1-6.
- "Paul Hansma's Website." *Paul Hansma's Website*. N.p., n.d. Web. 11 Aug. 2014.

#### **Related Activities**

My Atomic Force Microscopy images were used for the publication of the journal article detailing the project mentioned in this report: Muratore, Chris, et al. "Continuous ultra-thin MoS<sub>2</sub> films grown by low-temperature physical vapor deposition," *Applied Physics Letters* 104 (2014): 1-6.

2D THIN FILM GROWTH AND CHARACTERIZATION

Project No. 0189

Randall Stevenson  
University of Dayton

31 August 2014

Government Project Leader  
Dr. Andrey Voevodin  
AFRL/RXAN

Southwestern Ohio Council for Higher  
Education  
Student Research Program  
Agreement Number: FA8650-09-2-5800

## Acknowledgements

I would like to this opportunity to express my gratitude to SOCHE and the Research Facilities at the Wright-Patterson Air Force Base Air Force Research Lab for the opportunity to conduct my research. Specifically, I would like to thank Dr. Andrey Voevodin for providing a research project, laboratory space, and research guidance; I would like thank Dr. Christopher Muratore for the endorsement as my faculty advisor and for the leadership, guidance, and technical experience that he brings to the project; I would like to thank Mr. John Bultman for taking the time to train me on the instrumentation that is necessary to conduct this research; I would like to thank Mr. Art Saffriet for sharing his technical and design experience regarding precision machining and design fabrication; I would like to thank Dr. Michael Check for our discussions regarding theory and practical application of 2D materials in the development of nanoelectronics. I am sure that I have missed several individuals, but rest assured that I am eternally grateful for your assistance and/or guidance during my time the Wright Patterson Air Force Base Air Force Research Lab.

## General Description of Project

Molybdenum disulfide is a transition metal dichalcogenide (TMD) material, and is used commercially in bulk or thin film form as a solid-state lubricant and catalyst for hydrodesulfurization.<sup>2</sup> Recently, it was discovered that monolayer molybdenum disulfide, a 2D crystal with a direct bandgap<sup>3</sup> of approximately 2 eV, is a promising candidate for 2D nanoelectronic devices<sup>4</sup>. Together with conductive graphene and insulating hexagonal boron nitride (h-BN), molecularly-thin, semiconducting molybdenum disulfide rounds out the selection of 2D device building components.

Fundamental understanding of large area growth mechanisms and precise implementation of those mechanisms present the most critical step for any type of viable 2D technology. Mechanical exfoliation, or repeated shearing of layers of a bulk crystal,<sup>5,6</sup> produces nano to micro scale flakes suitable for laboratory research. The same is true for chemical exfoliation, where lithium ion intercalation followed by sonication is used to separate individual layers of van der Waals solids via generation of hydrogen gas<sup>7</sup>. Direct monolayer generation by sonication without intercalation has also been demonstrated<sup>8,9</sup> to produce nano-micro flakes. Such wet processes produce flakes that are useful for making composites<sup>10</sup> but they lack reproducibility with respect to uniformity and thickness of atomic layers as needed for device applications. Additionally, severe deformation of the layered atomic structure of TMD materials can occur from the intercalation process<sup>9,11</sup>, adversely affecting materials properties, and requiring high temperature annealing to restore the structure and physical/electrical properties to the underlying material. Hybrid chemical synthesis via anodic bonding followed by mechanical exfoliation is another technique used to develop 2D TMD materials. However, this approach has similar weaknesses as those associated with conventional mechanical exfoliation.<sup>12</sup>

The current, large-scale alternative to exfoliation is chemical vapor deposition (CVD). Growth of ultra-thin TMD films by dichalcogenization of oxidized transition metal layers was first described in 2005<sup>13</sup>, and later employed by others<sup>13</sup>. Direct growth from vapor phase precursors have also been reported. These CVD processes are at first glance capable of large area 2D TMD production, however, the films are discontinuous and comprised of isolated

islands on the order of 10 microns. In addition to poor thickness uniformity over large areas, the processing temperatures are exceedingly high, at over 700° C. Similarly, thermolysis processes of samples dip-coated in liquid precursors, require temperatures of up to 1000° C.<sup>13</sup> Lower processing temperatures have been reported for some CVD processes occurring directly from precursor decomposition, but those precursors present severe environmental health and safety issues and the absence of both continuity and lateral coherence remains.

This project builds upon these ideas by employing magnetron sputtering and pulsed laser deposition to produce two dimensional (2D) thin film materials of semiconducting transition metal dichalcogenides (TMD) and insulating metal oxides. The work involves the preparation and installation of samples in a thin film growth chamber and then coordinating a specific set of variables to produce a quality 2D material on a given substrate. The 2D materials are characterized using Raman Spectroscopy and X-ray Photoelectron Spectroscopy (XPS). In addition, X-Ray Diffraction (XRD), Atomic Force Microscopy (AFM), Scanning Electron Microscope (SEM), Transmission Electron Microscopy (TEM), various electrical probe measurements were used when deemed useful or appropriate. This information is used to determine the conductivity, morphology, chemical composition, thickness, and continuity of the 2D films.

## **Description of Research**

A novel, Ultra High Vacuum (UHV) synthesis technique for high quality, uniform 2D TMD materials over large areas at low temperatures (>350 °C) has been developed jointly between the University of Dayton and the Air Force Research Laboratory. This approach enables control of atomic structure and composition of monolithic layers of 2D materials without the need for breaking vacuum. This process eliminates the need to transfer samples in open air between depositions and reduces the likelihood of sample oxidation.

The 2D films are grown inside an UHV system using non-equilibrium physical vapor deposition (PVD) procedures previously established by the UD/AFRL coalition. The PVD synthesis process is based on magnetron sputtering and allows for growth of very thin (3-6 molecular layer) TMD films over very large layers. The 2D film growth is performed in an UHV environment to minimize surface and interface contamination.<sup>1</sup> The materials are grown on amorphous SiO<sub>2</sub>, Highly Ordered Pyrolytic Graphite (HOPG), Willow Glass ©, Sapphire, and other substrates as they become available.

All films were grown using magnetron sputtering using a solid 3.3 cm diameter TMD target of ultra high purity (>99.9% purity). All substrates, except for HOPG, are ultrasonically cleaned using a series of solvents and then rinsed with deionized water. HOPG samples were mechanically cleaved with tape immediately before placement in the UHV system to minimize contamination. The substrates were introduced into the UHV system through an attached vacuum load lock and mounted on an electrically grounded, heatable, and rotatable deposition stage. The samples were heated to 500-700 °C and allowed to rotate at approximately 100 rotations per minute while positioned 7 cm from the TMD target. Throughout the process, the temperature was measured with an IR pyrometer calibrated with a thermocouple for each substrate material. The chamber was then filled with ultra-high purity argon gas at a constant flow rate of 25 sccm to a pressure of 15 mTorr (2 Pa). Films were grown layer by layer over incrementally longer time

intervals at a constant rate of approximately 0.15 nm per second in order to prepare a 2D film with the desired thickness.<sup>1</sup>

Raman spectroscopy was then employed to characterize  $E_{2g}^1$  (in-plane vibrations) and  $A_{1g}$  (out-of-plane vibrations) peaks indicating atomic ordering of the TMD. See figure 1. A calibration curve relating  $A_{1g}$  and  $E_{2g}^1$  peak separations to the number of layers was developed by comparing the Raman spectra to the TEM for the cross sections of several samples grown at different time intervals of a TMD deposited on  $SiO_2$  to correlate the thickness and precisely identify the number of molecular layers.<sup>1</sup> See figure 2. The calibration curves obtained from this data was used to effectively identify the thickness and number of molecular layers for every 2D film produced thereafter.

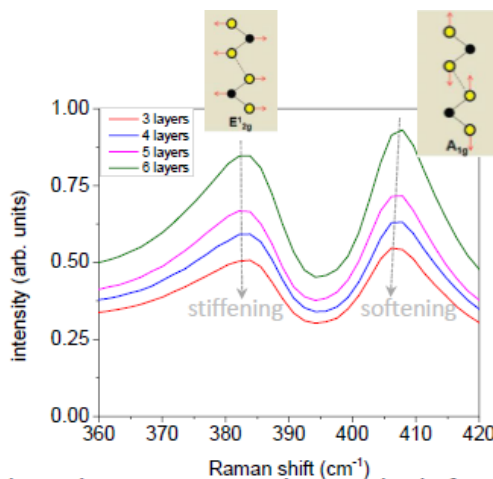


Figure 1. The frequency shift between in-plane and out-of-plane Raman peaks is correlated to the number of layers (Muratore 2014).

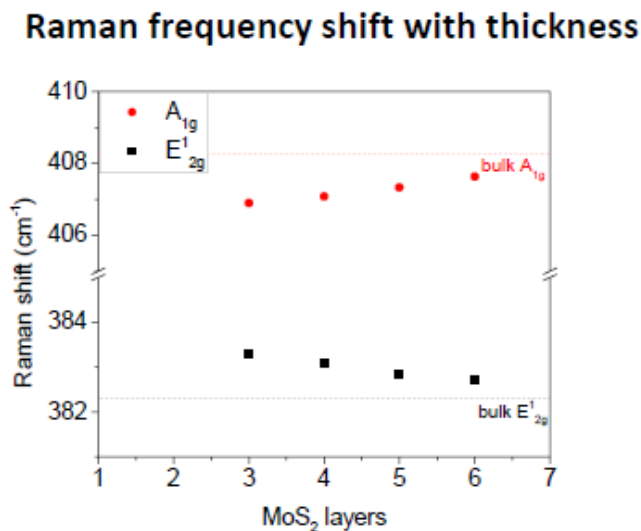


Figure 2. Correlation of the number layers relative to the observed Raman Shift (Muratore 2014).

Film-substrate interface chemistry was examined with X-ray photoelectron spectroscopy (XPS) on these 2D films. The XPS was performed *In vacuo* before the substrates could be exposed to the atmospheric conditions to insure that the surface would not be contaminated with carbon or oxidized by ambient Oxygen. The analysis of the film by XPS allowed for the quantification of the chemical composition of the 2D film to insure that the films were stoichiometrically correct. The XPS analysis was also used to determine the number and type of charged chemical species that were present in the film to help determine the reaction dynamics of the 2D film growth. See figure 3.

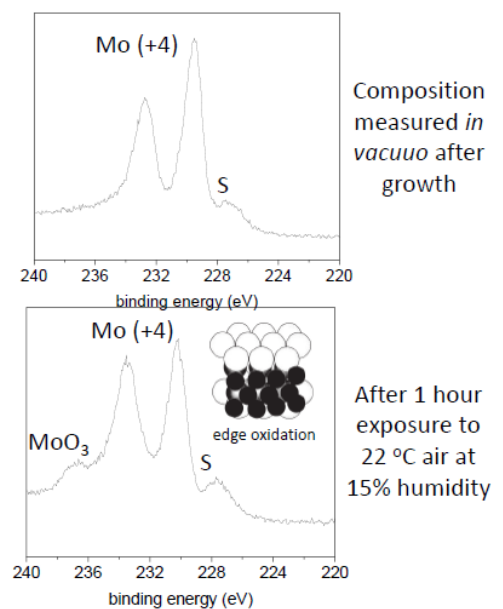


Figure 3. Typical XPS data for MoS<sub>2</sub> 2D film taken *in vacuo* (top) and 1 hour after exposure to ambient air (Muratore 2014).

In summary, the research centered on the production and characterization of multiple TMD 2D thin films by PVD growth. Ultimately, the 2D films produced as a result of this research move down stream to other researchers who are interested in exploring various applications for these 2D films (e.g field effect transistors, diodes, etc.).

## Results

The results from this study indicate that 2D TMD may be used as a substitute for graphene in the future of nanoelectronic devices. Using the procedure outlined above, it is possible to grow 2D films of uniform thickness over a relatively large area (at least 1” in diameter) on a variety of substrates. It is also possible to control the thickness of the films by adjusting the duration of the deposition on to the substrate. This information is useful because it allows research to be conducted on different nanoelectronic devices and the initiation of a study into the development of various TMD heterostructures. Additionally, the continuous nature of the 2D films grown

during this study is of great importance due to their intended use in nanoelectronic devices. The film must be continuous across the surface of the film to allow electron mobility and to reduce shorting of the underlying electronic device.

In summary, a scalable approach for uniform growth of 2D TMD films of a variety of substrates has been demonstrated. The PVD process allows for growth of 2D TMD in a predictable and reproducible manner. The materials produced by this method demonstrate the same mechanical properties as the materials exfoliated from the bulk material.

### Works Cited

- 1 Muratore, Christopher, et al. "Continuous ultra-thin MoS<sub>2</sub> films grown by low-temperature physical vapor deposition." *Applied Physics Letters* 104: 261604 (2014).
- 2 W.E.Jamison & Cosgrove, S. L." Friction characteristics of transition metal disulfides and diselenides." *ASLE Transactions* 14, 62-72 (1971).
- 3 Chianelli, R. R. *et al.* "Catalytic properties of single layers of transition metal sulfide catalytic materials." *Catalysis Reviews: Science and Engineering* 48, 1-41 (2006).
- 4 Mak, K. F., Lee, C., Hone, J., Shan, J. & Heinz, T. F. "Atomically Thin MoS<sub>2</sub>: A New Direct Gap Semiconductor." *Physical Review Letters* 105, 136805-136801 to 136805-136804 (2010).
- 5 Yoon, Y. "How Good Can Monolayer MoS<sub>2</sub> Transistors Be?" *Nano Letters* 11, 3768-3773 (2011).
- 6 Lee, C. *et al.* "Anomalous lattice vibrations of single- and few- layer MoS<sub>2</sub>." *ACS Nano* 4, 2695-2700 (2010).
- 7 Novoselov, K. S. *et al.* "Two-dimensional atomic crystals." *Proceedings of the National Academy of Sciences* 102, 10453-10456 (2005).
- 8 Huang, X., Zeng, Z. & Zhang, H. "Metal dichalcogenide nanosheets: preparation, properties and applications." *Chemical Society Reviews* 42, 1934-1946 (2013).
- 9 Sandoval, S. J., Yang, D., Frindt, R. F. & Irwin, J. C. "Raman study and lattice dynamics of single molecular layers of MoS<sub>2</sub>." *Physical Review B* 44, 3955-3962 (1991).
- 10 Gacem, K., Boukhicha, M., Chen, Z. & Shukla, A. "High quality 2D crystals made by anodic bonding: a general technique for layered materials." *Nanotechnology* 23, 505709 (2012).
- 11 Stender, C. L., Greyson, E. C., Babayan, Y. & Odom, T. W. "Patterned MoS<sub>2</sub> nanostructures over centimeter-square areas." *Advanced Materials* 17, 2837-2841 (2005).
- 12 Lee, Y.-H. *et al.* "Synthesis of large-area MoS<sub>2</sub> atomic layers with chemical vapor deposition." *Advanced Materials* 24, 2320-2325 (2012).
- 13 Liu, K.-K. *et al.* "Growth of Large-Area and Highly Crystalline MoS<sub>2</sub> Thin Layers on Insulating Substrates." *Nano Letters* 12, 1538-1544 (2012).

2 D MATERIAL SENSORS AND DEVICES

Project No. 0190

Jessica Dagher  
University of Dayton

31 August 2014

Government Project Leader  
Dr. Rajiv Berry  
AFRL/RXAS

Southwestern Ohio Council for Higher Education  
Student Research Program  
Agreement Number: FA8650-09-2-5800

## Acknowledgements

My acknowledgements are directed to my advisor, Dr. Christopher Muratore, for providing me with the academic and routine, experimental guidance, my POC, Dr. Rajiv Berry, for providing me with training in the computational area, to Dr. Rajesh Naik, and to all the members of their research groups who have provided assistance, namely, Dr. Christina Harsch, for providing me with the in-laboratory training and supervision.

## General Project Description

This project entails the prediction of adsorption-induced changes in measurable material properties, namely the peptide adsorption onto realistic, two-dimensional (2 D) transition metal dichalcogenide (TMD) surfaces, specifically molybdenum disulfide ( $\text{MoS}_2$ ) (Muratore 2014, Wang 2014, Li 2012). The main experimental objectives include: a) the determination of selectively binding peptides to  $\text{MoS}_2$  crystalline surfaces via phage display; and b) the characterization of the surface via X-Ray diffraction (XRD) and Raman spectroscopy and the confirmation of the binding interaction via imaging or spectrophotometric tools, such as immunofluorescence or atomic force microscopy (AFM).

The main computational objectives for this project include: a) the incorporation of a prior, parameterized force field into existing peptide models to compute the adsorption energies of the peptide to the pristine, inorganic surface; and b) the molecular dynamic (MD) simulations of the energetics of the peptide/TMD interfacial configurations at those surfaces.

## Description of Research

The determination of the selectively binding peptides was performed through phage display, which is described here as three cycles of panning (Figure 1). The peptides are expressed on the surface of M13 phage (pentavalent display of 12-mer peptides that are fused to the phage via protein pIII), which is commercially obtained as a random, combinatorial library from *New England BioLabs Inc.* The library is exposed to the  $\text{MoS}_2$  target, then the target is washed, and the remainder (bound) phage, expressing the binding peptides, is eluted and reused in the next cycle. The plaques from the phage titers are extracted for DNA sequencing. The characterization of  $\text{MoS}_2$  crystals is carried out using XRD (crystalline domains and planes in the crystal lattice) and Raman spectroscopy (signature of molecular vibrations within the sample surface), and X-Ray photoelectron spectroscopy (chemical bonding features).

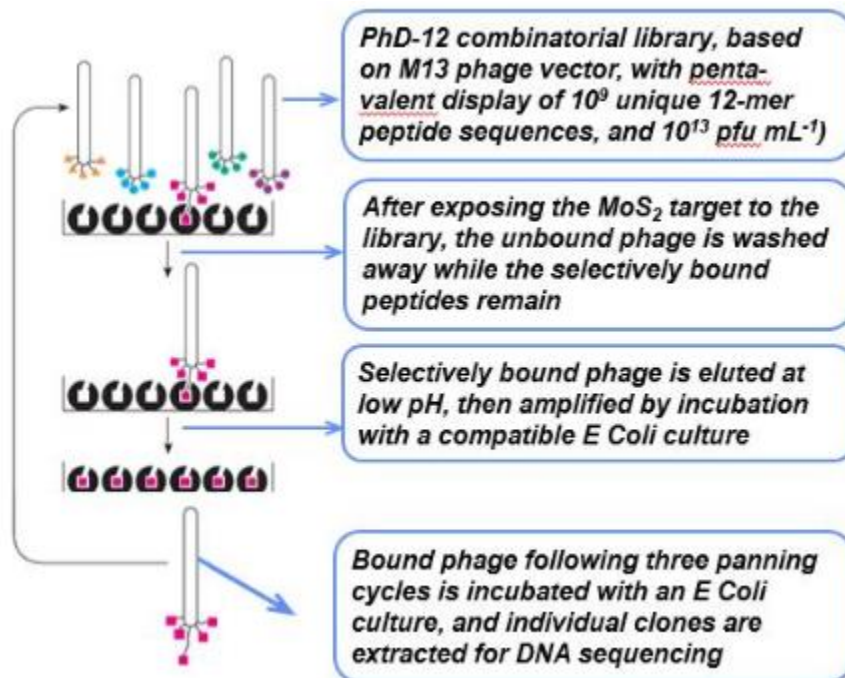


**Figure 65.** Bio panning technique indicating four steps per cycle: target exposure, washing, elution, and sequencing. (Left portion of figure adapted from New England Biolabs, <http://www.neb.com>)

## Results

To date, phage display has been performed in two replicates against the MoS<sub>2</sub> powder. Following three panning cycles, the extracted plaques from the phage titers were amplified and sent to *Genewiz Inc.* for DNA analysis. Table 1 below shows the identified sequences of the phage-expressed binding peptides. Three peptides were found to bind to MoS<sub>2</sub>, in powder form.

Current phage display experiments consist of allowing the phage M13 library to interact with the MoS<sub>2</sub> natural crystal flake, which has a distinct surface morphology, crystallinity, and lattice plane orientations, compared to the powder. The difference in binding will provide insight on the affinity of peptides to the variable, planar/edge surface ratios. Current efforts also include characterization of MoS<sub>2</sub> samples (Figure 2) and confirmation of the binding process using the immunofluorescence assay. The computational goal awaits the development of the force field, which is currently conducted by my colleagues within Dr. Berry's research group.

In the future, this project will involve the use of an experimentally-validated force field for the peptide-MoS<sub>2</sub> surface interactions. It is anticipated that simulations will include the impact of defects and their effect on binding to MoS<sub>2</sub>. Experimental work examining defect densities will complement the computational studies.

**Table 11.** The identified peptide sequences, their respective dominance in the two replicate panning cycles, and their theoretical isoelectric points (pI) at pH of 7.

Binding peptide sequence	Dominant	Theoretical pI
HLLQPTQNPF <del>RN</del>	yes	9.76
VH <del>WDFR</del> Q <del>W</del> W <del>Q</del> PS	no	6.71
W <del>V</del> P <del>W</del> P <del>Y</del> S <del>L</del> S <del>T</del> H <del>H</del>	no	6.92

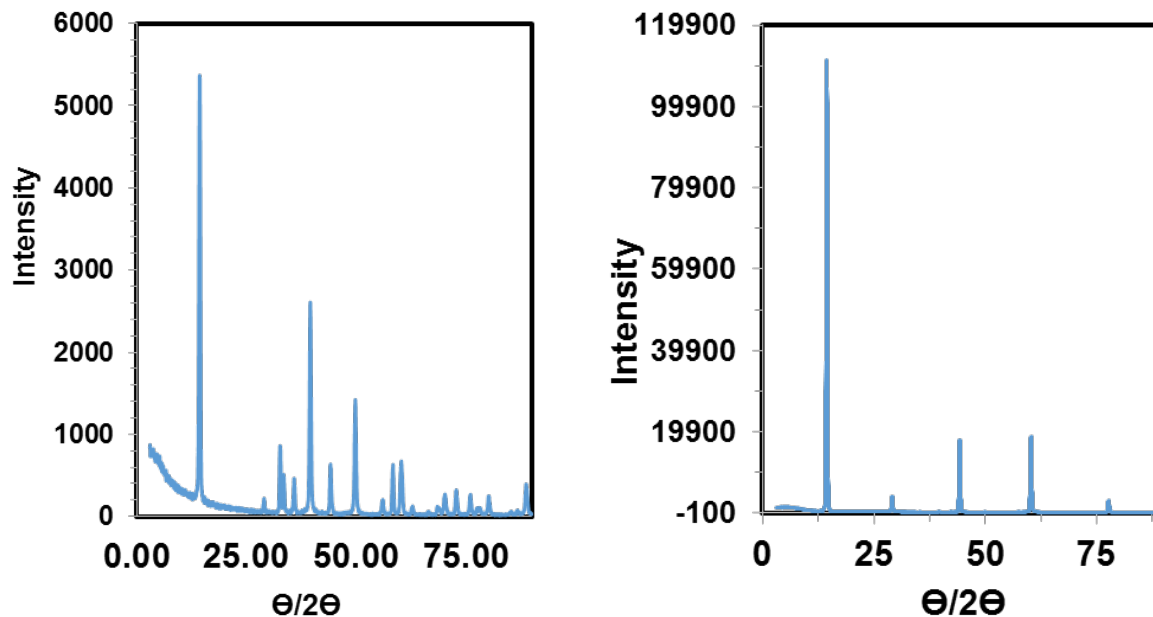


**Figure 66.** X-Ray diffraction pattern of the powder sample (Left) and the flake sample (Right) that are employed in the phage display experiments.

## Works Cited

- Muratore, Chris; Varshney, Vikas; Gengler, Jamie J.; Hu, Jianjun; Bultman, John E.; Roy, Ajit K.; Farmer, Barry L.; and Voevodin, Andrey A. "Thermal anisotropy in nano-crystalline MoS<sub>2</sub> thin films." Physical Chemistry Chemical Physics 16 (2014): 1008–1014.
- Wang, Qing Hua; Kalantar-Zadeh, Kouros; Kis, Andras; Coleman, Jonathan N.; and Strano, Michael S. "Electronics and optoelectronics of two-dimensional transition metal dichalcogenides." Nature Nanotechnology 7 (2012): 699–712.
- Liu, Keng-Ku; Zhang, Wenjing; Lee, Yi-Hsien; Lin, Yu-Chuan; Chang, Mu-Tung; Su, Ching-Yuan; Chang, Chia-Seng; Li, Hai; Shi, Yumeng; Zhang, Hua; Lai, Chao-Sung; and Li, Lain-Jong. "Growth of large-area and highly crystalline MoS<sub>2</sub> thin layers on insulating substrates." Nano Letters 12 (2012): 1538–1544.

## Related Activities

The work was presented in weekly group meetings, at two off site conferences, directed by Dr. Rajiv Berry and Rajesh Naik on July 22-24, 2014 and May 15, 2014 respectively, and at the student poster session, held at AFRL on July 15, 2014.

PROCESSING AND CHARACTERIZATION OF CERAMIC MATRIX COMPOSITES

Project No. 0191

Adam Donovan  
Wright State University

31 August 2014

Government Project Leader  
Dr. Craig Przybyla  
AFRL/RXCC

Southwestern Ohio Council for Higher Education  
Student Research Program  
Agreement Number: FA8650-09-2-5800

## **Acknowledgments**

I thank Craig Przybyla, Jennifer Pierce, and Larry Zawada for all their help with this and all my other projects. I would also like to thank Nick Engel, a fellow student who worked with me on most of my projects this summer. I appreciate the opportunity to work on this project, and look forward to all my future work here at AFRL.

## **General Description of Project**

Research was performed to determine the most effective way of characterizing oxidation in a SiC reinforced SiC ceramic matrix composite (CMC) material. The objective of this project was to connect the amount of oxidation in the microstructure to the changing strengths of different CMC coupons tested under varying conditions. Two main methods were employed to identify the amount of oxidation; namely, optical microscopy and scanning electron microscopy. In the particular effort here, the goal was to attempt to identify which of these two methods is the best way to identify the oxidation in the SiC/SiC CMC material. Once the most effective method for characterization of oxidation is determined, then oxidation in several samples exposed under different condition can be characterized and compared.

## **Description of Research**

In order to identify the amount of oxidation SiC/SiC CMC samples, both the Zeiss Optical Microscope and the Quanta Scanning Electron Microscope (SEM) were utilized. Exposed samples were sectioned, polished, and mounted prior to the microstructural characterization. The Zeiss microscope was employed to capture high magnification (up to 1000x) montage images of a sample to visualize regions of potential oxidation. EDS in the SEM, however, only required low magnification (50x) scans over large regions to measure the basic elemental compounds present on the surface of the sample.

It was originally hypothesized that the oxidation in the primary matrix of the SiC/SiC CMC material is observable optically as a bright white patches. These patches could then be quantified by area fraction through the use of image segmentation. To verify this hypothesis, the more robust method of employing EDS software in the SEM was needed to verify if the white patches observed optically were actually oxidized regions, and to evaluate whether there are other oxidized regions not visible optically.

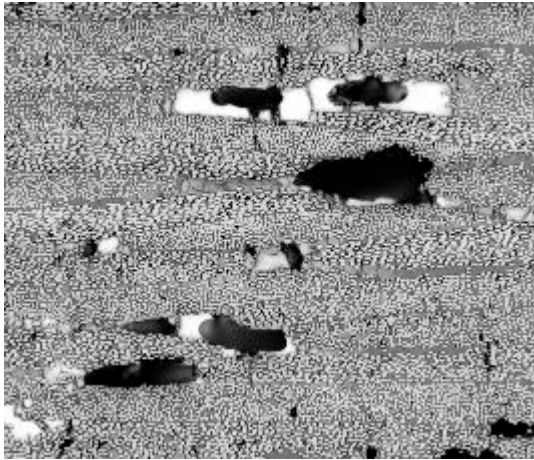


**Figure 1.** An exposed S200 material with oxidation in the matrix. Bright white areas show the proposed areas of oxidation.

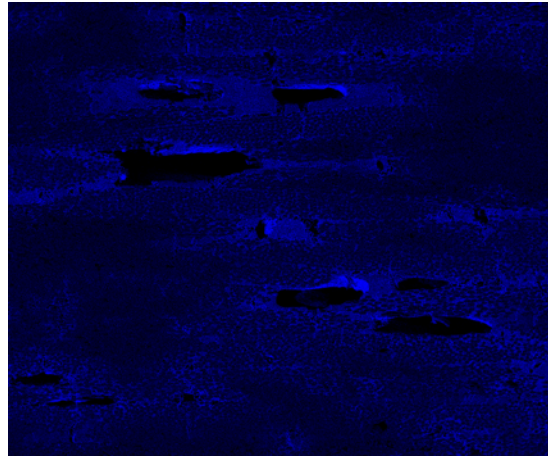


**Figure 2.** An EDS chemical map of oxygen in the S200 materials. Bright blue areas show high levels of oxidation.

After receiving the training required to use the SEM, the EDAX Genesis software was used to create EDS chemical maps of selected samples. These chemical maps qualitatively show the concentrated areas of all of the elements present in the sample. In this case, oxygen was of interest. These maps could be compared to the optical images to see if the previous assumption was correct.

In order to compare the two images, the EDS map was overlaid on the montage image obtained using the optical microscope. Overlay of the images was accomplished in Photoshop. Oxidized regions in the EDS maps are indicated by the blue pixels. Brighter blue areas in the EDS map indicate higher concentration of Oxygen in that area of the sample. In order to determine approximate concentrations of oxidation in the different regions of the EDS maps, spot scans were performed at different regions and the weight percent of each element was calculated. The brighter spots in the EDS map varied from 18.25 wt% to 34.75 wt% Oxygen. The darker spots in the map varied from 5.39 wt% to 8.25 wt% Oxygen.

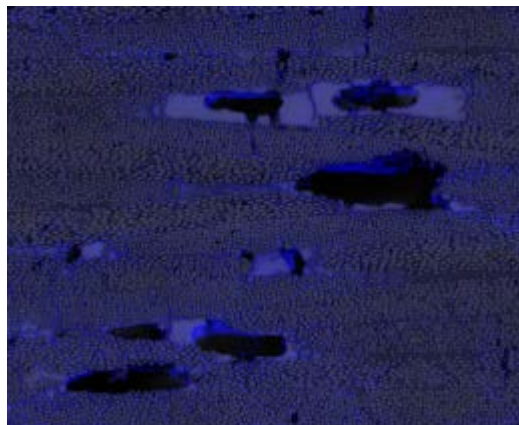


**Figure 3.** An EDS chemical map laid over the optical image of a sample of S200 material. Bright blue areas show high levels of oxidation.

## Results

After comparing the optical and SEM images, the results supported that the bright white areas shown in the optical images do in fact have higher amounts of oxidation than in other parts of the samples. However, there are other areas with just as much oxidation that do not show up as bright white areas in the matrix material. As a result, it is concluded that optical microscopy is not a sufficient means of characterizing all of the oxidation in the SiC/SiC CMC material.

Due to this, a new way to characterize this oxidation is needed. The current plan is to compare the chemical maps produced from exposed samples to those produced from non-exposed samples. By comparing these two and filtering out the noise in the data, it is anticipated that the highly oxidized portions of the samples will be identifiable. Finally, by comparing the oxidation results to the test conditions of different specimens, the relationship between oxidation and service exposure will be better characterized.

PROCESSING AND CHARACTERIZATION OF CERAMIC MATRIX COMPOSITES

Project No. 0192

Nicholas Engel  
Wright State University

31 August 2014

Government Project Leader  
Dr. Craig Przybyla  
AFRL/RXCCP

Southwestern Ohio Council for Higher Education  
Student Research Program  
Agreement Number: FA8650-09-2-5800

## **Acknowledgments**

I would like to thank Craig Przybyla AFRL/RXCCP, Larry Zawada AFRL/RXCC, and Jennifer Peirce (UDRI) for their help, support, and leadership throughout this research. I would also like to thank Adam Donovan for his support on the tasks required for this research.

## **General Description of Project**

Ceramic matrix composite (CMC) materials are being studied for use in aerospace applications, specifically as exhaust components. Exhaust components made from carbon fiber and layered silicon carbide matrices (C/SiC) are being flight tested in order to validate their use as a preferred spares over the original bill of materials in jet engines. Test specimens taken from flight tested components were characterized to determine the extent of material degradation with exposure to field service environments. Sections of material that correspond to the gage sections of the test specimens were evaluated visually, and with optical microscopy, to better relate the effects of the environment on the measured behavior of the material. The overall goal is to understand the relationship between microstructure, environment, and durability.

## **Description of Research**

The focus of this research was to document the extent of damage of C/SiC exhaust components after several hundred hours of field service. The following sections describe the methodology and equipment used and discusses the results of this research.

The methodology used to understand relationships between microstructure, environment, and durability was to measure the retained tensile strength of flight tested material and apply metallography techniques to study the material microstructure.

Test specimens were machined from a field tested component and the retained tensile strength was measured to gage its durability following use. Specimens were tensile testing using a MTS servo-hydraulic test system and the strength and modulus were measured.

The material microstructure was studied and characterized by developing and applying metallography and image analysis techniques to the CMC material. Careful planning and documentation was required to track material sample location. A master cut-plan was developed in AutoCAD software to show the locations of samples in reference to the machined component. Damage was expected to be more visible on the hot-aft side of the component due to the environment that the material is exposed to. For this reason, the orientation of the samples had to be maintained. Detailed notes of the orientation were kept to ensure the data were properly collected and each individual cut section was maintained.

Samples to be studied were cut from larger pieces, mounted and polished. The cutting process is an important step in the overall "material-ographic" characterization. It was determined that samples sandwiched between fiberglass tabbing materials reduces the effect of the shear lip from the saw and ensures a flat surface is maintained during sectioning. A low concentration diamond blade on a gravity fed Buehler Precision Cutting Saw at low RPM and minimal applied weight gave the best results.

Samples were mounted with PolyFast thermosetting resin made by Struers. This mounting material was pressed in a 1" mount at 180 °C and 170 psi of pre-load. An alumina wafer was used to mark the orientation of the sample with relation to the hot face and cold face

The samples were polished using a Buehler AutoMet 250, Buehler TexMet P, and a series of diamond suspensions including 6 $\mu$  and 1 $\mu$ . Once the outer phases of the matrix were nearly free of scratches, the samples were moved to a Buehler Vibromet automated polisher until the desired quality was achieved. The entire sample preparation process required up to several weeks.

The microstructures were documented and studied using optical microscopy. A Zeiss optical microscope equipped with an AxioCam video camera and AxioVision software was the preferred equipment. Images were studied for fraction of cracking and oxidization in the matrix and number of damaged fibers. A tiling method was developed to take a series of images across the surface of the sample at a high magnification (usually 320X). AxioVision software was used to connect the “tiles” of individual images into a “mosaic” image which shows the entire imaged. This method allowed a high resolution and high magnification image of the entire surface of the sample to be obtained.

## **Results**

The results of tensile testing specimens extracted from a field tested exhaust component showed that the retained strength varied with location along the component. The strengths varied from 100% to 50% of the as-manufactured strength of the material. The microstructural analysis was consistent with the tensile results. Near locations with visible material damage and lower strengths a higher amount of cracking and damage in the microstructure was observed.

After several hundred hours of field service, the CMC component showed to be durable but suffered damage due to use. The study of the relationships between the microstructure, location, and tensile strengths is on-going. Plans for analyzing another set of samples representing additional locations from the component have been developed.

CHARACTERIZATION OF TITANIUM ALLOYS FOR USE IN PROCESS MODELING  
AND LIFE-PREDICTION

Project No. 0193

Tyler Weihing  
Wright State University

31 August 2014

Government Project Leader  
Dr. Adam Pilchak  
AFRL/RXCM

Southern Ohio Council for Higher Education  
Student Research Program  
Agreement Number: FA8650-09-2-5800

## **Acknowledgments**

Many thanks go to those who contributed knowledge and time to this research. First and foremost thanks to Dr. Adam Pilchak for contributing time and energy answering many questions related to this research. Thanks to Dr. Joe Tucker for training with DREAM3D software package as well as technical direction. Thanks also to Dr. Michael Groeber and Dr. Michael Uchic as well as Mr. Michael Jackson for input and advice on research direction. Final thanks go to Michelle Harr from SOCHE for invaluable input on MATLAB coding.

## **General Description of Project**

The primary goal of this research was to develop faster and more efficient methods of quantifying micro-textured regions in structural materials. A micro-textured region is defined as groups of similarly oriented grains in a material. An abundance of research has shown that structural properties of a material and the material's microstructure (i.e. grain orientation and size) are closely related. Therefore, clusters of similarly oriented grains increase the effective size of the grain and impact structural properties more significantly.

The researcher used the DREAM3D software package to process existing 2D and 3D electron backscatter diffraction (EBSD) data in order to analyze size and quantity of micro-textured regions in titanium samples. Visualizations were creating using Paraview to validate the results. Once the researcher gained familiarity with the process, MATLAB code was developed to automate the DREAM3D portion of the research.

## **Description of Research**

DREAM3D uses "pipelines" to process a variety of datasets, ranging from EBSD to optical images. These pipelines consist of preprogrammed filters that are capable of manipulating massive datasets and performing calculations to gain information about said datasets.

The pipeline used for this research was finely tuned in order to discover information on the size, location and quantity of micro-textured regions in titanium samples. The code first segmented the data according to the misorientation of the grains, and once this was done the centroids of each grain were calculated. The program then used the centroids of each grain and searched for other centroids within a preset distance. This distance is the "multiples of average diameter" (MAD) parameter in the pipeline. DREAM3D then checks the c-axis orientation of each grain and if the grouped grains are within a set degree tolerance, they are recognized as micro-textured regions. This data is then stored in HDF5 formatting and excel spreadsheets are created as well. The data can then be evaluated to discover information about the location and quantity of the micro-textured zones. This information is then fed through forward models to verify existing models of processed metals.

A problem arises when using this method to find micro-texture. There are three main parameters required to run the pipeline effectively: the misorientation tolerance, the MAD and the c-axis misorientation tolerance. The first and last are kept static, but the MAD parameter must be dialed as a "knob" until Paraview can be used to confirm the proper value. In order to do this, many instances of the pipeline must be run in order to find the correct MAD result. When using high resolution data, each instance can take up to an hour so a method of automation

was needed in order to maximize effectiveness of the DREAM3D software. Thus, the researcher developed MATLAB code that would interface with DREAM3D and run multiple instances of pipelines at once with each instance changing the MAD property so that the proper results could be obtained.

Originally the code was developed as a script, i.e. a code that would be rewritten each time it was used. However, the project evolved and a MATLAB graphical user interface (GUI, shown in Figure 1) was developed in order to simplify the process and make it more user-friendly.

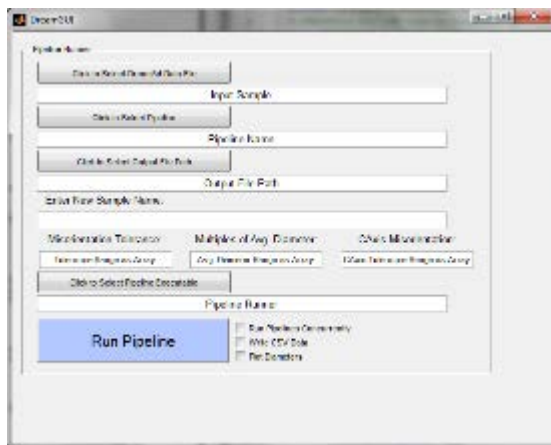


Figure 1. The MATLAB GUI screen.

This allows for other researchers unfamiliar with the code to use the GUI as well. The GUI is very straight forward in its presentation. The user is prompted to select the DREAM3D file they are analyzing along with an existing pipeline file. This is a file that can be created using DREAM3D. The software creates a text file that can be edited and ran with the software. The user then selects the folder in which they would like the data to go to and then from there can pick the misorientation tolerance, the MAD and the C-Axis orientation. These can be single numbers or entered as an array to run multiple instances at once. Once this is done the user finds the pipeline runner executable in their DREAM3D folder and clicks the Run Pipeline button. When the “Run Pipelines Concurrently” check box is selected, the computer can run all instances of the program at once (shown in Figure 2), saving a vast amount of time and labor. This only comes with the caveat of needing a computer with enough power to process the information.

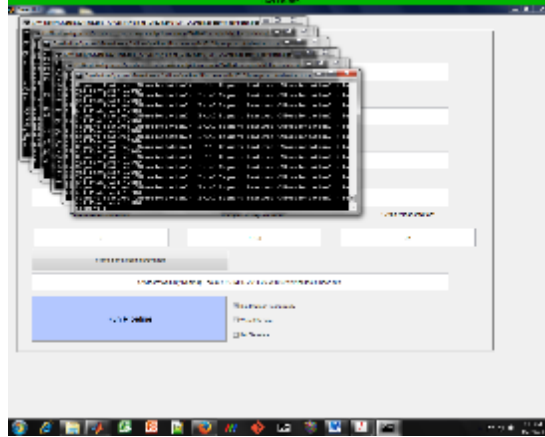


Figure 2. Multiple instances running at once. The MATLAB GUI creates cascading windows for each instance.

## Results

Once the GUI came into use, the researcher was able to use it to greatly reduce the time between EBSD data acquisition and data analysis. A large number of instances of the DREAM3D software must be run with each dataset and having the ability to run all at the same time is a vast improvement. However, there is still a bottleneck relating to the resolution of the EBSD data. As the resolution increases, the data file size increases and thus makes computational time increase exponentially. The researcher is now conducting experiments in optimizing the level of resolution to decrease this factor. These results will aid in reducing total time of future projects drastically.

COMPUTER SCIENCE 3D MODELING, GRAPHICS, ENGINEERING MODELING AND  
ANIMATION

Project No. 0194

Joshua Sommers  
Cedarville University

31 August 2014

Government Project Leader  
Mrs. Robyn Mack  
AFRL/RXOP

Southwestern Ohio Council for Higher Education  
Student Research Program  
Agreement Number: FA8650-09-2-5800

## Acknowledgments

I want to thank Robyn Mack for giving me the opportunity to work here and giving me positive feedback to help improve my abilities. I want to thank the Nick Richards, Douglas Haag, and Paul Deardoff for providing feedback on all that I work on. Lastly, I want to thank Lori Hughes and Ronald Maynard for giving me positive feedback on the projects and helping me to improve in my graphics ability.

## General Description of Project

First, this project involved creating 3D graphics to assist others in the making of 3D logos, 3D wireframes, and to create objects to use as static images. Second, it also involved the creation of 3D animations in Autodesk MAYA and Adobe After Effects. Third, it involved the learning of Adobe Photoshop and InDesign. Fourthly, it involved using PowerPoint to create slideshow presentations as well as dynamic diagrams. Lastly, it involved creating layouts of webpages for the Development Team at AFRL Materials & Manufacturing (AFRL/RX).

All of this was done to help with the Corporate Communications Team and the Development Team at AFRL/RX. They wanted these things to promote forward thinking at AFRL/RX and to bring the graphics up to speed. These things will be used on monitors throughout the AFRL/RX complex, on posters, and on webpages.

## Description of Research

The first main project worked on was documenting all of the graphics and posters throughout the AFRL/RX complex. A person walked through the complex with a camera and took pictures of every poster, picture, monitor, or other graphics material. These pictures were then photoshopped. A document was created that described where the pictures belonged (in which building, which floor, and where on that floor). Then in PowerPoint, blueprints of each floor of each building were added (one per slide). Then a triangle was placed on the blueprint indicating that there was some form of graphics at this spot (Figure 1). If a person clicked on the triangle, they are taken to another slide that contains all of the graphics located at this spot.

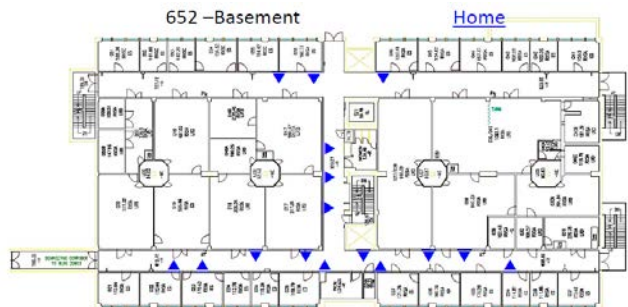


Figure 1. Screenshot of what a typical floor would look like.

The second main project worked on was working with a redesign of the new Intranet for AFRL/RX. Once the main ideas from upper management were composited and previous ideas for this design were looked at, a new design was mocked up. This was handed off to someone else, who took it even farther to what is currently beginning to be programmed.

The third main project worked on was working with the AFRL/RX logo. This logo only existed in 2D. This was taken in Autodesk Maya 2014 and turned into 3D. Once this was completed, the logo was updated to give it a more modern feel (Figure 2). Once these test renders were approved, a ten second animation was created in Autodesk Maya 2014 and then composited in Adobe After Effects CS4.



Figure 2. 3D logo designed and rendered in Autodesk Maya.

The last man project worked on was the updating of the RX Facebook. This involved editing people's pictures, and adding them to their respective division. Once this was accomplished, the pictures were hyperlinked to the folder of their pictures. If the person had a bio, their name was hyperlinked to their bio.

All of these projects went through many different stages of feedback from many different people.

## Results

Through this project, a greater understanding of topology was gained. Many of the projects required the use of 3D lettering. This is one of the hardest things to build in 3D. Simply spending the time building things in 3D has allowed a faster turnaround time and a greater understanding of quad theory and how it is used. This project also has brought a greater understanding of the Autodesk Maya and its many features.

MULTISCALE MECHANICS OF BOND SCISSION OF POLYMER COMPOSITES

Project No. 0196

Allison Ecker  
University of Dayton

31 August 2014

Government Project Leader  
Dr. Timothy Breitzman  
AFRL/RXCC

Southwestern Ohio Council for Higher Education  
Student Research Program  
Agreement Number: FA8650-09-2-5800

## **Acknowledgements**

I would like to express gratitude towards the Southwestern Ohio Council for Higher Education and Air Force Research Laboratory for this opportunity. Many thanks are extended to Drs. Stephen Barr and James Moller for providing guidance and technical support throughout the process. In addition, I would like to recognize Drs. Timothy Breitzman and Rajiv Berry for their leadership and Drs. Dhriti Nepal, Gary Kedziora, and Samir Naboulsi for their helpful discussion.

## **General Description of Project**

An increasing interest in thermoset polymers and their ability to provide a strong, lightweight material has led to research studying the methods of fracture through experimental and computational methods. There has been a void in methods that are both accurate on a quantum level and computationally viable, until the research which is currently underway. This research endeavors to undertake the responsibility by integrating a method which uses a quantum mechanics/ molecular mechanics (QM/MM) approach.

Current QM/MM methods consist of identifying a region prior to the beginning of simulation which will likely have a bond break, such as before a crack tip; this method is capable of detecting these areas during the course of simulation using internal stresses and distances between atoms. To develop this method further, tests are being completed to determine the correct size of the QM region.

Once the method is developed it will be used to explore the properties of the interphase and interface region of epoxy systems with fiber systems (Moller). Nano-infrared spectroscopy will be able to identify the species present within the interphase and at the interface. Once this information is obtained, it will feed into the computational simulations of interphase interactions and mechanical properties may be determined not only for epoxy systems, but for its composites as well.

## **Description of Research**

Molecular Dynamics simulations were performed to build and crosslink the systems utilized in the QM/MM method development. An important component of the study entailed producing a repeatable result; this was accomplished by building several configurations of the components listed in Table 1. Out of all systems built for the study, those listed in the table were chosen for their ability to be compared to literature (Glad). For each system, the curing agent used was methylene dianiline (MDA), shown in Figure 1. As part of the study, the chain length of the diglycidyl ether of bisphenol A (DGEBA) was varied; the repeat unit is shown boxed in Figure 2, which is a full schematic of two DGEBA molecules already reacted with one molecule of MDA. The monomers were labeled DGEBA<sub>n</sub>\_X, where X represents the number of repeat units present.

Table 1. The components of five key systems are comprised of molecules of epoxy and amine groups. Diluent molecules consist of epoxy chains with unreactive end groups.

System Number	Amine (number of molecules)	Epoxy (number of molecules)	Diluent (number of molecules)
1	MDA (246)	DGEBA <sub>n</sub> _0 (492)	-
5	MDA (147)	DGEBA <sub>n</sub> _1 (294)	-
9	MDA (82)	DGEBA <sub>n</sub> _3 (164)	-
13	MDA (57)	DGEBA <sub>n</sub> _5 (114)	-
29	MDA (15)	DGEBA <sub>n</sub> _11.5 (30)	DGEBA <sub>n</sub> _5 (63)

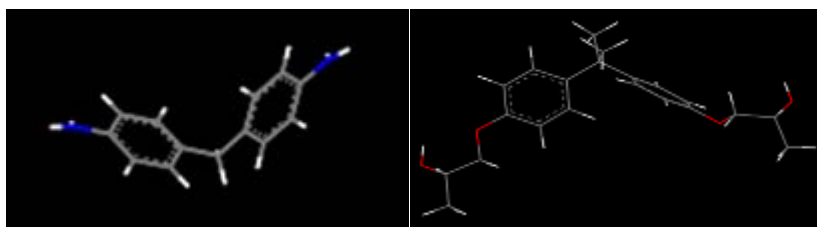


Figure 1. Materials Studio representations of MDA (left) and DGEBA<sub>n</sub>\_0 (right). The DGEBA molecule is shown with the epoxide ring broken, as it is formatted before the cross-linking process.

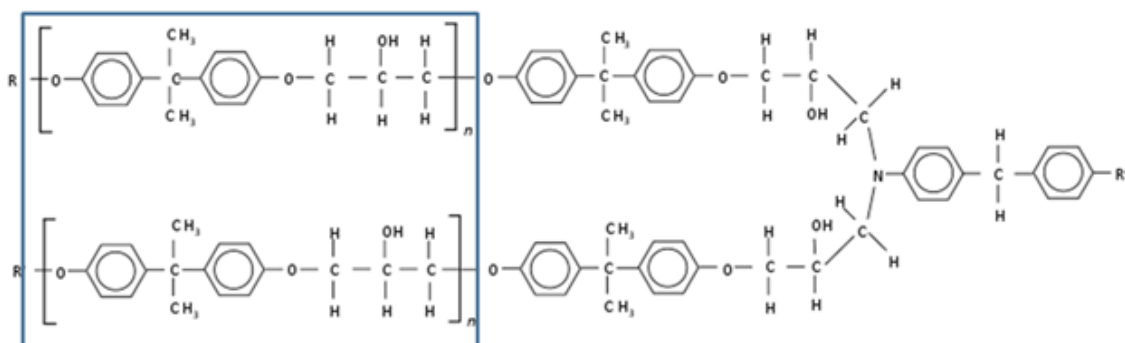


Figure 2. Diagram of a cross-linked system comprised of two DGEBA molecules and one MDA molecule. Shown boxed are the repeat units of the two DGEBA molecules, which were varied  $n = 0, 1, 3, 5$ .

The full uncross-linked systems were built using the Amorphous Cell engine within Materials Studio. The resulting configurations for each system are next cross-linked by creating bonds between the modified DGEBA resin end group, shown in Figure 3, and the amine group of MDA (Rigby).

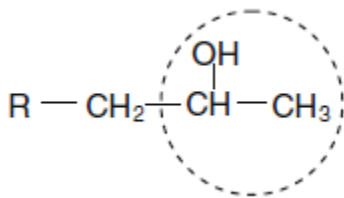


Figure 3. The modified DGEBA resin end group which reacts during the cross-linking procedure.

Once cross-linked, these systems will be used for other aspects of the project, including the QM/MM project mentioned above and several explorations into fracture properties through continuum scale modeling. Preliminary tests were run for uniaxial tension using LAMMPS software, with the results in the following section.

## Results

Before more complex strain methods or quantum mechanics are applied, the systems were run using the classical force field CVFF using LAMMPS software. Figure 4 shows a stress-strain curve for a DGEBA<sub>n</sub>\_0 and MDA system. Marked on the plot are the portions of the curve which indicate that the epoxy system experiences strain-softening, a phenomenon often seen in thermoplastics, before strain-hardening.

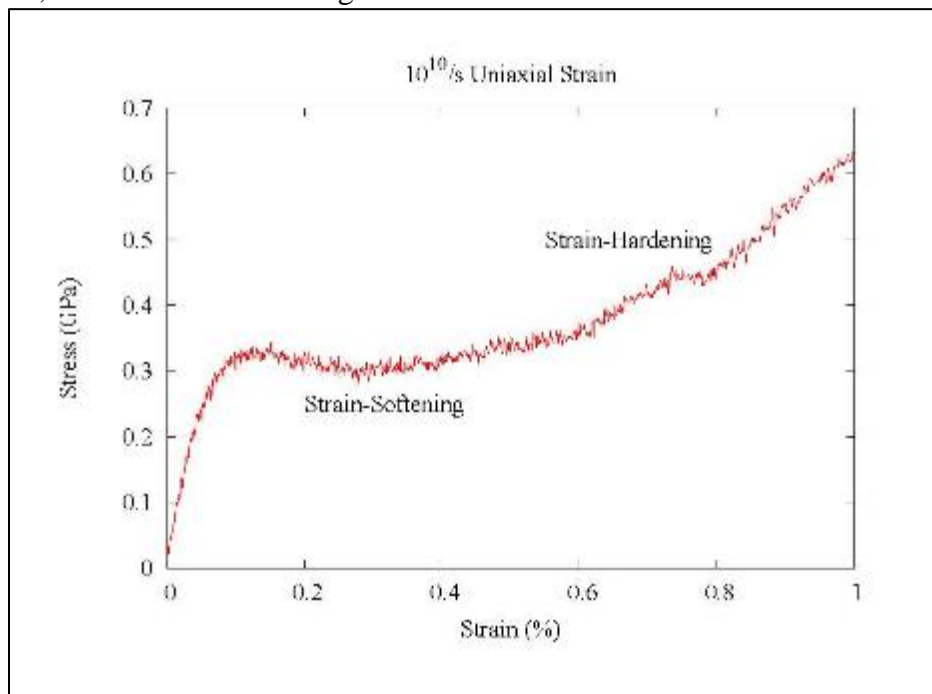


Figure 4. Strain-softening and strain-hardening are observed for the epoxy systems.

As mentioned in Moller et al, the tensile properties of epoxy systems can vary with the strain rate. The benefits to having a slower strain rate is that there was the ability to record a larger amount of data points for each strain value, enhancing the curves. However, as the strain rates reach closer to those available for experiments, the computational time drastically increases. Therefore, the strain rates in this preliminary test were restricted to those listed in Table 2.

Table 2. The strain rates used in the preliminary studies and the computational time required for each.

Strain Rate (1/s)	Computational Time After Equilibrium (hr)
$10^{11}$	.017
$10^{10}$	.17
$10^9$	1.7
$10^8$	17
$10^7$	177

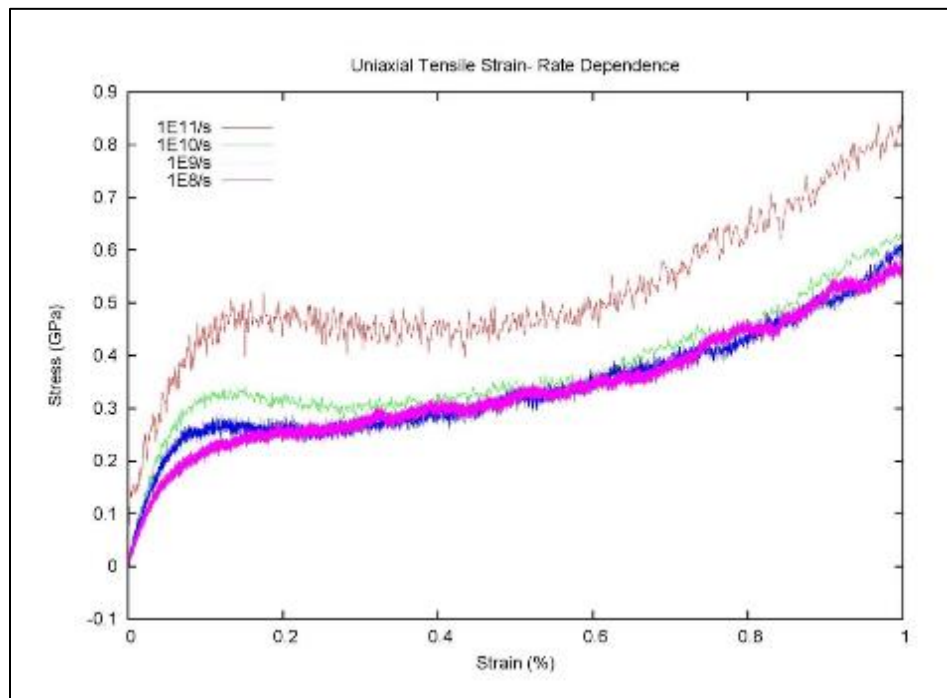


Figure 5. Stress-strain curves obtained for uniaxial tensile strain. Results for four strain rates shown, demonstrating the dependence of the shape of the curve on rate of strain.

## Works Cited

- D. Rigby and L. Subramanian. "Contract Research Report for Advanced Composite Polymers Project." San Diego, CA: Accelrys, Inc. 2009.
- Glad, M.D. and E.J. Kramer. "Microdeformation and Network Structure in Epoxies." *J.Mater.Sci.* 26 (1991): 2273.
- Moller, J.C. et. al. "Simulation of Fracture Nucleation in Cross-Linked Polymer Networks." *JOM* 65 (2013): 147-167.

## Related Activities

While working at Wright Patterson Air Force Base this summer, I have been exposed to several interesting topics not directly related to my project through summer student seminars, branch meetings, and a workshop for multiscale characterization of advanced materials. In addition, I was exposed to an abundance of literature concerning the computer simulation of thermoset polymers

COMPOSITE DAMAGE TOLERANCE ASSESSMENT METHODOLOGIES

Project No. 0198

Daniel Rapping  
Wright State University

31 August 2014

Government Project Leader  
Dr. David Mollenhauer  
AFRL/RXCC

Southwestern Ohio Council for Higher Education  
Student Research Program  
Agreement Number: FA8650-09-2-5800

## **Acknowledgments**

It has been a pleasure to work all summer at AFRL, and has helped me grow as a student and an engineer. I would like to thank SOCHE for hiring me and AFRL for investing in the future with this type of research. To my colleagues I want to express complete gratitude. To Ph. D. candidate Mark Flores I would thank you for your assistance in learning about composites and how to set up an experiment. To my advisor Dr. Mollenhauer, I want to thank you for your teaching and inclusive attitude. To Kevin Hoos, John Camping, Eric Lindgren and Kevin Shipley thank you for all the time spent teaching me about composites and aiding in the research.

## **General Description of Project**

Research was started into the compressive strength after impact of the composite system IM7-977-3. This research was done in order to bolster the modeling accuracy and predictive ability of AFRL/UDRI in house finite element analysis (FEA) software BSAM (B-Spline Analysis Method). This research was undertaken in order to better understand the failure modes of composites subject to low velocity impacts. The goal of compressive research is to understand how and why global buckling occurs in composites and be able to accurately predict when this failure will occur based on non-destructive evaluation (NDE) that can be completed in the field. This will provide a set level of fidelity needed by the NDE teams to provide enough data to accurately determine the remaining field life of active duty composite components.

## **Description of Research**

To understand how the in house software BSAM worked early time was spent learning the functionality of the pre-processing software called virtual textile morphology suite (VTMS) as well as the FEA software GMSH. This knowledge was key to understanding how to create functional finite element input models that could be placed under mechanical loads in order to predict stresses, strains, continuum damage mechanics, and fiber failure in modes that composite systems fail. Following the ASTM (American Society for Testing and Materials) D7136 standard for testing the impact resistance of composites, a matrix was constructed detailing the labeling of each panel and the fiber direction or layup of each panel (Table 1).

Table 1. Composite Layup Matrix

Composite Layup	Panels Size	Panel Number	ID#	Date Made	Plies
[45/0/-45/0/45/90/-45/0/0/45/0/-45]s	24"x24"	14030	A1	3/28/2014	24
[45/0/-45/0/45/90/-45/0/0/45/0/-45]s	24"x24"	14024	A2	3/14/2014	24
[45/0/-45/0/45/90/-45/0/0/45/0/-45]s	24"x24"	14026	A3	3/20/2014	24
[45/-45/45/-45/90/-45/0/45/-45/45/-45/45]s	24"x24"	14018	B1	2/20/2014	24
[45/-45/45/-45/90/-45/0/45/-45/45/-45/45]s	24"x24"	14022	B2	2/28/2014	24
[45/-45/45/-45/90/-45/0/45/-45/45/-45/45]s	24"x24"	14023	B3	3/6/2014	24
[45_3/0_3/-45_3/90_3]s	24"x24"	14009	C1	1/30/2014	24
[45_3/0_3/-45_3/90_3]s	24"x24"	14012	C2	2/6/2014	24
[45_3/0_3/-45_3/90_3]s	24"x24"	14007	C3	1/24/2014	24
[45/0/-45/90]3s	24"x24"	13085	D1		24
[45/0/-45/90]3s	24"x24"	13090	D2	12/26/2013	24
[45/0/-45/90]3s	24"x24"	14006	D3	1/21/2014	24

After labeling and inspection the panels were sent to Kerf Water Jet Inc. to be cut into specimens sized 4" by 6" as seen in below (Figure 1).

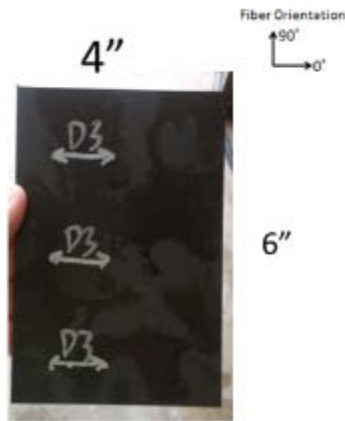


Figure 1. Sample specimen cut and labeled according to specifications.

After completing labeling of samples efforts were made to determine the best mesh density to use in the finite element examples. A mesh study comparing the results of a fine, medium and course density mesh was completed and it was determined that a course mesh works best currently. This is due to quick run times and limited edge effects. After a mesh was chosen boundary condition tests were run to determine the best bounds for the computer model. Several input files with layups matching panel C2 were compiled and ran in compression predicting a failure strength of 451 MPa for an un-impacted panel.

Since one of the panels (A2) was warped several of these specimens were used to make sure the test fixture worked, as well as providing base line data to compare to the computer models. Several panels were impacted at 10 J to make sure the impactor and data collection device functioned. These panels were c-scanned to see the pattern of delamination.

An impacted panel was then placed in the test fixture and compressed to failure at 195 MPa, while an un-impacted panel was compressed to failure at 205 MPa. These values are not impossible but significantly different from the computer model and it is currently unclear if this is a result of the warped panel or other factors.

For the compression tests digital image correlation and strain gauges were debated as possible methods to collect strain data. One of the compression tests used all strain gauges and this data was compared to a sample without gauges using digital image correlation. It was then decided that digital image correlation would be sufficient for collecting data, and ensuring the test fixture prevented shear buckling or displacement of the sample. Data from the BSAM simulations was output and interpreted via Matlab scripting files.

## Results

This summer research has created a solid base for the continuation of this research program. The capabilities of BSAM were pushed to their limits and already change within the program has begun. A mesh model has been established and created for future model runs. The panels were cut to size, and the test fixtures were checked to ensure usability. It is clear that there is something off about the computer simulation results but progress is being made on correcting material properties and other issues with the input files. There are several things yet to be decided such as the impactor head size and impact energy but work is still being done to determine this information. This research position was able to provide an education on how to run several finite element analysis software packages, how to set up a test matrix, and how run an experimental test program.

## Works Cited

- ASTM Standard D7136M, 2012, "Standard Test Method for Measuring the Damage Resistance of a Fiber-Reinforced Polymer Matrix Composite to a Drop-Weight Impact Event," ASTM International, West Conshohocken, PA, 2005, DOI: 10.1520/C0033-03, [www.astm.org](http://www.astm.org).
- ASTM Standard D7137M, 2012, "Standard Test Method for Compressive Residual Strength Properties of Damaged Polymer Matrix Composite Plates," ASTM International, West Conshohocken, PA, 2005, DOI: 10.1520/C0033-03, [www.astm.org](http://www.astm.org).
- C. Geuzaine and J.-F. Remacle. *Gmsh: a three-dimensional finite element mesh generator with built-in pre- and post-processing facilities*. International Journal for Numerical Methods in Engineering 79(11), pp. 1309-1331, 2009.

STRUCTURAL MATERIALS EVALUATION

Project No. 0199

Garrett DeFazio  
Wright State University

31 August 2014

Government Project Leader  
Dr. Jeff Calcaterra  
AFRL/RXSAS

Southwestern Ohio Council for Higher Education  
Student Research Program  
Agreement Number: FA8650-09-2-5800

## **Acknowledgments**

I would like to thank the following people for their professional guidance during this project. Dave Roberts for background information and supplying the parts for investigation, Jeff Calcaterra, Tim Swigart, Michael Hirsch, and Adam Long for informational support, Ed Porter for Non Destructive Inspection work, and Dave Pavlik and Steve Thompson for mechanical testing of the specimens.

## **General Description of Project**

The task at hand was to perform a failure analysis project that would provide an understanding of the failure analysis process. After completion of this project the student should have a new set of skills that can be applied to Air Force related projects. The project was oriented around a car (Cobra replica). The cars' alternator bracket fractured causing a series of events that led to the car crashing on a closed race course. The failure analysis process began by documenting and photographing the parts in question in the as-received condition. This documentation is critical to the researcher because components are normally destroyed in the failure analysis process. After the parts were photographed, they were examined using an optical microscope to be inspected for defects at magnifications up to 5x. Once the parts were examined, a series of equipment was used to inspect the parts on a microstructural level. This equipment consisted of a mounting press, polisher, and microscope. The sample would be suspended in a mount and then polished until there were no visible scratches. After polishing, the mount would be etched to bring out the microstructure. The microscope could then be used to examine and document the microstructure up to 500x. The purpose of doing all of this is to provide the customer with a cause of failure and a recommendation on how to fix or avoid the problem in the future. These results will help the customer make an informed decision on the material/design when reconstructing the vehicle in the future.

## **Description of Research**

Any failure analysis process starts off with background research. The researcher is to find important information on the materials and structure of the system in question. After the literature survey, the first task is to document the parts that are received from the customer. This includes documenting part numbers and taking a series of as-received photos. The as-received photos can be used to show the customer exactly how the researcher received them and can be referenced to later in the investigation.

The next step is to optically inspect the parts in question. This can be done visually and with an optical microscope. This allows the researcher to find and document any fractures or defects that are on the surface of the parts in question. When defects are found it's a good idea to document where they are so they can be inspected with a higher power microscope later.

After optical examination the parts need to be examined without hurting the current state they are in. This is called Non Destructive Inspection (NDI) and allows the researcher to keep the parts in an as-received state. The NDI process used on the parts was called Florescent Penetrate Inspection (FPI). Before FPI can be done the part must be cleaned thoroughly. FPI allows the researcher to see any other defects on the parts that they could not see with their eyes or the optical microscope. In this case there were no other defects found on the parts.

Once NDI is completed it is time to clean the parts so the fractures can be processed and examined. In this case there were two fractured parts. One was an LA 4140 steel bolt and the other was a 6061-T6 aluminum alternator bracket. The alternator bracket had not broken off completely so the fracture surface was opened in the laboratory. The fracture surfaces are now ready to be examined in a Scanning Electron Microscope (SEM). This allows the user to examine the fracture surfaces and take detailed pictures of the surfaces. The results from the SEM will help the researcher piece together exactly how the part started its fracture. In this case it helped find the initiation site, fatigue marks, and overload on the fracture surfaces. This information is crucial when investigating how a material failed.

After the researcher has an idea of what caused the failure it is important to verify the materials processing. This means that the material must meet specification provided by the customer. This was done by analyzing the microstructure, hardness, strength, and chemical composition of the materials. These properties can be checked with official Air Force documents to see if they meet a minimum requirement.

## Results

In this failure analysis project it was discovered that the aluminum bracket did not meet minimum specifications provided by AMS documents for tensile strength and hardness. The minimum tensile strength allowed was 42 KSI per AMS 4017. Since one test did not meet the minimum requirement it means the material is out of spec. It was also found that the dimensions of the alternator bracket may have been too small to effectively support an aftermarket alternator. These discoveries would prompt a design and possible material change. The failure mechanism of both parts was fatigue that then overloaded until the parts fractured. The recommendation in this case was for the customer to find a bracket with thicker dimensions in the support areas. In Figure 1 you can see the two parts in question. In table 1 you can see the tensile strength results.



Figure 1. As received photograph taken of the parts submitted for analysis. The fractured bolt and bracket were the main parts in question.

Table 1. Summary of mechanical properties of the aluminum bracket. Table provided by Dave Pavlik.

Specimen No.	Tensile Yield Strength, $F_{ty}$ (ksi)	Ultimate Tensile Strength, $F_{tu}$ (ksi)	Elongation (%)	Reduction of Area (%)	Elastic Modulus (msi)
T_1	39.7	42.3	17.1	59.8	10.4
T_2	39.5	42.3	17.1	60.9	9.6
T_3	39.4	41.9	18.1	59.7	11.1
AMS 4027				<i>n/a</i>	<i>n/a</i>